THE MOSES ROCK DIKE:
GEOLOGY, PETROLOGY AND MODE OF EMPLACEMENT OF A KIMBERLITE-BEARING BRECCIA DIKE, SAN JUAN COUNTY, UTAH

Thesis by

Thomas Richard McGetchin

In Partial
Fulfillment of the Requirements
for the Degree of Doctor of Philosophy

California Institute of Technology
Pasadena, California
1968

(Submitted November 9, 1967)

ACKNOWLEDGEMENTS

I am grateful to Drs. E. M. Shoemaker and L. T. Silver for material and moral support and guidance throughout the course of this project, and am indebted to both for criticism and many stimulating discussions. I am especially indebted to Dr. Shoemaker for suggesting the problem.

Many persons provided support of different kinds which aided in the completion of the field work, including: Mr. J. Alderman, G. Nakata, J. Van de Veer and D. Andrews, U. S. Geological Survey, Flagstaff, Arizona; Jim Hunt, Emory Hunt and the staff of the San Juan Trading Post, Mexican Hat, Utah; Dr. H. H. Schmitt, National Aeronautics and Space Administration, Dr. J. Zioney, U. S. Geological Survey; the Navajo Tribe and Navajo Rangers; and finally, Mr. Thomas Black, Mexican Hat, Utah, who was partially responsible for expediting the final week of field work.

Electron microprobe data were obtained with the assistance of A. A. Chodos. Drs. A. Bence, R. Naylor and A. L. Albee provided valuable advice and assisted in the computer reduction of microprobe data. Rudolph von Huene prepared polished thin sections for microprobe analyses. Dr. B. Kamb provided a single-crystal x-ray photograph of one specimen, and Mrs. Bep Bingham, x-ray diffraction analyses of several minerals. Mrs. Kathy Savin aided in the mineral separations. Mrs. Lilly Ray helped reduce the microprobe data.

Financial support was provided either directly or indirectly by: The Geological Society of America (Penrose Grant); the U. S.

Geological Survey (field support, including special aerial photographs, specially prepared topographic base maps, field vehicles and chemical analyses); Division of Geological Sciences, California Institute of Technology (research funds, research facilities and graduate teaching assistantships), National Aeronautics and Space Administration (graduate traineeship); the U. S. Atomic Energy Commission (research funds from grant AT (04-3) - 427); and the U. S. Air Force (funds covering some travel expenses during the terminal stages of preparation of this thesis, after the author was called to active Air Force duty).

I have benefited greatly from discussions with many persons in addition to my principal advisors, particularly staff and students at the California Institute, but also members of the U. S. Geological Survey, in Flagstaff, Menlo Park and Washington, D. C.

Mrs. Linda Bence and Mrs. Nancy Parker assisted in the preparation of the manuscript; Mrs. Ruth Talovich, Miss Cathy Clancy and Mrs. Florence Porter helped with the drafting; Mrs. Evelyn McGetchin assisted in the field, typed early versions of the manuscript and the final draft.

Finally I wish to express sincere gratitude to the Division of Geological Sciences and the California Institute for financial support, and most of all for an exciting tenure as a graduate student.

ABSTRACT

The Moses Rock dike is a well-exposed, four-mile long, kimberlite-bearing breccia intrusion in the east central Colorado Plateau, one of eight known kimberlite-bearing diatremes in the province. The dike occurs in gently dipping beds of the Permian Cutler Formation, 2 miles west of the Comb Ridge monocline in eastern Monument Valley, Utah. Contacts are little altered and the wall rocks generally undeformed. The present erosion surface is probably about 5,000 feet below the surface at the time of emplacement. By volume, the breccia in the dike consists of Cutler formation blocks, 72%; limestone fragments from underlying Paleozoic formations, 13%; crystalline rock fragments, 3%; and kimberlite, 12%. Essentially undiluted kimberlite occurs only locally, and occupies only about 1% of the exposed parts of the dike. Mineral constituents of kimberlite are generally dispersed through the unconsolidated breccias.

The breccias, including kimberlite, were probably emplaced as a fluidized solid-volatile system. This conclusion is based on the following observations: (1) No silicate melt was intruded at the level present erosion surface, (2) the breccias are particulate on all scales, (3) the particle size frequency distributions of the breccias are like those produced in comminution processes, (4) different types of breccias are intricately mixed, and (5) the mineral constituents of the kimberlite are commonly highly diluted with rock debris. Relationships of the breccia units suggests that flow of the fluidized system was concentrated in channels, now occupied by breccias that contain the largest <u>upward</u> displaced fragments and the largest crystalline rock fragments. Apparently the dike was emplaced along a fissure on which channels soon developed. A local joint system parallel to the contact, which cross-cuts regional joints, apparently played a key role in the dike formation and brecciation process.

Crystalline rock and mineral fragments found in the dike range from acid to ultramafic types and are believed to represent rocks derived from the vent walls during the eruption. On the basis of the relative size and abundance of the xenoliths, it is inferred that metabasalt, granite and granite gneiss are abundant in the upper part of the crust, along the dikewalls; diorite, gabbro, mafic amphibolite constitute intermediate crystal layers; and mafic granulite and possibly hydrated ultramafic rocks constitute the lower crust. The suite of presumed crustal rocks is predominantly metavolcanic or metaplutonic, not metasedimentary.

Dense and ultramafic fragments possibly derived from the mantle include antigorite-tremolite schist, jadeite-rich clinopyroxenite, eclogite, spinel-websterite, and spinel-lherzolite. The presence of garnet-periodotite at depth is inferred from the suite of mineral inclusions observed within pyropic garnets.

Kimberlite of the Moses Rock dike is believed to be derived mechanically from physically disaggregated spinel and garnet peridotite in the mantle. All other rocks are believed to be accidental inclusions from the vent walls. Tentative P-T assignments to kimberlite clinopyroxenes based on their compositions suggests they are derived from various depths ranging from 50 to about 150 kilometers where the indicated temperatures are modest, about 900 °C.

Titanoclinohumite observed in kimberlite and as inclusions in pyropes may contain most of the water in the upper mantle.

The Mohorovicic discontinuity apparently occurs in a petrologically complex region and may coincide with phase and compositional transitions, including hydration. A compositional transition between spinel and garnet periodotite with increasing depth in the mantle is consistent with the observations. The variety of ultramafic types and the complexity of the textures in the xenoliths suggest the mantle may be as complicated as the crust in composition and history.

Numerical hydrodynamic models of eruption show that flow velocities are probably controlled by viscous losses and expansion of a volatile phase near the surface. Field observations of the largest blocks transported upward in the dike suggest flow velocities of 10 to 50 m/sec at the level of the present surface. Upward extrapolation by use of theoretical models suggests velocities of about 400 m/sec for the erupting fluidized system as it reached the earth's surface.

The Moses Rock dike probably formed by eruption of kimberlite from a large reservoir in the mantle. The eruption was driven by volatiles, apparently mostly H_2O. The kimberlite consists of physically disrupted rock from the reservoir environment.

TABLE OF CONTENTS

LIST OF FIGURES

LIST OF TABLES

LIST OF PLATES

PART I INTRODUCTION

The Moses Rock dike is one of a cluster of kimberlite-bearing dikes and diatremes located on the Colorado Plateau. Of all the known occurrences of kimberlite in the world, none are better exposed than these.

Kimberlite pipes and dikes are of interest to geologists because they are the primary source of diamonds. The scientific significance of kimberlite pipes, however, is as great as their economic importance and to the student of the earth's interior, the wealth of information to be obtained about the deep subsurface from the study of kimberlites has a glitter almost as eye-catching as the diamonds themselves. Perhaps the first student of the kimberlites to grasp their significance was P. A. Wagner (1914, 1928) who recognized that the variety of exotic fragments contained as xenoliths in kimberlite must represent samples from the vent walls over long, perhaps vast, vertical distances over which the kimberlite traveled on its way to the surface. Some of these fragments may have been derived from depths within the earth far beyond man's reach by ordinary means of direct sampling.

Among the scientific problems that can be investigated by study of the kimberlite pipes are questions regarding the nature and composition of the earth's upper mantle, the composition of the earth's crust as indicated by the abundant and varied xenoliths, the nature of the processes by which the kimberlite is transported from an apparently deeply buried reservoir to the surface, and how these processes are related to the geologic history and tectonics of the region in which the kimberlite intrusions are found. The extent of current research bears witness to the consensus that the kimberlite pipes are, figuratively, telescopes directed downward into the earth's interior through which a surprisingly clear view of the earth to a rather great depth is emerging.

The most famous and well-studied kimberlite pipes and dikes are located in Africa (Wagner, 1914, 1928; Holmes, 1936; Williams, 1932; Dawson, 1962; Edwards and Howkins, 1966). Others are known, however, in Siberia (Krutojarky, 1958; Smirnos, 1959; Davidson, 1962), Czechoslovakia (Davidson, 1962) and placer diamond deposits in Australia and South America suggest their presence on those continents as well. In North America, diamond-bearing kimberlites are known in Arkansas (Miser, 1922, 1923; Miser and Ross, 1925) and dikes and pipes containing kimberlite or material closely related to kimberlite occur in the eastern United States (Brock and Heyl, 1961) as well as on the Colorado Plateau.

Kimberlite-bearing dikes and diatremes occur at 8 known localities scattered about the east-central Colorado Plateau (Figure 1). A cluster of vents occur in the east part of the Monument Valley along the Comb Ridge monocline which forms the eastern margin of the Monument uplift, two important structural elements of this part of southeast Utah and northeast Arizona. The Mule Ear diatreme, the northern-most of the known Colorado Plateau kimberlite vents, is an elliptical pipe which occurs near the axis of the monocline just south of the San Juan River. Five miles southwest lies the Moses Rock dike. Two miles northwest of the Moses Rock dike is a roughly semi-circular collapse structure, the Cane Valley diatreme. Approximately six miles southeast of the Moses

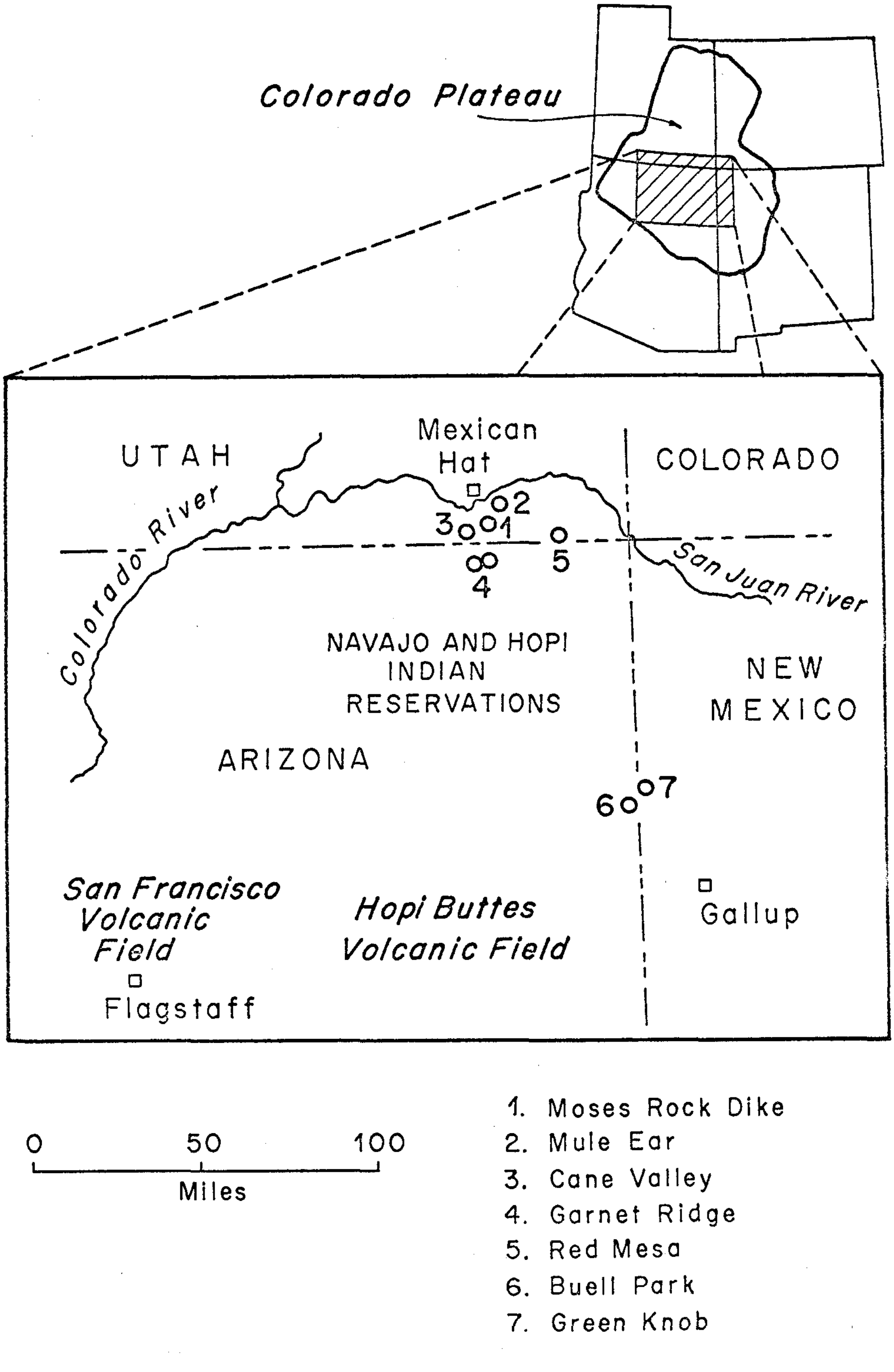

Figure 1. Index map showing location of kimberlite-bearing pipes and dikes on the Colorado Plateau

Rock dike, on the east side of the Comb Ridge monocline and just south of the Utah-Arizona border are two roughly elliptical diatremes at Garnet Ridge. At Red Mesa, Arizona, approximately 20 miles east of Garnet Ridge is a solitary kimberlite-bearing dike which at one spot widens into a nearly circular diatreme. Another cluster of diatremes occurs on the east flank of the Defiance uplift, along the Defiance monocline near the Arizona-New Mexico border northwest of Gallup, New Mexico. The largest is a circular kimberlite diatreme at Buell Park near Fort Defiance, Arizona. Two smaller kimberlite plugs occur at Green Knobs, approximately 5 miles northeast of Buell Park. Sketch maps of the Colorado Plateau kimberlite diatremes are shown in Figure 2.

The Moses Rock dike, near Mexican Hat, Utah, was chosen for study because of its unusual dike form, relatively large size and generally excellent exposure. The internal structure of the dike varies along its length and the processes by which it has been formed appear to have been arrested at various stages. An assemblage of crystalline rock fragments which is apparently typical of the Colorado Plateau kimberlite-bearing diatremes is found within the dike.

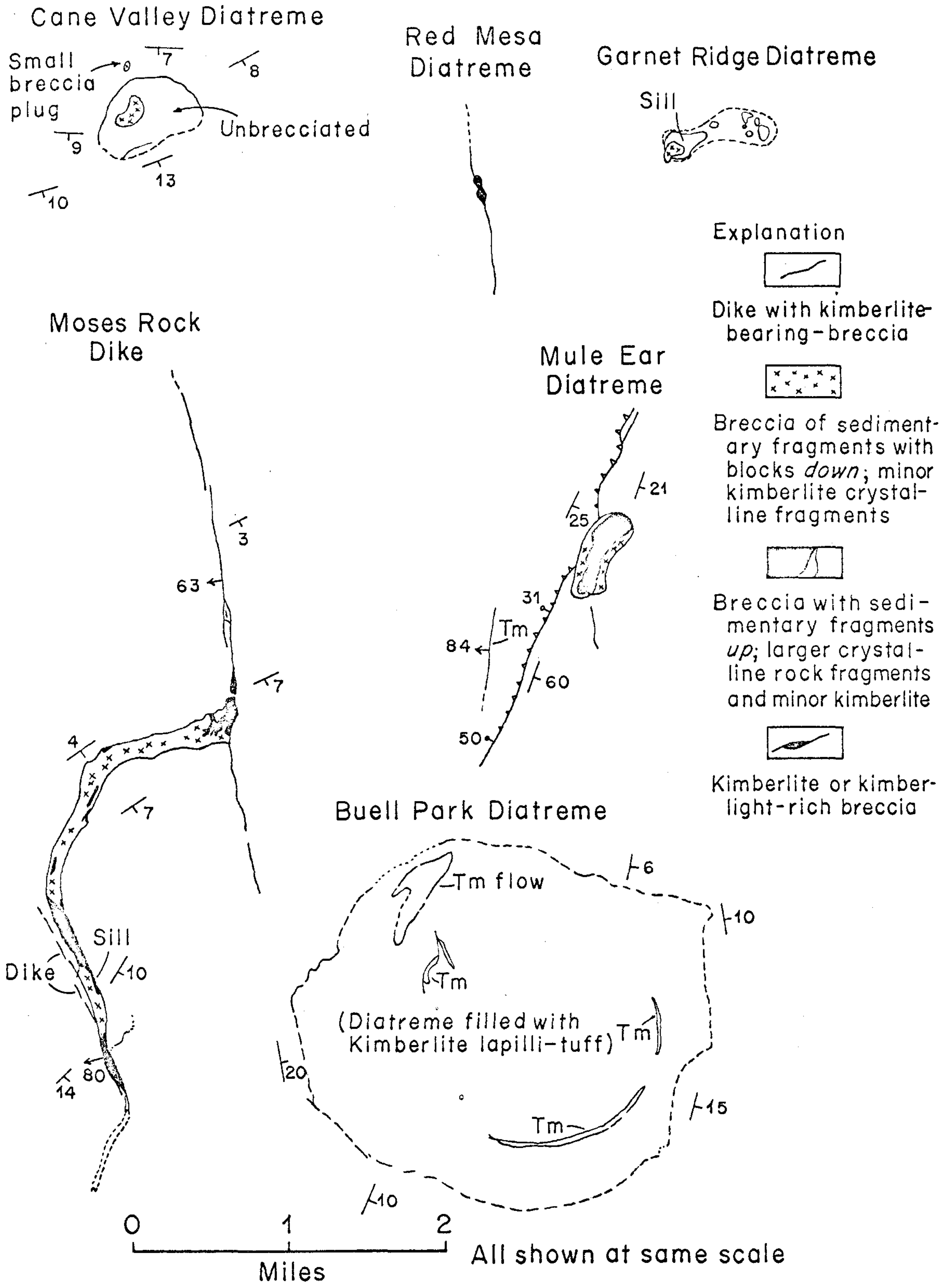

Figure 2 Sketch maps of several kimberlite bearing pipes and dikes on the Colorado Plateau

Previous Work

Sterrett (1909) is the first geologist known to have visited the kimberlite diatremes on the Navajo Reservation. He visited Buell Park and the cluster of diatremes along Comb Ridge in eastern Monument Valley, described pyropic garnets collected at the Moses Rock dike and suggested that the dike was a glacial deposit. Woodruff (1912), after noting the abundance and rounded nature of the exotic rocks occupying the surface of the ground at the Moses Rock dike also suggested that it was glacial in origin. In his classical reconnaissance of the Navajo country, Gregory first recognized the kimberlite-bearing diatremes as volcanic features (Gregory, 1915). Williams (1936) briefly described the abundant and varied crystalline rock fragments contained in the kimberlite diatremes in his reconnaissance study of the volcanic rocks of the Navajo and Hopi Reservations. He recognized the material in the kimberlite-bearing diatremes as kimberlite-like but suggested that it was probably weathered minette.

The first geologist to identify the green tuff-like serpentine-microbreccia as "kimberlite" was Balk (1954), after detailed petrographic and chemical analysis of material from Buell Park. A geologic map of the Buell Park diatreme was completed by Balk. Malde (1954) and Malde and Thaden (1963) mapped the geology of one of the two vents at Garnet Ridge, south of the Moses Rock dike and reported serpentine-rich breccia interspersed between large blocks of sedimentary rock. Shoemaker and Moore (unpublished map) mapped the geology of the Mule Ear diatreme during 1955 to 1957 and found blocks displaced approximately 5000' downward from their original stratigraphic position, a concentric pattern of the distribution of blocks in the diatreme and tuff-like kimberlite intrusive units. Blocks displaced downward are found generally around the outside of the vent. In the center are pipe-like bodies of material which has come up, including crystalline rock fragments. Shoemaker (1956, 1962) and Shoemaker, Roach and Byers (1962) have described the structure of kimberlite and alkali basalt diatremes of the central Navajo Reservation and monchiquite diatremes of the Hopi Reservation, and discussed the mechanics of their emplacement by a gas-boring and gas-transport process.

More detailed petrologic studies of the Colorado Plateau kimberlites have been undertaken recently. Watson (1960) described eclogites collected at Garnet Ridge. O'Hara and Mercy (1966) collected and described peridotite, eclogite and garnets at Garnet Ridge. Among the garnets collected were chromium-rich pyropic-garnets characteristic of South African kimberlites. No diamonds have been observed as yet in any of the Colorado Plateau kimberlites.

Scope of this Report and Methods of Investigation

This report focuses on two topics, the mode of emplacement of the Moses Rock dike and the petrology of the crust and upper mantle underlying the dike. A hydrodynamic theory for the mode of emplacement is based on detailed analysis of the dike and the rocks filling the dike, with emphasis on crystalline rocks derived from great depth. Inferrences about the crust and upper mantle are based on petrographic and microprobe investigations of minerals in kimberlite and in crystalline rock fragments.

The problems are treated in terms of 1) the sequence of events accompanying the emplacement of the dike, 2) the location of and conditions in the reservoir from which the kimberlite erupted, 3) the nature of the crustal-upper mantle column traversed by the erupting kimberlite, 4) the properties of the erupting medium, and 5) the mechanics of the eruption, itself.

The methods of investigation included geologic mapping, petrographic, chemical and microprobe analyses of rocks and minerals, and a theoretical analysis of the hydrodynamics of the eruption. The field investigation included mapping of about 30 square miles surrounding the Moses Rock dike at a scale of approximately 1:32,000, detailed geologic mapping of the Moses Rock dike at a scale of 1:2400, measurement of detailed stratigraphic sections near the dike, bulk sampling of material within the dike at 6 localities, and detailed collection of crystalline rock fragments at 28 localities, including collection of data on the size frequency distribution of the crystalline rock fragments.

The author's first visit to the Moses Rock dike was made in March, 1964; field work began in June, 1964, and was completeted in May, 1966. Two long field seasons (1964, 1965) were consumed in detailed mapping and sample collection.

The detailed mapping of the Moses Rock dike at 1:2400 was greatly facilitated by low altitude-high resolution, stereoscopic, vertical aerial photographs taken under a contract for the U. S. Geological Survey for this project. Much more detailed knowledge of the geology of the Moses Rock dike is available than will be presented in map form in this report. The entire dike is mapped at 1:2400 scale.

Reconnaissance petrographic study of a representative sample of crystalline rock fragments permitted selection of characteristic and interesting rock types for more detailed study including whole rock chemical analysis and microprobe work. Mineral separates from the kimberlite and polished thin sections of some of the dense xenolithic inclusions were analysed to establish details of mineral and rock composition.

The mode of emplacement is examined in light of the constraints imposed by the observations of the geological structure of the dike and the nature of the rocks filling the dike. A simple hydrodynamic theory is constructed to explain the observations from which the fluid properties of the erupting medium are inferred.

Outline of this Report

This report consists of three parts: 1) geology 2) petrology, and 3) mode of emplacement of the Moses Rock dike. The first part, the geology of the dike, is presented with emphasis on the structural relationships at the contact and between the breccia units which fill the dike. These observations form the basis for reconstruction of the sequence of events responsible for the emplacement of the dike.

In the second part, the petrology of the crystalline rock fragments and kimberlite are reviewed. Three problems are discussed: 1) the structure and composition of the crust as suggested by the relative size, relative abundance and petrographic character of the crystalline rock fragments, 2) the origin of the dense and ultramafic fragments which might be mantle rocks, and 3) the genesis of the kimberlite. The crux of this section involves interpretations of microprobe analysis of minerals from the kimberlite and dense rock fragments in terms of pressure and temperatures of formation and the reconstruction of the vertical stratigraphy of the crust and upper mantle.

The third part considers the mechanism of diatreme formation and treats the hydrodynamics of the flow of the kimberlite from its reservoir to the surface. First the geology is reviewed and the sequence of events established. A qualitative model for the emplacement mechanics is presented. Assuming initial P-T conditions in the reservoir inferred from the petrology, the fluid parameters velocity and dike width are calculated for simple flow models. In the calculations, kimberlite is inferred to be a physical mixture of volatile (H_2O) and solid phases, initially at about 1000° C and 100 kilometers. At high pressure, H_2O is nearly incompressible even at elevated temperatures, but as pressure decreases the water phase expands. During the eruption, at depth the kimberlite can be treated as an incompressible fluid but nearer the surface approximately as a polytropic gas. Approximations of the P-V-T relations of water-solid mixtures are inferred for various initial temperatures and water/solid ratios which permit evaluation of surface velocities. Corrections for viscous losses yield velocities in close agreement with independent estimates.

PART II

GEOLOGY

Regional Setting

The Moses Rock dike lies in the eastern part of Monument Valley, in southeast Utah, about 5 miles southeast of Mexican Hat, Utah, near the center of the Colorado Plateau province (Figure 3). Climate is arid, vegetation sparse and exposures generally excellent. This area lies just within the southern limit of the Canyonlands section of the Colorado Plateau, an area of high plateaus, mesa and buttes which has been deeply incised by the Colorado Riber and its tributaries (Fenneman, 1931). The San Juan River, a major tributary of the Colorado, occupies a 2500' deep canyon about 4 miles north of the main part of the Moses Rock dike. Elevation of this part of the region averages between 4500 and 5500 feet above sea level.

Sedimentary Rocks

Paleozoic and Mesozoic sedimentary rocks are exposed on this part of the Colorado Plateau. The Permian Cutler Formation is exposed over much of the Monument Valley area. Quaternary deposits occur locally.

Precambrian metamorphic and igneous rocks are exposed in the Grand Canyon, in the central part of the Zuni uplift, in valleys in the Uncompahgre Plateau and in the Black Canyon of the Gunnison. Crystalline basement rocks have been encountered in numerous drill cores throughout the region overlain by Cambrian sedimentary rocks at the base of the Paleozoic section. The crystalline rocks upon which these Cambrian sediments lie, thus, are Precambrian in age.

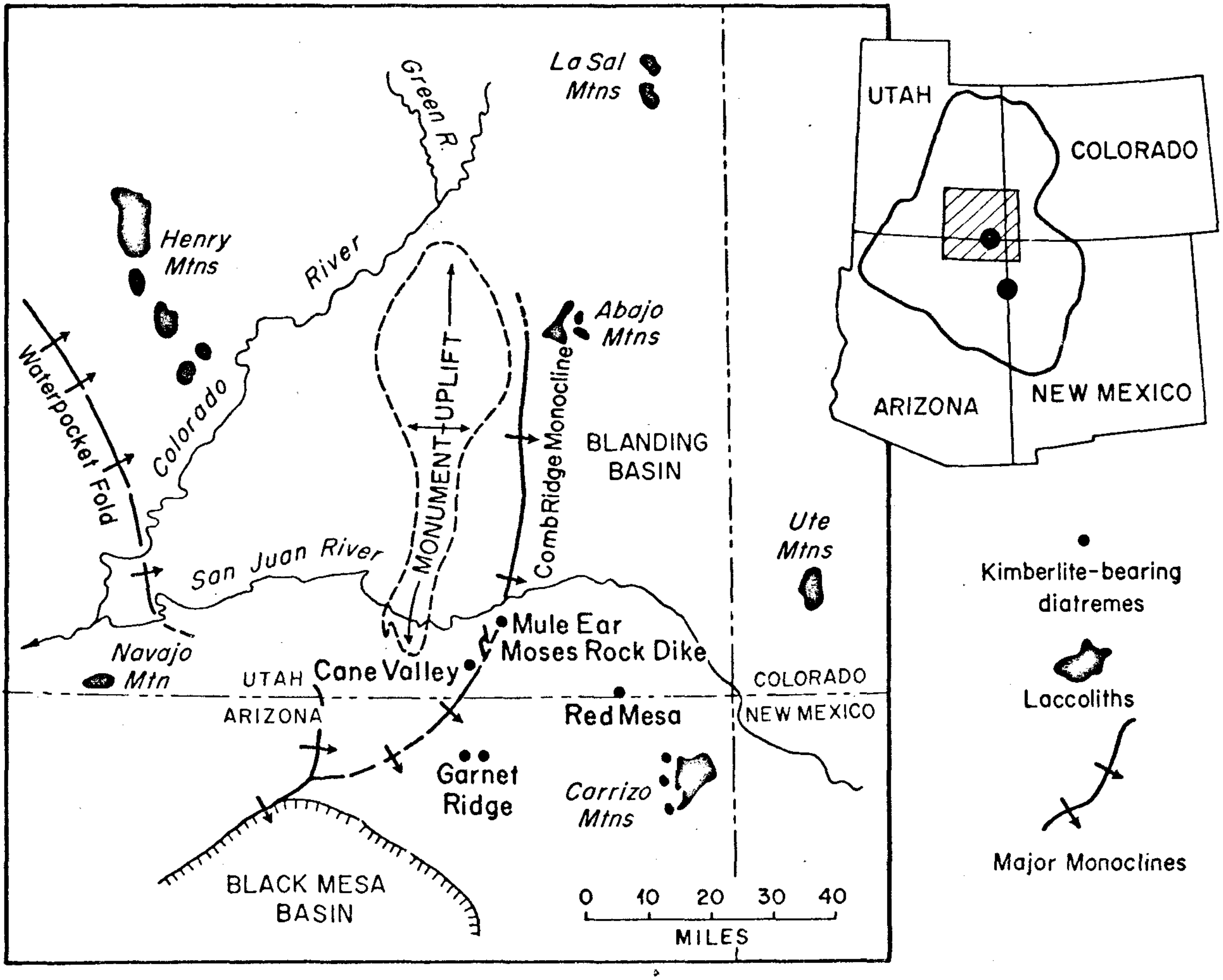

Figure 3. Location map for the region near the Moses Rock dike

The Paleozoic section in the region contains rocks of Cambrian, Devonian, Mississippian, Pennsylvanian and Permian age, and averages about 5000 feet in thickness. The Cambrian rocks are quartzite; Devonian through Pennsylvanian rocks are mostly limestone, dolomite and minor evaporite; the Permian rocks are arkosic sandstone and shale (R. O. Bass, 1963).

The Mesozoic sedimentary rocks of Triassic, Jurassic and Cretaceous age exposed in the region range from sandstone, siltstone, and shale, to limestone (Weeks and Garrels, 1959). The Mesozoic section is at least 6500 feet thick.

In the region, tertiary sedimentary rocks occur only in the major basins or locally, as in the Chuska Mountains, as an unconformable capping on folded older rocks. (Weeks and Garrels, 1959).

Igneous Rocks

Intrusive rocks, younger than the crystalline Precambrian basement, include stocks and laccoliths of the La Sal, Abajo and Henry Mountains in Utah, the Ute Mountains in Colorado, and the Carrizo Mountains in Arizona, which are mostly diorite porphyry and range from diorite to syenite (Hunt and others, 1953; Weeks and Garrels, 1959). Volcanic dikes and diatremes are common in the region (Shoemaker and others, 1962). In the Monument Valley area, most of the diatremes are filled with minette (phlogopite-sanidine-diopside basalt); a few contain kimberlite.

Structure

The Colorado Plateau province can be subdivided into structural units which include major basins with structural relief reaching

Figure 4. Tectonic map of a portion of the central Colorado Plateau

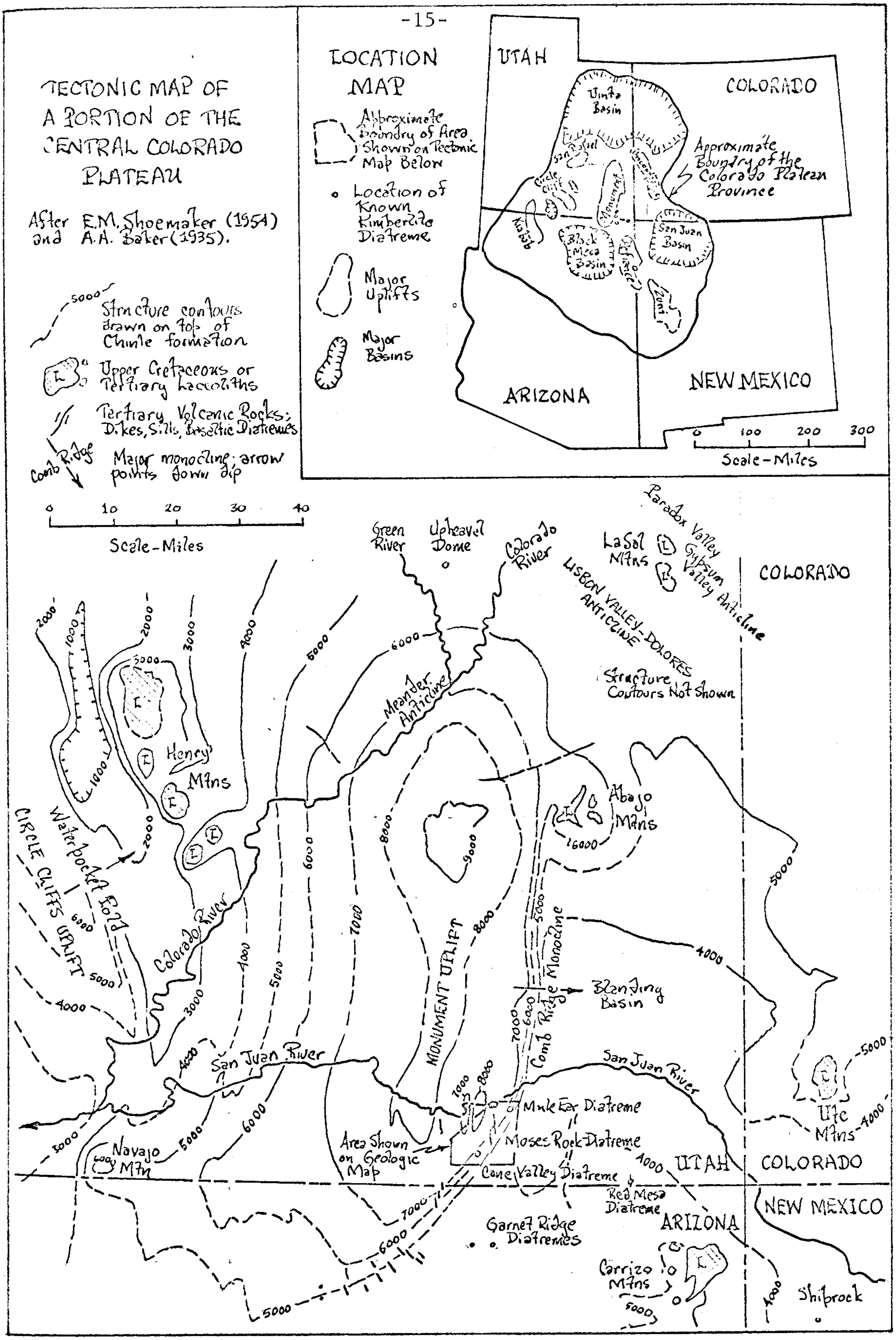

TECTONIC MAP OF A PORTION OF THE CENTRAL COLORADO PLATEAU

After E.M. Shoemaker (1954) and A.A. Baker (1935).

14,000 feet, major uplifts with structural relief up to 5000 feet, and areas occupied by benches, platforms, gently dipping slopes, saddles, arches and sags (Kelley, 1955; Shoemaker, 1954). Each basin and uplift is an assymetrical fold bounded on one side by a major monocline (Shoemaker, 1954).

The major structural elements of this part of the Colorado Plateau are the Monument uplift, and the Comb Ridge monocline. The Monument uplift is a broad, north-south trending, flat, assymetrical anticline approximately 50 miles wide by 100 miles long, upon which are developed a few minor folds (Baker, 1936; Shoemaker, 1954; Kelley, 1955). The eastern margin of the Monument uplift is defined by the Comb Ridge monocline. Eastward of the monocline strata dip very gently across the Four Corners Platform.

Geology of the Area Near the Moses Rock Dike

Rocks exposed near the Moses Rock dike are mostly red and reddish brown, siltstone, sandstone, shale, and evaporite of the Permian Cutler Formation, which here is approximately 2100 feet thick. The present surface of erosion ranges between approximately 4500 and 5000 feet above sea level and between 3800 and 5500 feet above the crystalline basement. Landforms in the vicinity are questas and hogbacks developed on dipping Permian beds. Total relief near the dike is about 300 feet.

The dominant local topographic and structural feature is Comb Ridge, a west facing scarp 600 feet high which extends nearly 50 miles north and south (Plate 1). The dike lies about two miles west of this hogback (Figure 5).

Rocks in the foreground are beds of the Organ Rock Tongue of the Permian Cutler Formation. Beds seen on the left include Cedar Mesa Sandstone and Halgaito Tongue Members of the Cutler Formation and Rico Formation. Beds to the right include deChelley Sandstone Member, and the Triassic Formations: Moenkopi, Chinle, Wingate, Kayenta, and Navajo. This view is between the two-fold axes of the Comb Ridge monocline. The spire seen in the background is Mule Ear, an erosional remnant of Wingate Sandstone. Just to the left and below this spire is the Mule Ear diatreme, a kimberlite-bearing pipe.

Plate 1. A northward view along Comb Ridge about 2 miles east of the Moses Rock dike.

Figure 5. Geologic map of area near Moses Rock dike, San Juan County, Utah

(Oversize, in pocket)

Sedimentary Rocks

Pennsylvanian through Jurassic and Jurassic (?) strata are exposed nearby. The Pennsylvanian formations occur in stream valleys in the northern part of the area mapped. Permian rocks are exposed over most of the area near the Moses Rock dike. Triassic and Jurassic rocks occur in Comb Ridge in the eastern part of the area (Figure 5).

Sedimentary rocks of Cambrian, Devonian, Mississippian and Pennsylvanian age, mostly limestone, dolomite and minor evaporite are known from exposure in the nearby San Juan River canyon or from drilling. A few miles east of the Moses Rock dike younger sedimentary rocks are exposed including lower Triassic Moenkopi Formation, reddish-brown siltstone and shale; the Triassic Chinle Formation, conglomerate and varigated mudstone; Jurassic Glen Canyon Group, red and white sandstone; Jurassic, San Rafael Group, sandstone, siltstone; and, Jurassic Morrison Formation, shale and sandstone. Quarternary deposits include terrace gravels, dune sand and aluvium. (A generalized stratigraphic column for southeast Utah is shown in Figure 6.)

The Cutler Formation is of particular interest because these are the present wall rocks of the Moses Rock dike and blocks derived from the Cutler are abundant within the dike. The Cutler Formation in Monument Valley was subdivided into five members which in ascending order are, the Halgaito Tongue, Cedar Mesa Sandstone, Organ Rock Tongue, DeChelley Sandstone and Hoskinnini Tongue (Baker and Reeside, 1929; Baker, 1936; Gregory, 1938; O'Sullivan, 1965). Stewart (1957) assigned the Hoskinnini Tongue to the overlying Moenkopi Formation and that usage is adopted here.

Figure 6

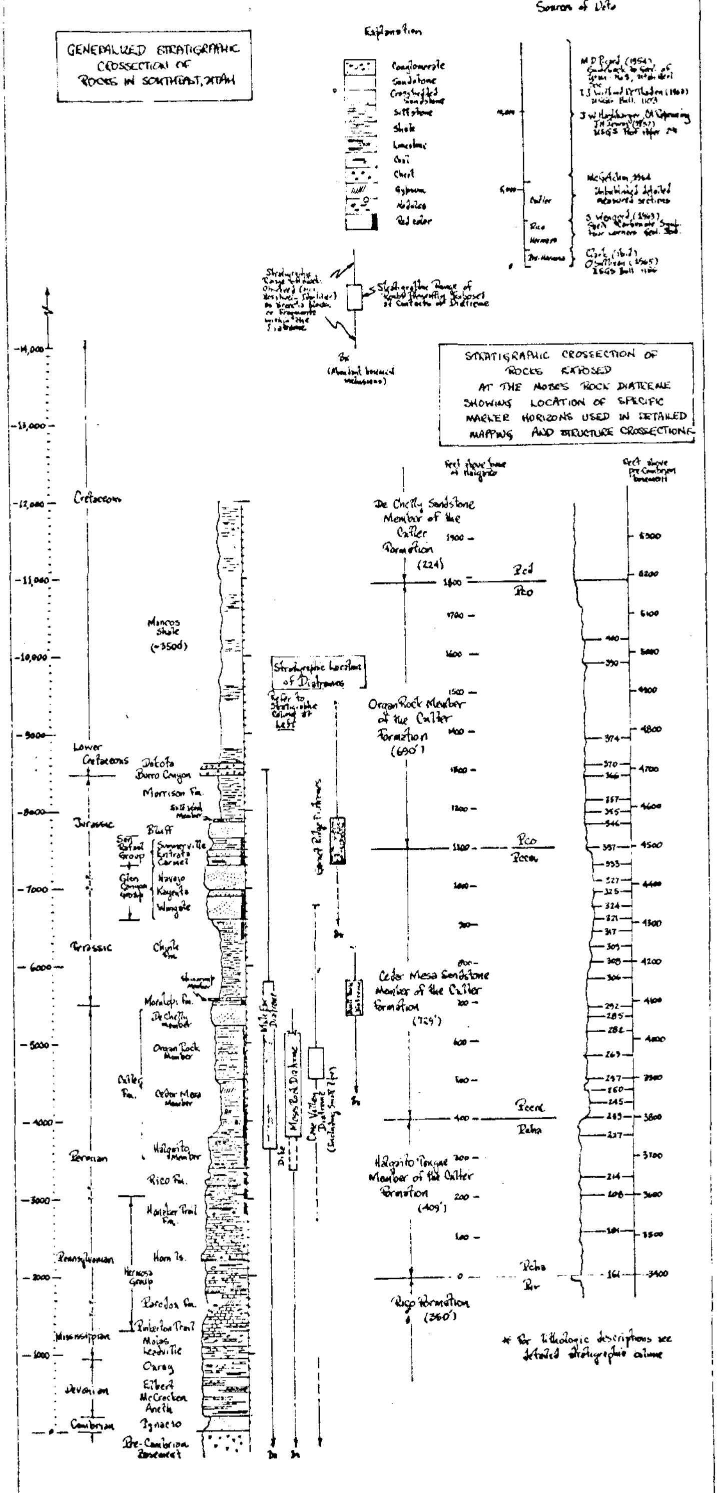
GENERALIZED STRATIGRAPHIC CROSSECTION OF ROCKS IN SOUTHEAST, UTAH
Explanation
Conglomerate
Sandstone
Crossbedded Sandstone
Siltstone
Shale
Limestone
Coal
Chert
Gypsum
Nodules
Red color
Sources of Data
M.D. Picard (1954)
I.J. Witkind
J.W. Harshbarger
J.H. Irwin (1957) USGS Prof. Paper
McGetchin, 1968
Unpublished detailed measured sections
S. Wengerd (1963)
Four corners Geol. Soc.
Clark (ibid)
O'Sullivan (1965) USGS Bull.
Cutler
Rico
Hermosa
Pre-Hermosa
Stratigraphic Range of Rocks Presently Exposed at Contacts of Diatreme
Bx
(Abundant breccia inclusions)
STRATIGRAPHIC CROSSECTION OF ROCKS EXPOSED AT THE MOSES ROCK DIATREME SHOWING LOCATION OF SPECIFIC MARKER HORIZONS USED IN DETAILED MAPPING AND STRUCTURE CROSSECTIONS
Feet above base of Halgaito
Feet above Pre-Cambrian basement
-14,000
-13,000
-12,000
-11,000
-10,000
-9000
-8000
-7000
-6000
-5000
-4000
-3000
-2000
-1000
Cretaceous
Mancos Shale (~3500)
Lower Cretaceous
Dakota
Burro Canyon
Morrison Fm.
Jurassic
Bluff
San Rafael Group
Summerville
Entrada
Carmel
Glen Canyon Group
Navajo
Kayenta
Wingate
Triassic
Chinle Fm.
Shinarump Member
Moenkopi Fm.
De Chelly member
Organ Rock Member
Cutler Fm.
Cedar Mesa Member
Permian
Halgaito Member
Rico Fm.
Honaker Trail Fm.
Pennsylvanian
Hermosa Group
Horn Is.
Paradox Fm.
Pinkerton Trail
Mississippian
Molas
Leadville
Ouray
Devonian
Elbert
McCracken
Aneth
Cambrian
Ignacio
Pre-Cambrian Basement
Stratigraphic Location of Diatremes
Refer to Stratigraphic Column at Left
Mule Ear Diatreme
Dike
Moses Rock Diatreme
Cane Valley Diatreme
Garnet Ridge
Bx
De Chelly Sandstone Member of the Cutler Formation (224)
Organ Rock Member of the Cutler Formation (690')
Cedar Mesa Sandstone Member of the Cutler Formation (729')
Halgaito Tongue Member of the Cutler Formation (409')
Rico Formation (360')
Pcd
Pco
Pcco
Pch
Pr
1900
1800
1700
1600
1500
1400
1300
1200
1100
1000
900
800
700
600
500
400
300
200
100
0
6300
6200
6100
6000
4900
4800
4700
4600
4500
4400
4300
4200
4100
4000
3900
3800
3700
3600
3500
3400
440
390
374
370
366
357
355
346
337
333
327
325
324
321
317
309
308
306
292
285
282
269
257
260
245
243
237
214
208
181
161
* For lithologic descriptions see detailed stratigraphic column

The Halgaito Tongue consists of 409 feet of dark red calcareous shaley siltstone and fine-grained silty-sandstone. Calcareous well-cemented beds that crop out as ledges alternate with softer beds which form slopes. The Cedar Mesa Sandstone, in the vicinity of the Moses Rock dike, consists of 729 feet of orangish-brown, very fine-grained sandstone and siltstone, commonly crossbedded, and interbedded gypsum. The Organ Rock Tongue consists of 690 feet of dark brownish-red siltstone, shale, shaley-siltstone and sandstone with minor conglomerate. The de Chelly sandstone is composed entirely of cross-bedded light-tan to yellowish-brown, weakly-cemented, well-sorted sandstone, about 224 feet thick.

Quarternary deposits are developed on the breccias, particularly at the south end of the Moses Rock dike. These consist of lag concentrates of crystalline basement rock and limestone fragments which cover the ground surface in and just outside of the dike. Locally these fragments are desert varnished. There are local remnants of a well-developed Pleistocene soil at several localities near the south end of the dike.

Detailed stratigraphic sections of the Cutler Formation were measured to permit precise stratigraphic identification of breccia blocks within the Moses Rock dike (Figure 7, in pocket). Distinctive beds within the Cutler Formation were given index numbers and are used to identify the stratigraphic positions of breccia blocks within the dike (Figure 6).

Stratigraphic units in the Grand Canyon, Arizona, equivalent to the Cutler Formation, in ascending order, are: 1) Supai Formation,

Figure 7. Composite and generalized stratigraphic crossection of sedimentary rocks exposed locally near the Moses Rock dike, San Juan County, Utah

(Oversize, in pocket)

2) Hermit Shale, 3) Coconino Sandstone, 4) Toroweap Formation, and 5) Kaibab Limestone.

Blocks derived from the Pennsylvanian strata which underlie the Cutler Formation are also abundant in the Moses Rock dike. In descending order these rocks are Rico Formation and the Hermosa Group consisting of the Honaker Trail and Paradox Formations, all of which are well exposed in the canyon of the San Juan River just north of the Moses Rock dike, or at the Honaker Trail near the Goosenecks of the San Juan River, an entrenched meander northwest of Mexican Hat (see Wengerd, 1963).

The Rico Formation consists of about 100 feet of red siltstone interbedded with minor crossbedded white sandstone; fossiliferous grey and greenish grey limestone and minor purple shale. The boundary between the Rico Formation and the overlying Halgaito Tongue of the Cutler Formation is occupied by a six-foot thick, nearly massive greenish-grey limestone bed with minor nodules, called the Rico limestone (Wengerd, 1963).

The upper 300 feet of the Honaker Trail Formation consists of interbedded dark red limey siltstones and subordinate fossiliferous grey sandy-limestone. The lower 450 feet consists of grey limestone commonly with chert, fossils, and oolites, interbedded with subordinate silty limestone beds. The top of the Honaker Trail Formation is occupied by a 15-foot thick greenish-grey fossiliferous unit called the Shafer limestone (Wengerd, 1963).

The Paradox Formation consists of about 800 feet of grey limestone and dolomite containing abundant fossils (Fusulina sp.), chert, oolites, nodules, and minor black shale, free sulfur and coal.

The cherts are a distinctive and useful feature in differentiating the strata in the Hermosa Group. Near the top of the Group in the upper part of the Honaker Trail Formation, chert nodules and chert replacements of fossils (brachiopods mostly) are dark red in color. In the lower half of the Honaker Trail Formation chert is grey. In the Paradox Formation chert is black.

Structure

The area mapped lies on the eastern flank of the Monument uplift where beds dip southeastward toward the Comb Ridge monocline. Structures include several folds, joints, three large kimberlite-bearing diatremes including the Moses Rock dike, two smaller kimberlite-bearing dikes, two minette dikes and one fault (Figure 5).

The dominant local structural feature is the north-trending Comb Ridge monocline, along which eastward dips reach 60° within the area mapped. Structural relief across the monocline is approximately 3500 feet.

Another important structure within the area mapped is the Raplee anticline, an assymetrical north-south trending, southward plunging open fold about 4 miles wide. On its east flank beds dip gently 4° to 12° toward the Comb Ridge monocline. Dips are steeper on its west flank, reaching 30° or more. This fold dies out toward the south in the area mapped (Figure 5).

Beds on the west flank of the Raplee anticline dip westward into another north-trending open fold, the Mexican Hat syncline. Structural relief on this fold diminishes toward the south and vanishes within the area mapped (Figure 5).

A system of through-going, nearly vertical joints trending east-west to N 60° W, averaging about N.80° W, is well developed throughout the area. This joint system appears to be orthogonal to the axes of the Comb Ridge monocline. A second set of nearly vertical cross joints is oriented nearly normal to the first set, is not as well developed, and generally does not cut through the first set.

Kimberlite Intrusions

Intrusive features in the area mapped include the Moses Rock, Mule Ear and Cane Valley kimberlite-bearing diatremes (Figure 5). The largest and most complex in terms of internal structure is the Moses Rock dike. The Mule Ear diatreme, though less complex structurally, contains the largest crystalline rock fragments and has sedimentary rock fragments derived from the greatest stratigraphic range observed in any of the kimberlite diatremes, including those at Garnet Ridge, just outside the area mapped. The Cane Valley diatreme has a very simple structure, contains only rare and very small crystalline rock fragments, and contains sedimentary rock fragments and blocks transported only short distances from their original positions.

The Mule Ear diatreme is located just south of the San Juan River on the Comb Ridge monocline. It has an elliptical shape, approximately .5 by .2 miles in plan and has been mapped at a scale of 1:2400 by Shoemaker and Moore (1957) and D. Stewart-Alexander (work in progress) and was described by Shoemaker (1962). The material in the Mule Ear vent has a concentric distribution in which blocks are displaced downward around the outside margin of the vent and material which has come up is concentrated in the center. Crystalline rock fragments and kimberlite are concentrated in the center. The largest crystalline rock fragment observed was fine-grained biotite granite gneiss about 25 feet in diameter. Fragments of lower Cretaceous Mancos shale are reported juxtaposed against Halgaito Member in the vent walls implying downward displacement of the Mancos shale blocks of approximately 5000 feet. This is also a minimum figure for the amount of overburden at the time of emplacement of the Mule Ear diatreme. A yellowish to buff colored tuff-like intrusive material composed of cemented sandstone grains with some crystalline rock fragments and rare pyroxene and garnet grains that was observed at Mule Ear is not present at the Moses Rock dike. Green serpentine-rich microbreccia (kimberlite) is observed at Mule Ear which appears to be identical with material exposed locally within the Moses Rock dike.

The Cane Valley diatreme occurs about 2 miles southwest of the Moses Rock dike (Figure 5). The outline of the structure was mapped by O'Sullivan (1965) who named it. A small elliptical satellite diatreme occurs about 600 feet to the northwest.

The Cane Valley diatreme is a kidney-shaped, trapdoor-like, structural depression apparently hinged along its southern edge, containing minor kimberlite-bearing dikes and a small off-center brecciated core (Figure 8). It is exposed within gently dipping rocks of the Organ Rock Tongue. The boundary of the diatreme is defined by an abrupt downfolding of beds at the contact. Wall rocks are undeformed and unmetamorphosed except for local bleaching on fractures well

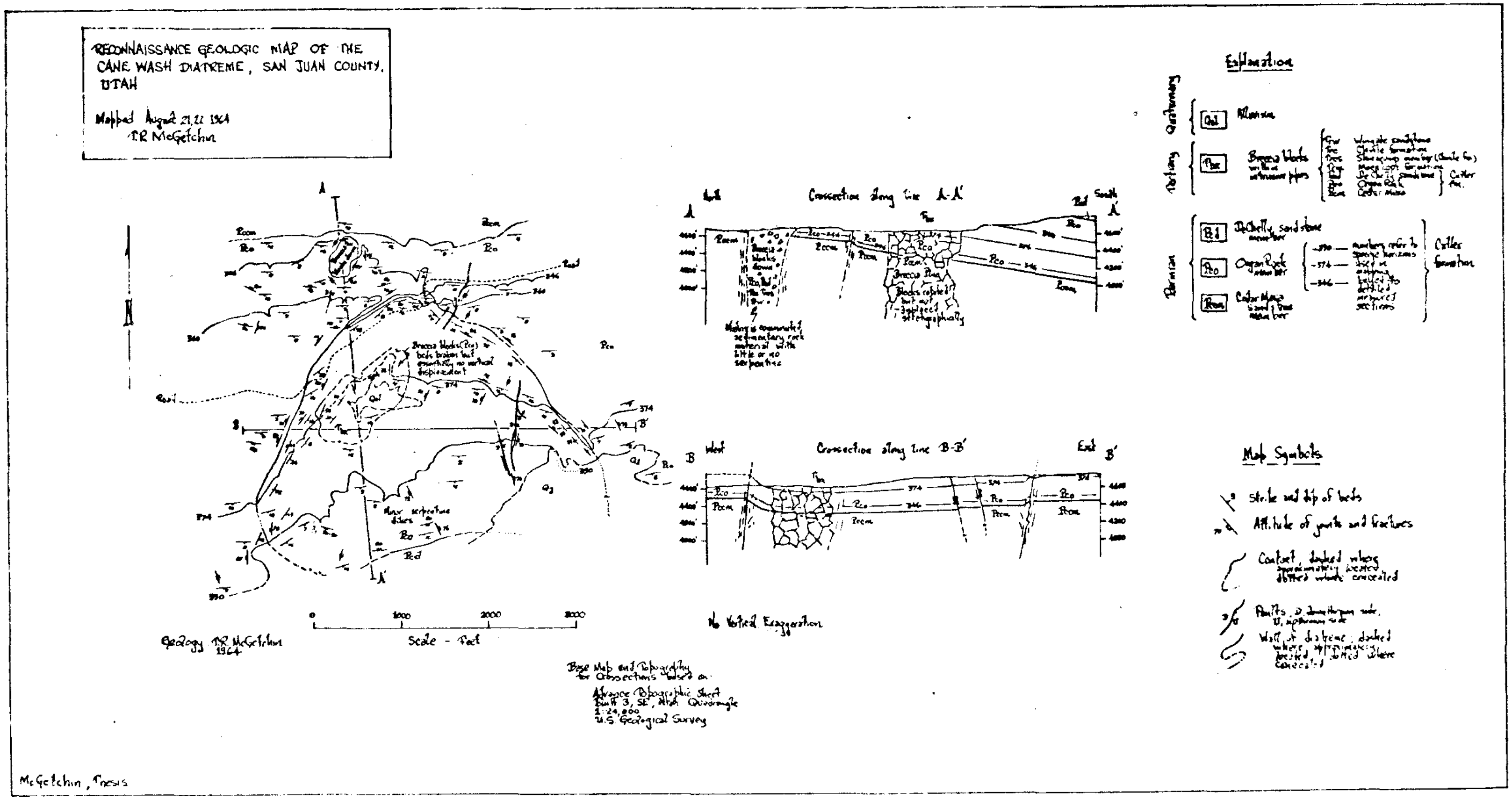

Figure 8. Reconnaissance geologic map of the Cane Wash diatreme, San Juan County, Utah

developed in the wall rock which parallel the contact of the diatreme.

The diatreme is filled with rocks derived almost entirely from Organ Rock Tongue strata exposed in the walls. Aside from a small brecciated core, bedding is not disrupted and the rocks are undeformed except for local bleaching along fractures. Small kimberlite-bearing dikes were observed in the south-central part of the diatreme. Crystalline rock fragments are present in alluvium, apparently derived from kimberlite but they are very rare and small. Downward structural displacement of the downfolded beds is approximately 170 feet in the north central part of the diatreme where the structural relief is greatest.

An irregularly shaped, off-center brecciated core approximately 1000 by 500 feet is located on the northwest side within the diatreme. Here beds of Organ Rock Tongue are broken into large blocks which have been rotated with respect to each other, but which are not displaced significantly from their original stratigraphic position, outside the brecciated core. Stratigraphic horizons can be traced through the brecciated core without difficulty. The matrix material between the breccia blocks appears to be almost entirely fine-grained fragments, mostly sand- and silt-sized, derived from the Cutler Formation.

About 600 feet northwest of the Cane Valley diatreme is a small elliptical vent about 800 by 500 feet in plan. It cuts gently dipping rocks of the Organ Rock Tongue just above the contact with the Cedar Mesa Sandstone. The diatreme is filled almost entirely with blocks derived from the overlying stratigraphic units: Organ Rock Tongue, de Chelly Sandstone Members of the Cutler Formation, and the Moenkopi, Chinle and Wingate Formations. Rare blocks derived from the underlying

Cedar Mesa sandstone member are observed. The largest blocks are approximately 60 by 30 feet. Their orientation appears to be random. The matrix material between the blocks contains very little or no kimberlite and appears to be comminuted clastic material probably derived mostly from the Cutler Formation, possibly from the subjacent, highly friable Cedar Mesa Sandstone Member. No crystalline rock fragments were observed within this structure. A fracture system paralleling the contact is well developed around the periphery of the structure in the rocks of the vent walls. The density of these fractures (number of fractures per unit distance measured normal to the contact) decreases as an inverse power function of the distance from the contact.

Two kimberlite-bearing dikes were observed outside the main diatremes. One occurs in Cane Wash, four miles west of the Moses Rock dike, where it cuts Cedar Mesa Sandstone Member at a low angle through an exposed distance of almost a mile and a half (Figure 5). Near the south end of this dike, another smaller and subparallel dike is developed and appears to coalesce into a small and poorly exposed diatreme. The kimberlite components of the breccia filling these dikes is highly diluted with clastic debris, although crystalline rock fragments up to several inches in diameter occur locally.

Approximately one mile east of the Moses Rock dike, a steeply dipping kimberlite-bearing dike cuts Cedar Mesa Sandstone, Organ Rock Tongue and de Chelly Sandstone Members (Figure 5; Plate 2 A,B,C). This dike is approximately a half mile long, is several feet wide, and is filled with kimberlite, clastic sedimentary fragments and locally contains crystalline rock fragments several inches in diameter. Flat plates

A. A view looking southeast; dike is in center of photo behind and to the right of rock hammer.

B. View of dike, here approximately two feet wide. Note lack of metamorphism or alteration at the contact. Outer margin of the dike is lined with a plate of fiberous calcite with fibers normal to contact.

C. Close-up of dike shows angular to well-rounded fragments of crystalline rock and limestone in matrix of comminuted sandstone mixed with kimberlite. Tabular chips of calcite show clearly at dike margins. Scale is given by hammer head which shows in upper right-hand corner.

Plate 2. Kimberlite-bearing dike in west flank of Comb Ridge a mile east of Moses Rock dike which intrudes beds of Organ Rock Member of Cutler Formation.

of fiberous calcite line the outer margins of the dike in which the calcite fibers are oriented nearly normal to the contact. (Microprobe analyses of chips of these plates showed it to be nearly pure calcium carbonate containing very little magnesium.)

Two dikes of minette occur in the vicinity, one, two and a half miles west of the Moses Rock dike, the other approximately a mile southwest of the Mule Ear diatreme (Figure 5). Both strike slightly east of north and dip steeply westward, and both are approximately a mile long. Fractures occur in the wall rocks parallel to the dike contacts; bleaching of wall rocks along these fractures is common near the dikes. The density of fractures parallel to the contact decreases as an inverse power function of the distance away from the dike. No crosscutting relationships exist between kimberlite and minette in the vicinity.

The largest fault observed in the vicinity is a westward dipping reverse fault west of the Mule Ear diatreme (Figure 5). It can be traced for about three and a half miles along or near the contact of the Halgaito Tongue and Cedar Mesa Sandstone Members. There is approximately 700 feet of reverse displacement on the fault near the Mule Ear diatreme, where, locally, kimberlite-bearing breccia is injected along the fault.

Minor normal displacement of a few feet is observed along the narrow westward dipping dike which forms the northern end of the Moses Rock dike (Plate 13).

The Moses Rock Dike

The Moses Rock dike has a complex geometric shape formed by the connection of two parallel north-trending, steeply westward-dipping, en echelon dikes. The dike is well exposed for more than 4 miles but its true length is unknown because the southern end is buried under recent sand dunes; it is probably not longer than 5 miles. Maximum width is about 1000 feet.

The form of the Moses Rock dike in map view is slightly suggestive of an insect and can be subdivided into sections which are called, allegorically, the "north feeler", "south feeler", "head", "body", and "tail" (Figure 9). This is useful in describing the structure of the dike because it is large and its internal structure, contact relations, topographic expression, and exposure vary considerably from place to place [Plate 3].

In the following pages the reader will be conducted on a section by section tour of the Moses Rock dike in which topographic expression, exposure, contact relations, internal structure and composition are described. However, before beginning this geological dissection of the dike it is necessary to do some detailed examination of the material which fills the interior of the dike. Having done this we can then inquire as to the manner in which this material is integrated to form the structure and hopefully to extract some useful clues about the history of the dike.

Rocks Filling the Dike

All material within the dike is breccia. Fragments range in size from silt-sized particles to blocks measuring 750 by 250 feet.

The fragments in the breccia are derived from widely different sources. A rough estimate of the composition of this material was made from the detailed map by estimating the area coverage of each map unit and estimating the composition of this material from field notes and from 500-pound bulk samples obtained from just below the surface at 6 localities. These map units will be described in the following section.

Approximately 72% of the fragments are red sandstone and shale derived mostly from the Cutler Formation. The components of kimberlite comprise about 12% of the fragmental material and most of these components are finely dispersed and mixed with rock debris. Only locally is kimberlite found as a distinct mappable rock unit. Limestone fragments transported upward from the Paleozoic section make up about 13% of the breccia. Crystalline rock fragments constitute about 3%.

Approximately 53% of all fragmental material in the dike is coarser than 1 foot, about 30% coarser than 10 feet, and 12% coarser than 100 feet. Most of the large blocks are sedimentary rocks from the Cutler Formation displaced downward with respect to their original stratigraphic position.

Breccia Units Mapped Within The Dike

The breccias are gradational but are usefully subdivided for mapping purposes into distinct units called kimberlite, diluted kimberlite, Cutler rubble and complex breccia.

Kimberlite as a mappable entity occupies about 1% of the surface area of the Moses Rock dike and occurs at about a dozen scattered

Subdivisions of the Moses Rock Dike

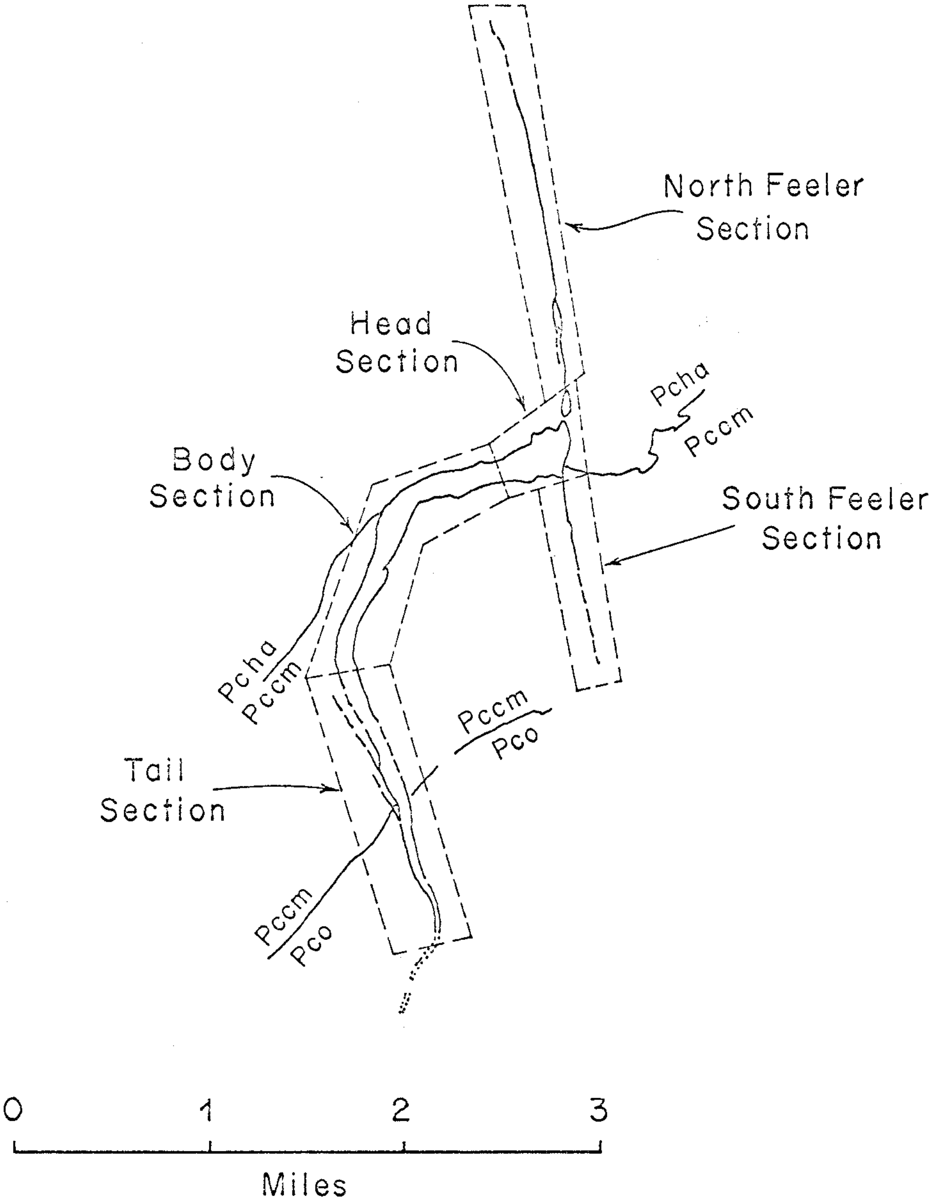

Figure 9 Subdivisions of the Moses Rock dike, showing location of detailed photogeologic maps

A. Southwest view across Moses Rock dike; shows negative topographic relief of body section of dike in foreground and positive relief of dike along tail section in background. Blocks in foreground are mostly Cutler Formation. Bedded rocks at contact are Cedar Mesa Sandstone Member which dip gently southeast. Prominent cliff in left-background is Comb Ridge, formed along the Comb Monocline where Triassic rocks are exposed.

B. Northward view along ridge in the southern or tail section of Moses Rock dike. This ridge stands about 40 feet above surrounding terrane. Blocks are Cutler Formation, Cedar Mesa Member; contact showing in foreground is nearly vertical; wall rocks are Cutler Formation, Cedar Mesa Member. Flat top of ridge is covered by lag concentrate deposit of crystalline rock fragments commonly with desert varnish. Ridge in background is top of Raplee ridge (and Raplee anticline) where beds of Halgaito Member and Rico Formation are exposed.

Plate 3. Local setting and topographic expression of the Moses Rock dike.

Composition of the Material Filling the Moses Rock Dike

FRAGMENT TYPE	FRAGMENT SIZE > 100'	10' to 100'	1' to 10'	less than 1'	
Clastic Sed. Rocks	12.0	17.1	21.1	21.8	72.0
Limestone	.3	.8	1.7	9.8	12.6
Crystalline Rocks	0	0	.2	2.7	2.9
Kimberlite { Discrete Rocks				1.0	12.5
Kimberlite { Dispersed				11.5	
TOTAL	12.3	17.9	23.0	46.8	100.0

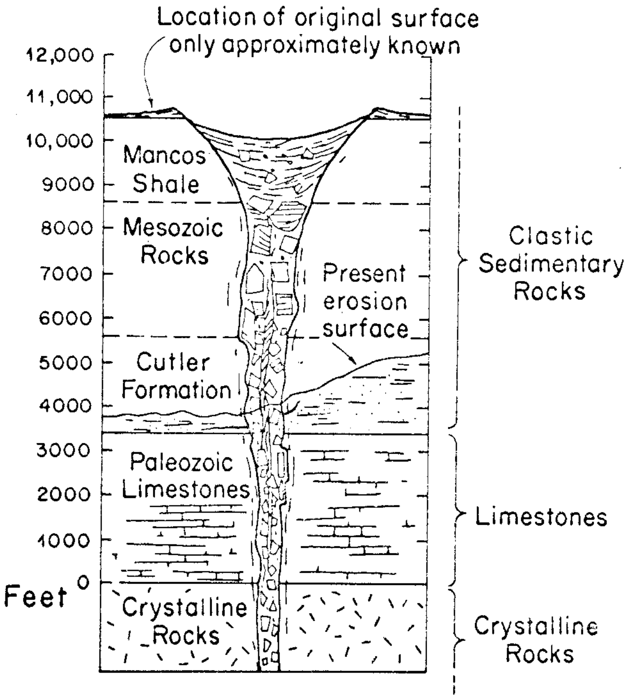

Table 1. Estimate of size and composition of all material filling the Moses Rock dike

localities [Plate 4]. It is a dark green to greenish-black microbreccia that consists mostly of serpentine fragments, minor olivine, pyroxene, garnet, and mica clasts, with subordinate angular rock fragments, mostly limestone and red shale and sandstone. The average grain size is about 1 mm. Bulk samples of the kimberlite show that 5% of the material is fragmental rock debris (Figure 10A, 10C Sample 133, Diagrams A, B). The largest rock fragments observed in the kimberlite are limestone fragments approximately 10 cm across the crystalline rock fragments about 1 cm across.

Kimberlite commonly grades into the second mappable unit, diluted kimberlite. The composition of the diluted kimberlite is widely variable but typically it consists of roughly equal parts kimberlite and comminuted sedimentary rock debris. Most of this debris is probably derived from the friable Cedar Mesa Sandstone Member of the Cutler Formation. Diluted kimberlite is light green in color and occupies about 2% of the area within the main dike. No bulk sample was taken.

About 35 to 40% of the area within the Moses Rock dike is occupied by a breccia unit composed of a rubble of sedimentary rocks mostly derived from the Cutler Formation, mixed with only minor amounts of kimberlite components and crystalline rock fragments. This unit is called Cutler rubble [Plate 5]. The breccia consists of large blocks set in a finer grained matrix the bulk of which is sand sized. Blocks are typically very large, up to several hundred feet, and are displaced only short distances downward from their original stratigraphic position. They are commonly rotated, but generally less than 60°. The components of kimberlite are found dispersed in the matrix of the breccia which

Stereoscopic view looking northwestward. Kimberlite occurs as 4 foot thick dike (or possibly sill) in large block of Cedar Mesa Sandstone Member of the Cutler Formation within the main Moses Rock dike. This block is displaced about 100 feet downward from its original position in the vent wall. This is the only location where blackish-green kimberlite was found. It occupied the center of the dike in an irregular seam several inches thick. (All the accessible black material was sampled, about 200 pounds.) Note man in photograph gives scale. (Precise location of this occurrence is in head section of the dike: Figure 13, northwest of coordinates N-7.)

Plate 4. Kimberlite at type locality in the Moses Rock dike (MR-1416A).

A. Road cut showing intrusive breccia composed of sedimentary blocks, in a matrix of comminuted sedimentary rock debris with minor amounts of kimberlite, and small basement and limestone inclusions. This is one example of an intrusive unit called Cutler rubble. Location of this photo on Figure 13 is northeast of coordinates C-3. Scale shown in photo is 6" long.

B. Close-up of same outcrop.

Plate 5. Intrusive material in the Moses Rock dike: Cutler rubble.

consists of sand-sized particles probably derived largely by communition of the large blocks, and only very minor amounts of small crystalline rock fragments. The matrix material is light lime-green in color and the kimberlite components are roughly estimated to constitute about 1 part in 10 of the matrix. Fragments are too coarse to effectively bulk sample this breccia.

Most of the Moses Rock dike, about 60% in area, is occupied by intricately mixed complex breccia composed of rock fragments derived from the Cutler Formation ranging from comminuted fine-grained debris to large blocks, mixed with fragments of limestone and crystalline rocks. The components of kimberlite are dispersed in the breccia. This unit is called complex breccia [Plate 6, 7, 8]. Most crystalline rock fragments in the breccia are generally well rounded and show no preferred orientation or foliation. The crystalline rock and limestone fragments derived from the complex breccia commonly form a lag gravel that obscures the underlying breccia. For purposes of mapping, the complex breccia has been subdivided according to the size of the crystalline fragments contained in it, into very coarse, coarse and medium complex breccia. (The matrix material in the Cutler rubble could be called fine complex breccia and would fit a continuum of breccia types.) Very coarse complex breccia contains crystalline rock fragments exceeding 12 inches in diameter; coarse complex breccia, exceeding 6 inches in diameter; medium complex breccia, less than 6 inches in diameter. (Fine complex breccia, the matrix between the breccia blocks in the Cutler rubble has only very small crystalline rock fragments, less than 1".) Of the 60% of the dike occupied by complex

A. Southwest view into stream-cut bank; intrusive material is coarse complex breccia. Basement xenoliths are large; breccia blocks visible are Halgaito (ellipsoidal, reddish-brown block just above hammer), Rico and Hermosa group limestone fragments, rounded basement inclusions, in a matrix of kimberlite and comminuted clastic sedimentary debris.

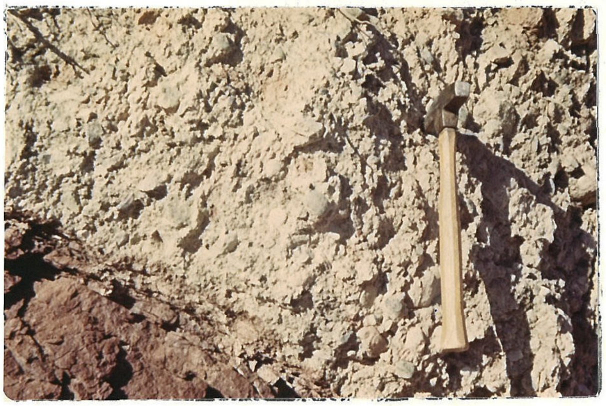

B. Close-up of same locality, showing chaotic nature of breccia; spheroidal green clots are crystalline rock fragments, light-colored ellipsoidal clots are limestone fragments.

C. Close-up of surface of the ground at same locality. This shows concentration of basement inclusions in surface deposit, which is generally rich in caliche and 2 to 6" thick. Basement inclusions may be concentrated by as much as a factor of 4, although this concentration is not observed universally.

Plate 6. Intrusive material in Moses Rock dike: coarse complex breccia.

This locality is in the head section of the Moses Rock dike (Figure 13, approximately N-7, looking southeast). Scale is indicated by greasewood bushes on slope which are 12 to 18 inches high. Large rock fragments are derived from the Cutler Formation (mostly Halgaito Tongue), Rico Formation and Hermosa Group.

Plate 7. Characteristic appearance of well-exposed coarse and very coarse complex breccia.

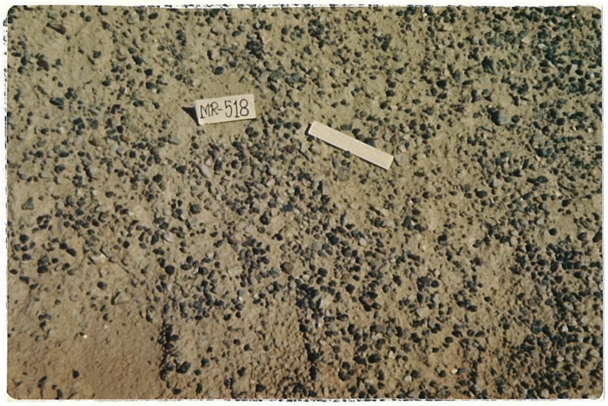

A. Surface deposit in medium complex breccia in which largest crystalline rock fragments do not exceed 6" but which do exceed 1". Ruler is 6" long.

B. Surface deposit developed over coarse complex breccia. Note desert varnish on many crystalline rock fragments. Light grey fragments are Paleozoic limestone. Pen is 5" long. Such a surface deposit covers much of the south (tail) section of the Moses Rock dike, and occurs locally elsewhere.

Plate 8. Surface deposits consisting of lag concentrations of crystalline rock fragments. Characteristically, these form a thin layer over complex breccias in the Moses Rock dike.

breccia, about 20% is very coarse and coarse; 40%, medium complex breccia.

Bulk samples were obtained of very coarse, coarse and medium complex breccia (Figure 10; MR 151, 109, 114, 139, 119). The composition of these breccias is highly variable from place to place. However there is a systematic variation in the composition of the breccia samples which suggests that the content of kimberlite-components decreases as the basement fragment size increases (Figure 10A). The very coarse and coarse complex breccia consists of 1 part kimberlite components to between 1 and 2.5 parts fragmental debris. It appears that within the complex breccias, as the crystalline basement fragments become larger the kimberlite components are more diluted with all types fragmental debris.

The size frequency distributions of various constituents in the complex breccias were determined (Figure 10: 151, 109, 114, 139, 119; Diagrams C and D). Of particular interest are the cumulative size frequency distributions (diagram D). The subject of size reduction by mechanical means is a topic of some importance in many industrial processes as well as in scientific problems. Thus comminution has been the subject of a considerable amount of research by mechanical engineers. Grinding processes very commonly generate size frequency distributions which have characteristic shapes when weighed fractions of material in log size intervals are plotted against the log of the cumulative weight percent finer than the given size fraction. Meloy (1963) found an algebraic expression which generates typical comminution curves (Figure 11). In almost any comminution process, size frequency

Explanation for Figure--10

B diagrams:

k, serpentine fragments and olivine, pyroxene, and garnet crystals not obviously derived from crystalline rock fragments

ss, sandstone and siltstone mostly derived from Cutler Formation

ls, limestone debris derived from Paleozoic rocks underlying the Cutler Formation

bx, rock fragments derived from the Precambrian crystalline basement

C and D diagrams:

△———△ Basement crystalline rocks observed in surface sample

▲——▲ Basement crystalline rocks in subsurface sample

⊡———⊡ Limestone fragments derived from Paleozoic rocks underlying the Cutler Formation in subsurface sample

⊙——⊙ Clastic sedimentary rock fragments and debris; mostly red sandstone and siltstone derived from Cutler Formation in subsurface sample

See figure 14 for location of samples. For each sample four diagrams are given. Diagrams for entire subsurface sample are A, size distribution of all components; B, debris components in various size fractions. Diagrams for each debris component in subsurface sample and for basement-rock fragments observed in sample totaled to 100 percent and treated independently of each other are C, composition of various size fractions; D, cumulative composition.

Figure 10. Size distribution and composition of six bulk samples of intrinsive material (next six pages).

Composition of bulk samples of the intrusive material

Sample No. - - - - - - - -	151	109	114	139	119	133
Map Unit		Complex Breccias				Kimberlite
		Very coarse	Coarse		Medium	
A, Weight percent of all material in subsurface bulk sample						
Kimberlite - - - - - - - -	13.4	28	20.7	27	50	95.0
Precambrian basement rock	13.8	8	3.8	2	11	.7
Limestone - - - - - - - - -	8.7	42	7.5	28	32	3.1
Clastic material - - - - - -	64.1	22	68.0	43	7	1.2
	100.0	100	100.0	100	100	100.0
B, Intrusive material normalized to kimberlite (dilution of kimberlite)						
Kimberlite	1.00	1.00	1.00	1.00	1.00	1.00
Precambrian basement rock - - - - - - - -	1.03	0.29	0.18	0.07	0.22	0.01
Limestone - - - - - - -	.65	1.46	.36	1.04	.64	.03
Clastic material - - -	4.72	.79	3.29	1.59	.14	.01
	6.40	2.54	3.83	2.70	1.00	.05
C, Largest fragments observed						
Part of bulk subsurface sample (g):						
Precambrian basement rock - - - - - - - -	2,079	2,788	1,341	34	66	1
Limestone- - - - - -	2,095	4,795	2,832	2,455	112	9.8
Local occurrence, maximum dimension (cm):						
Precambrian basement rock - - - - - - - -	37	40	27	13	14	3.5
Limestone- - - - - -	60	35	22	30	12	4.5

Breccia Unit	Not sampled		Complex Breccia					
	is	sk	ixvc	ixvc	ixc	ixm	ixm	
			very coarse		coarse	medium		k
Approximate % Map Area of Moses Rock Dike	37	2	20	*	*	40	*	1

Subject to revision when detailed map is drafted. Values should be considered to be accurate within about ± 20% of value shown.

* Considered to be least typical of unit when more than one sample is obtained from single map unit

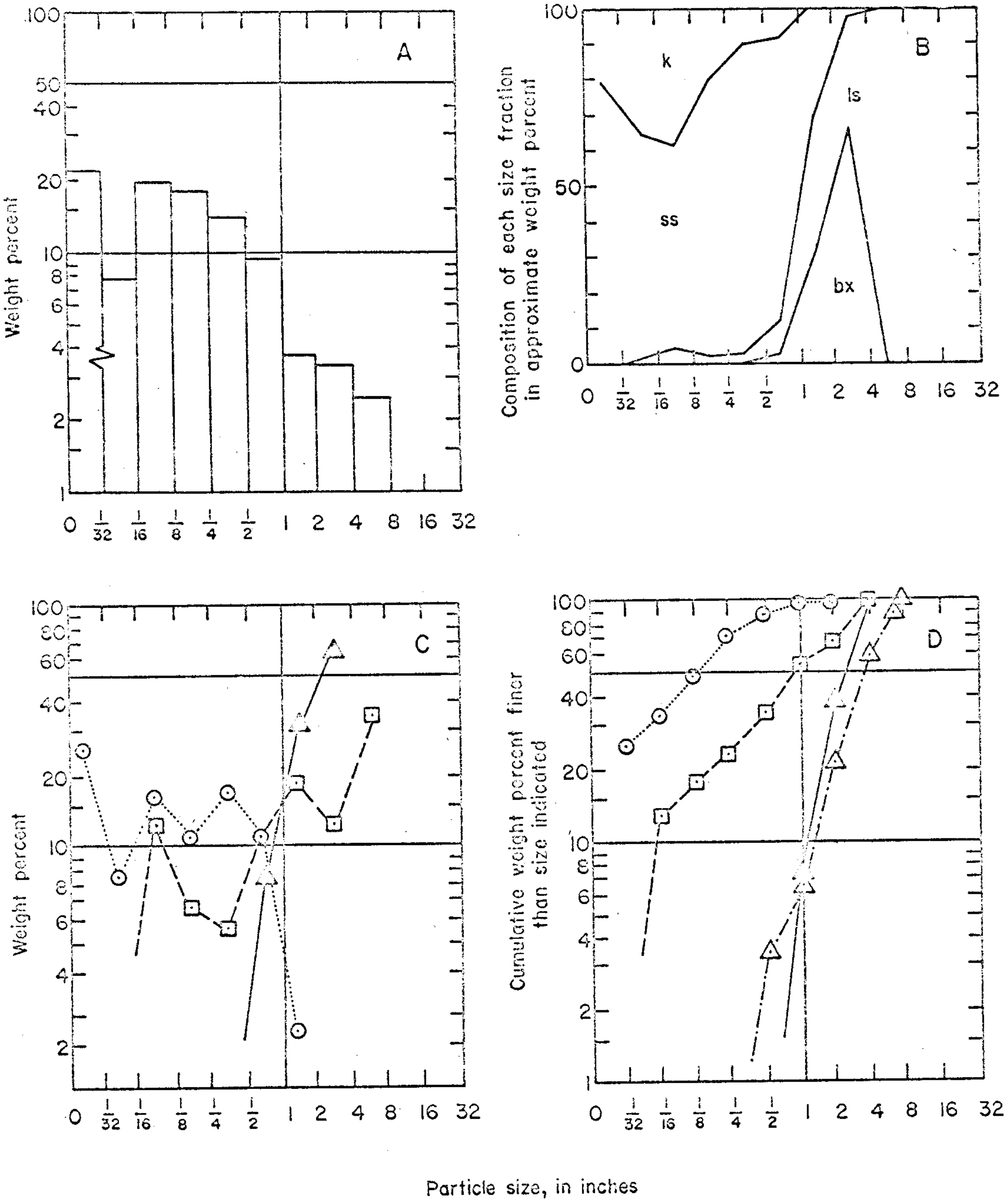

Sample 151

Figure 10 (cont.)

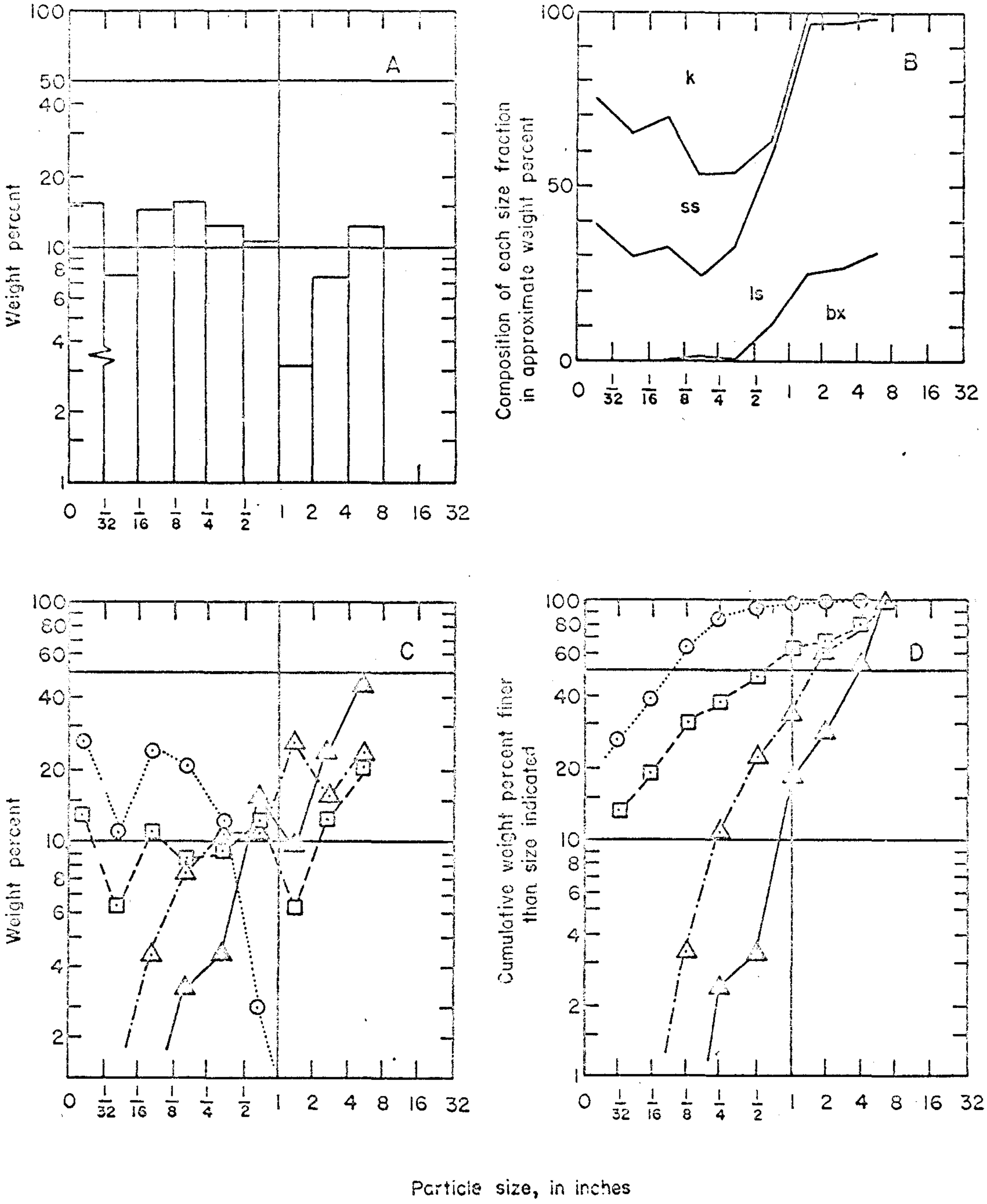

Sample 109

Figure 10 (cont.)

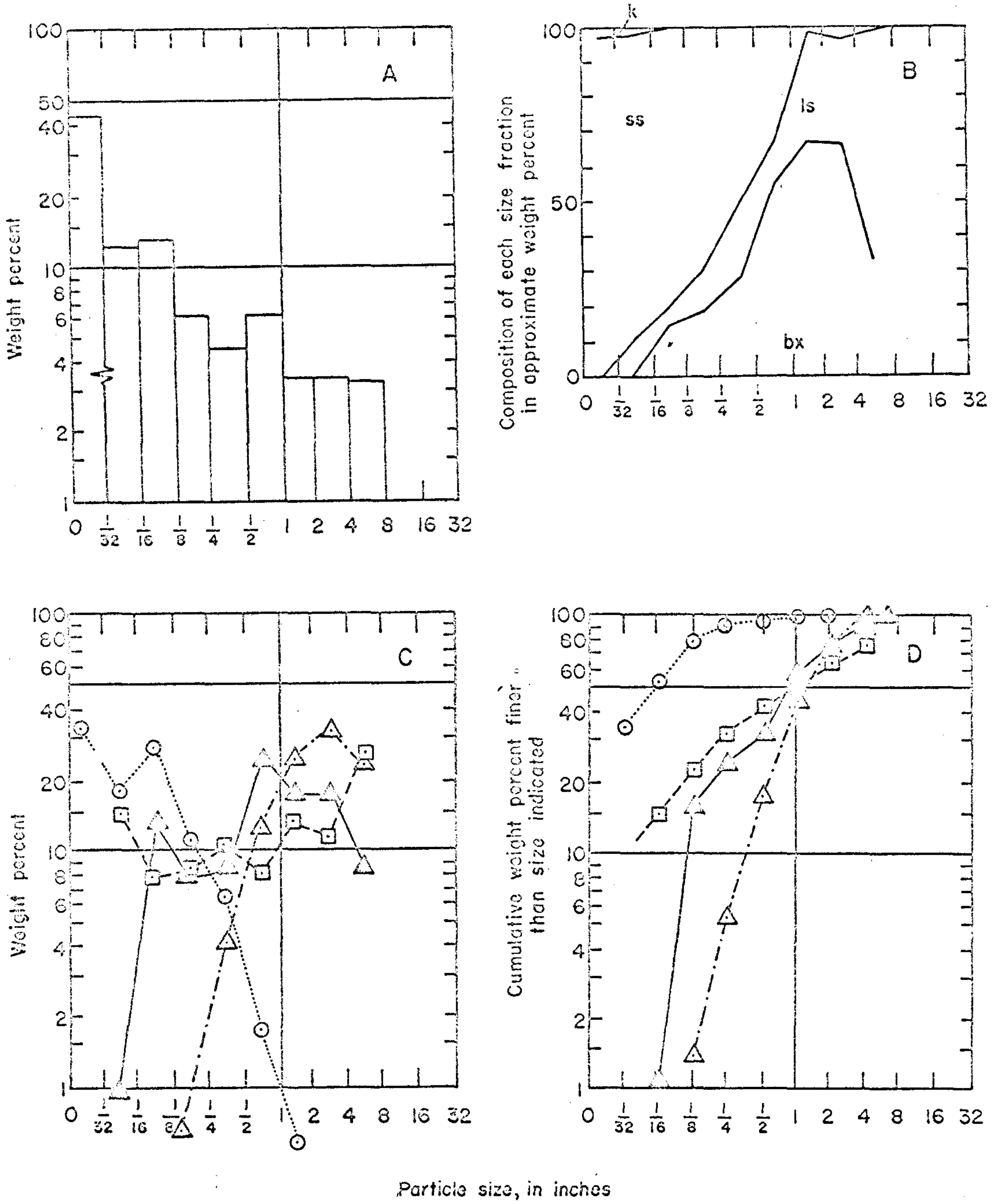

Sample 114

Figure 10 (Cont.)

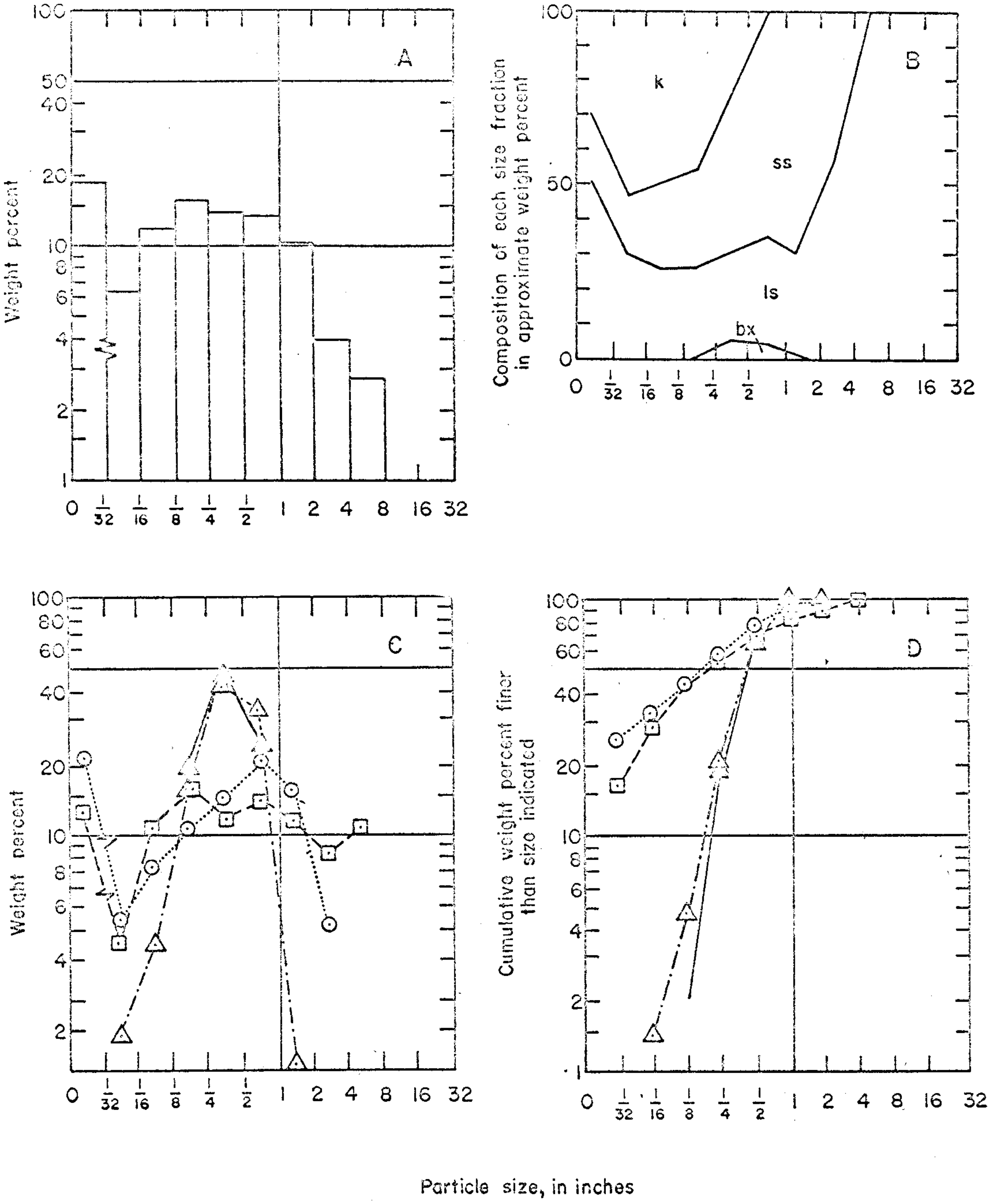

Sample 139

Figure 10 (Cont.)

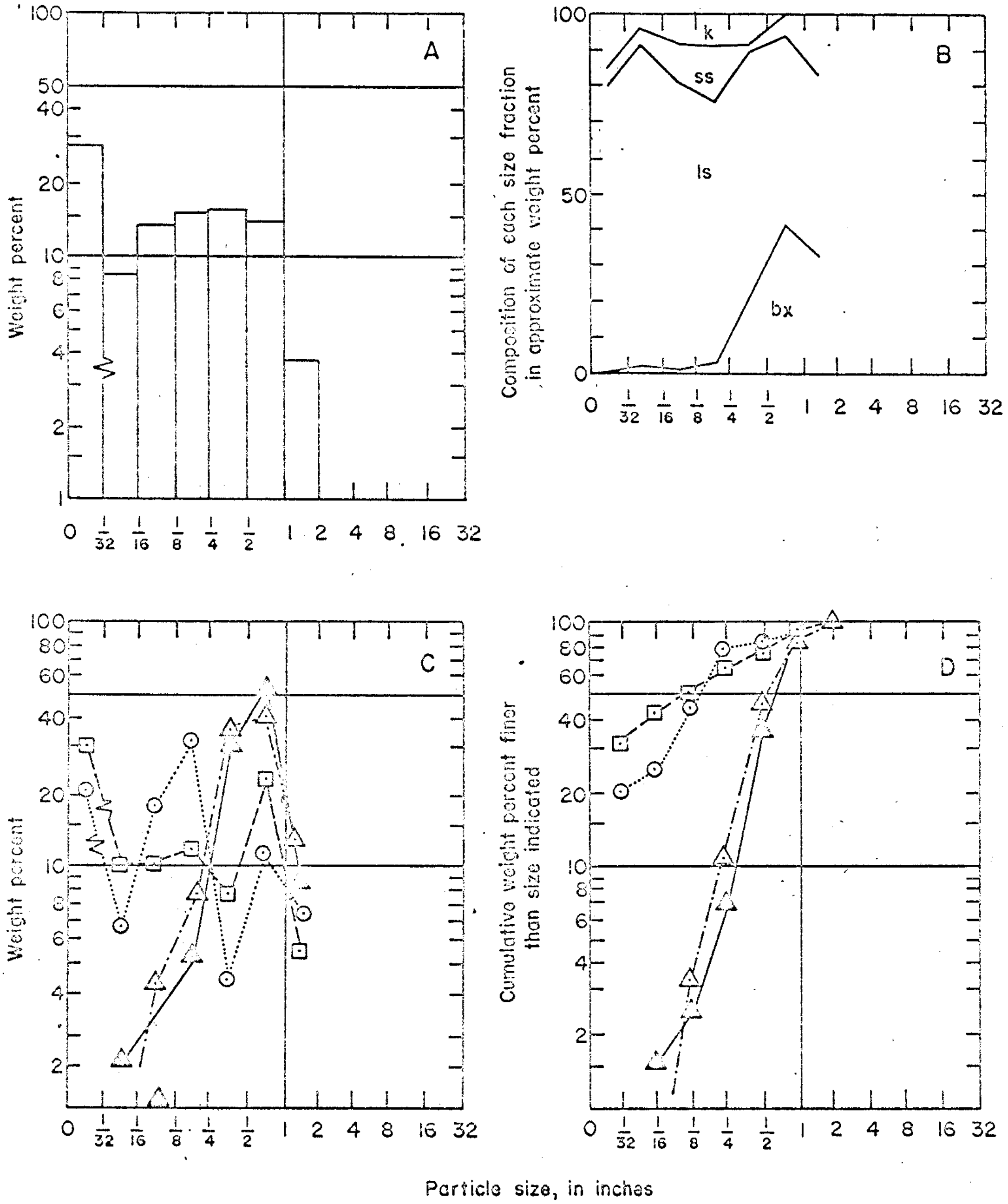

Sample 119

Figure 10 (Cont.)

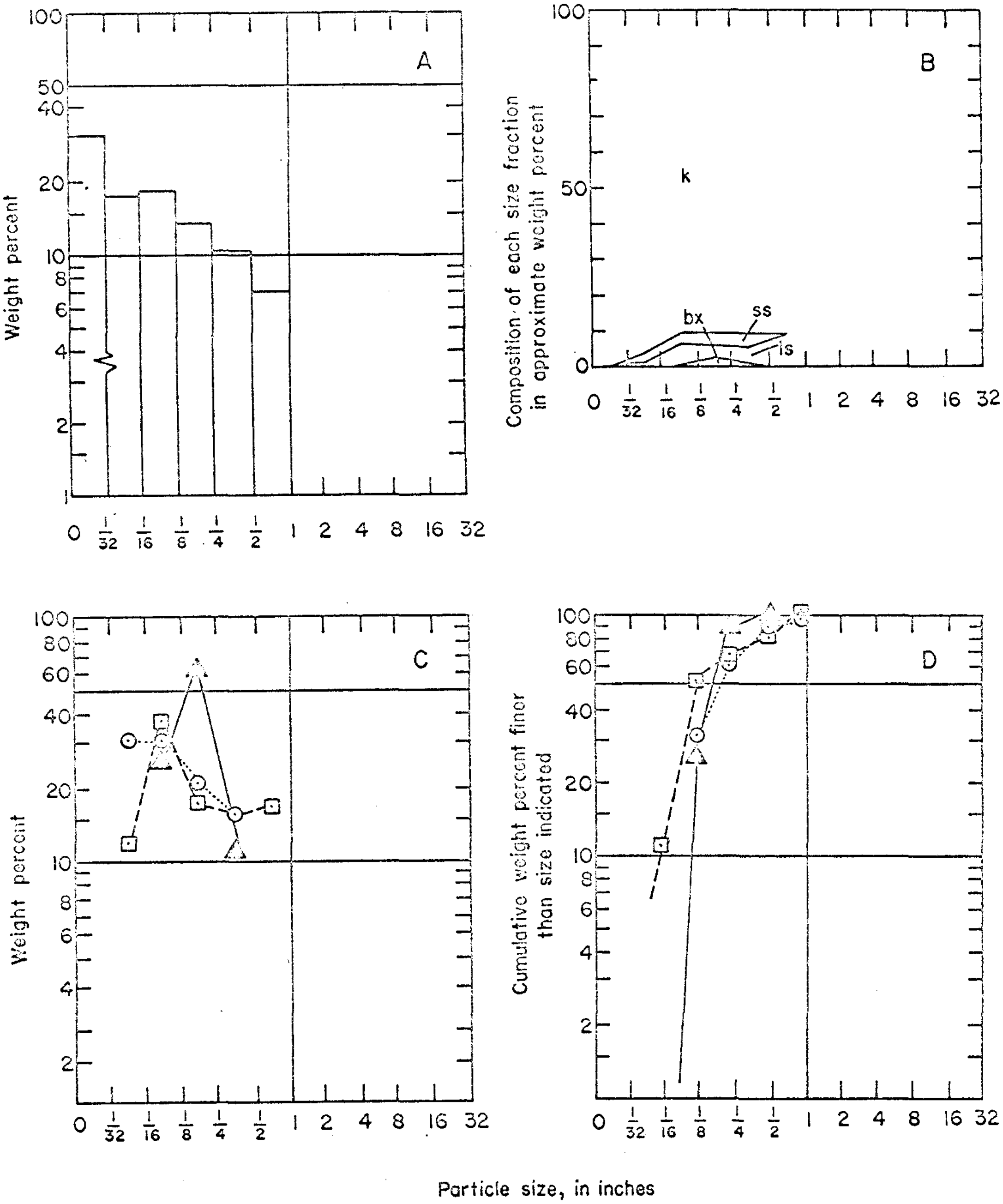

Sample MR 133

Figure 10 (Cont.)

Typical Size Frequency Distribution
Curves for Comminution
of Homogeneous Material of
Uniform Initial Size

Curves shown are for solutions to:
$M(x) = 1 - (1-x)^r$
(after T.P. Meloy, 1963).

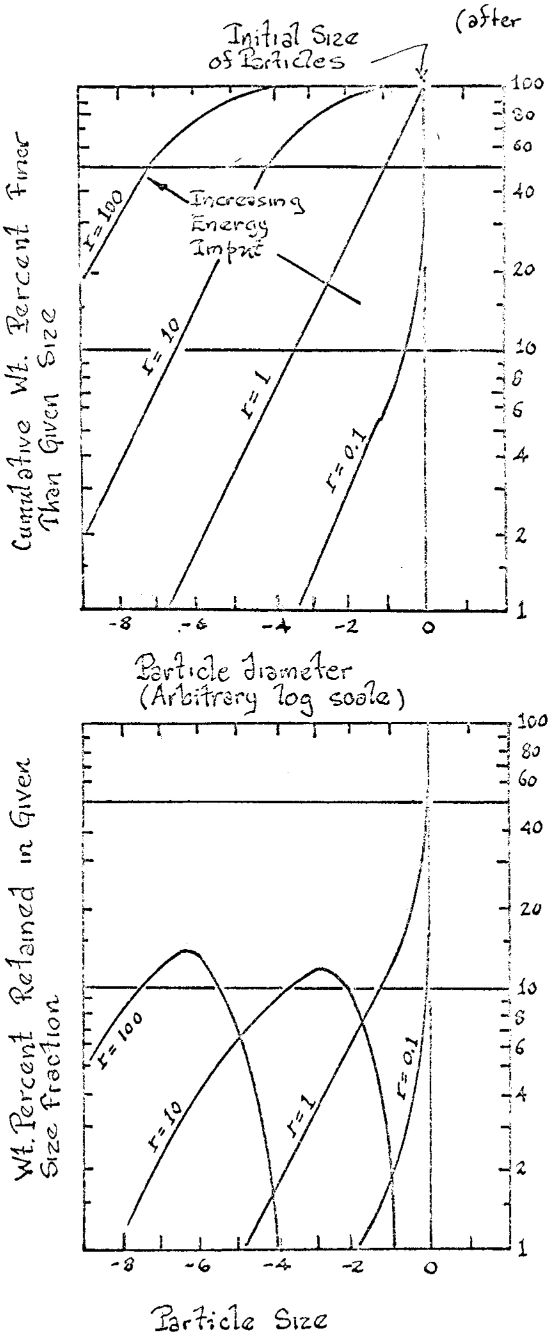

Figure 11. Typical size frequency distribution curves for homogeneous material of uniform initial size

distributions evolve through a family of curves which are quite characteristic of grinding processes. Initially, on the cumulative percent finer diagrams (Figure 11A) grinding curves are concave upward as only a few fine particles are generated. As comminution proceeds the size frequency curve becomes linear. Eventually it assumes an almost steady-state shape consisting of a convex upward region from the largest particle to the median size, and a linear region in the finer fractions (Figure 11A). The cumulative size frequency curves of the components of the complex breccia (Figure 10: 151, 109, 114, 139, 119; diagram D) can be compared to these curves. Inspection of these curves suggests that the sandstone and shale fragments have curves quite characteristic of a mature state of comminution, limestone fragments of an intermediate stage and crystalline rock fragments of the least mature stage. These relationships are best developed in the very coarse and coarse complex breccia (151, 109, 114). These curves suggest that the debris has been subjected to a grinding process and the differences between the curves probably reflects differences in strength of the rocks. That is, differences in their histories in the breccia.

To sum up, the Moses Rock dike is filled with distinct but completely gradational breccias. For purposes of mapping, these breccias can be usefully subdivided into units which will have structural significance. In an approximate way, the compositions of the breccias can be represented schematically as a continuum (Figure 12).

The breccia filling the dike is quite different from section to section. The southern, or tail section, is filled mostly with coarse complex breccia with lesser amounts of very coarse and medium complex

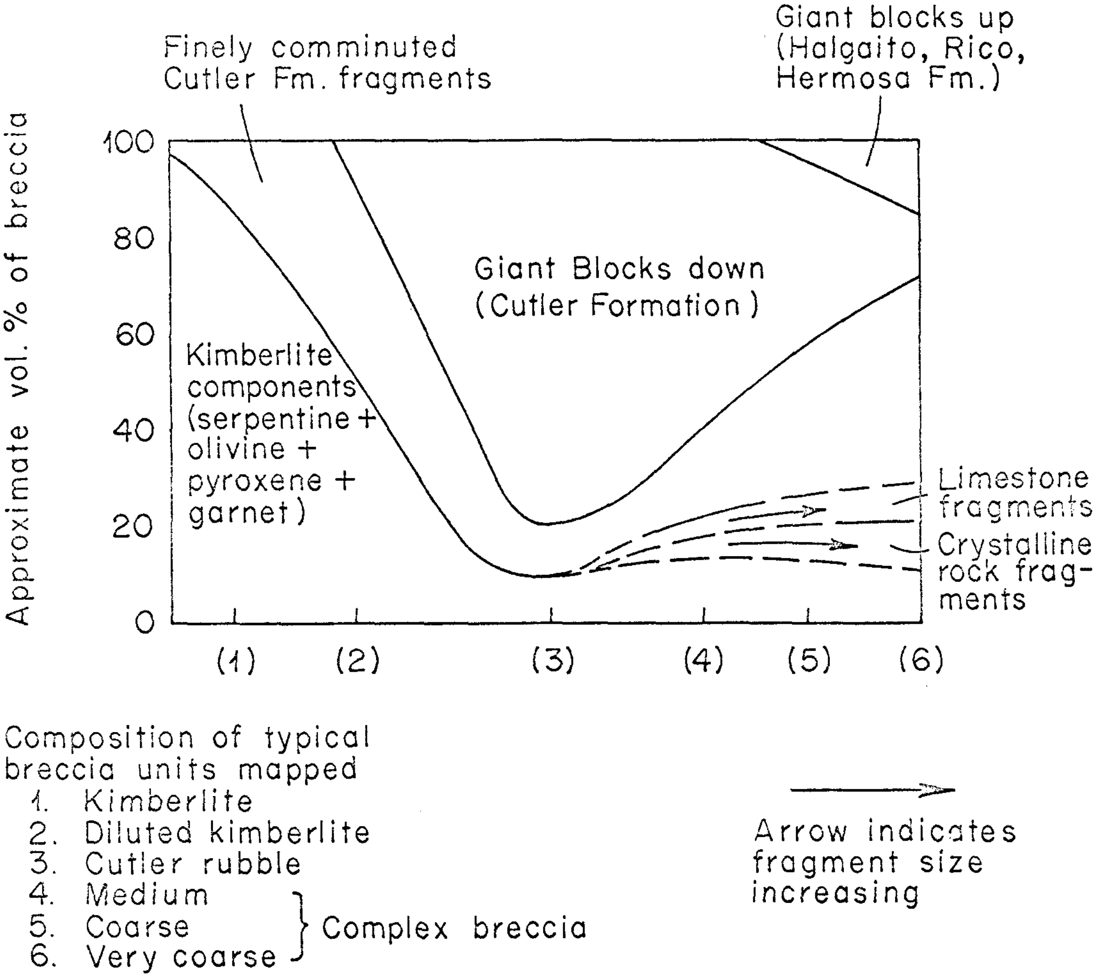

The compositions of the typical breccia units defined and described in the text are indicated along the abscissa. This sequence probably represents the time sequence of development of the breccias, left to right.

Figure 12. Schematic summary diagram showing approximate relative proportions of materials which constitute the breccia units

breccia. Some Cutler rubble and kimberlite also occurs in the tail section but in subordinate amounts. The body section consists of Cutler rubble with minor amounts of medium complex breccia, kimberlite, and diluted kimberlite. The head section is mostly very coarse and coarse complex breccia. The feelers are mostly medium or fine complex breccia. The pod or vent developed along the north feeler is filled with Cutler rubble around the edges and very coarse and coarse complex breccia in the center. The relationships between these mapped units are significant and will be examined section by section.

Structure of the Dike

Having dissected the material in the dike and subdivided it into mappable units, we may inquire into the way these structural elements fit together with the rocks in the walls to constitute the structure of the dike.

So, let us begin at the south end of the Moses Rock dike, the tail section, and proceed northward through its body, head and feelers, examining as we go its topographic expression, exposure, contact relations, structures in the wall rocks, and internal constitution and structure.

A generalized geologic map of the entire dike is shown in Figure 13 and will be used to fit the parts together. A coordinate system is superimposed on this map which will permit specific localities of interest to be located from references in the text.

Geological cross sections (Figure 15) will be referred to in the text by number. Location of these cross sections can be found in Figure 14. Cross sections are presented at a scale of 1:2400 and are based on

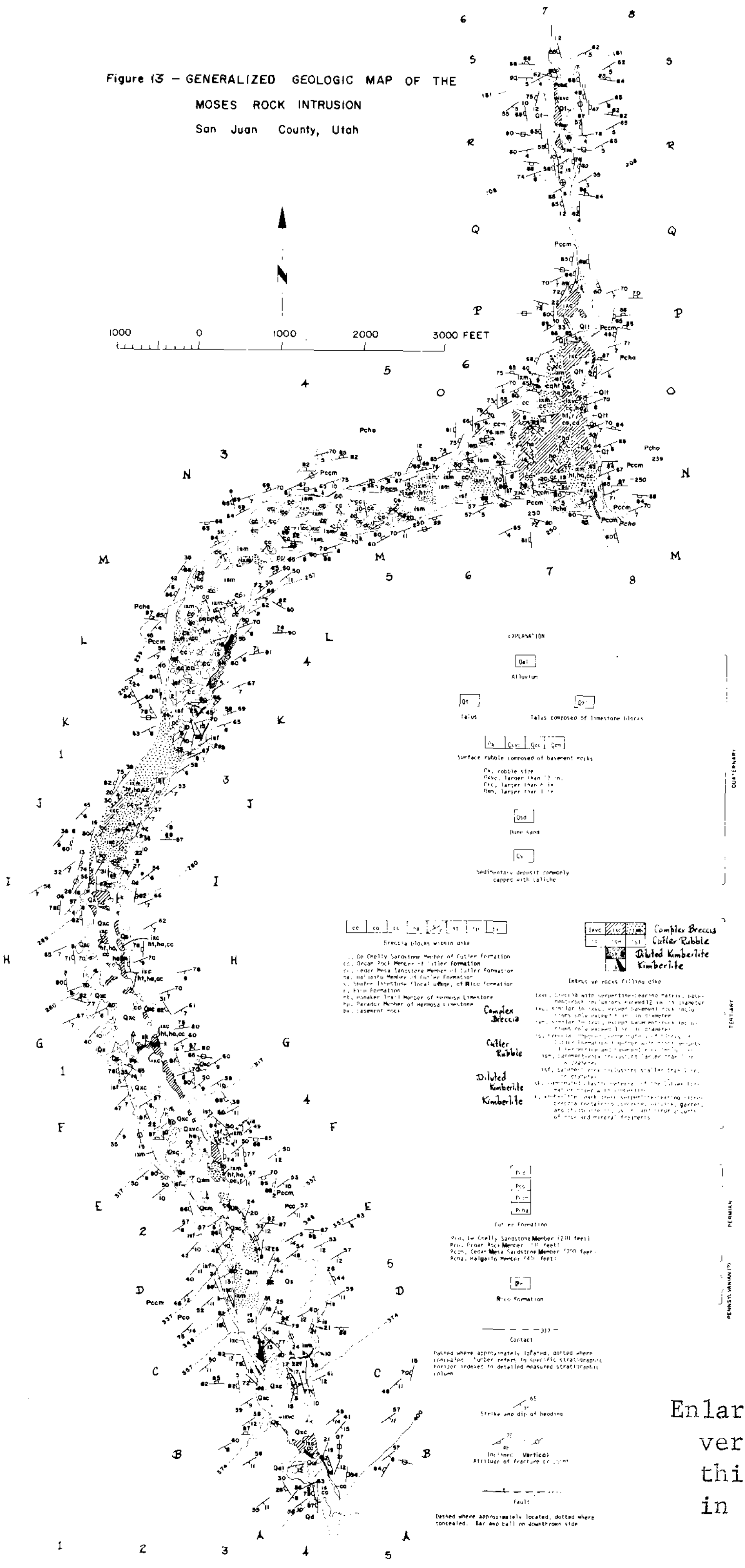

Figure 13 – GENERALIZED GEOLOGIC MAP OF THE MOSES ROCK INTRUSION San Juan County, Utah

Enlarged version of this map in pocket

Figure 14-- INDEX MAP OF MOSES ROCK DIKE
San Juan County, Utah
Showing Roads, Geologic Sections, and Sample Localities

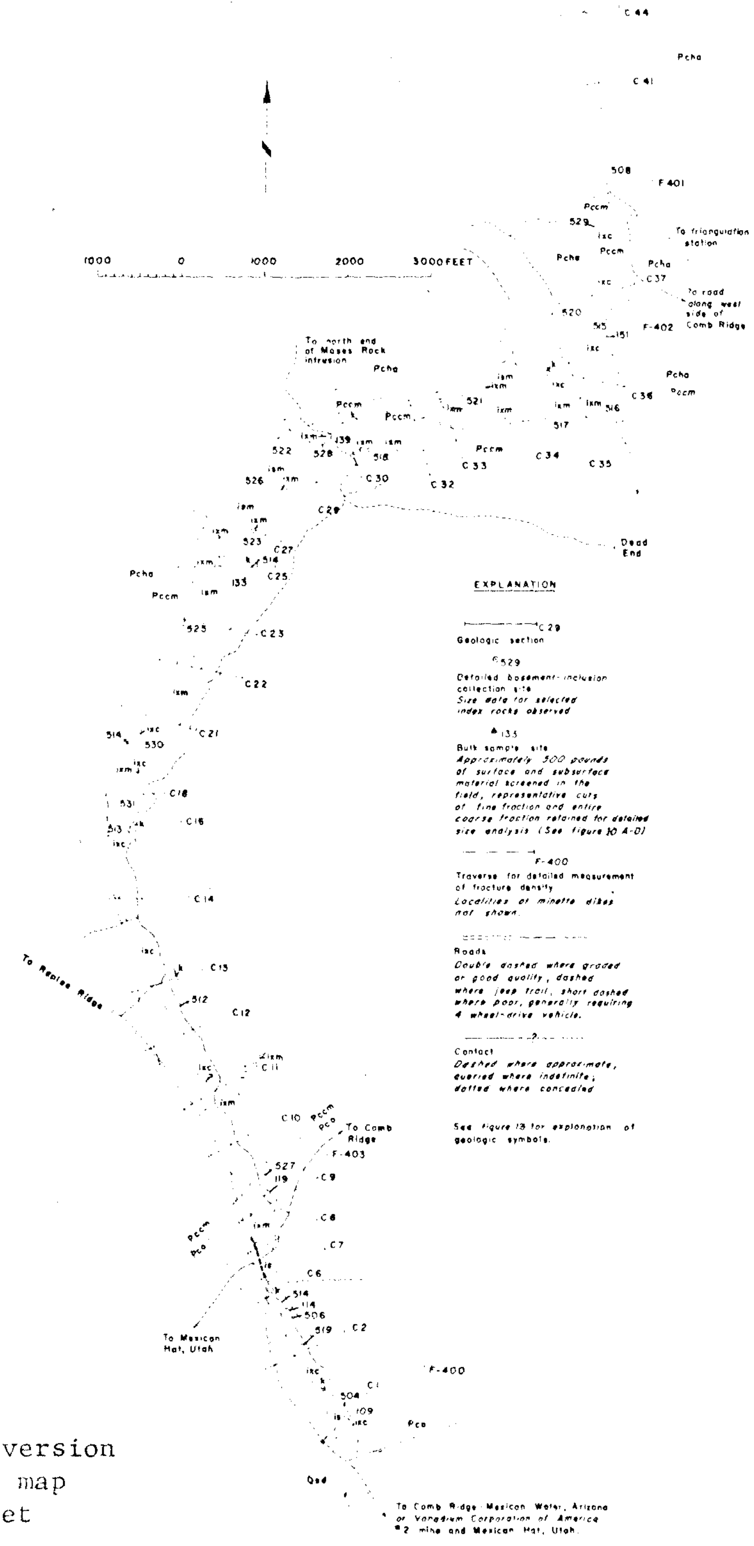

Enlarged version
of this map
in pocket

Explanation

Shown are four representative detailed structural cross-sections of the Moses Rock dike chosen from Appendix F. As will be discussed later in the text, these four cross sections probably represent the major stages of development in the dike: early stages of dike propagation (C-41); intermediate stages which include brecciation, kimberlite dike and sill emplacement in the wall rocks and initial stages of channelling (C-25, 34); late stages including stong channelling and transport of large blocks upward in the channels, stong dilution of the kimberlite with rock fragments and presence of large crystalline rock fragments in the breccia.

Figure 15 Selected detailed geological cross sections of the Moses Rock dike (1:2400 scale)

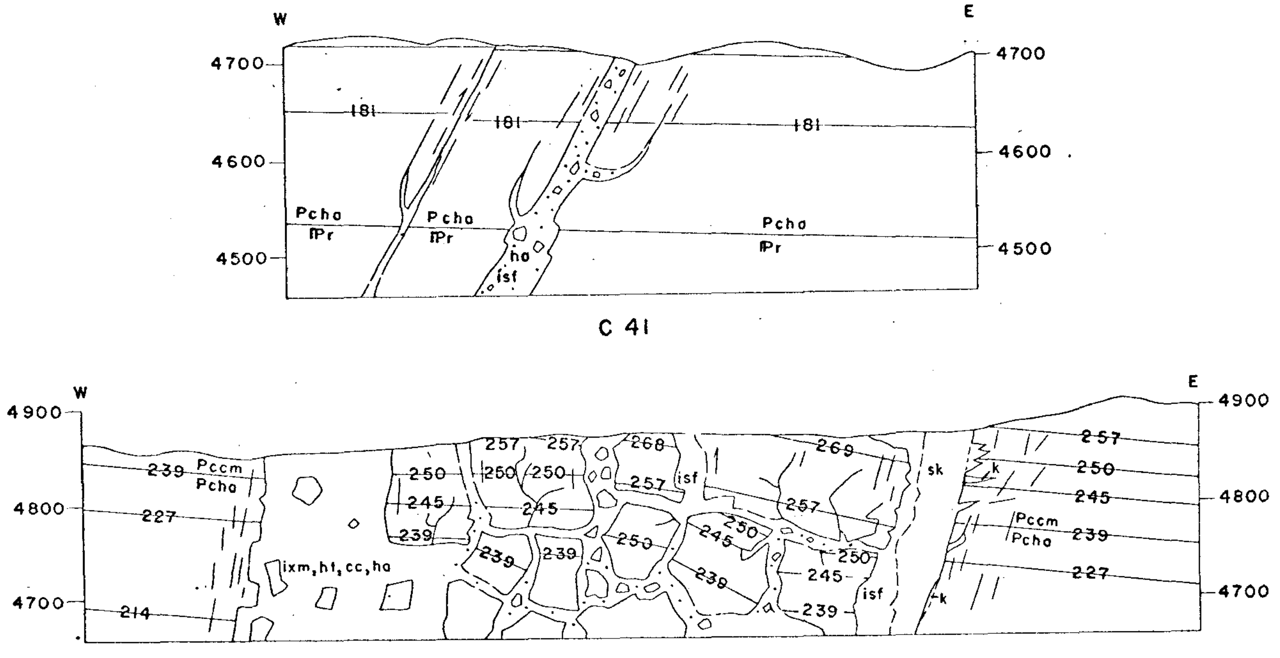

C 41

C 25

Figure 15a

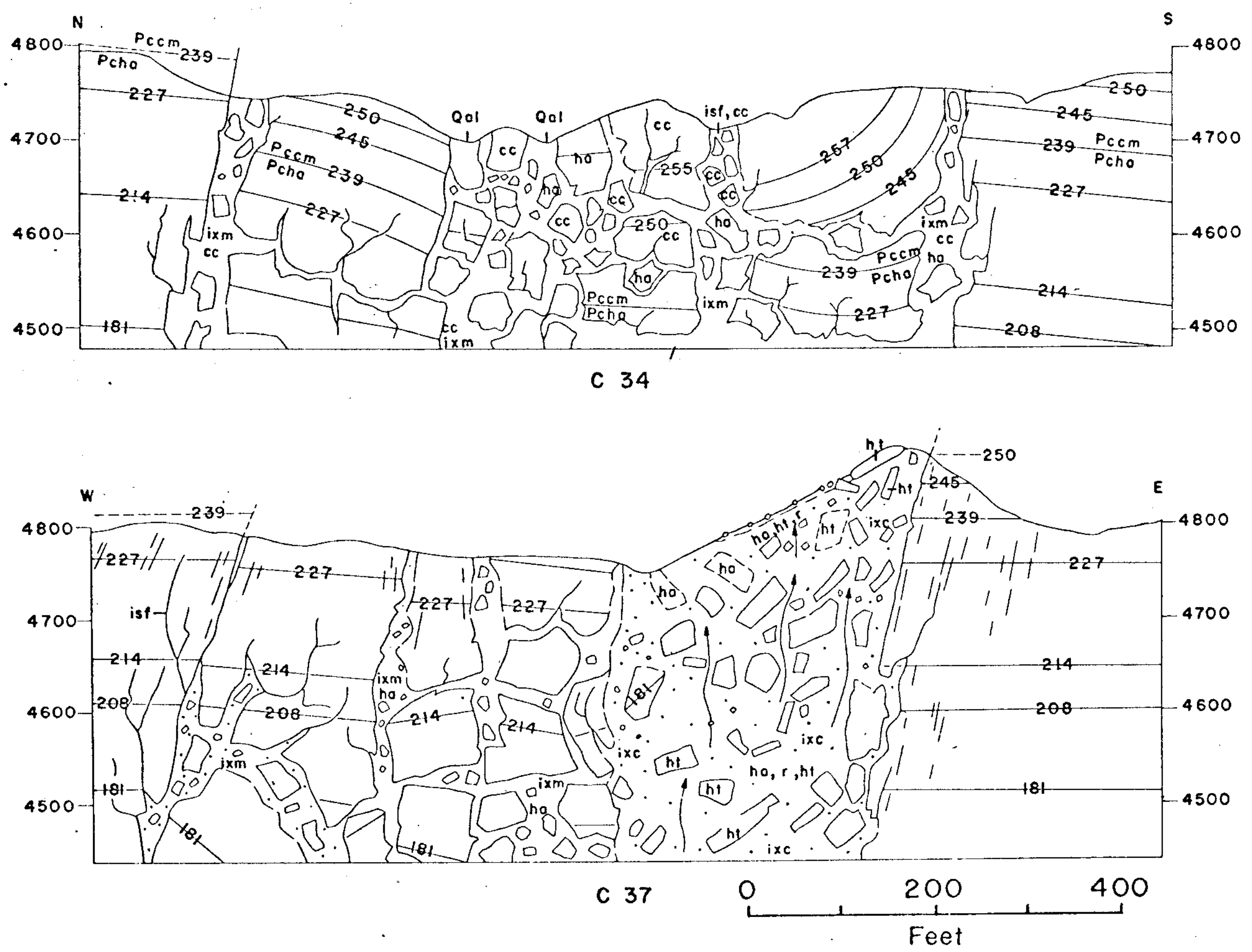
N
S
4800
4700
4600
4500
Pccm
Pcha
239
227
250
245
214
181
208
257
255
Qal
isf, cc
cc
ha
ixm
C 34
W
E
isf
ht
ixc
ha, r, ht
ha, ht, r
C 37
0
200
400
Feet

Figure 15b

detailed mapping. Topographic control was a topographic base map of 10 foot contour interval (with supplementary 5 foot contours locally) prepared by the U.S.G.S. photogrammetrically from the same photos used in the detailed mapping. Thus the topographic relations shown in the cross sections are quite good. Subdivisions of Cutler Formation strata shown on the cross sections are based on detailed descriptions of stratigraphic columns measured in beds in the dike walls or near the dike (Figure 7). Identification of the original stratigraphic position of blocks shown at the surface in the cross sections is done with confidence.

Southern Section: The Tail

The tip of the tail is not exposed. Recent sand dunes cover the south end of the Moses Rock dike but crystalline rock fragments found in the sand at the surface suggest its presence at least 1/3 mile southwest of the limit of present exposures.

For most of its 8000 feet of exposed length, the tail section forms a long, undulating, broadly rounded ridge trending about N 10° W (Figure 13, A4 to I2). It stands up to 100 feet above the surrounding Cutler beds, which dip gently southeastward 6° to 15° and are eroded to gentle questas of 3 to 15 feet relief. From a distance the ridge appears green in color and stands out predominantly from the surrounding red, orange and buff colored Cutler rocks (Plate 3A).

In the tail section, the dike varies in width between approximately 300 and 600 feet.

Exposure of the internal structure of the dike in this section is poor because the ground surface is covered with an unconsolidated lag deposit several inches thick consisting mostly of crystalline rock fragments which commonly are coated with desert varnish.

The rocks exposed at the contact range from lower Cedar Mesa Sandstone Member at the north end of the tail section to the upper part of the Organ Rock Tongue Member at the south end.

The contact dips steeply westward, about 80° on the average.

As elsewhere in the dike, contacts are generally undeformed, however in this section of the dike only, local folding and faulting are observed. Satellite dikes parallel to the contact are common in the vent walls on the west side; sills and low angle dikes on the east side. A well developed set of joints parallel to the contact exists everywhere in the vent wall rocks.

Folding is better developed on the east side of the dike than on the west. A broad synclinal fold tilts beds of Organ Rock Tongue upward in the walls at the contact along a 1500 foot section (Figure 13-E3 to C4 and Figure 15, Cross sections 6, 7, 8, 9). Structural relief is about 40 feet and deformation dies out about 300 feet east of the dike.

Folding of the same type occurs on the west side of the dike but generally dies out less than 100 feet from the contact.

Many small kimberlite-bearing dikes are developed along the vent walls on the west side of the dike which dip steeply westward but which commonly strike 10 to 15 west of the trend of the main dike. Several can be traced for nearly a mile along the west side of the main dike. In several instances these dikes join the main body of the dike (Figure 13-C3, D3).

A small anticline several hundred feet long occurs in the east wall of the dike near the top of the Cedar Mesa Sandstone beds. Structural relief is about 15 feet and deformation dies out about 60 feet from the contact. The axis of the fold parallels the dike contact (Figure 13-E3 and Cross section 10)-

Two sills of kimberlite-bearing breccia are emplaced in Cedar Mesa Sandstone beds along the east contact (Figure 13-3F, 4C and Cross section 11). One sill (at 4F) is well exposed in the questas and is about 6 feet thick for a distance of about 240 feet from the contact, where it abruptly changes thickness and nearly pinches out. It is clear that the enclosing strata have been forced apart along bedding planes to make room for the sill.

Faults with displacements of several feet at most are common parallel to the dike contact on both sides of the dike. Regardless of which side of the dike the fault occurs on, the block nearest the dike is down relative to the other (Figure 13-C4).

A well developed joint system parallel to the contact of the dike is observed everywhere in the vent walls near the contact. This is true throughout the dike regardless of the strike of the contact. The spacing of the joints decreases as an inverse power function of the distance from the contact (Figure 16). At the contact spacing of 1 inch or less is commonly observed, however wide variations exist from place to place. This set of joints generally vanishes 200 to 300 feet away from the contact.

Wall rocks are commonly bleached along joints near the contact. Bleaching is generally restricted to a narrow zone near the contact and bleached rock is generally 1 to 2 millimeters in width next to the joint.

A. Stereo view, nearly vertical contact of breccia at left with essentially undeformed and unaltered Cedar Mesa Sandstone at right. Blocks are mostly Cedar Mesa Sandstone. Northward view along east contact of southern section of the Moses Rock dike (near coordinates F-3 in Figure 13).

B. Stereo view, looking south of nearly vertical contact of intrusive breccia on right, with Cedar Mesa Sandstone on left; note lack of deformation and alteration at the contact. Foreground is within dike. The contact runs out of photo to left foreground. Ground surface in foreground is covered with typical thin surface deposit of concentrated crystalline rock fragments (map unit Qxr). Location of this photo is approximately G-2, Figure 13.

Plate 9. Characteristic contact relations of dike with wall rocks.

An important relationship exists between the joints and folded beds near the dike contact on the east side of the tail section (near D3,5, Figure 13). East of the dike, the undisturbed Organ Rock Tongue strata has an attitude N 60° E 12° SE; at the contact N 30° E 20°-25° SE. The joints, however, are parallel to the nearby contact regardless of the attitude of the beds in which they occur. This implies that the folding preceeded the formation of the joint set.

The dikes, the faults, and local joints all approximately parallel the dike contact.

All the breccia units are present in the tail section of the dike and the structural relationship between them is well exposed at several locations. Kimberlite occurs as pods within the dike (Figure 13-C3, B4), as slabs plastered against the outside wall of the dike (Figure 13-G2, I2 and Cross section 13). Kimberlite occurs in dikes outside the main dike in the vent walls (Figure 13-4C, 3D). Parts of the tail section are occupied from wall to wall by coarse and very coarse breccia (Figure 13 - C4 to B4; F3 to I2), and shorter sections by medium complex breccia (Figure 13, D3 to E3).

Dikes of coarse and very coarse complex breccia which propagate into the wall rocks apparently truncate kimberlite bodies locally (Figure 13 B3,5). Kimberlite is juxtaposed against Cutler rubble (Figure 13, B3) and Cutler rubble which locally fills the dike from wall to wall (Figure 13, E3). Quarternary surface lag deposits consisting of crystalline rock and limestone fragments cover the ground surface over areas of the dike filled with complex breccia (Figure 13-B4 to B3; D3 to H2). Elsewhere diluted kimberlite occurs as a transition unit between kimberlite and other breccias (Figure 13-G2). Some rather large limestone blocks and fragments from the Hermosa Group are scattered around the surface along the tail section.

Geological cross sections numbering from 1 to 16 are constructed across the tail section (Figure 15). Because the complex breccias are poorly exposed due to the surface rubble, the internal structure is not known in as great detail as elsewhere in the dike.

Middle-Section--The Body

About 8000 feet from the exposed south end, the Moses Rock dike changes trend rather abruptly from N 10° W to about N 15° E. This marks the junction of the tail and body sections. For 4000 feet the body section trends N 15° E, then changes to about N 70° E and continues on eastward for 3000 feet where it meets the head and feeler sections at the east end of the dike. Thus, the body section is a cross link between two north-trending dikes (Figure 13-I1 to N6).

This section is about 7000 feet long and varies in width from about 200 to 1000 feet.

Accompanying the abrupt change in trend from the tail section is an equally abrupt change in the character of the dike.

Whereas the topographic expression of the dike in the tail section was a ridge, in the body section, the Moses Rock dike is a shallow topographic trench, generally bounded on the south side by the steep face of a questa. On the north side, beds generally dip into the dike with almost no relief across the contact.

Local relief within the dike is locally up to 50 feet but generally is less and consists of a rough knobby or hummocky surface formed by scattered randomly oriented blocks of sedimentary rocks protruding from below the surface.

Exposures are generally very good. The surface lag deposit which covered the tail section is present only locally in the body section.

Strata exposed at the contacts range from the uppermost surface of the Halgaito Tongue, exposed for nearly 5000 feet along the north side of the section, to beds of Cedar Mesa Sandstone Member about 180 feet above the Halgaito contact. The strike of the beds in the walls changes slightly along the length of the body section from about N 60° E to N 70° E; dips range from 8° to about 11° southeast.

The contact dips steeply northwest or north, about 80°.

The structure of the contact of the body is quite different than in the tail section. No folds were observed in the wall rocks; very few dikes; occasional sills; and no faults. The ubiquitous joint set parallel to the contact is present and well developed.

There are two interesting contact relations in this section. First, at several different places along the contact large blocks of the wall rock are partially separated from the wall by fractures filled with kimberlite-bearing breccia (Figure 13-J2, K3). Some blocks appear to be "hanging by a thread" to the wall. By searching along the contacts throughout the entire dike it is possible to find blocks in all stages of separation from the wall. Some of the best examples occur in this section (for example, Cross sections 21, 22, 29, 32).

The other interesting contact relationship is the presence of small sills of kimberlite in the south wall (Figure 13-K3, L3).

The interior of this section of the dike is occupied by Cutler rubble with subordinate amounts of kimberlite, diluted kimberlite and medium complex breccia.

This is the area of the typical Cutler rubble. The dike is occupied from wall to wall by large blocks of Cutler Formation commonly exceeding 100 feet and displaced only short distances downward, generally a few tens of feet, and set in a light-lime-green, fine complex breccia matrix.

Kimberlite occurs as slabs plastered against vent walls (Figure 13-2-G; 2-H. N-4, I2) within large blocks in the dike; as sills emplaced in the walls at the contact (Figure 13-K3); and, as large pods bounded by diluted kimberlite (Figure 13-L3).

Irregular pod-like bodies of medium complex breccia are enclosed in Cutler rubble (Figure 13-L3, M3, N4, N5). These bodies appear to be irregular vent-like intrusions of medium breccia into the surrounding Cutler rubble.

Since exposures are generally excellent,geological cross sections of the section contain much detail (Cross sections 18-34). Some of the more important features are shown in these cross sections. Huge blocks of wall rock detached along joints hang from the contact. As separation of blocks from walls occurs, joints are filled with breccia. Blocks are displaced and rotated in varying amounts, but always only short distances, at most a few tens of feet, and rotations generally are less than 60° (Cross sections 18, 21, 22, 23, 25, 29, 32). Kimberlite sills intrude the vent walls (Cross section 25) and medium complex breccia intrudes into Cutler rubble in small irregular blob-shaped vents (Cross sections 22, 25, 27).

Northeast Section: The Head

At the northeast end of the eastward trending body section, the dike widens out into a roughly triangular shaped area about 3000 by 1500 feet with an abrupt eastern boundary which trends almost northward. This is called the head section (Figure 13-06 to N6 to P7). The feelers sections are two parts of what appear to be the same long dike which projects about a mile southward and 3 miles northward from the east side of the head section. Thus, the head section occupies the intersection of two structural units: the east trending body section and the north trending feelers. Its internal structure is quite different than that observed in the other parts of the Moses Rock dike.

The topographic expression of this section is generally a trench but with many knobby mounds protruding from the dike (Plate 10). Wall rocks stand higher than the dike by a few feet around most of the contact. However, along the east side the dike consists of two rounded knobs which stand with about 120 feet of relief above the local terrane These are prominent topographic features and are strewn with large limestone blocks giving them a distinctive knobby appearance (Plate 11). Within the dike, there is local relief of 50 feet commonly consisting of large sedimentary rock blocks and small stream valleys cut between them.

Exposures are good to excellent generally, although surface lag concentrations of limestone and crystalline rock fragments obscure the underlying deposits locally. Surface deposits are not as extensive as in the tail section, and desert varnish is not as well developed on

A. Stereo view of north end showing negative topographic exposition of dike; rocks at the contact are uppermost Halgaito member, Cutler Formation and lowermost Cedar Mesa Member. Location is approximately O-7, Figure 13, looking west-southwest.

B. Stereo view showing nearly vertical contact of intrusive breccia (right) with lowermost Cedar Mesa Member and uppermost Halgaito Member of the Cutler Formation, which dip gently to the south (left). Large block in near foreground is Cedar Mesa Member dipping northward (right). Prominent light-colored block in mid-foreground just across gully is Rico Formation block stratigraphically up approximately 500 feet. Contact can be traced in photo from left foreground to center background. Location is approximately N-7, Figure 13, looking westward.

Plate 10. Topographic expression of dike, head section.

A. Northward view along east contact. Shows large breccia blocks of Hermosa Group limestone displaced upward at least 700 feet. Talus deposit, is composed of limestone fragments and blocks, mixed with a few large crystalline inclusions which cover the slope to the west (left). The jeep is parked on the top of the Halgaito Member. The pink unit stratigraphically above is lowermost Cedar Mesa Member. The contact with the dike is essentially undeformed and unaltered. Its attitude is about N 05° W-70°W. A fracture system in the wall rocks is well exposed here and dips westward into the dike. The intrusive material is very coarse complex breccia, bearing large crystalline rock fragments and large limestone blocks in a matrix of comminuted sedimentary debris and rather highly diluted kimberlite.

B. Southward view on opposite side of knob shown above.

C. Close-up of talus slope on west (left) side of Plate 11-A. Blocks and fragments are limestone and occasionally crystalline rock; bush in foreground is about 2' in diameter.

Plate 11. Photos of knob at northeast end of Moses Rock dike littered with large Paleozoic limestone fragments.

crystalline rock fragments. Rubble deposits consisting of limestone fragments cover much of the ground surface on the topographic knobs described above (Plate 11).

Rocks exposed in the vent walls range through a vertical distance of only about 110 feet straddling the contact between the Halgaito Tongue and Cedar Mesa Sandstone Members. In the vent walls on the northwest leg of the triangle forming this section, Halgaito beds are exposed, locally as much as 40 feet below the contact with the Cedar Mesa Member. Along the east contact rocks in the vent walls are both Halgaito and Cedar Mesa strata. Commonly the weak mudstones of the lower-most Cedar Mesa are stripped off, leaving an erosion surface consisting of the resistant dark red calcareous siltstones and sandstones at the top of the Halgaito Member. Cedar Mesa beds 70 feet above the Halgaito contact are preserved locally on the east contact (Cross section 36; Plate 10). Along the southern contact wall rocks are Cedar Mesa Sandstone, zero to 50 feet above the Halgaito contact.

The contact is well exposed almost everywhere.

Along the northwest edge of the section the contact dips northwestward 60° to 80° westward; and along the southern edge, 70° northward to vertical.

Structures in the wall rocks are not well developed. No faults, folds or sills and only a few minor dikes were observed. The joint set in the walls parallel to the contact is well developed here as it is everywhere else. The few dikes observed were parallel to the contacts locally and generally were projections of the contact into the wall rock where the contact jogged locally (Figure 13-07).

There is an interesting structural relationship involving the two prominent topographic knobs along the east edge of the section. These knobs appear to be local openings or vents along the dike which makes up the two feeler sections (Figure 13-07, P7). The connection between these closely juxtaposed and large vents, both several hundred feet in diameter, however consists of three very thin and insignificant looking dikes. In fact, because of a local surface deposit of limestone rubble, it is not possible to demonstrate that these small dikes actually contact the two vents at all (Figure 13-07-5).

The internal structure of the head section is very well exposed and is as complicated as any in the dike and probably is the most interesting. Most of the area is filled with very coarse and coarse complex breccia. Sedimentary rock fragments are commonly very large and are displaced both upward and downward with respect to their original position in the vent walls. A giant block of Cedar Mesa Sandstone Member measuring about 750 x 200 feet is detached from the north wall and has settled a few feet downward into the vent (Figure 13-07).

Kimberlite occurs as a dike in a Cedar Mesa sandstone block (Figure 13-N7; Plate 4 and Cross section 36). This occurrence is the type locality for kimberlite in the Moses Rock dike and is the only locality where dense blackish-green specimens were obtained.

Large areas of very coarse complex breccia occur in this section. The outlines of these areas are very irregular and they appear to be vents of very coarse complex breccia implaced through areas occupied by medium breccia or Cutler rubble. The kimberlite dike in the Cedar Mesa block previously described appears to be cut off by the vent of very coarse complex breccia nearby (Cross section 36).

Fragments of de Chelly Sandstone Member occur displaced downward between 1450 and 1600 from their original stratigraphic location (Figure 13-07).

Limestone fragments of Rico Formation and Hermosa Group nearly 100 feet in size are common (Plate 11; Cross sections 36, 37). A block of Rico Formation measuring 210 x 100 feet, and at least 20 feet thick is displaced about 500 feet upward from its original position (Plate 12; Figure 13-N7).

Geological cross sections through the head section are detailed because exposures at the surface are good (Cross sections 35, 36, 37). Generally they show mammoth blocks of Cedar Mesa Sandstone Member detached at the north and south vent walls and displaced downward. Kimberlite dikes or sills are preserved rarely in these blocks and medium complex breccia occupies the joints separating these huge blocks from the wall rocks. The center and east edge of the head section appear to be vents of very coarse complex breccia in which large sedimentary rock fragments are found transported significant distances both upward and downward from their original position in the walls.

East Dike Section: North and South Feelers

So far we've traced the Moses Rock dike from the southern tail section through its body to its head along a course which curves eastward but which very abruptly terminates at a long north-trending dike. This dike dips steeply westward and can be traced both north and south from the head section. These extensions from the head are called the north and south "feelers".

(Location is approximately coordinates M-7, Figure 13.) White block in foreground is sandstone from Rico Formation. Just across gully in middle ground is a cluster of very large fragments of Rico Formation, displaced upward about 500 feet from below. In the center of the gully in the left background, the green material is a kimberlite dike in a large block of Cedar Mesa Sandstone Member, at the type locality for kimberlite at Moses Rock. A close up of this locality is shown in Plate 4.

Plate 12. Northwestward view across head section of the Moses Rock dike.

The south feeler extends about one mile from the head section, as a narrow dike a few feet wide which has little topographic expression (Figure 13-M8). It cuts beds of the lower 2/3 of the Cedar Mesa Sandstone Member where they dip southeastward about 5° and form shallow questas which are incised by streams forming gullies 5 to 15 feet deep. Here the Cedar Mesa Sandstone Member commonly contains gypsum beds which form a puffed-up, cauliflower-like surface layer with a light-orangish-buff and grey color. Over the dike is a surface deposit which is light lime-green in color, and since the dike has no marked topographic expression, its presence is most apparent from a color change in the soil. No deformation was observed along the south feeler; no folds, faults, dikes or sills. Joints parallel to the dike contact are present, however.

The north feeler is much more interesting than the south. This dike extends about 3 miles north of the head section across the large questas formed in strata of the Halgaito Tongue, all the way to the Canyon of the San Juan River where it pinches out in the Pennsylvanian beds exposed in the Canyon walls (Figure 13-Q7; Plate 13). Relief across the questas in the Halgaito Tongue commonly exceed 100 feet. The dike is very well exposed for much of its length and its topographic expression is generally negative in the resistant calcareous siltstones of the Halgaito Tongue.

Along the north feeler, the dike trends about N 08° W and dips westward 75° to 80° westward.

Displacement of wall rocks is observed across the dike in which the westside is down about 8 to 10 feet locally with respect to the

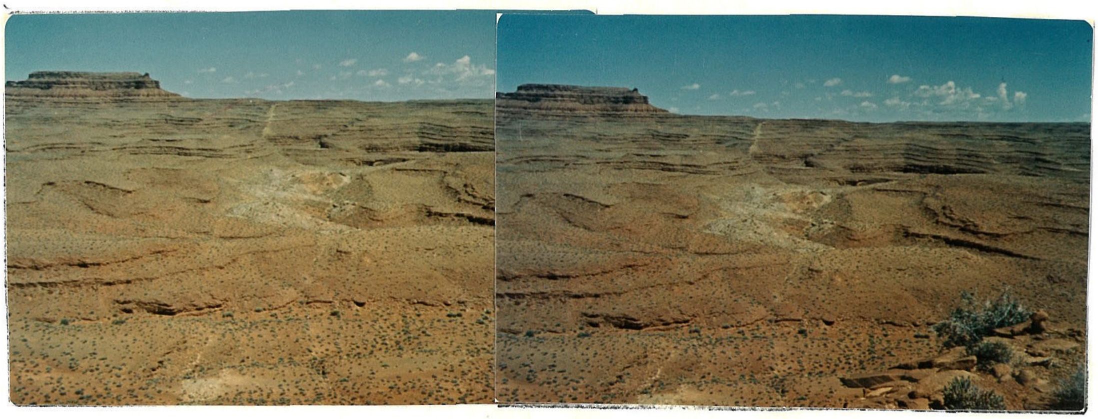

Northward stereo view from location near P-7, Figure 13. Dike dips steeply westward in rocks of Halgaito Member. In the distance, displacement on the dike is apparent with the west side down (normal). The intrusive material filling the local widening (small diatreme about 1/4 mile away) is breccia composed of blocks from the Halgaito Member and some large blocks from the limestone units below. Note the cluster of limestone blocks in the right near corner of the body. These are Rico Formation fragments. Crystalline inclusions reach 5-6 feet in diameter within this body (biotite-granite-gneiss).

Plate 13. Northward view of east dike (feeler) section showing dike and widening along dike north of main part of the Moses Rock dike.

eastside. Thus, the sense of the displacement is "normal" (Plate 13). Note that this is opposite to the sense of displacement on the low angle, westward dipping, thrust fault west of the Mule Ear diatreme along which the westside is up relative to the east.

No folds were observed.

Joints are present in the wall rocks which parallel the contact of the dike.

About 2000 feet north of the head section along the north feeler, the dike widens to about 300 feet for a distance of about 1000 feet along the dike (Figure 13-R7). The internal structure of this area is quite similar to the head section. The topographic expression of this vent is negative with respect to the wall rocks. Its surface is hummocky and is incised with several small streams producing local relief of about 50 feet (Plate 13).

The thin dike composing the south feeler and the north feeler (except the vent developed about 2000 feet northward from the head section) is filled with fine and medium complex breccia.

The dike is generally thin, 3 to 5 feet wide along much of its length. Fractures in wall rocks are common and pervasive near the contact, parallel to the dike contact.

The dike widens into a small vent along the north feeler (Figure 13-R7). Very coarse and coarse complex breccia occurs in two irregularly shaped blobs in the core of the vent. Limestone fragments are common; crystalline rock fragments up to 6 feet in diameter are present (biotite-granite gneiss). In the rest of the vent the areas around the margins are filled with Cutler rubble and fine complex breccia. Along the walls at the north and south end of the vent are large blocks of wall rock bounded by faults or pervasive fractures which are in an incipient stage of separation from the dike wall.

Joints

Two well developed systems of joints are present in the walls of the Moses Rock dike; a regional set striking about N 80° W near the dike and nearly vertical which apparently is oriented normal to the major folds in the area, and the system of joints in the wall rocks of the dike.

The spacing of both sets decreases as an inverse power function of the distance measured normal to the dike contact (Figure 16). At the contact joints they are commonly observed with one inch spacing. Joint frequency is not uniform from place to place along the contact but data are not sufficient to state how it varies with lithology of the rocks in the dike wall, width of the dike, intrusive material or other factors.

Both sets are present in blocks within the dike.

A second set of subordinate joints are present locally parallel to the dike contact but with dip inclined to it.

Bleaching of wall rocks along joints is pronounced on the set parallel to the dike contact but occurs locally on the regional set in subordinate amounts. It is restricted to zones several millimeters wide on both sides of the joints, and consists of a color change in red sandstone, siltstone, and shale to yellow or very light grey-green. Bleaching is generally restricted to joints within about 10 feet from the contact but rarely is observed as much as 100 feet from the contact.

Figure 16. Fracture density in wall rocks at Moses Rock diatreme and at nearby minette dikes

Location of profiles at contacts of the Moses Rock dike are shown in Fig. 14.

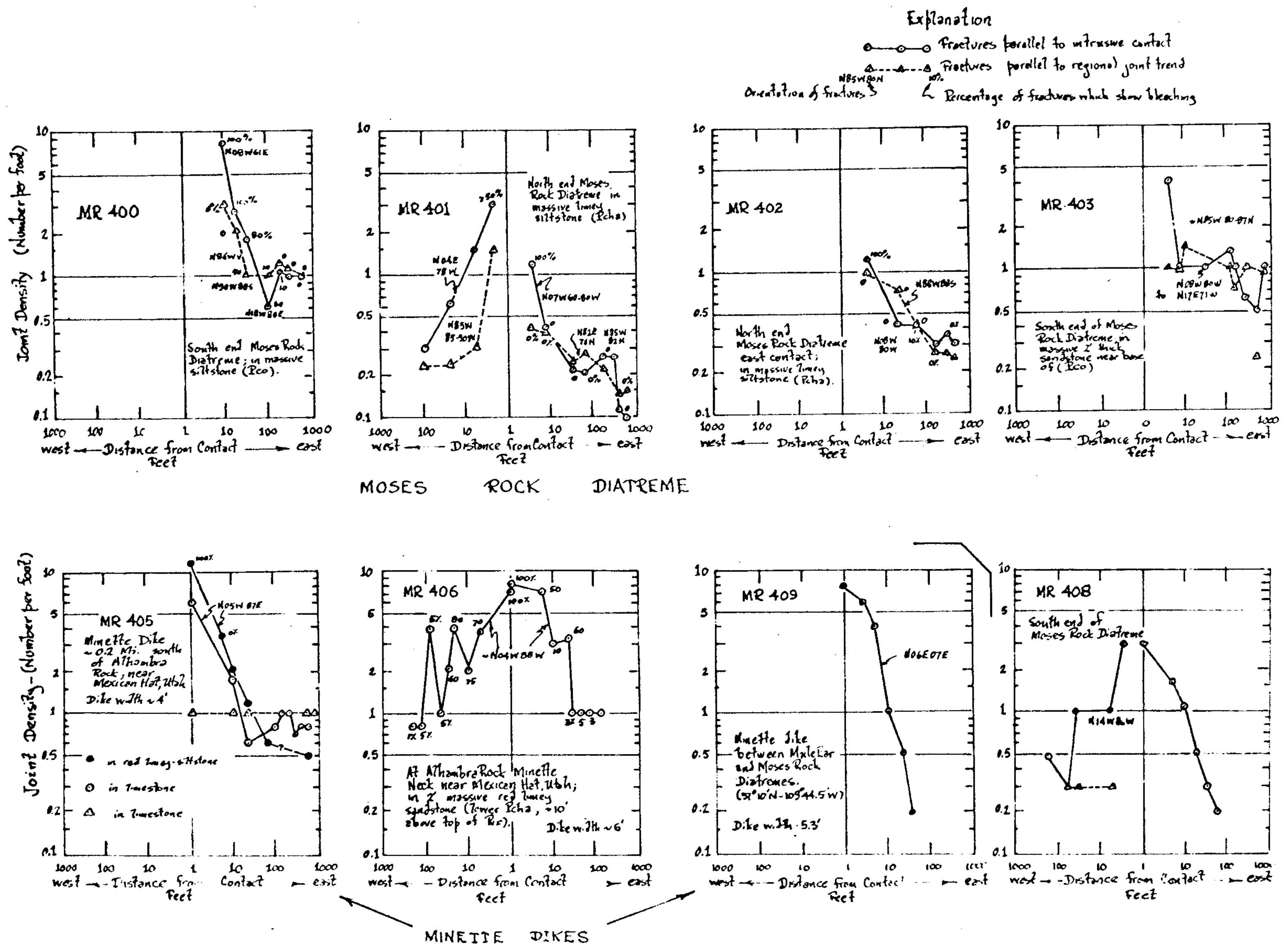
Explanation
Fractures parallel to intrusive contact
Fractures parallel to regional joint trend
N85W80N
Orientation of fractures
10%
Percentage of fractures which show bleaching
MOSES ROCK DIATREME
MR 400
South end Moses Rock Diatreme; in massive siltstone (Pco).
100%
N08W61E
0%
100%
80%
N86WV
N90W80S
N8W80E
MR 401
North end Moses Rock Diatreme in massive limey siltstone (Pcha)
N04E 78W
N85W 85-90W
750%
100%
N07W60-80W
N81E 71N
N85W 82N
0%
MR 402
North end Moses Rock Diatreme east contact; in massive limey siltstone (Pcha).
100%
N86W80S
N08W 80W
10%
0%
MR 403
South end of Moses Rock Diatreme in massive 2' thick sandstone near base of (Pco)
N85W 80-87N
N08W80W to N17E71W
MINETTE DIKES
MR 405
Minette Dike ~0.2 Mi. south of Alhambra Rock, near Mexican Hat, Utah
Dike width ~4'
N05W 87E
100%
0%
in red limey siltstone
in limestone
in limestone
MR 406
At Alhambra Rock Minette Neck near Mexican Hat, Utah; in 2' massive red limey sandstone (lower Pcha, ~10' above top of Pc).
Dike width ~6'
N04W88W
100%
50
60
70
75
80
MR 409
Minette dike between Mule Ear and Moses Rock Diatremes. (37°10'N-109°44.5'W)
Dike width 5.3'
N06E07E
MR 408
South end of Moses Rock Diatreme
N14W80W
Joint Density (Number per foot)
10
5
2
1
0.5
0.2
0.1
1000
100
10
1
10
100
1000
west ← Distance from Contact → east
Feet

Bleaching is also present along bedding planes in strata of the dike wall which extends locally 100 feet or more away from the contact.

The Relationship Between Block Size and Displacement

Detailed mapping within the dike has shown that most of the large blocks are derived from the Cutler Formation and have not been displaced greatly from their original stratigraphic position. Most are displaced downward, a few tens of feet and slightly rotated. Block displacement, however, varies greatly from place to place and is correlated with the nature of the breccia.

In the Cutler rubble unit which occupies most of the body section of the dike, large blocks are displaced only slightly, everwhere downward. The largest block observed within the dike, about 750 by 200 feet in plan, is a Cedar Mesa Sandstone fragment displaced downward a few feet along the north contact near the junction of the body and head sections of the dike.

Large blocks within the medium complex breccia are also all derived from the Cutler Formation and all displaced downward.

In the coarse and very coarse complex breccia large blocks are displaced both upward and downward. The largest block displaced upward in the entire dike is a fragment of Rico Formation 210 x 100 feet in plan by at least 20 feet thick; it is displaced upward about 500 feet. Many large fragments of Rico Formation and Hermosa Group measuring 50 feet on a side are common within the very coarse complex breccia unit, particularly in the head section.

The largest crystalline rock fragment is a very well-rounded ellipsoidal block of fine-grained biotite-gneiss 6 feet in diameter found in the vent along the north feeler, in very coarse complex breccia. Similar blocks of the same lithology nearly as large are common in the head section.

Several blocks of de Chelley Sandstone Member were observed displaced downward 1400 to 1650 feet, in the head section in very coarse complex breccia. This is significant because it places a lower limit on the amount of erosion which has occurred since the emplacement of the dike, and also a limit on the depth of the present erosion surface below the ground surface at the time of eruption. At the Mule Ear diatreme, Mancos shale fragments are observed displaced 5000' downward, a minimum figure for the amount of erosion since the time of emplacement and suggests the overburden was at least a mile at that time.

A significant relationship exists in the population of blocks which have been transported upward from their original stratigraphic position. Nearly all such blocks occur in the very coarse complex breccia unit. Within the population of upward displaced blocks there is an inverse relationship between the largest block observed from a given horizon and the depth to that horizon (Figure 17). For example, in the head section where the very coarse complex breccia is best exposed, the largest Rico Formation block is 210 feet across; the largest Hermosa Group block, 60 feet; the largest Paradox Formation block, 25 feet; the largest crystalline rock fragment, about 6 feet. Thus, in a general way, for blocks whose original stratigraphy is known, the farther down the vent the material originated (or the greater the distance transported), the smaller are the observed fragments (Figure 17). This is an important result because if a similar inverse size-depth relationship holds for the crystalline rock fragments, then the relative size of these fragments may be a clue to the relative depth from which they originated in the vent walls.

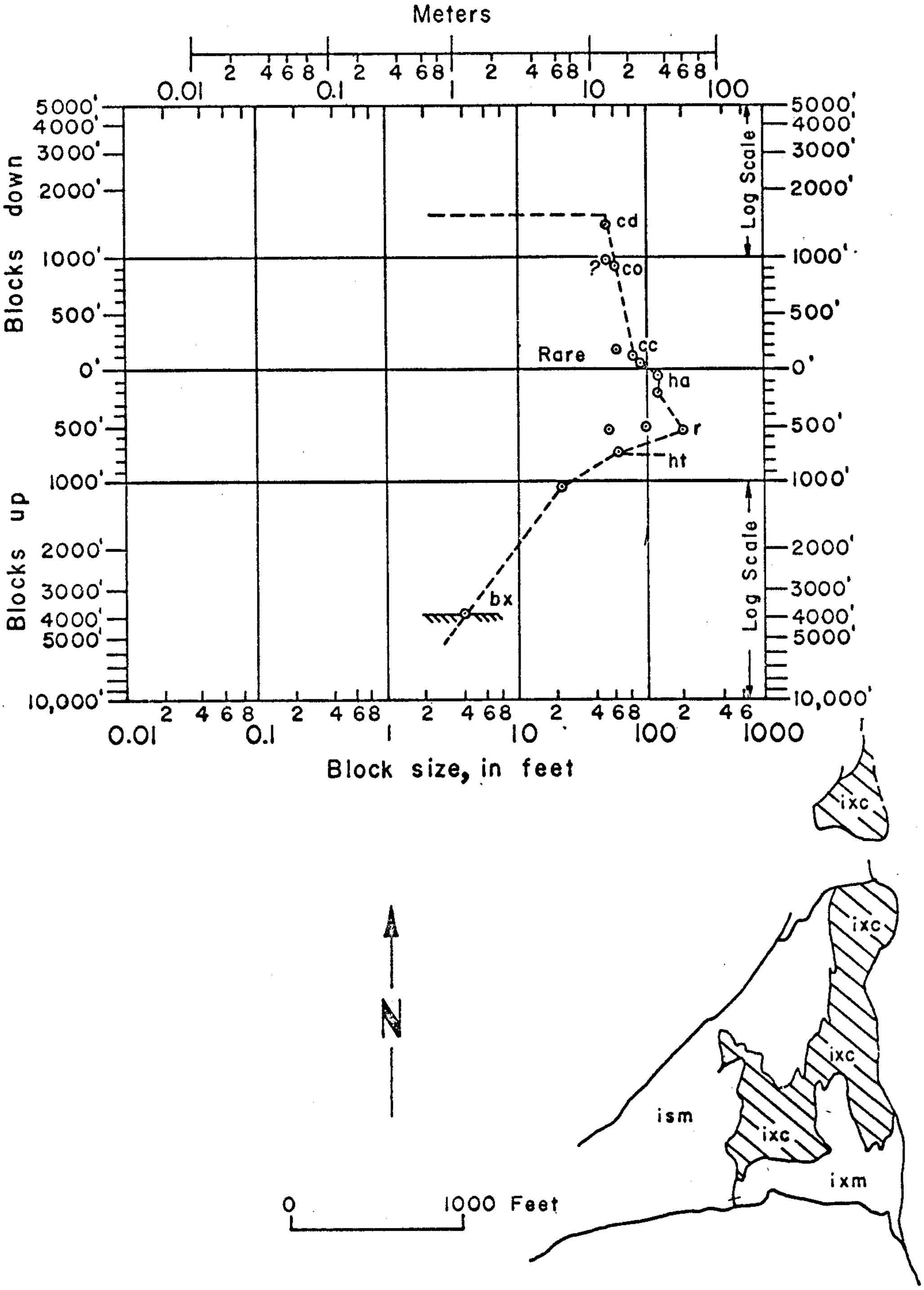

Figure 17. Fragment size plotted against stratigraphic displacement for rock fragments at northeast (head) section

Fragment Displacements at Other Kimberlite-bearing Diatremes Compared With Moses Rock and the Maturity of Eruption at Various Vents

There is an interesting systematic relationship between rocks in the various kimberlite-bearing diatremes which may reflect the maturity of the eruption at each vent. The distance which sedimentary rock blocks are displaced downward in various vents differs. At Mule Ear blocks are down 5000 feet; at Garnet Ridge, about 1200 feet; at Moses Rock, 1450 to 1600 feet; at the Cane Valley diatreme, about 80 feet. Also, the size of the largest crystalline rock fragment in each diatreme varies. At Mule Ear fragments of granite gneiss 25 to 30 feet in diameter are present, at Garnet Ridge, crystalline fragments about 7 feet in diameter were observed, at Moses Rock 6 to 7 feet, at Cane Valley about an inch, and at Red Mesa, 2 to 3 feet. When these data are plotted a good correlation results (Figure 18). There exists a limit to the distance of downward displaced blocks, that is, the total thickness of overburden.

It is suggested that both these factors reflect the maturity of development at a given vent. Apparently, the eruption at the Mule Ear diatreme reached a greater stage of maturity than at the other diatremes. The Moses Rock dike and the Garnet Ridge vents were arrested at about the same stage of development which was somewhat less developed than at Mule Ear. The Cane Valley diatreme was arrested early in its development.

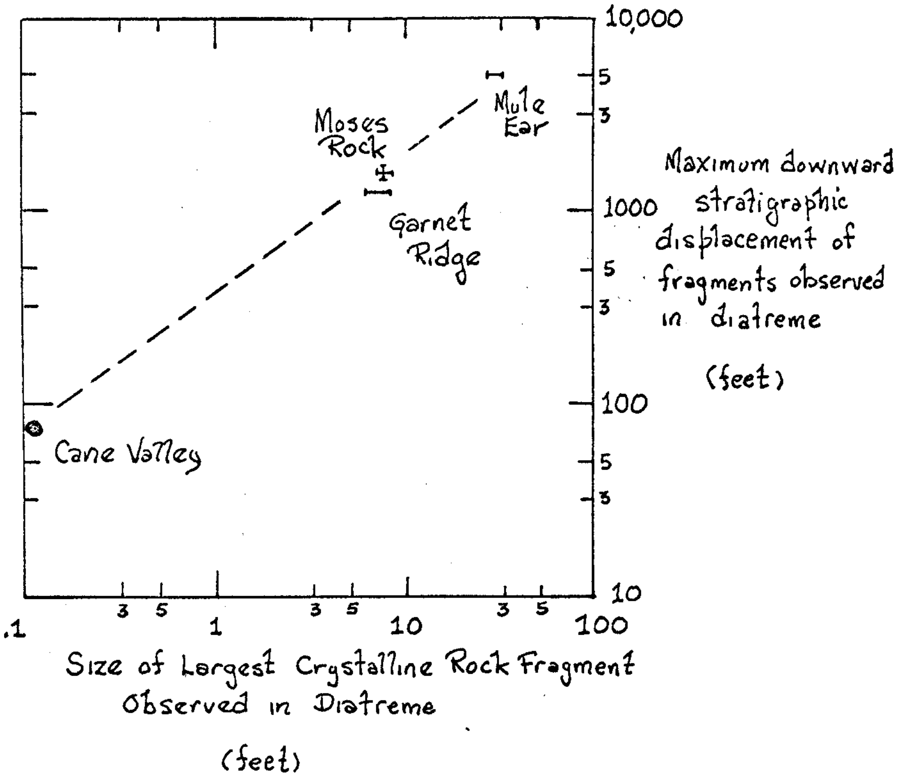

Figure 18. Plot of size of largest crystalline rock fragment and maximum downward stratigraphic displacement of fragments observed in Moses Rock, Mule Ear, Garnet Ridge, and Cane Valley diatremes.

Age of the Moses Rock Dike

The age of the Moses Rock dike is not precisely known. It is well known that mineral dates from kimberlites are commonly at variance with their geological ages.

A rough lower bound can be established using the estimated erosion rate. The Mule Ear and Moses Rock diatremes are probably contemporaneous. The Mule Ear diatreme contains blocks of Mancos shale displaced about 5000 feet downward from their stratigraphic position in the undisturbed beds of the vent wall. Hunt (1956, p. 71) cites an estimate of the present average erosion rate over the entire Colorado Plateau of 1 foot per 2150 years based on the rate of silt accumulation in Lake Mead. At this rate of erosion it would take about 11 million years to erode 5000 feet of strata.

Radioactive age dates have been obtained on minette from near Mexican Hat of 29 million years. These were K-Ar ages on biotite (J. Zioney, private communication). This age, however, must be regarded with suspicion because the minettes are potassium rich and may have contained significant amounts of excess radiogenic argon. Thus, one might anticipate that age dates on the minettes would tend to error on the high (old) side. Furthermore, the age relationship between the kimberlite and minette in the vicinity of the Moses Rock dike can only be inferred. It is believed that the minettes and kimberlites are pene-contemporaneous but no field relationships prove this.

Preliminary results of lead isotopic analyses of lead from zircons separated from rhyolite and granite rock fragments in the Moses Rock dike show that these fragments are Precambrian, about 1460 million years old, and the systems probably were disturbed in the Tertiary, very approximately 30 to 40 million years ago. The data at hand are insufficient to bracket this disturbance more precisely, furthermore one is not justified in assuming that the disturbance was a result of the eruption itself.

The dike is certainly older than the youngest fragments of sedimentary rocks contained in it. The youngest fragments in the Moses Rock dike are Permian de Chelley Sandstone Member. The Mule Ear diatreme contains Cretaceous Mancos Shale fragments. Thus, a maximum age for the kimberlite diatremes is Cretaceous.

In the vicinity of Buell Park, the Eocene Chuska Sandstone unconformably overlies the folded Paleozoic and Mesozoic rocks in the Defiance monocline. The kimberlite diatremes cut the Chuska and the minettes cut the kimberlite (Allen and Balk, 1954). However, there is no sound basis for saying that the vents near Buell Park are contemporaneous with the cluster along Comb Ridge, so no inference regarding ages is justified.

The Moses Rock dike is almost certainly Tertiary in age. It seems most plausible that the cluster of kimberlite dikes and pipes along the Comb Ridge are contemporaneous. Lacking evidence to the contrary, it is believed that the minettes are roughly the same age, perhaps slightly younger. Thus, an age of 10 to 40 million years is probably most consistent with the data at hand.

Summary of the Geology

The Moses Rock diatreme is a north-striking, hook-shaped composite dike about 4 miles long, cutting gently dipping strata of the Cutler Formation two miles west of the axis of Comb Ridge monocline. Contacts of the dike are vertical to steeply westward dipping. Structure at the contact is relatively simple. Rocks in the vent walls are generally undeformed and unaltered except for jointing parallel to the contact, and local bleaching and local minor folding. Most commonly beds are simply abruptly truncated at the contact. Dikes and sills of kimberlite or kimberlite-bearing breccia are observed in the vent walls but they are not pervasive. Jointing appears to play a key role in the incorporation of large blocks into the dike, as all stages between simple jointing and separation of blocks from the vent wall, rotation and comminution are observed.

The dike is filled with breccia composed of kimberlite (green serpentine-rich microbreccia), kimberlite diluted with comminuted clastic sedimentary debris--probably mostly from the Cutler Formation, rubble composed of large to small blocks of Cutler Formation and complex breccia composed of kimberlite components highly diluted with comminuted clastic debris intricately mixed with blocks of Cutler Formation, rock fragments from the limestone units below and well-rounded fragments from the crystalline basement. Of all the material in the dike, approximately 72% is derived from the Cutler Formation, and only 12% is kimberlite, most of it finely dispersed through the various breccias. Only about 1% of the exposed area of the dike is occupied by kimberlite as a discrete mappable unit. About 12% of the breccia is composed of limestone fragments, 3% crystalline basement fragments. In terms of fragment size, about 12% are larger than 100 feet long, 18% between 10 and 100 feet, 23% between 1 and 10 feet, and 47% less than 1 foot across.

The size frequency distributions of the fragments collected in the bulk samples are similar to distributions produced in comminution processes, such as mechanical grinding in a ball mill. The Cutler fragments exhibit the most mature curves, limestones intermediate, and crystalline basement rocks, least mature curves, which probably simply reflects the relative resistance of these rock types to fragmentation. Smaller limestone fragments and most crystalline basement fragments are very well rounded, many approaching spheres in shape.

Kimberlite occurs as small dikes within large breccia blocks with the main dike, as small sills emplaced in the vent walls, as small dikes outside the main dike, as small bodies plastered against the outside wall rocks at the contact, and as pods within the dike. Diluted kimberlite occurs as pods or layers separating kimberlite from other breccia blocks. Cutler rubble generally occupies large areas within the dike extending from wall to wall. Medium complex breccia commonly occurs in irregular pod-like bodies within Cutler rubble. Coarse and very coarse complex breccia occupies large irregularly shaped vents as in the head section or fills sections of the dike from wall to wall.

The occurrence of the various breccia units within the dike suggests that kimberlite and kimberlite-rich dikes were emplaced early in the sequence. Rubble composed of large blocks of Cutler was next, and finally the complex breccias carrying progressively larger fragments of crystalline basement rocks. Those with large sedimentary blocks displaced upward and large crystalline rock fragments were emplaced last, through the rubble units.

Dilution of the kimberlite components by rock debris is very slight in the rare type kimberlite dikes, the order of 1 part in 20. In the rubble, however, kimberlite components are found only interstitially between very large blocks and where they are highly diluted with debris probably derived largely from the comminuted surface of the blocks themselves (mostly Cedar Mesa Sandstone Member). In the complex breccias containing abundant basement fragments, dilution of the kimberlite components varies with the size of the basement fragments. Kimberlite components are characteristically diluted by factors of 1 part kimberlite to between 1 and 3 parts rock fragments in those complex breccia units where basement inclusions are relatively small, less than 6" maximum. In the complex breccias where crystalline fragments are very large, greater than 12", dilution of the kimberlite reaches 2 to 7 parts debris to 1 part kimberlite components.

The largest block observed in the dike is Cedar Mesa Sandstone Member measuring 750 by 200 feet. It is displaced downward a few tens of feet. The largest block displaced upward is a fragment of Rico Formation measuring 210 x 100 feet which is at least 20 feet thick, displaced about 500 feet from its original stratigraphic position. A fragment of de Chelley Sandstone Member is observed displaced downward about 1400 feet.

At the northeast end of the Moses Rock dike, in the head section where mixing of blocks from the widest stratigraphic range occurs, one observes an inverse relationship between maximum size of blocks from any specific horizon and depth to that horizon. Thus, for blocks which have risen in the vent, the greater the distance of rise, the smaller are the observed blocks.

The Cane Valley diatreme and the associated small elliptical diatreme exhibits many of the same features described at the Moses Rock dike, except that they are not nearly as well developed. Probably, the Cane Valley diatreme represents an early immature stage in development of the kimberlite-bearing diatremes, when compared with the more developed structures at Garnet Ridge and Moses Rock. The Mule Ear diatreme probably reached the most mature state of development of those in the cluster along Comb Ridge.

Principal Inferrences of Significance to the Mode of Emplacement

The field observations of importance when considering the mode of emplacement of the Moses Rock dike include structural setting of the dike, contact relations of the dike with the surrounding wall rock, internal structure, nature of the breccias, size and displacement of fragments in the dike. Important conclusions drawn from those observations are listed below.

1. If the Comb monocline passes downward into a fault, this fault could have been the avenue along which the erupting kimberlite found easy access to the surface. The cluster of kimberlite-bearing diatremes near the Moses Rock dike occur along the Comb Ridge monocline. The Moses Rock dike itself approximately parallels the axes of this fold. Elsewhere on the Colorado Plateau, basement rocks exposed along

monoclines are faulted (Kelley, 1955; Shoemaker, 1954).

2. The Moses Rock dike parallels the minette dikes exposed locally, suggesting the stress field was similar at the time of emplacement of both features. No crosscutting relationships exist between the kimberlite and minettes in this vicinity, so nothing can be said regarding their relative ages. (At Buell Park, minette cuts kimberlite. Allen and Balk, 1954).

3. Minettes and the Moses Rock dike cut the well-developed east-west vertical regional joint set nearly at right angles. Blocks of wall rock contained within the Moses Rock dike contain these joints suggesting that the joints preceeded the dike.

4. Observations of the contact relations suggest that initially the stress normal to the dike walls was high (the maximum principal stress), sufficient to produce sills but subsequently this stress dropped sufficiently to permit tensile failure parallel to the wall. Sills and folds are developed only locally in the east wall of the dike along the south or tail section. Dikes are well developed in the west wall of the south section. A well developed set of through-going joints parallel to the contact is present everywhere in the wall rocks. The few faults observed in the wall rocks have downward displacements on the side nearest the dike. The sills and folds suggest that at some time during the eruption the fluid exerted sufficient stress normal to the vent walls to cause compressive deformation and sill formation. The joints parallel to the contact and normal faulting suggest that generally the normal stress across the vent walls was the minimum principal stress and tensile fracturing, and normal faulting occurred. Jointing

in folded beds at the contact is parallel to the contact locally suggesting that folding preceeded jointing.

5. Rocks forming the dike walls are generally undeformed and are only slightly or unaltered. Most generally wall rocks at the contact are simply abruptly truncated and show no alteration or contact effects except the jointing and minor bleaching along joints near the contact.

The frequency of the joints, that is, the closeness of their spacing, varies from place to place, but everywhere joint frequency decreases as in inverse power function of the distance away from the contact.

6. The internal structure of the dike suggests:

   (a) Blocks are introduced into the dike by separation from the walls along joints paralleling the dike contact.

   (b) Once introduced into the dike these blocks of wall rock are rotated, displaced upward or downward and eventually comminuted to smaller fragments. The bulk of the material in the dike was formed this way.

Perhaps the most important general observation of the internal structure of the dike concerns the blocks derived from the vent walls. Many stages of separation of blocks from the walls are observed. The joints which exist everywhere in the dike walls parallel to the contact play an important role in the separation of the blocks from the walls.

Locally small displacements are observed on joints, always with the down-side nearest the dike. Large blocks of wall rocks are observed with separations of a few inches along these joints, which are filled with kimberlite-bearing breccia. Elsewhere large blocks are separated from the dike wall by a few feet and have small rotations, and slight downward displacements relative to their original position in the walls. Progressively larger rotations, separations and displacements are observed. Large blocks are observed broken into several smaller blocks and blocks of all sizes appear to have contributed fine debris to the complex breccias in which they are enclosed. This fine material appears to have been derived by the larger blocks by abrasion or erosion of material from their surfaces during the eruption.

7. The character of the breccias suggest that the eruption which produced the dike was violent in nature (at the level now exposed) and that the intruding material could accurately be described as a "fluidized" system. Three observations support this view:

(a) The intrusive material is particulate on all scales. Even the kimberlite at the type locality (MR-1416A) is serpentine-rich microbreccia in which the fragments, even in thin sections down to 10μ size, are discrete particles.

(b) Constituents of the breccias are intricately mixed. In the complex breccias and in the Cutler rubble, constituents of kimberlite (particulate fragments of serpentine, olivine and pyroxene predominantly) are finely dispersed throughout the fragmental rock debris derived from sedimentary and crystalline rocks.

(c) The size frequency distributions of fragments derived from the sedimentary strata in the vent walls are like comminution curves produced by mechanical grinding processes. In this case the comminution is probably due to multiple impacts. Also, the crystalline rock fragments are characteristically well rounded. This probably implies abrasion during transport perhaps deeper in the vent rather than fragmentation.

8. Relationships between the various breccia units filling the Moses Rock dike suggest that the sequence of intrusion of the breccia units was first kimberlite, then Cutler rubble with diluted kimberlite, and finally in progression, medium, coarse and very coarse complex breccia.

Kimberlite as a mappable unit and diluted kimberlite commonly occur as small dikes in very large fragments of wall rock now contained within the dike, which are now surrounded by complex breccia. Elsewhere, blob-shaped kimberlite bodies are cut off by coarse complex breccia. Kimberlite bodies also are observed locally as sills in the vent walls or as slabs plastered against the wall rocks. No kimberlite apophyses were observed intruding into any other breccia units; rather the kimberlite appears to be chance remnants of material emplaced early in the sequence of events. The occurrence of medium complex breccia in the body section of the dike as blob-shaped patches within Cutler rubble suggests that these are irregularly-shaped <u>vents</u> cutting through the Cutler rubble. In a similar way in the head section, very coarse and coarse complex breccia apparently cuts medium breccia and Cutler rubble in what appears to be very irregularly-shaped vents.

9. The distribution of the breccia units just described suggests that "channelling" developed and that the flow became concentrated along a few preferred paths during the eruption which produced the dike.

10. Large blocks displaced upward in the diatremes provide useful information about the carrying capacity of the erupting medium. In the Moses Rock dike the largest upward displaced block is a tabular fragment of Rico Formation measuring 210 x 100 feet in plan and probably 20 feet thick, displaced about 460 feet upward from its original stratigraphic position. So whatever the fluid properties were, the medium was capable of carrying such a block.

11. Blocks displaced downward indicate the minimum thickness of overburden at the time of emplacement. This provides a means of estimating a very rough lower limit on the age of the diatreme by the amount of erosion which has taken place, by comparison with estimates of the present erosion rates in the Colorado Plateau. In the Moses Rock dike several blocks of de Chelley Sandstone Member are displaced downward within the vent and are now juxtaposed against beds at the top of the Halgaito Tongue Member about 1450 to 1600 feet below. At the Mule Ear diatreme, Shoemaker and Moore (1957) report Mancos Shale juxtaposed against Halgaito Member about 5000 feet stratigraphically downward. It is very likely that the two neighboring bodies are contemporaneous so it is likely that the overburden above the present surface at the Moses Rock dike at the time of eruption was also, at least, 5000 feet. This is a minimum but perhaps also a reasonably close estimate of the actual overburden.

PART III

PETROLOGY

Introduction

Petrography and petrology of the crystalline rock fragments and kimberlite permit several important problems to be discussed. Among these are 1) the structure and composition of the crust under the Moses Rock dike, 2) the nature of the upper mantle, 3) the Mohorovicic discontinuity, 4) the source rock and genesis of the kimberlite, and 5) the conditions and site of kimberlite genesis.

The general character of the population of crystalline rock fragments is discussed first. Included in this discussion are observations of their relative size, relative abundance and petrographic character.

Because the dense crystalline rock fragments may be derived from the upper mantle a suite of these fragments is described in detail. Microprobe and whole-rock analysis provide detailed compositional data which allow some constraints to be placed on the conditions of formation of certain of these rocks and minerals.

Next the kimberlite is described. Modal analyses of thin sections of kimberlite and microprobe analysis of mineral grains leads to the conclusion that the source rocks for the kimberlite are spinel and garnet-lherzolite; rocks consisting of the assemblages: 1) spinel, aluminum-rich pyroxenes, olivine and 2) garnet, aluminum-poor pyroxenes and olivine plus accessory titanoclinohumite, mica and volatiles. Some mixing of mineral phases from other sources has occurred even in the most uncontaminated kimberlite samples but this is probably not important quantitatively.

The conditions in the reservoir from which the kimberlites erupted are inferred from the compositions of minerals found in the kimberlite. The phase relationships in synthetic and natural minerals in the systems diopside-enstatite and pyrope-diopside have been investigated recently by workers of the Geophysical Laboratory of the Carnegie Institution. Coexisting natural mineral pairs in both these systems were discovered in the kimberlite from the Moses Rock dike. Microprobe analyses of these phases permit pressure and temperature information to be extracted using experimentally determined phase diagrams. It is inferred that the minerals in the kimberlite were derived over a depth range in the mantle extending to about 50 kilobars (150 km) and 950° C.

Other petrologic questions of interest include the absence of diamond in the Colorado Plateau kimberlite, the transition between spinel and garnet-bearing peridotite assemblages in the upper mantle, and the presence of volatiles, particularly H_2O, in the upper mantle.

Crystalline Rock Fragments

The rocks within the Moses Rock dike which have been transported upward from below the Paleozoic section include the kimberlite and a diverse suite of crystalline rocks which occur as discrete, nearly spherical, unaltered fragments within the unconsolidated breccias. Since the reservoir from which part or all of the kimberlite originated apparently was located at great depth, apparently within the upper mantle, these clasts represent samples, badly scrambled, from a very long vertical section through the crust, and possibly, through part of the upper mantle.

Crystalline basement rock fragments constitute about 3% by volume of the intrusive material filling the Moses Rock dike. They range in size from silt-sized particles to very well-rounded blocks up to 6 feet in diameter. Generally, these fragments are very well rounded and show little or no evidence of zonal metamorphism when the edge of broken fragments is compared with the center.

Approximately 75% of the crystalline fragments are unfoliated rocks with igneous or altered igneous textures. The most common types are meta-basalt, gabbro and diorite; present but less abundant are rhyolite and granite types. Approximately 25% of the fragments are foliated metamorphic rocks of greenschist, amphibolite and granulite grade. The most abundant metamorphic type is basic granulite, (retrograded-plagioclase-pyroxene and garnet-plagioclase-pyroxene rocks). Acid granulite, amphibolite and greenschist grade rocks are present but not as abundant. Dense fragment types ($\rho > 3.2$ gm/cc) include in decreasing relative abundance, 1) jadeite-pyroxenite, 2) eclogite, 3) spinel-bearing websterite, and 4) spinel-bearing lherzolite, which together form less than 1% of the total assemblage of crystalline fragments. Antigorite-tremolite schist is properly included in the ultramafic suite and is the most abundant type.

The basic crystalline rocks (basalt and gabbro) commonly show greenschist grade alteration. Diorite, granite and rhyolite types are relatively unaltered. The granulite grade rocks are retrograded usually and their original character is inferred in part from well preserved textures, since feldspars are largely altered to epidote, sericite and clay minerals and pyroxene to amphibole.

Among the metamorphic types, carbonate or carbonate-derivative rocks are absent as are ordinary pelitic types. Aluminous schists are common but they contain little free quartz. Quartzite was not observed (aside from fragments of Ignacio (?) Formation). Quartzo-feldspathic and basic types are the most abundant compositions, with the basic types predominating.

The suite appears to be metavolcanic or metaplutonic rather than metasedimentary in origin, with basic types predominating.

Petrographic descriptions of a representative suite of the crystalline fragments is contained in the appendices, with chemical and modal analyses, and measured densities on selected specimens. Specimen numbers used in the text hereafter (for example, X-50B) refer to samples described in the appendices.

Petrographic Summary of Crystalline Fragment Types

Igneous rocks of acid, intermediate and basic composition are present. Metabasalt (X-13, X-19, X-153) and gabbro (X-100, X-190) are the most abundant types. Included in the group called metabasalt are unfoliated, fine-grained rocks which have experienced greenschist grade metamorphism with no obvious deformation fabric (X-13, X-19). White "phenocrysts" of altered plagioclase, in some cases 20% by volume, occur in forms ranging from irregular shaped blobs to euhedral psuedomorphs after plagioclase. Gabbroic rocks commonly show greenschist grade alteration but no evidence of deformation. Diorite (X-95) is undeformed and generally unaltered. Rhyolite (X-6, X-7, X-60), unfoliated, unaltered and undeformed, has a microcrystalline groundmass and quartz and alkali-feldspar phenocrysts. Medium and coarse-grained granites are present (X-103, X-105). Medium-grained foliated biotite granite (X-66) is the most abundant type of acid rock but a porphyritic sphene-biotite leucogranite (X-260) is common.

Metamorphic rocks of low, intermediate and high rank are present and they vary in composition. The most abundant metamorphic rocks are retrograded pyroxene-plagioclase (X-48) and pyroxene-garnet-plagioclase (X-148) rocks commonly having a granular but coarsely layered structure. The pyroxene in these rocks generally is altered to hornblende and the plagioclase to epidote, zoisite, sericite and clay minerals. Garnetiferous felsic granulites (X-37, X-25), some with blue quartz are observed commonly, generally with perthitic feldspars and no hydrous phases present.

Basic amphibolites (X-220) are common and highly aluminous schists of amphibolite grade (X-61, X-4) also are fairly common. The aluminous rocks generally have less than 10% free quartz which is significantly lower than common pelitic rocks believed to be derived from shales. Calcareous and magnesian assemblages of amphibolite grade were not observed.

Greenschist grade rocks are observed; most abundant are basic compositions. Calcite was observed in a few low-grade schists (X-128) but generally is subordinate in abundance. These rocks are basic rather than calcareous in bulk composition.

Four types of dense basement rock fragments observed were eclogite (X-1, X-50B) in which garnet abundance ranged from 1 to 40% by volume; jadeite-rich pyroxenite with trace rutile and pyrite (X-44); spinel-bearing websterite (X-1307, X-39, X-57), a granular-textured orthopyroxene, clinopyroxene, spinel rock; and a spinel-lherzolite (X-2), consisting of olivine, orthopyroxene, clinopyroxene and spinel with a coarse granular texture. These rocks are described in detail later.

Relative Abundance of Crystalline Rock Fragments

The relative abundance of specific types of crystalline rock types now observed at Moses Rock reflects the influence of many factors including the relative area exposed in the vent walls, the physical character of the rocks themselves, the nature of the transporting medium, time changes in introduction rate, and many others. It is of interest, then, to evaluate the relative abundance of fragment types since, among other things, it is related to the character and structure of the column traversed by the erupting medium.

Sampling aimed at providing information about relative abundance of fragment types was carried out in different ways; 1) visual qualitative estimates were taken at about 28 localities within the dike, 2) quantitative collectionsof basement fragments were made at 5 localities at which approximately 500 lbs. of material was sampled from just below the surface, screened in the field, bagged and shipped, and classified in the lab, 3) quantitative collectionsof basement fragments from the ground surface at the same 5 localities were made by use of a 200 point rectangular grid, in which the grid intersection points were separated by 12 inches.

The visual estimates of the relative abundance of the major rock types at 20 localities were made by noting those categories which were most abundant, common, rare or unobserved. A compilation of these field estimates was made by ranking the types at each locality, and summing over the twenty localities. For example, meta-basalt was the most abundant type at 10 of 20 localities, and the second most abundant type at 4 others, the third most abundant at 2 others.

The results of this tabulation (Table 2) suggest that meta-basalt is the most abundant type, gabbroic igneous and basic granulite-grade metamorphic rocks are next, followed by a variety of metamorphic and igneous types in decreasing order. The least abundant rocks are the high density pyroxene and garnet-pyroxene types, and peridotite.

Table 2. Estimates of Relative Abundance of Crystalline Basement Rock Fragment Types Based on Qualitative Observations at 20 Localities in the Moses Rock Dike

	Type	Relative Abundance	Examples
1.	Meta-basalt	Very abundant	X-10,19,153
2.	Gabbro	Abundant	X-100,190
3.	Granulite		X-148
4.	Granite gneiss	Common	X-66
5.	Coarse granite		X-105,260,103
6.	Low-grade schists		X-128
7.	Diorite	Common	X-95
8.	Rhyolite		X-6,7,8,60,111
9.	Basalt		X-26
10.	Amphibolite		X-220
11.	Serpentine schists		X-51,47
12.	Jadeite-pyroxenite	Rare	X-44
13.	Eclogite		X-1,3,508
14.	Websterite		X-39,57,1308
15.	Lherzolite (Peridotite)	Very rare	X-2

At 5 localities, 500 pound bulk samples were obtained from just below the surface from a 6 x 6 foot area. The location of these samples is shown on the index map of the dike (Figure 14). This material was sieved in the field and the crystalline rock fragments from the coarse fractions were saved. Splits were taken of the material finer than 1/2". These collections were transported to the laboratory where the samples were subdivided by rock type and weighed. The size frequency distribution of the crystalline rocks shows that the bulk of the mass is included in the largest fragments. For this reason, only the largest 10 to 15 fragments generally represent 90% or more of the mass of coarse material from each collection. Fragments from these coarse fractions were weighed and included in this tabulation.

The weight percent of each major rock type at each of these localities is shown in Table 3. The average of the five localities is shown and the types ranked according to this average. Again meta-basalt is the most abundant type. The serpentine-rich schist perhaps is not as abundant as suggested because of the biasing effect of one very large fragment at sample locality #109. Granites occur as large blocks and are not uniformly distributed, so indicated abundance is perhaps less than true abundance.

Table 3. Weight Percent of Crystalline Rock Fragment Types Collected in Bulk Samples from Five Localities

Type	Average of 5 Samples	Sample Locality				
		151	109	114	139	119
1. Meta-basalt	30 wt.%	56		21	21	54
2. Antigorite-schist	18 *		68*	1	8	12
3. Gabbro	15	14	5	34	24	
4. Basalt	10	2		10	41	
5. Diorite	9	1	13	22		10
6. Granulite rocks	8	18	10	10		
7. Rhyolite	3	1				16
8. Low-grade schists	2+		4			7
9. Amphibolite	2-	8				
10. Granite gneiss	1				6	
11. Eclogite	1			2		
12. Granite	-					
13. Jadeite-pyroxenite	-					
14. Websterite	-					
15. Lherzolite	-					
	99					

* Strongly influenced by one large block in one sample; probable value ~25%.

At the same 5 localities where the bulk samples were collected, samples of the crystalline basement rock fragments were taken using a preset rectangular grid. The grid was constructed by measuring points along the edge of a 10 by 20 foot rectangle, at one-foot spacing. Rock fragments lying at the intersection of strings were collected.

These samples were subdivided according to crystalline rock types and weighed. The results, shown in Table 4, show the weight percent for each of the five localities and the average of the five. Rock types are shown listed in decreasing order of abundance according to the average of the 5 localities.

The results are similar to the bulk samples; meta-basalt is the most abundant rock type, gabbro and granulite grade metamorphic rocks (mostly garnet-plagioclase-pyroxene, and plagioclase-pyroxene rocks) are abundant. Basalt and diorite are common; less common are rocks of lower metamorphic grade and granite. Least abundant are the eclogite and pyroxenite types.

Table 4. Relative Abundance of Crystalline Rock Fragment Types in Weight Percent as Observed in Samples Collected Using a Rectangular Grid at Five Localities

Type	Average of 5 Localities	Sample Localities				
		151	109	114	110	133
1. Meta-basalt	30 wt.%	4		72		75
2. Granulite	20	6	72	-	-	22
3. Gabbro	19	77				15
4. Basalt	10	2		24	23	
5. Diorite	10	-	24		26	
6. Amphibolite	3				16	
7. Low-grade schists	2		4		11	
8. Antigorite schist	2					10
9. Granite	1	1		4		
10. Eclogite	1				2	
11. Rhyolite	<1					
12. Granite gneiss	<1					
13. Jadeite-pyroxenite	<<1					
14. Websterite	<<1					
15. Lherzolite	<<<1					

If the three sampling techniques are weighted equally and averaged, the sequence of relative abundance of basement rock types is shown in Table 5. The resulting estimate of the approximate weight percent of each type is shown. The sequence generally agrees with the writer's qualitative impressions obtained during the course of collection and mapping. Some bias probably is included in the sampling. For example, granite and rhyolite types are concentrated somewhat locally and the granite clasts, especially, are typically large. Also the granitic types weather more readily than many other crystalline rock types (Plate 14). The sampling methods may contain some bias against these types, but probably by no more than a factor of 2 or 3. The granite types may be more abundant than amphibolite grade rocks or schists but are certainly less abundant than the diorite-basalt types.

Thus, Table 4 (Column 1) represents the present best estimate of the relative abundance of various crystalline rock fragment types.

Relative Size of Crystalline Rock Fragments

The detailed mapping of the Moses Rock dike established that for populations of blocks of sedimentary rocks within the dike whose original stratigraphic position is known, there is an inverse relationship between maximum observed block size and distance of transport up the vent from the original position in the undisturbed stratigraphic sequence. For the stratified rocks, at least, the deeper the origin, the smaller the size of fragments. If a similar relationship were true for the basement fragments, then fragment size would be a potential means of establishing the relative depth of origin of the various crystalline basement rock fragment types. The smaller the maximum observed block size for the rock type, the deeper its origin.

Table 5. Preferred Estimate of Relative Abundance of Crystalline Rock Fragment Types

Relative Abundance in Decreasing Order	Estimated wt. % *		
	1	2	3
1. Meta-basalt	34	26	85
2. Gabbro	19	21	55
3. Granulite	17	26	50
4. Diorite	11	26	52
5. Basalt	10	9	55
6. Low-grade schist	2-3	17	55
7. Serpentine-schists	2-3	17	55
8. Amphibolite	2	21	27
9. Granite gneiss	1	4	73
10. Granite	1	16	75
11. Rhyolite	1	11	28
12. Eclogite	< 1	11	25
13. Jadeite-pyroxenite	< 1	4	35
14. Websterite	<< 1	2	4

* estimated probable error 25 to 50% of value shown

1 Best estimate of relative abundance of fragments

2 Number of collection localities where type was observed out of a total of 26

3 Mean size index (defined in following pages)

Plate 14. Weathered debris of granite boulder. Debris forms white patch in center of photograph. Slide rule is approximately 6 inches long. This demonstrates the relative instability of granitic boulders to weathering and might account for their unexpectedly low relative abundance in the crystalline rock fragment populations. Matrix is coarse complex breccia.

With this in mind, observations were made of basement fragment populations at 28 localities within the Moses Rock dike, or in nearby dikes and sills. Since the variety of rocks is so great, size data were gathered only on a suite of representative rocks (described in the appendix). At each sample site an arbitrary radius was drawn, not constant from site to site, and the fragment population examined. The largest specimen of each member of the representative suite was located and measured. In addition, previously unrecognized specimen types were collected. The size (maximum dimension) of the largest fragment of a given type was the most easily obtained statistic of the population and probably is the most important one. Most fragments are highly spherical. Estimated sphericities of 0.8 are common.

These data permit one to compare the relative size of the crystalline rock fragments at a single locality. It would be desirable to compare results from many localities and to statistically combine the results. For this purpose, the size (maximum dimension) of the largest crystalline fragment of any type at each locality was set equal to 100 and size of other fragment types at that locality expressed proportional to 100. This number is called the size index. Averaged overall 28 sample localities, the mean size index, N, is a measure of the relative size of the various selected representative crystalline basement rock fragment types.

Mean size index was computed for 23 selected basement fragment types, using data from all 28 localities. These data are plotted in Figure 19, and arranged into petrographically similar groups. The axis is mean size index, N, ranging from 0 to 100. The bar indicated is the standard deviation of the mean size index.

In the insert are shown data including limestone fragments (whose size index generally exceeds 100 because limestone fragments generally exceed the largest basement rock in size). The data in the inserts show that on the average limestone fragments are larger than granitic fragments; granite larger than basic granulites, and basic granulites larger than eclogite fragments.

Mean size indices for the various fragment types fall roughly into three groups. A group with mean size index greater than about 65 includes granite types and meta-basalt. An intermediate group between about 35 and 65 contains some igneous and/or unfoliated metamorphic equivalent types (diorite, gabbro granite gneiss, basalt-andesite) and most of the foliated metamorphic types (greenschist, amphibolite and granulite-grade rocks). A third group with size index less than 35 contains rhyolite, aluminous schist and the dense fragments (eclogite, jadeite-pyroxenite, websterite and lherzolite).

In an attempt to enhance the statistics, the data from the localities where largest fragments exceeded 20 cm in diameter were treated. It was felt that these sites offered the best data because recognition of fragments is easier, and generally a wider range in size was observed since particles smaller than approximately 1 cm became difficult to recognize and identify. Twelve localities were included in this tabulation.

Mean size indices with standard deviations are shown in Figure 20. They yield essentially the same results as are obtained from all 28 localities. No attempt was made to treat the data from the 14

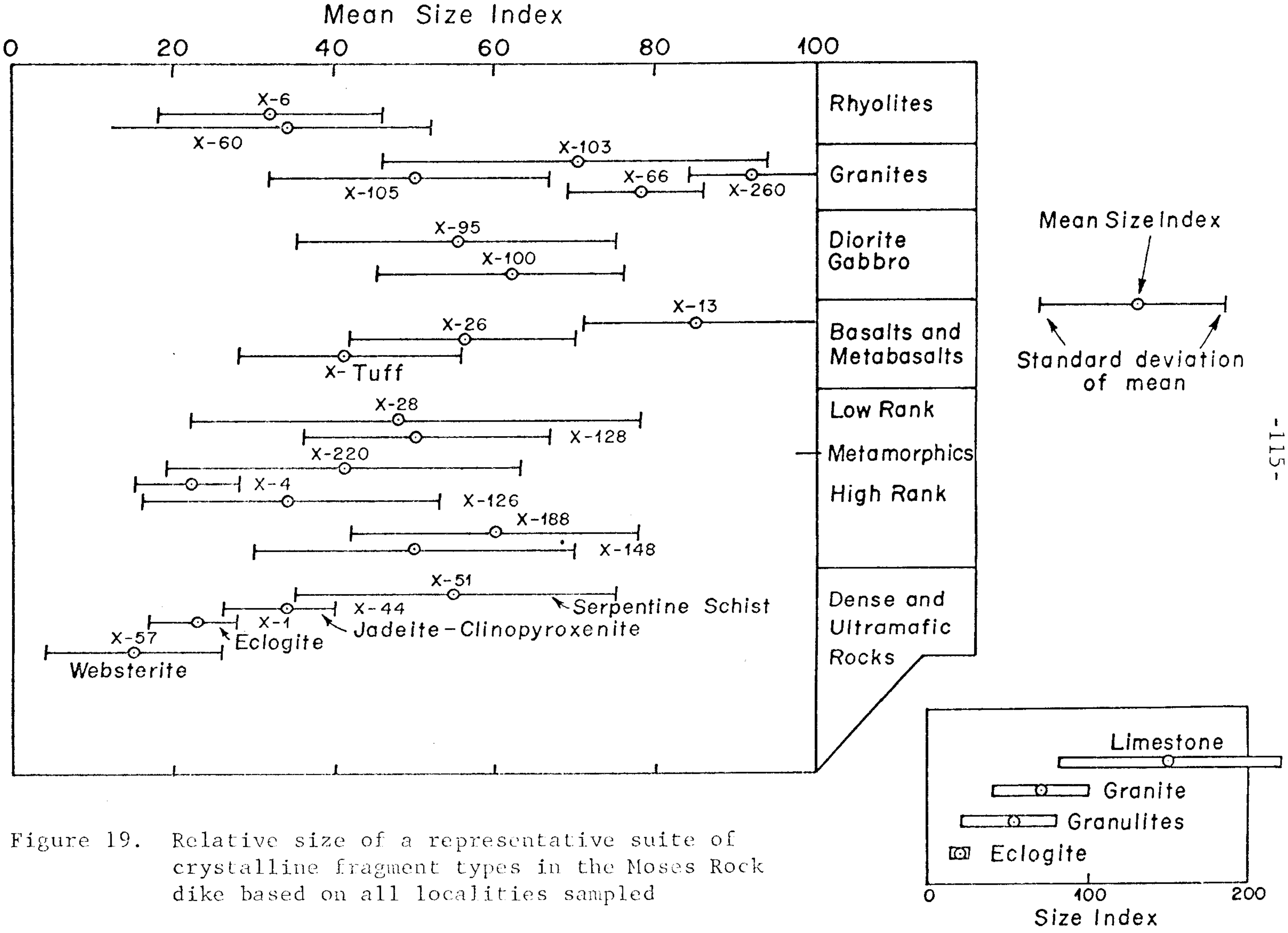

Figure 19. Relative size of a representative suite of crystalline fragment types in the Moses Rock dike based on all localities sampled

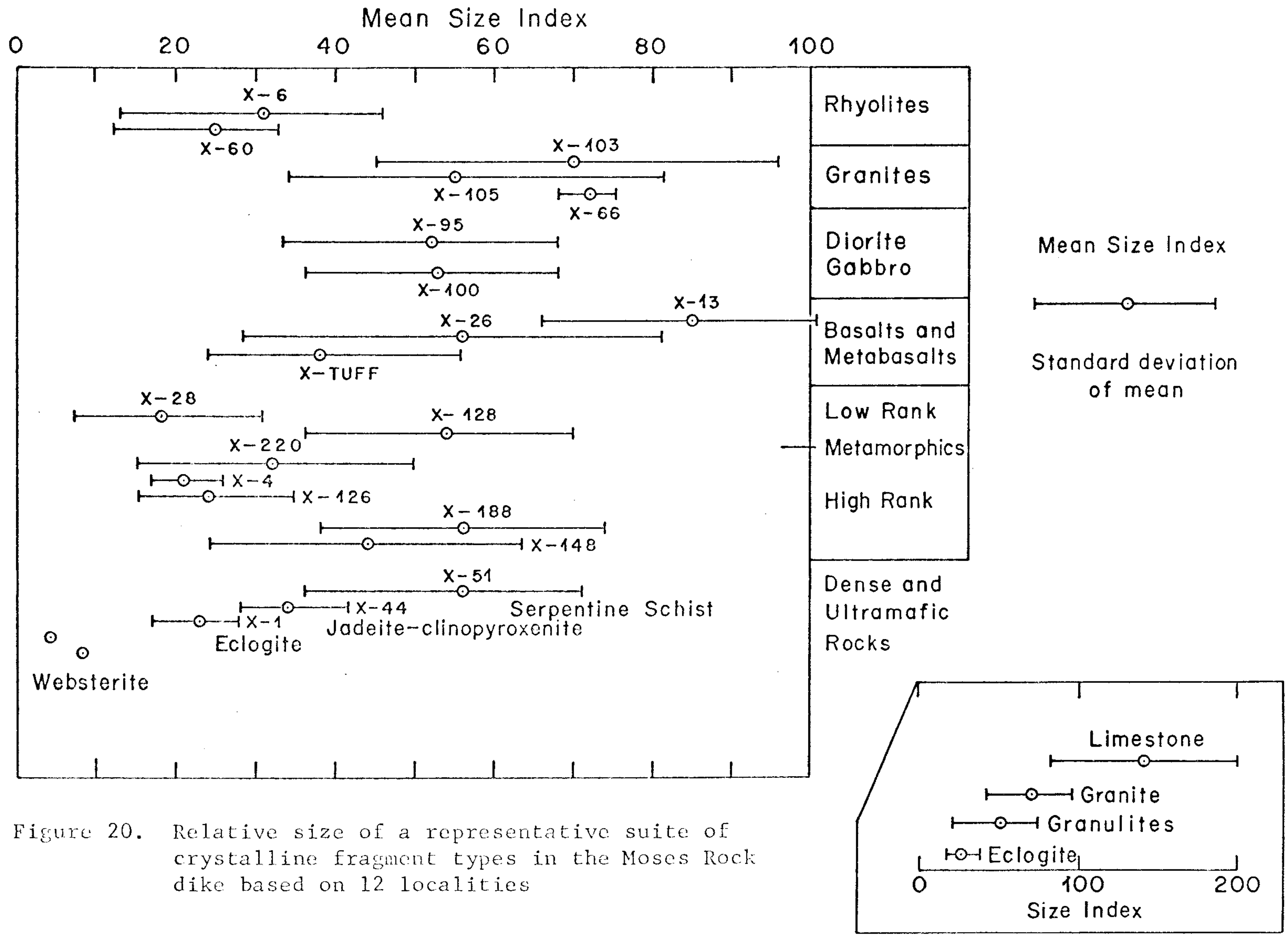

Figure 20. Relative size of a representative suite of crystalline fragment types in the Moses Rock dike based on 12 localities

localities not included here to contrast "coarse" and "fine" sites.

The mean size index plotted against measured density, (Figure 21) suggests a rough inverse correlation between size and density.

To sum up, the fragment types fall roughly into three major groups according to relative size: a group of large fragments, principally granite types and meta-basalts, an intermediate group of intermediate and basic igneous types and metamorphic types, and a group of small fragments which includes the dense rocks and rhyolite.

Not all the representative rock types were observed at all the sample localities. This could simply reflect abundance or it could reflect real differences in the persistence of specific fragment types within the dike. If one compares the order of relative abundance of specific types (Table 5) with the number of sample localities where that type was observed, a general correlation between relative abundance and the number of localities is observed (Figure 22a). It is no surprise that the most abundant types at a single locality tend to be observed most frequently. Granite gneiss (9) and basalt (5) are missing from many sample sites. Possibly failure to make distinction in the field between the very abundant meta-basalt and basalt may account for the apparent absence of basalt from localities. Granite gneiss (9) commonly occurs as large fragments. This type weathers very easily by granular disintegration (Plate 14). Its absence from many sample sites could reflect both of these effects. Presence and absence at specific sample sites apparently reflects relative abundance.

Both fragment size and relative abundance are important factors

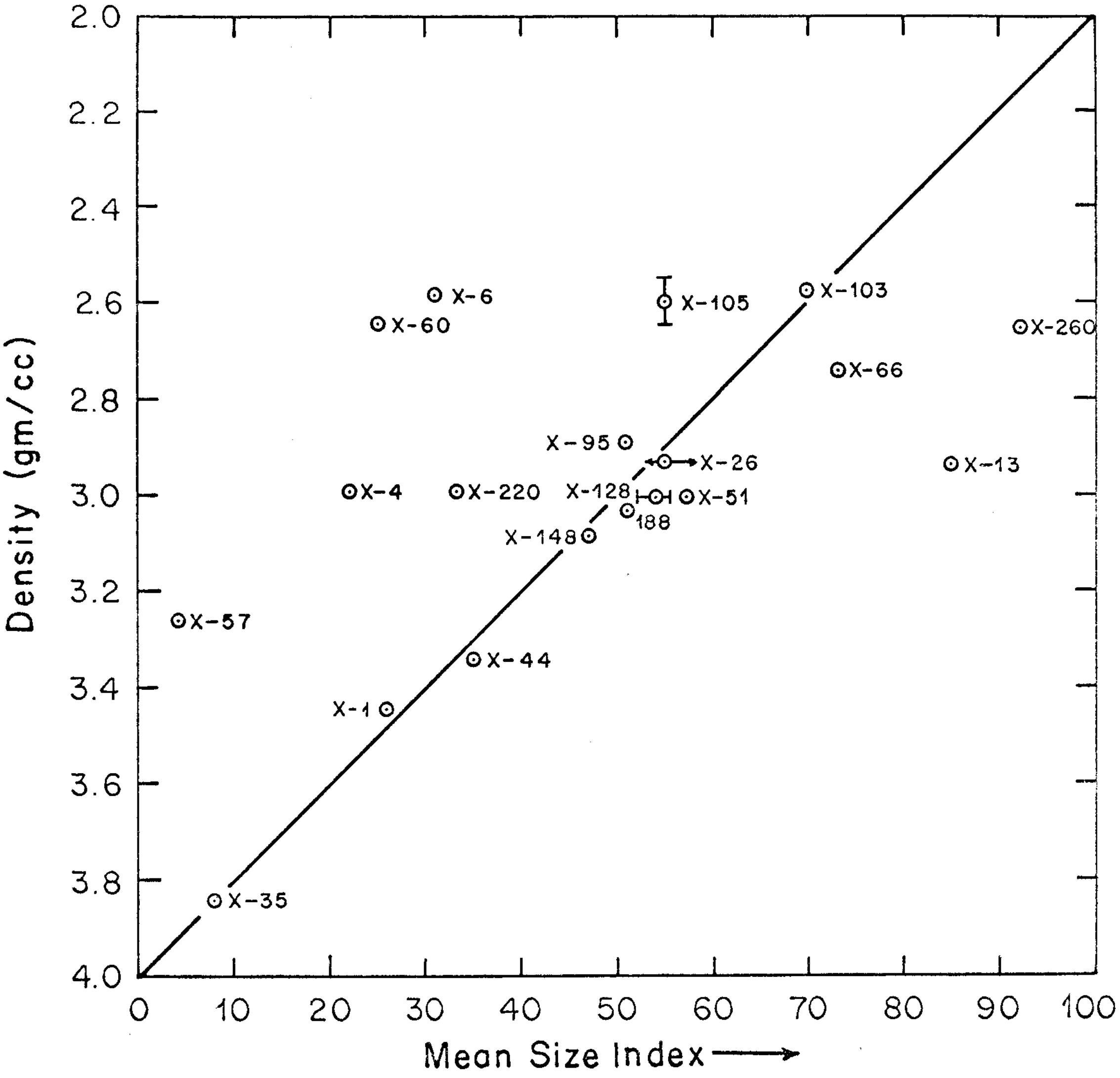

(Size of Rock Type Relative to Largest Fragment of any type Observed at Each Site; Mean Value Plotted for Average of 30 Localities.)

Figure 21. Plot of "mean size index" against measured density of representative suite of crystalline fragment types

to be considered in attempting to evaluate the structure and composition of the crustal section. Later we will turn to this problem and attempt to use these data along with the seismological and other petrological information, drawn from the dense fragment types and kimberlite, to reconstruct the crust and upper mantle from the various fragment types.

Comparison of mean size index with order of relative abundance (from Table 16) shows that there is a very rough positive correlation between them (Figure 22a). However, gabbro (2), granulite (3), perhaps diorite (4) and amphibolites (8) may have smaller size indices than their relative abundance would suggest (if size were a function of abundance alone). Also, granite gneiss (9) and coarse-grained granite (10) fragments are significantly larger than their relative abundance would suggest. It was noted in the field that granite-type fragments are typically large. (The largest crystalline rock fragment observed in the entire Moses Rock dike is a biotite granite gneiss, a nearly spherical fragment of about 7 feet in diameter.)

Persistence of specific types throughout the dike, as indicated by their presence and absence at sample sites, and fragment size, as suggested by the size index, apparently are correlated with relative abundance but certainly are not functions of it alone.

Dense Inclusions

In the discussion of the kimberlite which follows, it is concluded that the most probable site of the minerals in the kimberlite originated over depths ranging to 100 kilometers or more, well within the upper

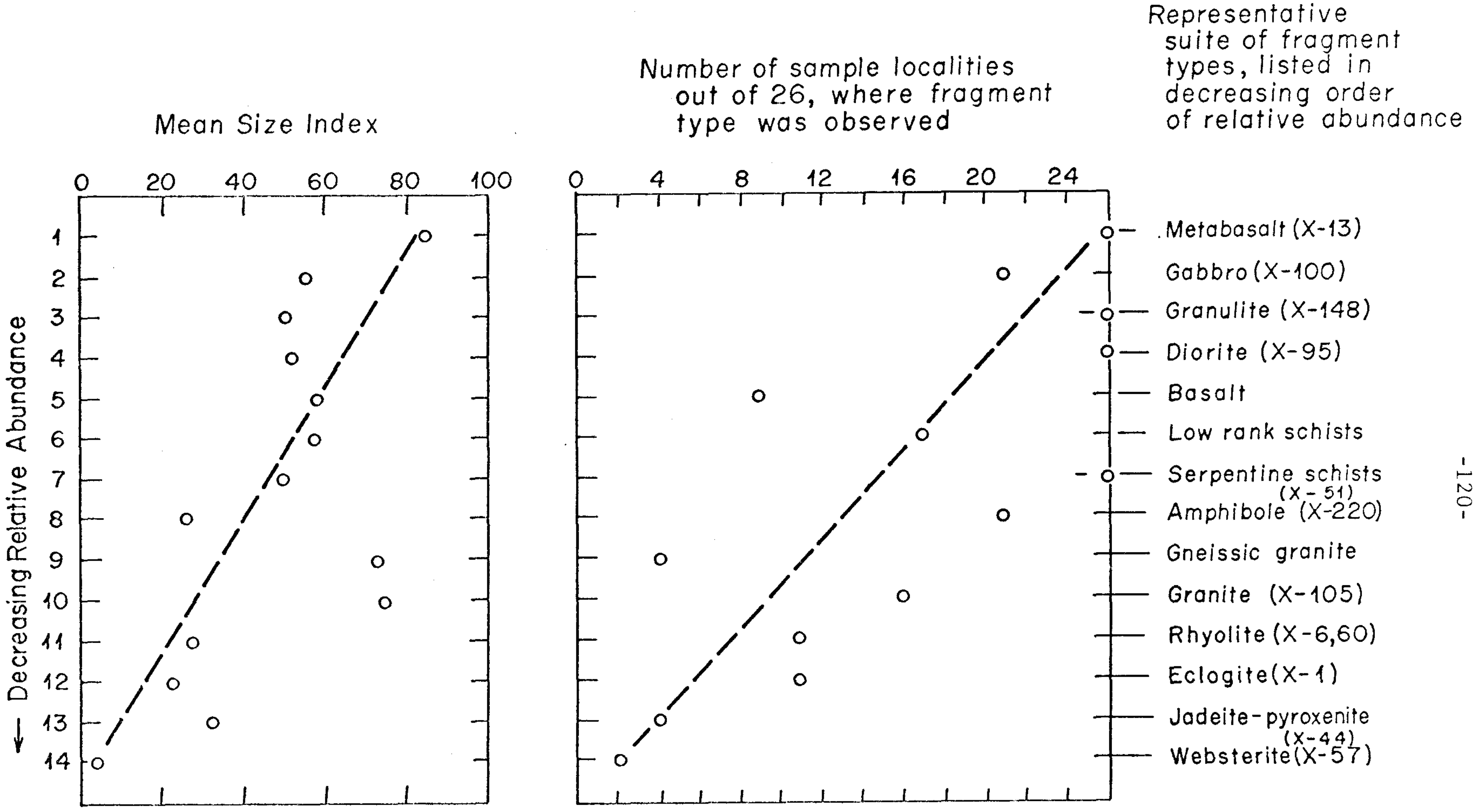

Figure 22. Plot of relative abundance of crystalline fragments against (a) mean size index and (b) number of localities where each type was observed

mantle. Thus, the dense rock fragments in the Moses Rock dike are particularly interesting since, on one hand, they may be samples of the mantle derived from within the reservoir, from the walls of the vent within the mantle or lower crust, or, on the other hand, they could be related to the kimberlite by some magmatic process such as partial melting residues or crystal accumulates. The dense and ultramafic rock types observed are listed in the table below.

Table 6. Dense and Ultramafic Crystalline Rock Fragments Observed in the Moses Rock Dike

Observed as Discrete Rock Fragments	Specimens
1. Antigorite-tremolite schist	X-51
2. Jadeite-rich clinopyroxenite	X-44
3. Eclogite	X-1,-50B
4. Spinel-bearing websterite	X-1307
5. Spinel-lherzolite	X-2
Inferred from Inclusions in Pyropes	
6. Garnet-lherzolite	

The most abundant dense inclusion types at Moses Rock are pyroxene and garnet-pyroxene rocks. Eclogite (X-1, X-50B) and jadeite-rich clinopyroxenite (X-44) are the most abundant dense types. Present but rare is spinel-websterite (X-39, -57, -1307), a clinopyroxene-orthopyroxene rock. Still more rare is the only true peridotite observed, spinel-lherzolite (X-2). It seems odd that the dense inclusions are predominantly pyroxenites when the kimberlite is olivine-rich. Another rock, far more abundant than any of these types, which is properly included in a discussion of dense and ultramafic (possible mantle) rocks is the serpentine-rich schist (X-51).

Whole-rock chemical analyses were obtained on specimens of all these rocks, except the spinel-lherzolite. (It was discovered too late to include in the analysed suite.) Microprobe analyses of minerals in polished thin sections of these analysed specimens were obtained on all except the antigorite schist (X-51). Thus, abundant compositional data are available to discuss the genesis of these rocks and their possible relationship to the kimberlite.

Spinel-Websterite

Websterite inclusions are coarse-grained granoblastic intergrowths of medium-green clinopyroxene and drab olive-green orthopyroxene, with minor interstitial spinel. Large irregular green pyroxene megacrysts are observed in a granular groundmass in some specimens. Very rare small interstitial grains of brown spinel were observed in two thin sections.

Three different specimens were studied in detail (MRX-39, MRX-57, MRX-1307). Compositional data are available on minerals from two. They are believed to be similar compositionally. A significant textural relationship is best developed in specimen X-1307A, so the discussion will focus on this specimen.

The textures observed in thin section are remarkable and beautiful because of the high contrast in birefringence and setting of the pyroxenes. A granoblastic coarse-grained groundmass of orthopyroxene and clinopyroxene contains large megacrystic pyroxene domains (Plate 15,16). The groundmass appears to be a classic granoblastic intergrowth (Plate 16B). The boundaries of the megacrysts have been made ragged by recrystallization (Plate 16C, D). Lamellae are well developed within the pyroxene megacrysts composed of exsolved orthopyroxene and clinopyroxene parallel to (100). These lamellae are commonly deformed and fractured (Plates 16). Clusters of granular crystals similar to those in the groundmass are observed locally along lamellae (Plate 16E). Such granular recrystallization may be recognized within the groundmass as linear arrangements of granular pyroxene grains. In one specimen (MRX-57) some recrystallization and alteration to phlogopitic material was observed parallel to fractures.

The ratio of the pyroxenes in the lamellae within the megacrysts is approximately $cpx_{65 \pm 5}$: $opx_{35 \pm 5}$ whereas the groundmass is approximately $cpx_{55 \pm 5}$: $opx_{45 \pm 5}$ (on specimen MRX-1307A). Modal analysis of a uniform granoblastic textured specimen (MRX-39) revealed the pyroxene composition: cpx, 60: opx, 40.

The textural relationships suggest a sequence of events responsible for their formation, which can be inferred from the textures alone. First, the very coarse-grained pyroxene megacrysts were developed consisting of crystals of a single pyroxene solid solution, up to one inch in length as suggested by the optical continuity of the large grains in the right side of Plate 16A. These single crystals exsolved to two pyroxenes forming lamellae of clinopyroxene and orthopyroxene parallel to (100). Subsequently, the large crystals were structurally deformed, apparently prior to the formation of the granular groundmass because the deformational fabric or fractures are not observed in the groundmass. Recrystallization occurring at the boundaries of the large exsolved crystals resulted in the growth of a coarse-grained granular groundmass. Recrystallization along lamellae occurred simultaneously within the large crystals. Locally relics of the lamellae structure were retained in the arrangement of granular grains in the groundmass. Finally, some phlogopitic alteration occurred along subparallel fractures within the large grains and in the groundmass (MRX-57) under (stress and chemical) conditions quite different from those preceeding.

Whole rock chemical analysis of MRX-1307 revealed a very high R_2O_3 content for a pyroxenite ($Al_2O_3 + CR_2O_3 = 8.65\%$, Appendix D-3, Analysis 5). The sodium content of the rock is 0.54 wt. %, thus the solid solution of $NaRSi_2O_6$ type pyroxenes is not great and the high R_2O_3 content must be the result of solid solution of Tschermak molecule in the pyroxenes. Mineral compositions obtained on pyroxenes from specimens MRX-1307A and MRX-57 (Table 6) confirm this. There is some jadeite component in the clinopyroxenes, about 6% by weight, but there is roughly 7% by weight solid solution of Al_2O_3 in the pyroxenes in excess of that present as NaR_2SiO_6 molecules.

Cr_2O_3 in the whole rock analysis is expressed as part of the Al_2O_3 value. Chromium was not determined in the microprobe investigation of the minerals. The difference between Al_2O_3 content for the whole rock (8.65%) which is actually $Al_2O_3 + Cr_2O_3$, and the Al_2O_3 content of the rock determined by the microprobe analyses of the two

Diameter field is 25 mm. Minerals are clinopyroxene and orthopyroxene. Crossed nicols. Note large megacrysts with deformed, exsolved pyroxene lamellae and ragged edges. The granular textured groundmass consists of orthopyroxene and clinopyroxene of very similar composition to those forming the lamellae in the megacrysts. The pyroxene are notably aluminous.

Plate 15. Photomicrograph of spinel-bearing websterite
(MRX-1307A)

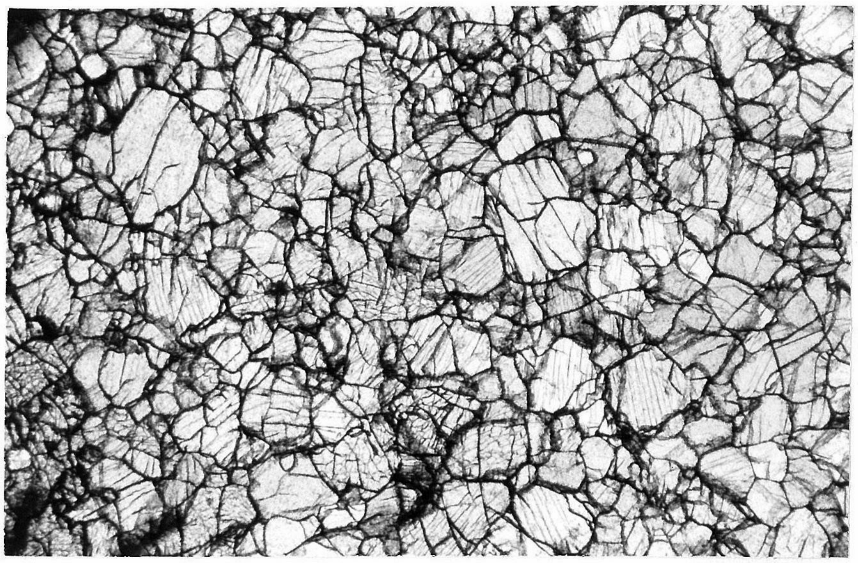

A. Groundmass pyroxenes in ordinary light. Diameter of field is about 10 mm.

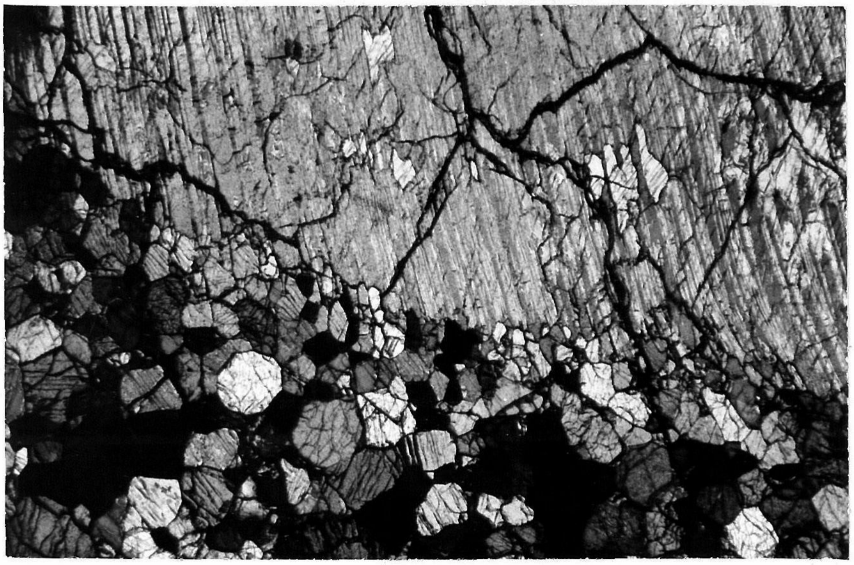

B. Contact of megacryst with groundmass showing deformation of lamellae, ragged contact, and insipient growth of granular textured grains within megacrysts. Diameter of field is about 10 mm.

Plate 16. Photomicrographs of spinel-bearing websterite (MRX-1307A)

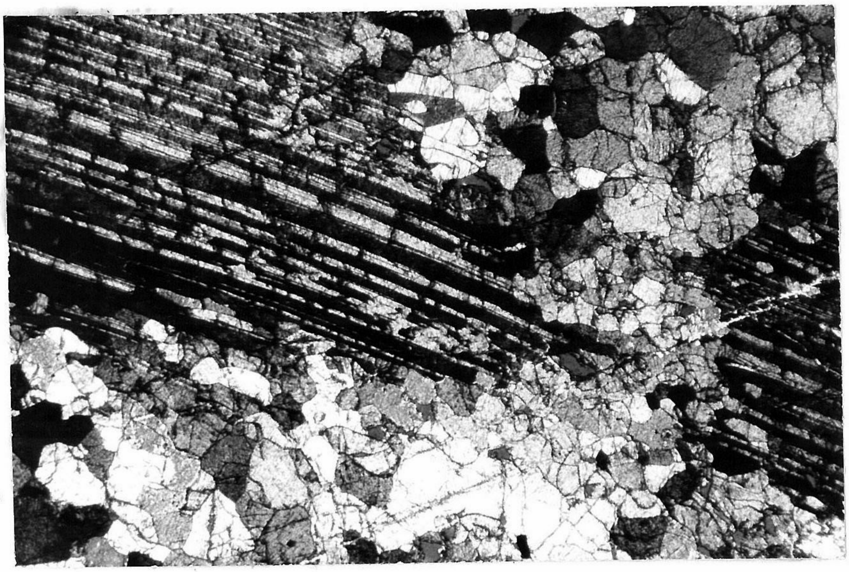

C. Megacrysts partially recrystallized to granoblastic groundmass. Lamellae in the megacrysts are deformed and the grain is fractured. Along the fractures (which run from 2 to 8 o'clock in this photograph) is a light micaeous mineral, perhaps phologopite, sercite or talc.

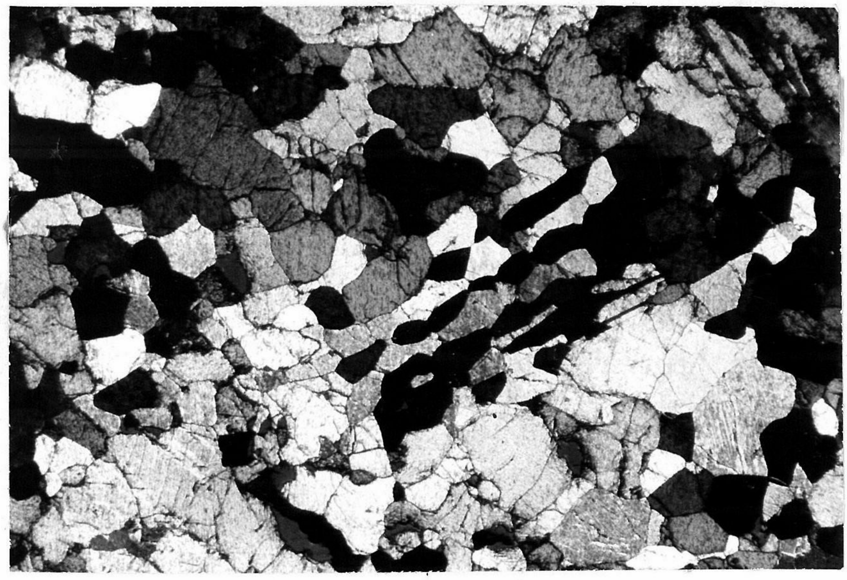

D. Linear orientation of granular groundmass grains, apparently a residual texture produced by recrystallization of the pyroxene lamellae in the megacrysts. Diameter of the field, about 10 mm.

Plate 16. (Cont.) Photomicrographs of spinel-bearing websterite (MRX-1307A)

pyroxenes (Table 7) (about 7.2%), probably implies a pyroxene chrome content of the order of 1%. (The spinel represents something less than 1% of the volume of these rocks).

Compared to other websterites described in the literature, the most distinctive feature of the Moses Rock specimens and their pyroxenes is a high alumina content. Compared to analysed pyroxenes from metamorphic rocks and from Bushveld websterite, these are notably aluminous (Mercy and O'Hara, 1965, Table 1). Previously published analyses of websterite pyroxenes (Table 8) have Al_2O_3 contents ranging from about 1 to 4 wt. % Al_2O_3, compared to 6 to 8 wt. % for the Moses Rock examples. White (1966, Table 8C, p. 285) reports Al_2O_3 contents of websterite nodules in Hawaiian basalts as 3.7, 4.1, 4.2 and 7.1 wt. % for orthopyroxene and 6.6, 6.3, 6.4, and 8.6 for respective coexisting clinopyroxene. Hence, the Moses Rock websterite pyroxenes are at the upper extreme of the range of Al_2O_3 content in websterite nodules in Hawaiian basalts.

Table 7. Partial Chemical Analyses by Electron Microprobe of Groundmass Pyroxene Grains from Two Websterites

	MRX- 1307A		MRX - 57	
Mineral	Cpx	Opx	Cpx	Opx
Grain #	30	31	7	6
SiO_2	50.5	52.3	49.8	52.4
Al_2O_3	7.63	6.84	8.03	7.24
MgO	13.7	30.2	14.8	30.5
FeO	2.56	8.05	2.86	7.94
CaO	22.3	0.38	21.48	0.37
Na_2O	1.00	.03	1.04	.06
	97.7	97.8	98.0	98.5
	Molecules (wt. %)			
Jd	6.0	0.2	6.1	.3
Ca-T	13.0	1.5	13.6	1.4
Mg-T	--	12.7	--	13.6
Wo	39.0	--	37.9	--
Fs	4.7	14.7	5.3	16.7
En	34.4	66.2	37.2	66.4
	97.1	95.3	99.3	99.4

Specimen No.	Clinopyroxenes 664*§	G.8	N.23* 10270	7666	WEB.	Orthopyroxenes 644*§	G.8	N.23* 10270	7666	4
SiO_2	52·67	52·47	53·69	54·07	54·38	53·51	53·05	55·63‡	55·94	55·76
TiO_2	0·17	0·19	0·16	0·21	0·04	0·04	0·19	0·11	0·11	tr.
Al_2O_3	3·83	3·58	2·43	2·08	1·29	2·99	2·63	1·60	1·61	1·66
Cr_2O_3	0·50	0·03	0·20	0·98	0·28	0·26	n.d.	0·028	0·45	0·33
Fe_2O_3	1·61	2·39	0·86	0·56	2·19	2·66	2·84	1·81‡	0·97	1·34
FeO	2·46	5·35	2·83	2·53	0·94	9·87	17·09	9·44‡	7·15	7·17
MnO	0·10	0·11	0·062	0·09	0·09	0·23	0·19	0·19	0·19	0·21
NiO	0·046	n.d.	0·058	0·04	0·00	0·085	n.d.	0·082	0·07	n.d.
MgO	15·06	13·44	16·32	17·39	16·96	29·63	23·76	31·21	32·12	32·42
CaO	22·19	20·66	22·37	22·12	23·71	0·82	0·49	0·53	1·48	0·74
Na_2O	1·23	1·79	1·05	0·41	0·14	0·07	0·08	n.d.	0·00	0·03
K_2O	0·02	0·01	<0·01	0·00	0·08	0·03	0·04	n.d.	0·00	0·04
P_2O_5	0·004	0·03	0·004	n.d.	0·10	0·002	n.d.	0·003	n.d.	0·10
H_2O+	n.d.	0·21	n.d.	0·04	0·14	n.d.	n.d.	n.d.	0·09	0·43
H_2O-	—	0·03	—	0·06	0·08	—	n.d.	—	0·00	0·08
Total	99·89	100·29	100·03	100·58	100·42	100·20	100·36	100·63†	100·18	100·31

* Analysis on sample dried at 110° C for 2 hours. † Also contains 0·0051 per cent CoO.

‡ Values not published previously.

§ Structural interpretation of the analyses of the pyroxenes from the Glenelg websterite, 664, on basis of 6 oxygen atoms.

Clinopyroxene: $[Ca_{0.868}Na_{0.088}Mg_{0.819}Fe^{2+}_{0.075}Mn_{0.003}Ni_{0.001}Fe^{3+}_{0.044}Cr_{0.014}Al_{0.097}]\ [Si_{1.923}Ti_{0.005}Al_{0.068}]\ O_6$.

Orthopyroxene: $[Ca_{0.031}Na_{0.005}Mg_{1.565}Fe^{2+}_{0.293}Mn_{0.007}Ni_{0.002}Fe^{3+}_{0.071}Cr_{0.007}Al_{0.026}]\ [Si_{1.898}Ti_{0.001}Al_{0.099}]\ O_6$.

n.d. = not determined.

KEY

644 = Pyroxenes from pyroxenite specimen, Glenelg.

G.8 = Pyroxenes from garnet-hornblende-pyroxene rock, Glenelg. (O'Hara 1960.)

N.23 = Pyroxenes from garnet-websterite, Kalskaret, Tafjord, Norway. (O'Hara and Mercy 1963.)

7666 = Pyroxenes from bronzitite, Malips Drift Camp, Bushveld Complex. (Hess 1949, 1952.)

WEB, 4 = Pyroxenes from websterite, Webster, North Carolina. (Hess 1949; Hess and Phillips 1940.)

Table 8. Compilation of analyses of pyroxenes from websterites from various sources. Table reproduced from Mercy and O'Hara, 1965

Spinel observed in the websterite (MRX-1307) is brown and isotropic. Only qualitative data are available on its composition. Microprobe wave-length scan revealed the presence of Al, Cr, Mg, Fe with trace Mn, Ni, Co.

The compositions shown in Table 9 are considered to be approximate average composition for groundmass and lamellae pyroxenes. These data were accumulated by averaging partial analyses of about 10 points for each pyroxene in each textural site.

Table 9. Partial Microprobe Chemical Analyses of Pyroxene Grains of Granoblastic Groundmass and Exsolution Lamellae in Pyroxene Megacrysts from Websterite (MRX-1307A)

		Granoblastic Groundmass		Exsolution Lamellae	
		Cpx	Opx	Cpx	Opx
Wt. %	CaO	21.5	0.4	20.4	0.2
	FeO	2.5	8.0	2.3	7.8
	MgO	13.5	29.3	12.9	27.4
Mole % Summed to 100	Wo	50.5	0.8	51.1	0.5
	Fs	5.0	13.0	4.5	13.6
	En	44.5	86.2	44.4	85.9

Traverses across grains revealed no major compositional zoning and no significant compositional differences (in excess of 5%) between pyroxenes in the groundmass and lamellae within the megacrysts. Thus, the groundmass and exsolved pyroxenes appear to be similar in composition.

These compositional data and textural relationships are interesting in the context of recent experimental work on synthetic pyroxene systems. The phase relationships in coexisting clinopyroxene and orthopyroxenes on or close to the compositional join diopside-enstatite have been studied at one atmosphere by Boyd and Shairer (1964) and at 30 kilobars by Davis and Boyd (1966). Experimental results revealed that a sensitive geothermometer exists in the system. The amount of solid solution of orthopyroxene in clinopyroxene is quite sensitive to temperature and rather insensitive to pressure. The important feature is the shape of the solvus boundary for diopside solid solution which crosses the temperature composition field at an oblique angle to the compositional coordinate. The composition of clinopyroxene solid solution in equilibrium with orthopyroxene solid solution provides a very sensitive thermometer in a geologically interesting range. For comparison, the diopside solvus at 1 atmosphere and 30 kilobars (shown in Figure 23) is nearly independent of pressure.

Using this diagram it is possible to make a tentative statement about the formation temperatures of the pyroxenes in the websterite. Partial chemical analyses of coexisting pyroxenes in websterite shows that virtually no orthopyroxene exists in solid solution in the clinopyroxene, either in the groundmass or the exsolution lamellae of the megacrysts. The diopside-enstatite phase diagram shows that above 900° C, some orthopyroxene exists in solid solution in clinopyroxene. For this reason it is believed that the groundmass and lamellae pyroxenes, exsolved at temperatures less than 900° C.

Pyroxenes in the websterites contain significant amounts of Al_2O_3 and FeO. The effect of Al_2O_3 on the diopside-enstatite solvus, according to O'Hara (1964), is to expand the miscibility gap. Temper-

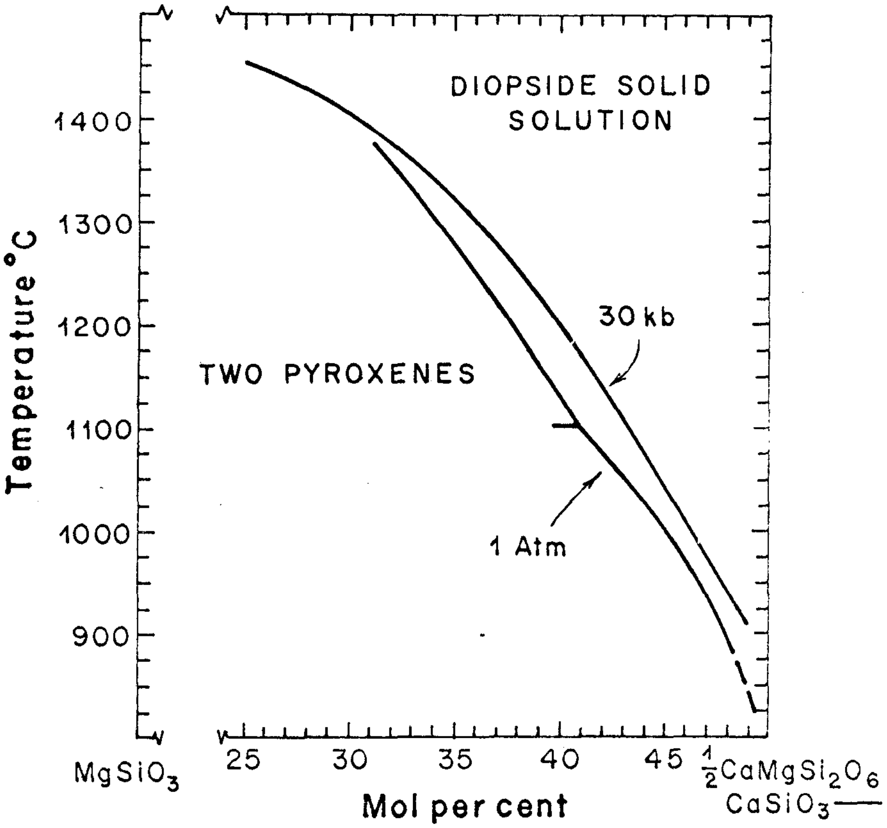

Data from:

1 Atm: Boyd and Schairer, 1964
30 kb: Davis and Boyd, 1966

Figure 23. The diopside solvus in the system $CaMgSi_2O_6$ (diopside)-$Mg_2Si_2O_6$ (enstatite) (Boyd, 1966)

atures inferred from this phase diagram would tend to be too low.

A genetic explanation for the observed textural relationships does not follow from the compositional data and phase relations in any simple way. Plotted on the diopside-enstatite phase diagram at 30 kilobars (Figure 24) are the approximate compositions of the megacrysts, the granoblastic groundmass and the bulk composition of the rock (for specimen MRX-1307A). These data suggest that the large pyroxene megacrysts may have been a simple phase, diopside solid solution, at a temperature above 1300° C, which exsolved later to two pyroxenes. No orthopyroxene-rich megacrysts have been observed in thin section.

The groundmass appears to have grown at the expense of the large exsolved pyroxenes by recrystallization along the edges and by growth of granoblastic grains along the lamellae. It is quite clear that the megacrysts predate the recrystallization of the granoblastic groundmass. It is tentatively concluded that the recrystallization of the groundmass and exsolution of the megacrysts took place at less than 900° C.

The observations of significance to the history of this rock are: 1) spinel is present, 2) the pyroxenes are aluminous, 3) there is very little mutual solid solution between the pyroxenes, 4) spinel and pyroxenes coexist in the groundmass, a granoblastic (equilibrium?) texture. This may imply recrystallization in the high temperature portion of the (sub-liquidus) spinel-peridotite field as defined by O'Hara (1967, p. 396) between about 12 and 20 kilobars and somewhere near or above 1000° C.

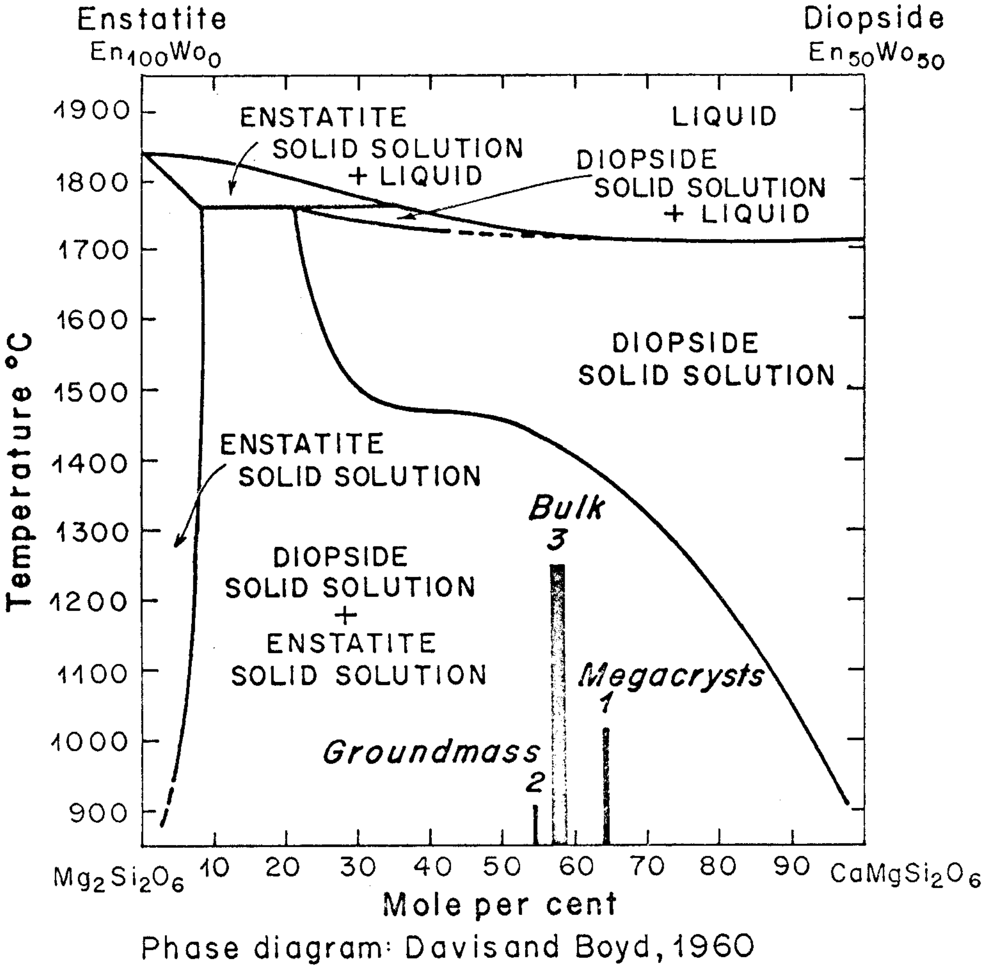

1. Approximate composition of pyroxene megacrysts based on pyroxene ratio: cpx 65: opx 35.

2. Approximate composition of granoblastic groundmass with pyroxene ratio: cpx 55: opx 45.

3. Bulk composition of rock based on chemical analysis (Appendix D3)
   3A: Normative En-Di ratio (Di 56.5)
   3B: Distribution of CaO, MgO directly to px molecules (Di 59.3)

Figure 24. Phase relations along the join $MgSiO_3$-$CaMgSi_2O_6$ at 30 kilobars, showing compositional data from groundmass, megacrysts and bulk rock composition for spinel-websterite (MRX-1307A)

If the megacrysts formed at 1300^{o} C at that depth, this implies a severe deviation from normal steady-state geotherms or mass motion within the mantle across isotherms. Certainly, the thermal event responsible for the megacrysts was not directly responsible for the kimberlite emplacement because of the abundant textural evidence for a slow recrystallization (well-developed lamellae and granular groundmass composed of moderate temperature pyroxene). A significant time had to elapse between the formation of megacrysts of diopside solid solution and the incorporation of the websterite in the kimberlite and subsequent transport to the surface.

Jadeite-Clinopyroxenite

This rock is a nearly monomineralic clinopyroxenite with accessory rutile and pyrite which occurs in abundance roughly equal to eclogite. It is the most abundant dense crystalline fragment type. (Antigorite schist, an altered ultramafic rock, is more abundant than either). Its distinctive features are: 1) the pyroxene contains approximately 65% jadeite molecule, and 2) the texture of the pyroxenes, which occur as large subhedral-zoned prismatic grains in a moderately well-foliated fine-grained groundmass (Plate 18). Measured specific gravity is 3.34. The unaltered nature and densely intergrown texture of the pyroxenes result in a rock of unusual strength. A photomicrograph is shown in Plate 17.

Pyroxene grains vary in size and shape for 1 cm long subhedrons to .1 mm anhedral groundmass crystals.

Whole rock chemical analysis revealed the rock to be highly aluminous and sodic (Appendix D3, Analysis 3). Ferric iron is also

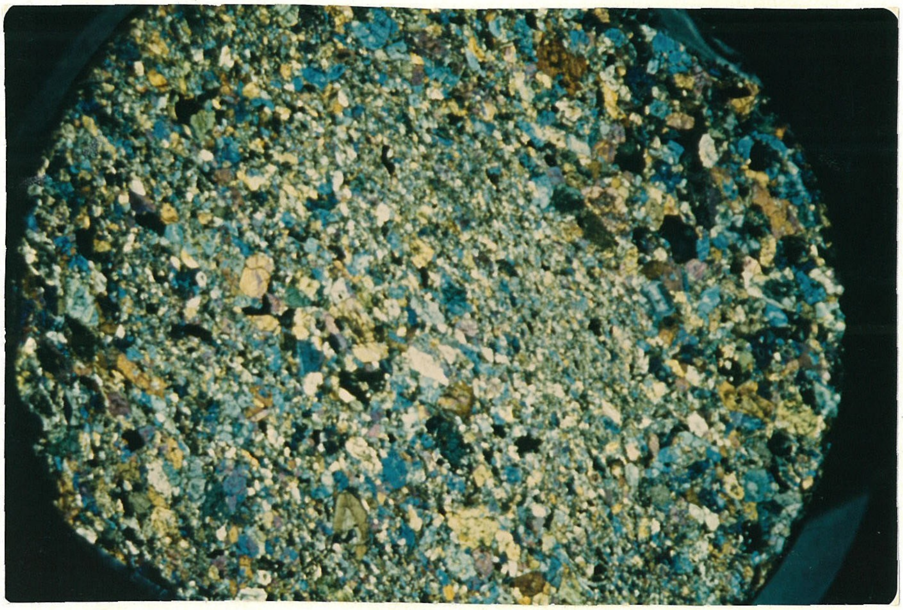

Rock is 95% clinopyroxene (jadeite-rich), about 2% interstitial rutile, 1% pyrite, and rare garnet. Note the foliation running approximately from 10 to 4 o'clock. The pyroxene occurs as subhedra which are zoned and which occur in bands juxtaposed with bands of fine-grained pyroxenes. Diameter of field is 25 mm; crossed nicols.

Plate 17. Photomicrograph of jadeite-rich pyroxenite (MRX-44)

high, suggesting the presence of acmite ($NaFe^{+3}Si_2O_6$) and probably ureyite ($NaCr^{+3}Si_2O_6$), as well as jadeite molecule. The norm contains abundant normative albite.

The large pyroxene subhedra are generally optically zoned (Plate 18; Figure 25). Microprobe traverse of such grains showed the cores to be jadeite-poor relative to the edges. Analysis of the core of a typical large subhedral crystal indicated a pyroxene composition (by weight) $jd_{64}ac_{12}di_{14}fs_7$ $others_3$ (Table 10). Traverse of this grain revealed the core to be enriched in diopside molecule and depleted in jadeite molecule relative to the edge. The textures suggest a recrystallization of an anhedral core but it is impossible to establish from the textures whether this is igneous or metamorphic in origin.

The opaque mineral appears bright yellowish-gold in reflected light and was tentatively identified optically as pyrite. Wave-length scan revealed Fe, S, Ni; microprobe analysis showed the phase to be stoichiometric, FeS_2. X-ray diffraction patterns revealed all the principal and secondary pyrite lines and a strong line at the location of the principal pyrrhotite peak but none of the secondary peaks. The data confirm the presence of pyrite but are not conclusive on the presence or absence of pyrrhotite.

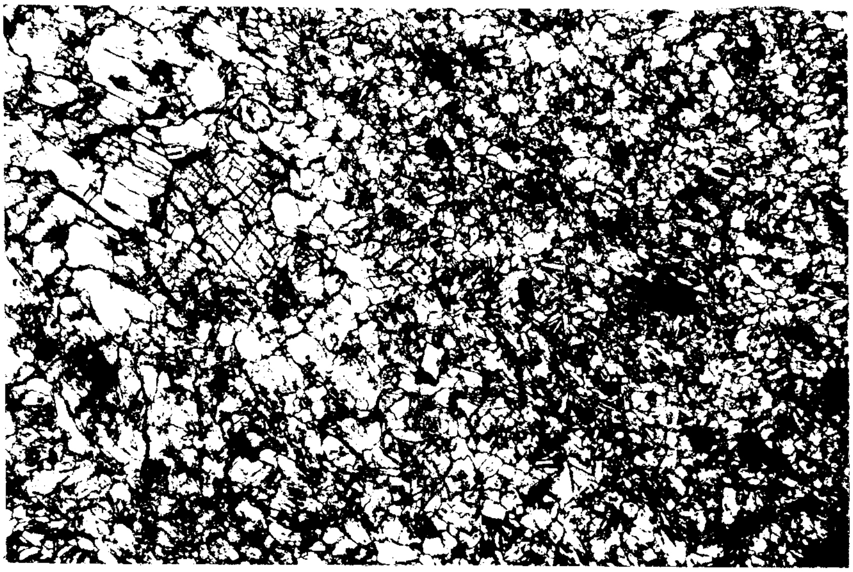

A. Diameter of field is about 5 mm. Note the large grain in the upper left of the field. It is pyroxene in a typical subhedral habit. The fine-grained prismatic crystals are also pyroxene. The opaque mineral is pyrite. Rutile is also present. Closeups of the large subhedron are shown in Plates 18B and 18C.

Plate 18. Photomicrograph of jadeite-rich clinopyroxenite (MRX-44)

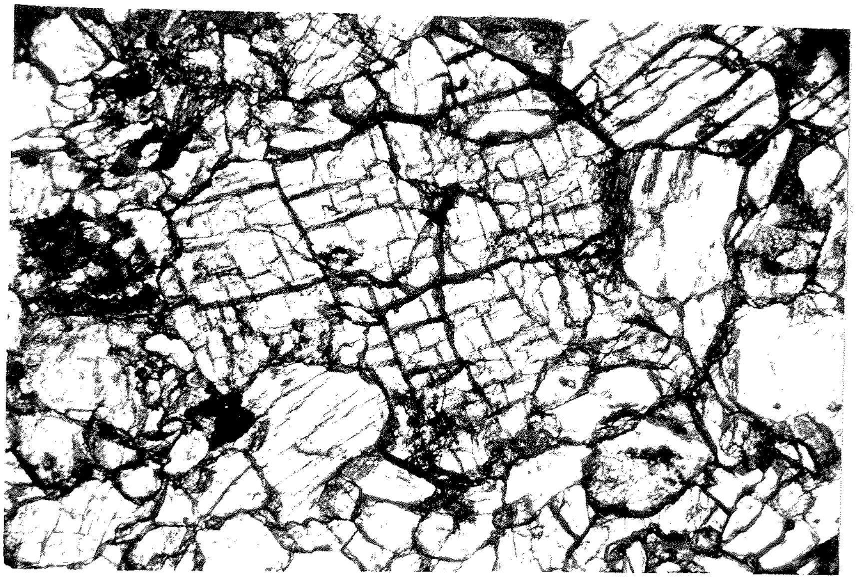

B. Clinopyroxene subhedra shown in ordinary light. Diameter of field is about 2 mm.

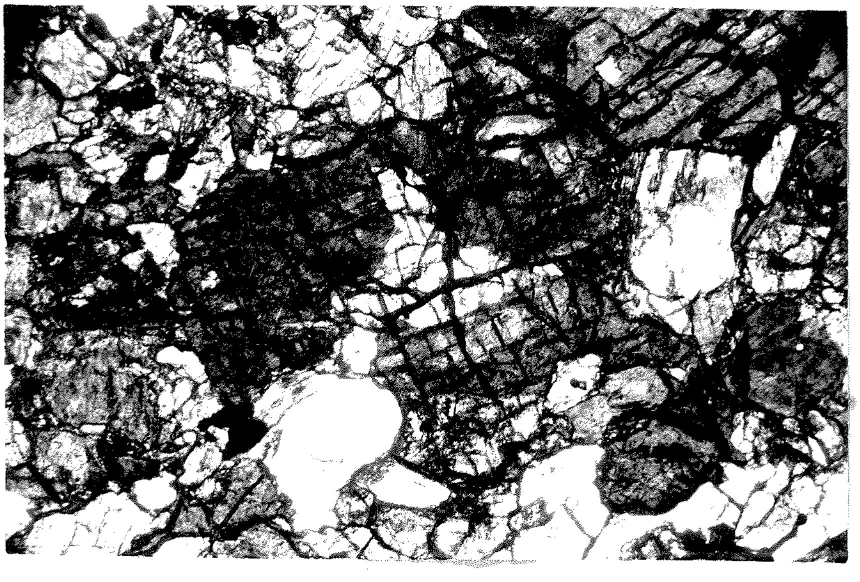

C. The same grain as above in plane-polarized light (crossed nicols) showing irregular, optically continuous domains suggestive of zoning or disequilibrium.

Plate 18. (Cont.) Photomicrographs of jadeite-rich clinopyroxenite (MRX-44)

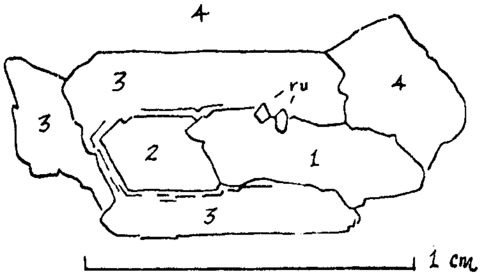

1. Anhedral clinopyroxene core, more jadeite-rich than edges

2,3,4. Optically continuous domains of jadeite-clinopyroxene (ru = rutile grains)

Figure 25. Sketch of large-zoned pyroxene subhedron in jadeite-rich clinopyroxenite (MRX-44)

Table 10. Partial Chemical Analysis by Microprobe of the Core of Large Clinopyroxene Subhedron in a Jadeite-rich Clinopyroxenite (MRX-44)

		Molecules		
			wt %	mole %
SiO_2	57.6	ac	12	12
Al_2O_3	18.1	jd	64	68
FeO	5.51	di	14	14
CaO	4.02	fs	7	6
MgO	2.62	wo	1	1
Na_2O	12.5			
	100.3			

O'Hara and Mercy collected a very similar but garnet-bearing specimen at Green Knobs (GK-6, O'Hara and Mercy, 1966, p. 341), which is not as aluminous (Al_2O_3 = 13.74) and not as sodic (Na_2O = 9.01) as the clinopyroxene analyzed from the Moses Rock specimen. Thus, the jadeite content of pyroxene in the Green Knobs specimen (GK-6) is not as high as observed in MRX-44. The garnet in GK-6 is very iron-rich (FeO = 24.00, Fe_2O_3 = 1.07) relative to magnesium (MgO = 9.52).

None of the garnet-bearing jadeite-pyroxenites from Moses Rock were examined in detail although specimens similar to those described by O'Hara and Mercy (1966) were observed and collected at Moses Rock.

If one compares the composition of the pyroxenes from MRX-44 and GK-6 (O'Hara and Mercy, 1966) with analysed pyroxenes from eclogites as defined by Coleman and others (1965), they are found to occupy a gap in the field of previously analysed pyroxenes. (The apparent gap in this figure has been filled by later work).

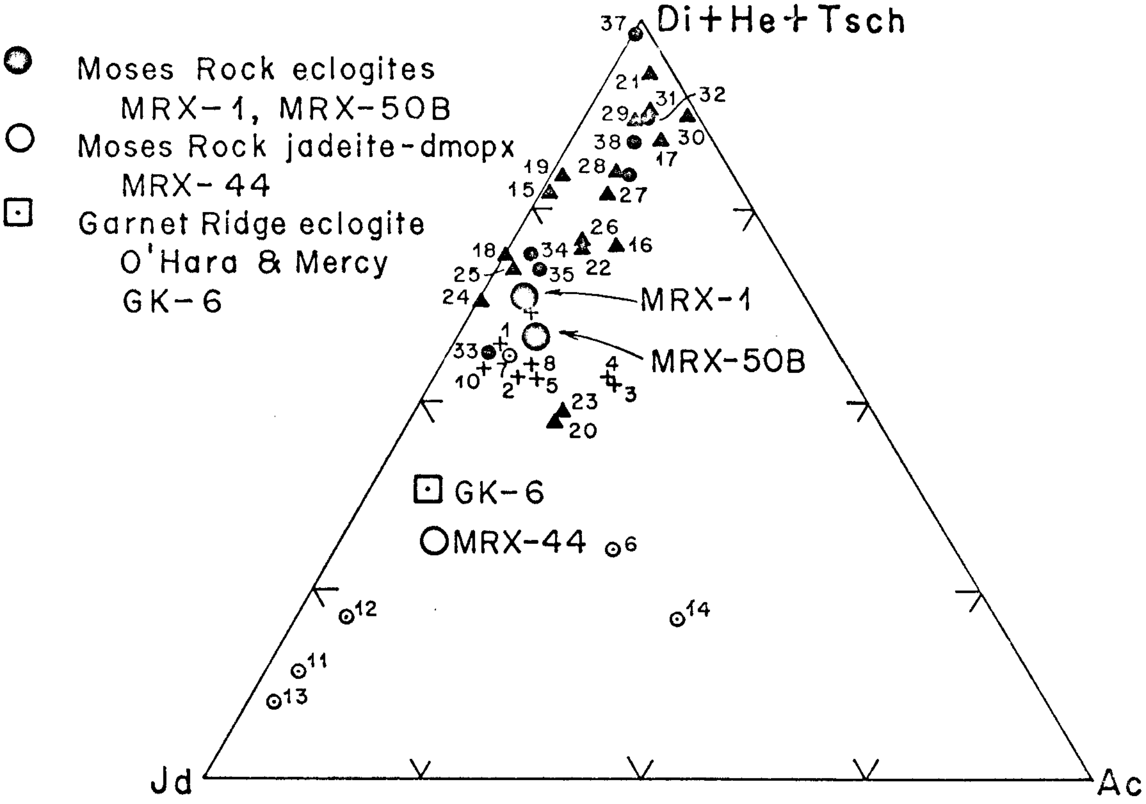

Figure 26. Summary diagram showing pyroxene compositions from eclogites (Coleman and others, 1965)

The garnet in GK-6 is iron-rich and contains approximately 36% pyrope molecule. Such garnets are typically associated with pyroxenes with high jadeite content and are characteristic of type C eclogites of Coleman (1965). In particular this garnet, (GK-6), is an interesting one because it is transitional between garnets from group C and group B eclogite and appears to be more typical of garnets from charnockites and granulites rather than glaucophane schists (Figure 27).

The origin of this rock is intriguing because of its texture and the jadeite-rich nature of its pyroxenes. However, the pyroxenes are not pure jadeite and they contain significant amounts of diopside and acmite molecules. Therefore, both the jadeite-diopside or jadeite-acmite phase diagrams are of interest. The wide range in grain size, the swirly bands of fine-grained crystals and foliation, the subhedral zoned reaction or overgrowth relationship in the large crystals suggest disequilibrium, either during crystallization from a melt without complete reaction or during subsolidus (metamorphic?) reactions.

If the textural relationships in the jadeite-rich clinopyroxene rocks are accepted as arguments that the pyroxenes crystallized from a melt, then it follows from jadeite phase diagrams (Figure 28) that they formed at pressures exceeding 23 kilobars and 1200° C. However, probably the strongest statement which can be made is that the textures imply disequilibrium, since the zoning and foliation could have been produced in the solid state.

Analysis of the detailed composition of the sulfide phase further

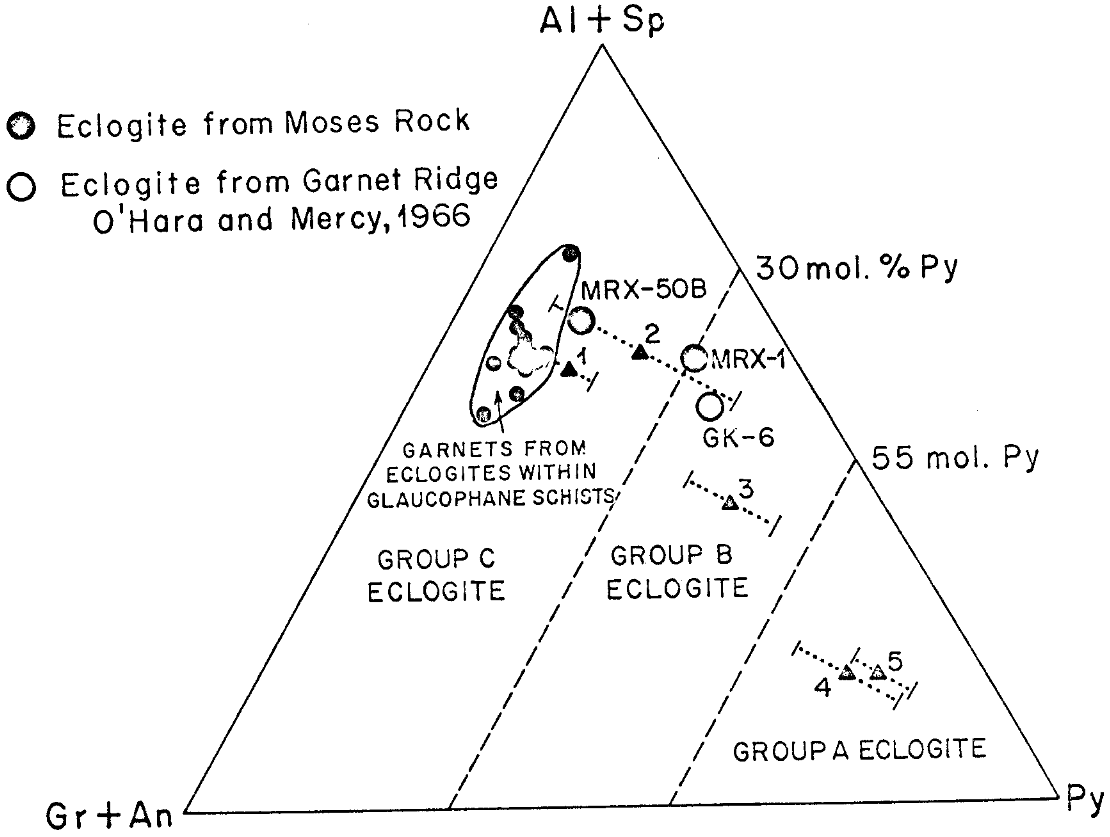

Triangular diagram showing relative proportions of (al + sp), (gr + an), py garnet end members for garnets in eclogites and related rock types. Dots represent all known analyses of garnets from Group C eclogites; triangles, average composition of garnets given by Tröger (1959) for garnets from certain rock types; dotted lines, the range in composition for the following averages: 1-garnets from amphibolites, 2-garnets from charnockites and granulites, 3-garnets from eclogites occurring in gneissic or migmatite metamorphic terrains, 4-garnets from eclogites associated in kimberlite pipes, 5-garnets from eclogites within ultramafic rocks such as dunite and peridotite. Diagonal dashed lines set off compositional ranges based on the pyrope content of the garnet as related to the geological groupings of the eclogites.

Figure 27. Summary diagram showing garnet compositions from eclogites. (Plot from Coleman and others, 1965)

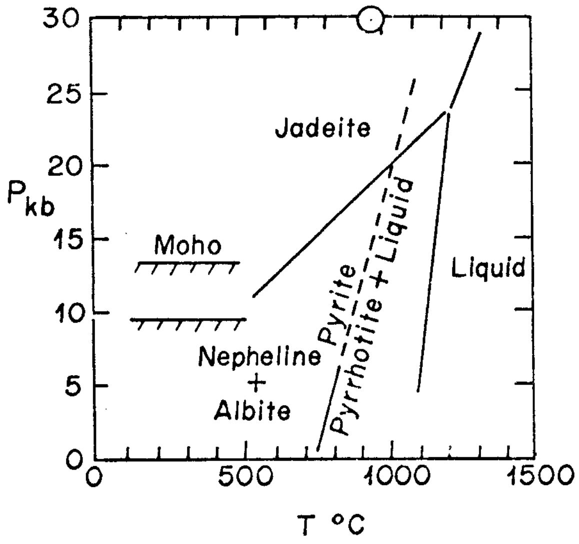

○ Inferred conditions in Moses Rock kimberlite reservoir

Pyrite-Pyrrhotite data from Kullerud (1964)

Figure 28. Summary diagram showing stability fields for jadeite and pyrite-pyrrhotite systems

constrains the possible conditions. Kullerud (1964) has reported the phase relationship between pyrite and pyrrhotite + liquid and his equilibrium curve is shown to 5 kilobars pressure (Figure 28). Electron microprobe analysis revealed this phase to be stoichiometric FeS_2 and x-ray diffraction patterns contained the principal and secondary peaks of pyrite. If pyrite formed in equilibrium with the pyroxene, then extrapolation of the pyrite stability curve to higher pressures suggests formation temperatures below the liquidus.

It is interesting to consider the textures in the context of the sub-solidus relationships in the 30 kilobar, diopside-jadeite diagram. The pyroxenes and whole-rock analyses for MRX-44 can be expressed as jadeite (albite + nepheline) and diopside components which sum to approximately 86 mole percent. The system jd-di was investigated by Bell and Davis (1965) at 30 kilobars and the approximate location of the whole-rock analysis and microprobe analyses (recast so that jd + di molecule = 100%) are shown on this phase diagram (Figure 29). The whole rock analysis is $jd_{88}di_{12}$, core of subhedral crystal $jd_{83}di_{17}$ and edge of subhedral crystal $jd_{90}di_{10}$. If the textures are interpreted as recrystallization in the solid state, it is significant that only jadeite-rich pyroxenes were observed.
No diopside-rich pyroxenes were observed. In the compositional range where minerals from this rock lie (di_8jd_{92} to $di_{20}jd_{80}$, roughly), on the <u>30 kilobar diagram</u> there is a broad two-pyroxene field below about 1340° C. So if recrystallization occurred below this temperature in a system with a bulk composition of $jd_{88}di_{12}$, diopside-rich and jadeite-rich clinopyroxenes would coexist. There is, however, on

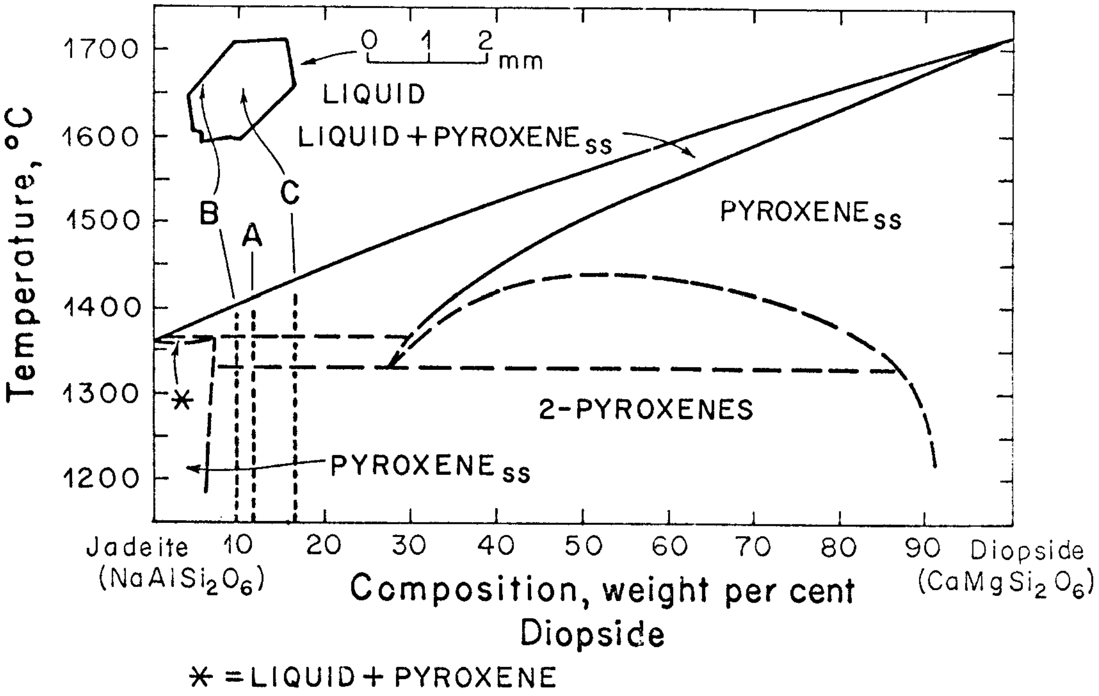

A. Whole-rock composition based on norm (Appendix D-4) jd (ab + ne) 72.3: di_{14} $(jd_{88}di_{12})$.

B. Outside edge of large subhedral grain of clinopyroxene.

C. Core of large subhedral grain of clinopyroxene.

Figure 29. Temperature-composition section at 30 kb for the system jadeite-diopside (Bell and Davis, 1965), with compositional data for jadeite-rich clinopyroxenite (MRX-44)

the 30 kilobar diagram, a small region where two jadeite-rich pyroxene phases coexist between about 1330° and 1370° C. The topology and details of the diagram are not known at lower pressures although it is clear (from Figure 28) that albite and nepheline will appear at higher temperatures in the sub-solidus region. The presence of pyrite precludes such high temperatures, however.

It is possible that this rock formed within the lower part of the crust, at low temperatures, below 600° C, but pressures above 13 kilobars (Figure 28). It is also possible that it formed at higher pressures, perhaps 20 to 30 kilobars, and relatively modest temperatures below 1000 to 1200° C.

No definitive statement can be made regarding the petrogenesis of this rock. If it did, indeed, crystallize from a melt, then it unambiguously formed at pressures in excess of 25 kilobars. This interpretation, however, is precluded by the presence of pyrite. A metamorphic origin of the textures is possible at conditions ranging from a crustal to deeper mantle conditions. This assemblage would have been stable in the conditions inferred for the kimberlite reservoir.

Eclogite

Eclogite specimens form about 1/2 % of the crystalline rock fragments found in the Moses Rock dike and are approximately as abundant as the jadeite-rich clinopyroxenite. Two eclogite specimens were studied in detail (MRX-1; MRX-50B); both are true eclogites consisting of omphacitic clinopyroxene and almandine-pyrope-grossularite garnet. Observed garnet concentrations in eclogitic rocks varies from 40% to 2% by volume. The jadeite-pyroxenite (MRX-44) may represent the zero-garnet end member of a spectrum in garnet-pyroxene ratio in the eclogite assemblage. Rutile and an opaque mineral are common accessories. No plagioclase or kyanite-bearing specimens were observed.

Many eclogite specimens were collected, 18 examined in thin section and two studied in detail. One of these two (MRX-50B) consists of 55% green clinopyroxene, 15% alteration aggregates (possibly anthophyllite-zoisite after aluminous enstatite or cordierite), 30% garnet, minor rutile and trace magnetite surrounded by hematite rims. Grain boundaries are ragged, garnets embayed and poikilitic with inclusions concentrated near the center. (Plate 19). Rock is slightly foliated.

The other specimen studied in detail (MRX-1) is free of alteration, and consists of 67% pyroxene, nearly colorless anhedral grains, some very slightly zoned; 30% garnet, nearly colorless, free of inclusions, rarely euhedral, generally sub- and anhedral; 2-3% magnetite with hematite rims and about 1% rutile. Grain boundaries are not ragged as in MRX-50B (Plate 20).

The two specimens MRX-50B and MRX-1 represent two contrasting textural types observed in the suite of eclogites. The first group is foliated, slightly altered, with ragged grain boundaries and embayed poikilitic garnets (a texture similar to MRX-50B). The second group is less foliated, unaltered, has subhedral grains with clean boundaries, unembayed and non-poikilitic garnets (as in MRX-1).

Compositions of coexisting garnet and pyroxenes from specimens

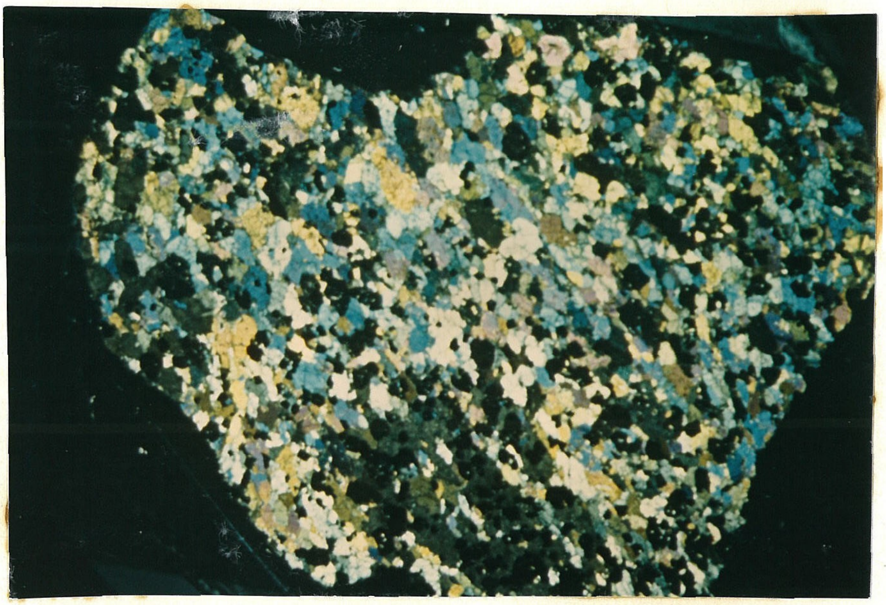

Crossed nicols. Diameter of field is 25 mm. Highly birefringent grains are omphacitic clinopyroxene; extinguished grains are garnet. Rock contains minor rutile and opaque. The rock contains fibrous alteration aggregates containing zoisite, inferred to be altered calcic-plagioclase.

Plate 19. Photomicrograph of eclogite (MRX-50B)

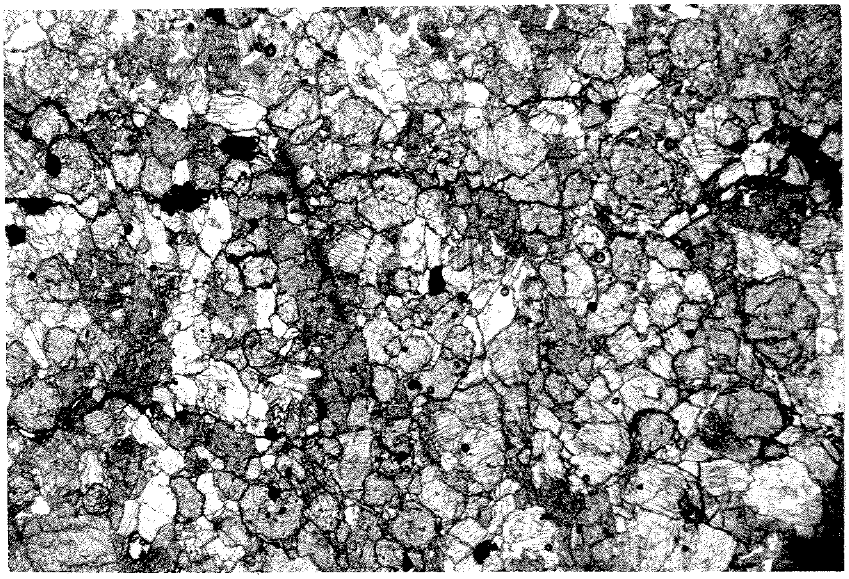

A. Ordinary light

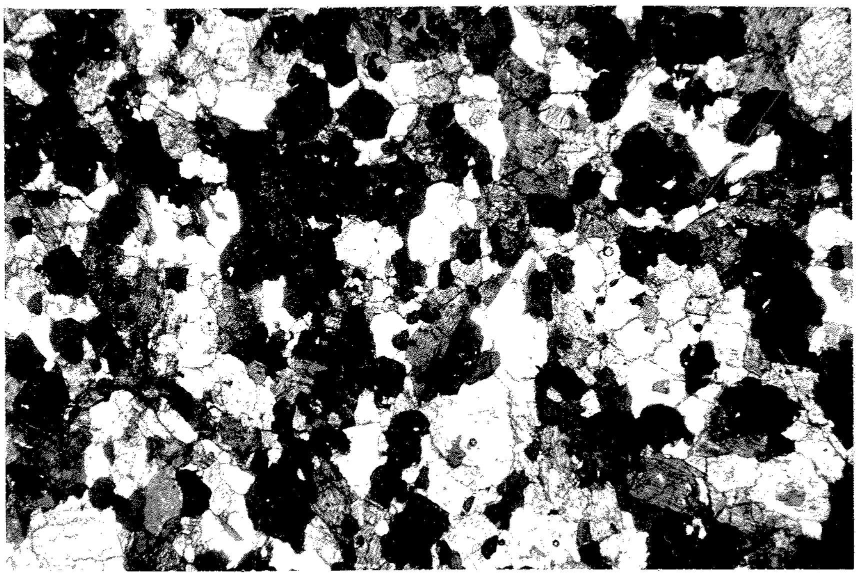

B. Crossed nicols

Diameter of field is about 10 mm. Pyroxene 70% (unextinguished in Plate B). Rock contains opaques and rutile (high-relief, very small grains) in Plate A, and is granular texture.

Plate 20. Photomicrographs of eclogite (MRX-1)

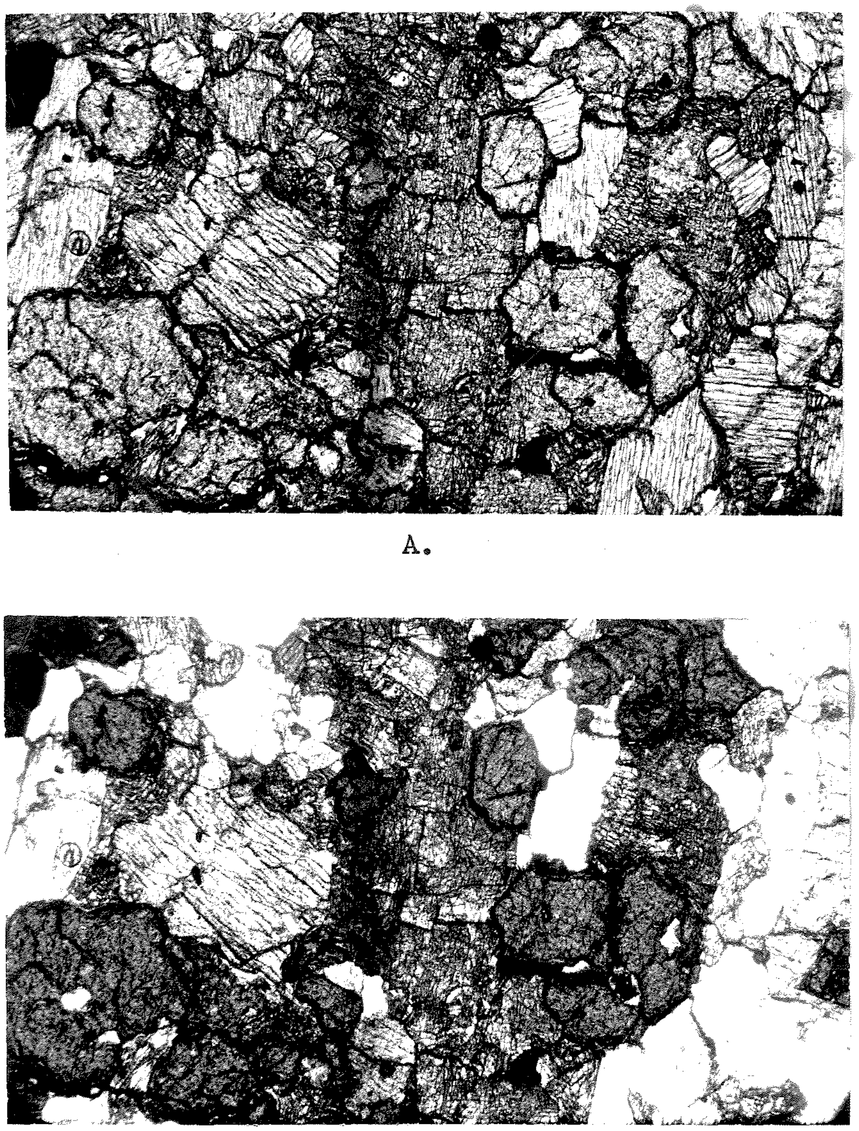

A.

B.

Rock is 70% omphacitic clinopyroxene (unextinguished in Plate B), 30% garnet (extinguished in Plate B), minor rutile and magnetite. Garnets are subhedral generally; pyroxenes anhedral very faintly optically zoned.

Plate 20. (Cont.) Photomicrograph of eclogite (MRX-1)

MRX-1 and MRX-50B were determined with the microprobe (Table 10). Pyroxenes contain significant amounts of jadeite molecule in solid solution and garnets are chiefly almandine molecule with pyrope and grossularite.

The alteration product in specimen MRX-50B (partial analysis shown in Table 11) is of interest. O'Hara and Mercy (1966) described a similar alteration mineral in their specimen GR-1. In thin section the grains occur in matted aggregates of small prismatic crystals. The microprobe data indicate that the white alteration aggregates consist of a highly aluminous, magnesium silicate with only minor calcium, thus is compositionally similar to a severely altered cordierite ($Al_3Mg_2Si_5AlO_{18}$) or possibly an altered aluminous orthopyroxene. X-ray diffraction patterns on separates of this mineral however revealed the principal peaks of zoisite ($Ca_2Al_3Si_3O_{12}\cdot OH$). The principal peaks occurred at 2.88, 2.695 Å and the secondary peaks at 4.05, 5.1, 5.04, and 2.79 Å. This composition would suggest that the alteration product was probably derived from calcic plagioclase.

Watson (1960) has reported lawsonite ($CaAl_2(OH)_2Si_2O_7\cdot H_2O$) from eclogites at Garnet Ridge in a similar petrographic setting. No lawsonite has been observed to date in the Moses Rock eclogites.

The garnet-pyroxene rocks described by O'Hara and Mercy (1966) and collected at Garnet Ridge can be matched by specimens found at Moses Rock. For example, O'Hara and Mercy's (1966) specimen GK-6, is texturally and compositionally similar to the jadeite-rich pyroxenite (MRX-44) previously described. GK-6 contains about 2% garnet;

similar rocks are observed at Moses Rock. The garnet and pyroxene compositions in GK-6 and MRX-1 are quite similar although GK-6 contains about 2% garnet, while MRX-1, about 30%.

Table 11. Partial Chemical Analysis by Microprobe of Coexisting Pyroxene and Garnet in Eclogite (MRX-1; MRX-50B)

	Eclogite MRX-1		Eclogite MRX-50B		
	Clinopx 28	Garnet 9	Clinopx 32	Garnet 12	Fine-grained Aggregate (Zoesite?)
SiO_2	54.40	38.28	55.27	38.11	36 ± 2
TiO_2	n.d.	n.d.	n.d.	n.d.	n.d.
Al_2O_3	9.72	23.58	11.49	22.27	31 ± 2
Cr_2O_3	n.d.	n.d.	n.d.	n.d.	n.d.
FeO	3.75	25.96	6.53	27.58	~ 7
CaO	13.66	3.90	10.67	4.46	~ 3
MgO	9.35	9.65	7.38	4.86	~ 21 ± 2
K_2O	n.d.	n.d.	n.d.	n.d.	n.d.
Na_2O	6.77	.04	8.25	.07	~ .1
H_2O	n.d.	n.d.	n.d.	n.d.	
Total	97.67	101.41	99.59	97.33	

Molecules
Wt. %

Jd=34.20	Gr= 10	Jd=40.43	Gr= 12
Ac= 5.74	Alm=58	Ac=10.43	Alm=64
Di=50.49	Py= 31	Di=39.85	Py= 16
Wo= 1.18		Wo= 0.71	
Fs= 3.59		Fs= 6.02	
CaT= 0		CaT= 0	
MgT= 0		MgT= 0	
95.20	101	96.77	92
No excess Al_2O_3		No excess Al_2O_3	

Eclogites at Moses Rock are a particularly interesting part of the crystalline fragment suite. Diamond-bearing eclogites in the South African kimberlite pipes demonstrate that at least some eclogites are mantle rocks (Williams, 1932). The significance of eclogites to broad petrologic problems, especially to the composition of the mantle, the nature of the Mohorovicic discontinuity and the origin of basaltic magmas, is now well established in the literature.

Coleman (1965) summarized the eclogite literature and concluded that eclogites fall generally into three groups: Group A, inclusions in kimberlite, basalts or layers in ultramafic rocks; Group B, bands or lenses in high-rank gneissic terrains; and Group C, bands or lenses in alpine-type (glaucophane schist) metamorphic terranes. Each group has compositional characteristics but the most striking are: 1) the jadeite content of the clinopyroxene decreases from Group A to B, and 2) the pyrope content of the garnet is distinctive as follows: Group A, greater than 55% pyrope, Group B, 30-55% pyrope; Group C, less than 30% pyrope.

The compositions of coexisting garnets and pyroxenes in the Moses Rock eclogites subdivide themselves into the natural groupings just described when plotted on A-F-C diagrams. Eclogites from Moses Rock (Table 9) and from Garnet Ridge and Green Knobs diatremes (O'Hara and Mercy, 1966) are similar and show affinities to eclogites of Group B (see Figure 30), eclogites in high rank metamorphic terrains. On A-F-C diagrams the eclogites from the Colorado Plateau diatremes fall into two groups. Furthermore they contrast sharply with eclogites from South African pipes. Garnet-pyroxene joins of the two Colorado

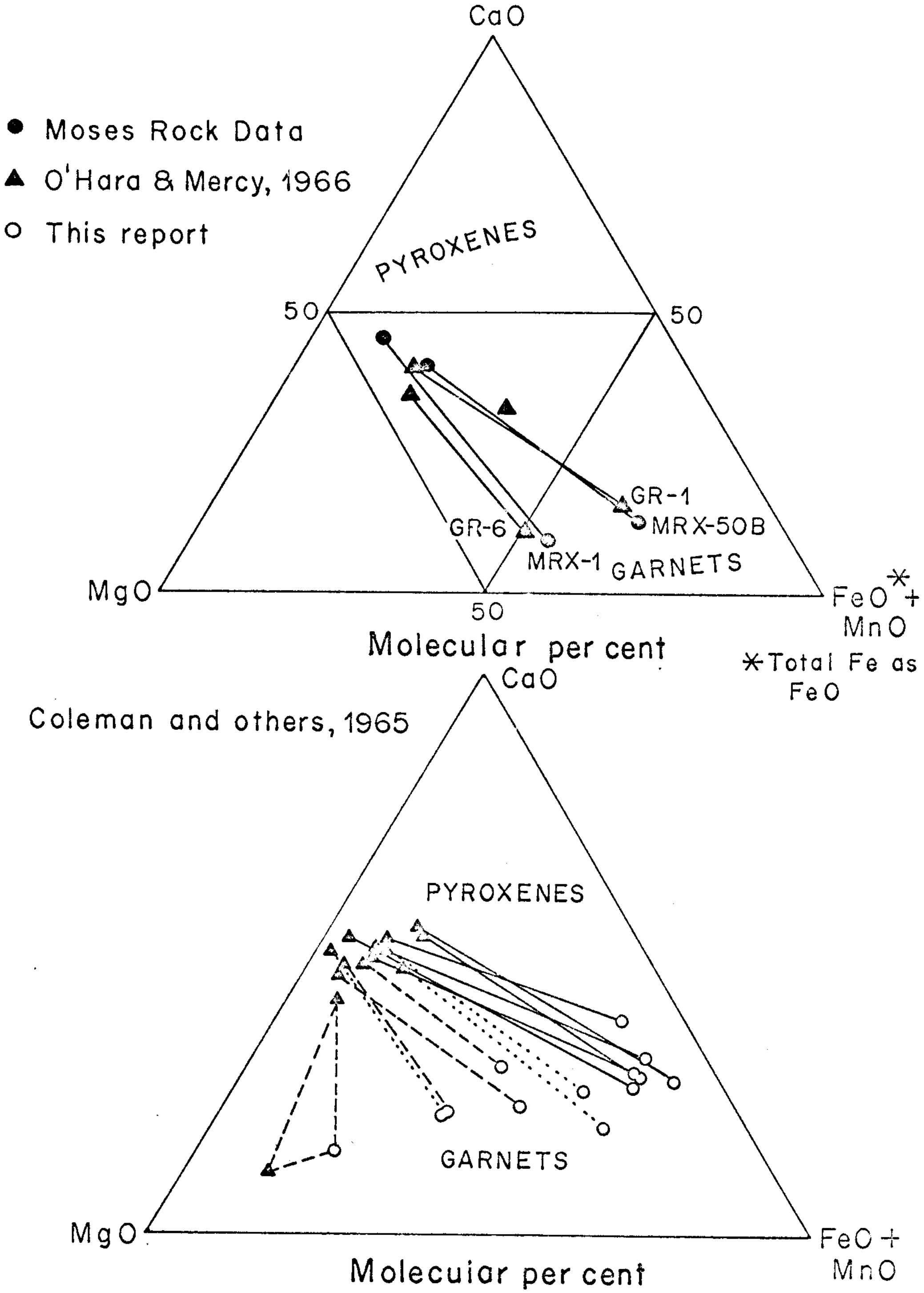

CFM plot of coexisting garnet-pyroxene pairs from individual eclogites. Tie line connects these pairs. Dashed line, Group A eclogites; Dotted line, Group B eclogites; Solid line, Group C eclogites. Rock compositions are not plotted, to avoid diagram confusion.

Figure 30. CFM plot of coexisting garnet and pyroxene from eclogite (after Coleman and others, 1965) with data shown for Moses Rock eclogite

Plateau groups cross. Also, the Colorado Plateau garnets and pyroxenes are iron-rich, relative to the South African specimens. These generalizations apply also to the two specimens from Moses Rock.

No definitive statement can be made now regarding the origin of the Moses Rock eclogites. It is apparent that the Colorado Plateau eclogites so far examined are not closely similar to eclogites in the South African pipes. The Colorado Plateau specimens most probably originated in a high rank metamorphic terrain within the lower crust, although they could be derived from the upper mantle, but at a somewhat shallower depth than the diamond-bearing eclogites of South Africa.

Yoder (1962) and O'Hara(1963) have stated that eclogites of different bulk compositions which crystallize at similar P-T conditions will be composed of garnet-pyroxene pairs whose compositions will plot as non-intersecting lines in A-F-C diagrams. There is an interesting scatter in the analyses of minerals from eclogites from the Colorado Plateau (Figure 30). The pyroxene-garnet joins taken together form a fanning array rather than a parallel or even sub-parallel array of tie-lines. This suggests that the eclogites observed in the Colorado Plateau diatremes may have formed at various and different P-T conditions. Furthermore, the differences can be observed at a single diatreme (MRX-1 and MRX-50B) which show almost the entire range observed. Perhaps the differences are not lateral or geographic, but rather represent vertical differences.

A thorough investigation of the suite of eclogites, including comparison of bulk composition and composition of individual mineral phases, would establish whether the apparent series of garnet contents ranging from perhaps 0% to 40% observed in eclogites from the Moses Rock dike represents only change in bulk composition or implies differences in conditions of formation.

To sum up, the eclogites from the Moses Rock dike (and Colorado Plateau diatremes generally) contain minerals like group B eclogites as defined by Coleman (1965), those from high rank granulite gneissic terranes. There appear to be differences in texture as well as mineral compositions which are believed to imply different conditions of crystallization, probably differences in depth.

Spinel-Lherzolite

A single specimen of spinel-lherzolite (MRX-2) was collected about 1.5 inches in diameter, with a medium-grained granular texture. In thin section, the rock has a granoblastic texture with grain size averaging about 1 mm. Olivine rarely exhibits poorly developed twinning and is commonly incipiently serpentinized. Orthopyroxene occurs in large anhedral fragments, clinopyroxene in small anhedral, equant grains. Spinel, dark brownish-green in ordinary light, occurs interstitially to the olivine and pyroxene. More rarely it is observed altered to an opaque in a field of serpentine. Modal analysis of this rock (Table 12) showed that it is approximately 18% altered to serpentine, but before alteration was approximately olivine 54%, orthopyroxene 37%, clinopyroxene 7% and spinel 2%.

Table 12. Modal Analysis (1000 pts) of Thin Section of Spinel-bearing Lherzolite (MRX-2)

Spinel-lherzolite Mineral	MRX-2 Volume %	
Olivine	40	54
Serpentinized olivine	14	
Orthopyroxene	33	37
Serpentinized opx	4	
Cpx	6	7
Cpx intergrowth	1	
Spinel	0.5	2
Altered spinel	1.5	
		100

Partial chemical analyses of the constituent mineral phases were obtained with the microprobe (Table 13), but the specimen was not discovered in time to include in the suite of rocks sent for whole-rock analysis. The rock composition (Table 12-13) was calculated on the basis of the modal analysis and the composition of the phases.

Table 13. Partial Chemical Analyses of Minerals from Spinel-bearing Lherzolite (MRX-2)

MRX-2 Lherzolite

	Olivine		Clinopyroxene		Ortho-Pyroxene	Spinel
	1	2	3	4	5	6
SiO_2	39.24	39.84	51.17	50.64	54.27	.04
TiO_2	.01	.01	.11	.10	.03	.01
Al_2O_3	-	-	5.61	4.68	4.70	54.64
Cr_2O_3	.08	-	.86	.78	.50	12.66
MgO	49.57	49.65	17.77	18.33	34.28	17.50
FeO	9.53	9.44	1.82	1.81	6.24	15.24
CaO	-	-	22.06	22.08	.31	.01
Na_2O	.04	.03	1.23	1.12	.03	.02
MnO	.15	.15	.09	.07	.15	.15
Total	98.56	99.12	100.72	99.61	100.51	100.27

Fe as FeO
Structure Formulae

	1	2	3	4	5	6
Si	.978	.985	1.846		1.868	.000
Ti	.000	.000	.003		.001	.000
Al	-	-	.283		.191	1.711
Cr	-	-	.025		.014	.266
Mg	1.841	1.830	.956		1.759	.693
Fe	.199	.195	.055		.180	.338
Ca	-	-	.853		.012	
Na	-	-	.086		.002	
Mn	.003	.003	-		.004	.003
Total	3.023	3.015	4.062		4.030	3.011
O	4.000	4.000	6.000		6.000	4.000
Mg/Mg+Fe	.903	.894	.945		.908	
Ca/Ca+Mg			.471	.478		

Table 14. Calculated Rock Composition of Spinel-bearing Lherzolite Based on Mode and Mineral Analyses

	(1)	(2)
SiO_2	44.6	45.85
TiO_2	0.02	0.41
Al_2O_3	3.33	2.05
Cr_2O_3	0.57	0.48
MgO	41.0	41.63
FeO	7.90	7.14
CaO	1.78	1.76
Na_2O	0.13	0.15
MnO	0.15	0.15
K_2O	-	0.08
NiO	-	0.26
P_2O_5	-	0.03
	99.48	99.99

(1) Spinel-lherzolite, (MRX-2)

(2) Garnet-lherzolite nodule in kimberlite KA 64-16, Dutoitspan Mine, South Africa, recalculated with Fe as FeO. Rock used by Ito and Kennedy (1967) in experimental determination of melting and phase relationships.

The calculated chemical composition of spinel-lherzolite (MRX-2) is similar to the garnet-lherzolite used by Ito and Kennedy (1967) in their high pressure experiments on melting and phase relationships (Table 14). They believe that this material has the approximate average composition of garnet-lherzolite from kimberlite pipes.

If the spinel-lherzolite (MRX-2) were converted to a garnet-bearing assemblage by the reaction:

spinel + 3.2 enstatite + 0.4 diopside =

(pyrope + grossularite) + forsterite

the resulting assemblage on a <u>volume</u> basis would be approximately

olivine	56
orthopyroxene	32
clinopyroxene	6
garnet	6

O'Hara and Mercy (1966) observed neither garnet nor spinel in lherzolites from Green Knobs and Buell Park.

The conditions of formation of the mineral assemblages in lherzolites can be inferred from the composition of the coexisting phases, in particular the calcium-rich pyroxenes. The coexisting orthopyroxene and clinopyroxene in the specimen described by O'Hara and Mercy (1966, pp. 339-340) contain 4.00 and 4.86 wt % Al_2O_3 respectively, somewhat less than the Moses Rock spinel-bearing specimen (MRX-2). The amount of mutual solid solution of orthopyroxene and clinopyroxene in the two specimens is similar. In the spinel-bearing lherzolite from Moses Rock (MRX-2) the atom ratios Ca/Ca+Mg for the clinopyroxenes were .471 and .478 suggesting temperatures near 950 to 1000° C. Using Mercy's (1967, p. 396) interpretive diagram and his treatment of pyroxene compositional data, the Moses Rock lherzolite assemblage was in equilibrium at roughly 16 kilobars and 1200° C; the specimen from Buell Park, about 27 kilobars and 1150° C. The details of the arguments leading to these conclusions will be discussed later.

Conclusions are tenuous because the composition of natural minerals deviate from the simple compositional systems used in experimental determination of the phase diagrams. The natural spinel had 15% FeO, 13% Cr_2O_3, and the pyroxenes 4 to 6% Al_2O_3 and some iron. In lieu of experimental data on systems more closely approximating these natural minerals, it is concluded that the spinel-lherzolite (MRX-2) crystallized in the mantle at about 48 kilometers depth and 1200° C.

Serpentine-Schist

Although this rock is not dense (MRX-51; SG = 2.53 ± .01), chemical analysis has shown that it is, indeed, an ultramafic rock (Appendix D-3, Analysis 11). It is far more abundant than any of the dense crystalline fragments, and it is the most abundant ultramafic inclusion type in the Moses Rock dike. The CIPW norm consists predominantly of pyroxene, olivine and plagioclase. It differs chemically from the analysed Moses Rock kimberlite in its higher silica, alumina, lime and alkali content (Table 18).

Hand specimens are commonly found as ellipsoidal or flat disc-shaped fragments, always well rounded or as broken pieces of well-rounded fragments. The rocks are light lime-green in color and consist of an aggregate of sheet structure minerals, generally coarse grained, which are quite weak and easily broken apart. In thin section the rocks are a matted intergrowth of serpentine and chlorite group minerals, in a fiberous habit.

The x-ray powder diffraction patterns of whole rock samples revealed the principal lines of antigorite ($Mg_6Si_4O_{10}(OH)_8$) and tremolite ($Ca_2Mg_5Si_8O_{22}(OH)_2$). The intensity ratios of the principal lines indicates that the antigorite is much more abundant than the tremolite. This is consistent with the chemical analysis. In some thin sections small remnant pyroxene grains were observed within the matted groundmass but compositional data are not available on these minerals.

The serpentine-rich schists apparently originated by hydration of a pre-existing ultramafic rock. The phase relationships in hydrous magnesium-silicate systems are known to 30 kilobars (Kitahara, Takenouchi and Kennedy, 1966). For a normal shield or continental geotherm, near the shield geotherm calculated by Clark and Ringwood (1964), an orthopyroxene-olivine rock in the presence of water would begin to hydrate above approximately 21 kilobars (63 kilometers) by conversion of orthopyroxene to forsterite + talc. Above about 15 kilobars (45 kilometers) serpentine is stable and given sufficient water, the rock could consist entirely of hydrous phases.

This serpentine-rich schist could originate in the upper mantle, in the crust or at the surface by hydration of a pre-existing ultramafic rock. Since concentric hydration of the schist fragments from the outside inward is not generally observed, it is believed that these fragments were not altered while at the surface, rather existed at depth as antigorite-rich schists.

Summary

Five dense or ultramafic crystalline rock fragment types have been observed and investigated. The compositional data accumulated on the mineral phases in these rocks are summarized at the end of this section.

The antigorite-tremolite schist is the most abundant ultramafic fragment type. It is believed that these rocks originated by hydration (at depth) of pre-existing ultramafic rocks. Since serpentine is not stable above about 600° C, this rock must have formed at relatively shallow depth, probably less than 15 kilobars (45 kilometers).

The jadeite-rich clinopyroxenite has a texture which suggests disequilibrium. Minerals are zoned and quite unequal in size and shape. It is not certain whether this is an igneous or partial recrystallization texture. The presence of pyrite and jadeitic pyroxene is consistent with either an origin in the lower crust or mantle.

The two eclogite specimens examined had roughly equal garnet to pyroxene ratios but the minerals had quite different compositions and textures. One contained an aggregate of white alteration minerals, mostly zoisite and possibly another unidentified phase, believed to be altered calcic plagioclase. The range of variations observed in eclogites from all the Colorado Plateau diatremes has been observed in the two specimens from the Moses Rock dike. It is believed that the eclogites represent a range in conditions of formation, probably depth.

The spinel-bearing websterite fragments contain highly aluminous pyroxenes in a spectacular and informative textural relationship. Megacrysts, now exsolved into lamellae of two pyroxenes, are believed to have crystallized as diopside solid solution at high temperature. Granoblastic groundmass pyroxenes have encroached upon the megacrysts. Pyroxenes in the lamellae and groundmass are nearly identical in composition; very little mutual solid solution of calcium-rich and calcium-poor pyroxenes exists, implying that the recrystallization has occurred at temperatures below 1000° C. It is apparent that the websterites have experienced a complex crystallization and recrystallization history which must span a long period of time, prior to the inclusion of these rock fragments in the erupting kimberlite. This rock could have originated in the lower crust or mantle.

The spinel-lherzolite is believed to be a fragment of mantle. The clinopyroxenes indicate crystallization at about 16 kilobars and 1200° C. Olivines and orthopyroxene are partially serpentinized.

No garnet-lherzolite fragments were observed in the Moses Rock dike, but its presence as a rock type at depth is inferred from inclusions in pyrope garnets and minerals in the kimberlite. This will be discussed in the next section.

The table on the following page summarizes the compositional data on mineral phases in these rocks.

Table 15. Summary of Dense and Ultramafic Crystalline Rock Fragment Types Observed in the Moses Rock Dike

1. Antigorite-Tremolite Schist (x-51)

	Mg/Mg+Fe= .899
whole rock	SiO_2 (dry)= 50.9
	Al_2O_3 (dry)= 3.9

2. Clinopyroxenite (x-44)

97%	Clinopyroxene	$di_{14}jd_{68}ac_{12}fs_6wo_1$
2	Rutile	
1	Pyrite	

DECREASING ORDER OF RELATIVE ABUNDANCE

3. Eclogite

(x-1)	67%	Cpx	$di_{51}jd_{34}ac_6fs_4others_5$
	30	Garnet	Mg:Fe:Ca=31:58:10
	1	Rutile	
	2	Opaque	
(x-50B)	55%	Cpx	$di_{40}jd_{40}ac_{10}fs_6others_4$
	30	Garnet	Mg:Fe:Ca= 18:69:13
	tr	Rutile	
	15	Alteration aggregate (zoesite?)	

4. Spinel-Websterite (x-1307)

39%	Orthopyroxene	Mg/Mg+Fe=.871; Al_2O_3=6.8
60	Clinopyroxene	Ca/Ca+Mg=.537; Al_2O_3=7.6; Na_2O=1.0; FeO=2.6; Mg/Fe+Mg=.906
1	Spinel	Mg, Fe, Al, Cr

5. Spinel-Lherzolite (x-2)

54%	Olivine	Mg/Fe+Mg=90
37	Orthopyroxene	Mg/Fe+Mg=91; Al_2O_3=4.7; Cr_2O_3=0.5
7	Clinopyroxene	Ca/Ca+Mg=.47; Al_2O_3=5.6; Cr_2O_3=0.9; Na_2O=1.2; FeO=1.8; Mg/Fe+Mg=.945
2	Spinel	Mg/Fe+Mg=60-70; Al/Al+Cr=60-80

6. Garnet-Lherzolite

(INFERRED FROM INCLUSIONS IN PYROPIC GARNETS)

Olivine	Mg/Fe+Mg=94
Garnet	Mg:Fe:Ca=69:19:12
Clinopyroxene	Ca/Ca+Mg=48 to 50; Al_2O_3=2 to 3; Cr_2O_3=1 to 2; Na_2O=1 to 2; FeO= 1.3 to 2.6
Orthopyroxene	Mg/Mg+Fe=94; Al_2O_3=0.5 to 1%
Clinohumite	TiO_2= 4 to 6
Rutile	Cr, Fe in solid solution
Ilmenite-Geikielite	TiO_2=56; FeO=30; Mg=13

Kimberlite

Introduction

The occurrence and petrographic character of the kimberlite and microprobe analyses of mineral grains separated from it permit some important inferences to be drawn regarding the genesis of the kimberlite and the composition and physical state of the mantle.

At the type locality in the Moses Rock dike, kimberlite is a micaceous, heavily hydrated, ultramafic microbreccia composed of angular fragments, most of which are partially serpentinized olivine, with orthopyroxene, clinopyroxene, garnet, spinel, mica, and rare rock fragments set in a particulate, fine-grained groundmass of serpentine-type minerals. Petrographically this rock is similar to kimberlite at the Kimberley Mine in South Africa as described by Williams (1932), except that no diamonds were observed despite a diligent search. Its most important characteristic is its brecciated texture. It is composed of discrete angular mineral fragments, in no way displaying textural features of a melt.

Understanding the genesis of the serpentine is critical in establishing the genesis of the kimberlite. "Serpentine," is used rather loosely here to refer to magnesian sheet structure minerals, which occur in very distinct textural modes. The first mode is as fine-grained groundmass, and a second, as an alteration product of larger olivine. Alteration of orthopyroxene fragments is less pervasive than olivine. Reconnaissance compositional data were obtained in the context of the textures and will be discussed. Did the serpentine form at depth, during transport to the surface, or after emplacement?

Occurrence and Description of Kimberlite

The mineral constituents of kimberlite make up about 12% of the breccia filling the Moses Rock dike, however, over 90% of these minerals are intricately mixed on a fine scale and dispersed throughout the various breccia units. Only at several scattered localities within the dike is kimberlite observed as a discrete mappable unit.

Kimberlite at the type locality occurs as a thin dike within a large breccia block of Cedar Mesa sandstone member near the northeast end of the dike (Plate 4). Here it is a dark greenish-black microbreccia containing olivine, serpentine, rare phlogopite, garnet, pyroxene and small lithic fragments. The greenish-black rock from the center of the dike was sampled in hand specimens and in bulk (MR-1416A). The descriptions and chemical and mineral analyses of kimberlite are from this occurrence. There is a thin contact zone about 1-2 cm thick between the kimberlite and overlying pale orangish-red sandstone. The contact zone is a light lime-green powder which x-ray powder diffraction revealed to be antigorite, with minor talc, no quartz, and no other mineral in significant abundance. The red sandstone at the contact showed only minor bleaching. The lower contact is against a similar light lime-green unit, consisting of kimberlite minerals apparently diluted with silt- and sand-sized sedimentary rock debris. The lower contact is not well exposed.

In thin section, kimberlite is composed of millimeter sized, angular fragments, mostly olivine, which exhibit varying degrees of alteration to serpentine. These fragments are set in a fine-grained groundmass, apparently also serpentine, but of a clearly different texture than the alteration product of the angular fragments of olivine (Plate 21). Remnant patches of olivine are optically continuous. Other common mineral phases include yellowish orthopyroxene, red to wine-colored garnet, green clinopyroxene, and large grains of mica. Amphibole and calcite are much less common. Relatively rare are clinohumite, opaques, green and brown spinel, plagioclase and zircon. Pyroxenes are unzoned and show no evidence of exsolution. Serpentinization of olivine grains is commonly pervasive; alteration of orthopyroxene is relatively slight. Lithic fragments, generally limestone and siltstone, show no apparent alteration in contact with the enclosing groundmass. Garnets commonly have thin kelyphitic rims of chlorite and magnetite (?). Small veins of fibrous carbonate are observed within the groundmass. Small chips of platy-fibrous carbonate are commonly observed in the breccias or on the surface of the ground within the dike. (One mile east of the Moses Rock dike at the base of Comb Ridge in the Organ Rock Member, a nearly continuous plate of this material separates the wall rock from the kimberlite-bearing breccia (Plate 2B, C)). Microprobe analysis of plates sampled from the satellite dike and from carbonate veins in kimberlite from Moses Rock dike revealed that this material is nearly pure $CaCO_3$ with less than 1% $MgCO_3$ present. Optical determinations showed that it is calcite, not aragonite.

Modal analysis of kimberlite (MR-1416A) showed that the rock is approximately 85 to 90% serpentine; about 50% serpentine groundmass.

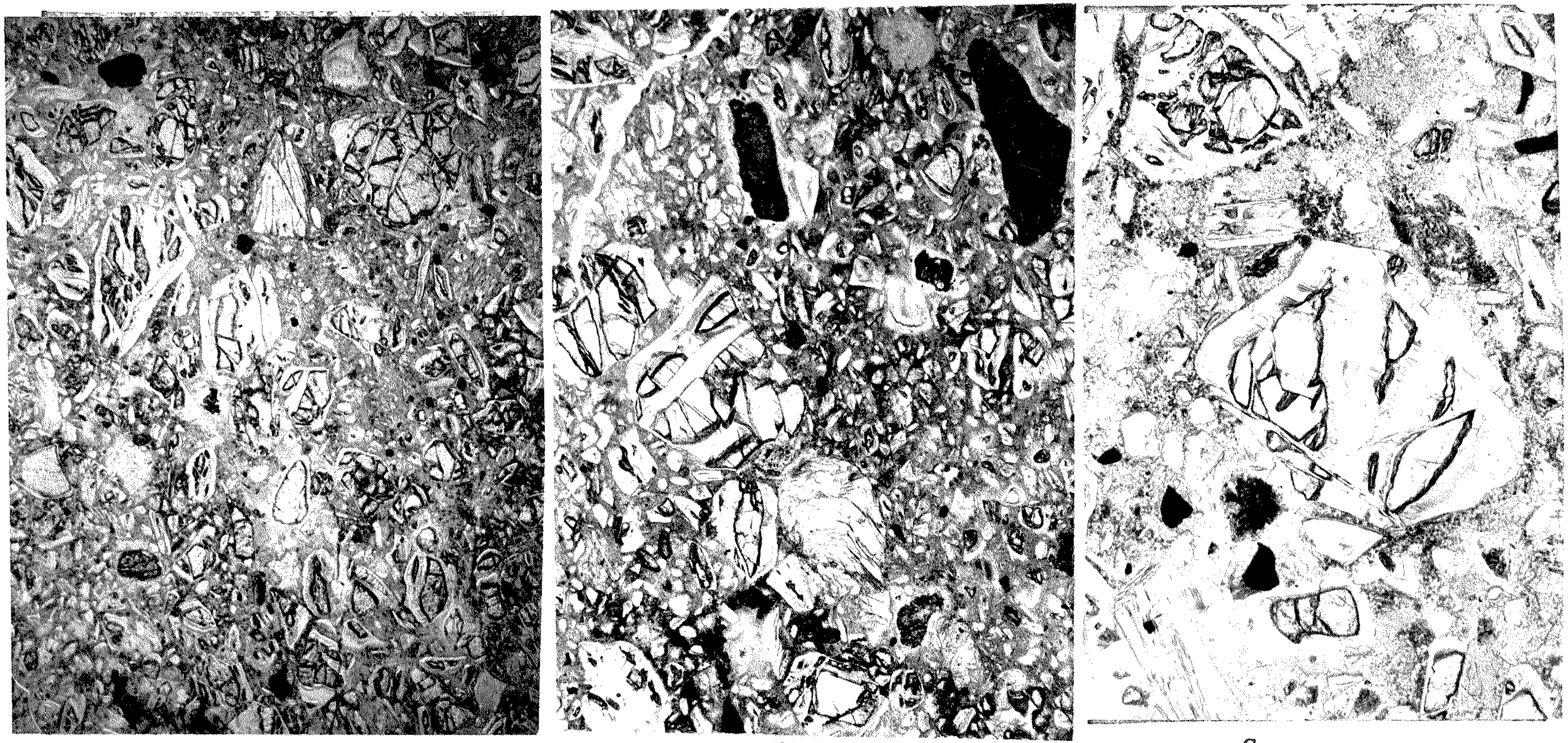

A. B. C.

Sampled from small dike shown in Plate 10A in large breccia block of Cedar Mesa sandstone. The fine-grained groundmass is light-green serpentine, the large angular fragments mostly olivine, but generally serpentinized. Note the textural contrast between the groundmass serpentine and the alteration product of the olivine. Other grains include garnet, ortho- and clinopyroxene, mica (biotite-phlogopite) and lithic fragments.

Plate 21. Photomicrographs of kimberlite from type locality in the Moses Rock dike (MR-1416A).

Unaltered olivine is only 5 to 10% by volume. Approximately 45% of the rock is olivine or altered olivine. Large sheet structure minerals (mica and chlorite) form about 1% by volume; orthopyroxene and altered orthopyroxene, about 2% (Table 16).

Table 16. Modal Analyses of Kimberlite (MR-1416A) Based on 1000 Points

Kimberlite MR 1416A Minerals	Thin section 1		Thin section 2	
Groundmass serpentine	46		50	
Olivine	10	46	6	43
Serpentinized olivine	36		37	
Opx	1	1.6	1.0	2
Serpentinized opx	0.6		1.0	
Clinopyroxene	0.0		1.8	
Lithic fragments	4.3		0.0	
Garnet	0.0		0.4	
Mica	0.4		1.6	
Carbonate	1.6			
Opaques	0.6		1.6	
Miscellaneous	0.9			
	100		100	

X-ray diffraction analysis of the pulverized rock revealed serpentine, subordinate talc and possibly chlorite group peaks.

The general petrographic character of kimberlite at the type locality is quite similar to kimberlite from South Africa as described by Williams (1932) and subsequent workers. (In particular, compare Plate 21A, B, C with Williams, 1932, Plates 57 through 70). The major difference is that no diamonds have been observed or reported in any of the Colorado Plateau kimberlites. As in South Africa, the kimberlite is breccia. It is a rock composed of angular mineral fragments, mostly olivine, mixed with a few rock fragments, set in a fine-grained groundmass of serpentine which itself, appears to be composed of small particles. The rock generally is unfoliated, and shows no deformational fabric.

Heavy mineral concentrates were obtained from a large sample of kimberlite (MR 1416A) and the approximate relative proportions of olivine, pyroxene, garnet, spinel and opaques determined. The concentration technique used involved mechanical crushing, a Wilfley vibrating table, heavy liquids and magnetic separations. Dense phases of spherical geometry are preferentially concentrated, particularly on the vibrating table. Minerals of specific gravity greater than 2.95 were retained in the heavy liquid processing. Principally, serpentine, calcite, quartz and feldspar are removed by these procedures. A total of 29 fractions were weighed and the relative abundance of minerals visually estimated by counting techniques used in petrography of unconsolidated coarse-grained sediments. Many fractions were homogeneous, so that no counting was required.

The results (Table 17) should reflect the present approximate relative abundance of unserpentinized mineral grains in the kimberlite. As in the modal analyses, the unaltered olivine to orthopyroxene ratio is about 10 to 1 and the clinopyroxene is less abundant than the orthopyroxene. Garnet is more abundant in the concentrate than in the modal analyses which reflects preferential concentration of the garnet relative to pyroxene and olivine because of its higher specific gravity, equant habit and lack of cleavage.

Table 17. Approximate Weight Percent of Heavy Minerals Concentrated from Kimberlite (Sample MR 1416A)

Olivine	79
Orthopyroxene	8
Clinopyroxene	2
Garnet	6
Opaques ± spinel	4
Misc.	1
	100%

Chemical Composition of Moses Rock Kimberlite

Chemical analyses of two specimens of kimberlite from Moses Rock were obtained (Table 18, Analyses 7 and 8). Both specimens analysed are from the type locality, however MR-1416B (Analysis 8) is lighter in color and appears to be more altered than MR-1416A (Analysis 7). Compared to kimberlites from South Africa the Moses Rock kimberlite is relatively rich in MgO and poor in Al_2O_3, CaO and the alkalis. Relative to the kimberlites at Buell Park, Arizona, the Moses Rock kimberlite is depleted in silica, lime and alkalis and enriched in MgO.

In its bulk chemistry, the kimberlite at Moses Rock is similar to kimberlite elsewhere. That is, it is a hydrated, magnesian-rich ultramafic rock.

The kimberlite analyses recalculated on a volatile-free basis (1 and 10) is very similar to the calculated spinel-lherzolite composition (11). The analysed antigorite-tremolite schist fragment is enriched in SiO_2 and Na_2C, and depleted in MgO. It possibly was derived from a pyroxene-rich rock, rather than an olivine-rich assemblage.

Table 18. Chemical Analyses of Kimberlite from Moses Rock, Buell Park, Arizona and Africa

	Buell Pk.	S.Af.		Basutoland		Peridot
	(1)	(2)	(3)	(4)	(5)	(6)
SiO_2	47.50	43.27	36.58	30.72	30.13	40.81
Al_2O_3	1.38	3.49	7.15	4.04	4.72	.10
Fe_2O_3	4.34	5.78	6.69	6.65	8.15	.00
FeO	2.37	2.94	4.99	4.57	6.68	9.46
MgO	31.26	23.47	22.55	32.40	25.87	49.12
CaO	.65	7.71	6.05	6.30	7.05	.07
Na_2O	.11	1.08	.28	.17	.45	.01
K_2O	.37	2.57	.47	1.00	.96	.00
H_2O^+	10.88	4.45	8.51	8.90	6.96	.11
H_2O^-	1.15	1.50	3.31	.57	1.55	
CO_2	.00	1.10	-	2.01	5.32	
TiO_2	.08	1.70	2.67	1.81	3.60	.035
P_2O_5	.02	.10	.38	.77	.34	
MnO	0.12	.14	.34	.16	.12	.15
	100.23	-	99.96	100.77	100.38	100.19

1. Kimberlite Tuff; Buell Park, Balk (1954) New Mexico Mine and Min. Res., N. M. Inst. of Tech. Bull. 36.

2. Ave. of 8 kimberlites, So. Africa: quoted by Balk, *ibid.*

3. J. W. Dawson (1962) Basutoland kimberlites, G.S.A. Bull. 72, p. 545-560.

4. *Ibid.*

5. *Ibid.*

6. Olivine in Dunite, Peridote, Arizona. Ross, Foster, Myers, p. 707, Am. Min., v. 39, p. 693-737.

Table 18. (Cont.)

	Moses Rock					
	(7)	(8)	(9)	(10)	(11)	(12)
SiO_2	39.16	40.07	45.63	46.84	44.60	50.93
Al_2O_3	1.58	2.73	1.84	3.19	3.90	3.85
Fe_2O_3	3.34	3.18	7.76	7.23	7.90	3.71
FeO	3.65	3.33				2.82
MgO	36.97	34.05	43.07	39.80	41.00	34.76
CaO	1.14	2.10	1.33	2.45	1.78	3.00
Na_2O	.05	.08	.06	.09	0.13	.66
K_2O	.06	.08	.07	.09	-	.13
H_2O^+	11.20	11.50	-	-	-	-
H_2O^-	.85	1.02	-	-	-	-
CO_2	1.20	1.27	-	-	-	-
TiO_2	.09	.11	.10	.13	.02	.04
P_2O_5	.03	.04	.03	.05	-	.03
MnO	.09	.10	.10	.13	.15	.07
	99.47	99.70	99.99	100.00	99.48	100.00

7. Moses Rock kimberlite: Blackish-green dense kimberlite: MR-1416A.

8. Moses Rock kimberlite: Light lime-green kimberlite: MR-1416B.

9. Analysis 7 recalculated water and carbon dioxide free.

10. Analysis 8 recalculated water and carbon dioxide free.

11. Calculated composition for spinel-lherzolite (MRX-2) based on modal analysis and microprobe analysis of minerals (Anhydrous).

12. Antigorite-tremolite schist (MRX-51, Recalculated anhydrous).

The whole rock chemical analyses permit further limits to be placed on the abundance of certain minerals. The CaO content bounds the possible clinopyroxene abundance; TiO_2, the titanoclinohumite abundance; K_2O, the phlogopite content, and Al_2O_3, the pyrope abundance.

The CaO content of the kimberlite is 1.3%; the observed CaO range in kimberlite clinopyroxenes is 16 to 23%. Neglecting the CaO contributed from dolomite chips known to be present, we find a maximum clinopyroxene content is 5.3%. No other major Ca-bearing phases are known. Thus, in view of the dolomite fragments, the 3% concentration of clinopyroxene assumed in the calculations is reasonable.

If we assume all TiO_2 in the kimberlite analyses is contributed by titanoclinohumite, we can place an upper bound on the abundance of this phase. Kimberlite analyses (recalculated, volatile free) had .10 and .13 TiO_2; the TiO_2 content of the titanoclinohumite ranged between 4 and 6%. Taking an average TiO_2 content of 5%, results in a maximum clinohumite abundance of 2 and 2.6%. Other titanium-rich phases, particularly the opaque minerals, are known to exist in the kimberlite, therefore these must be over estimates. The volatile content of clinohumite is approximately 2% by weight H_2O. If no other hydrous phases are present, the assemblage would be .04% by weight. Local concentration of 1% by weight, water would require complete dehydration of a volume 25 times. The volume occupied by the reservoir rocks, a concentration of 10% water by weight would have required a volume of 250 times larger than the reservoir.

The kimberlite analyses yield .09% weight K_2O. Phlogopites, generally contain about 9% K_2O, so a maximum abundance of 1% phlogopite is implied.

The Al_2O_3 content of the kimberlite, 1.8%, is somewhat biased by included shale and siltstone fragments, however it can be used to place upper bounds on the aluminous phases in the kimberlite. Pyropic garnets contain, on the average, 23% Al_2O_3, therefore a maximum 7-8% pyrope is possible. Pyroxenes and serpentine, however, are known to be aluminous. The estimated garnet modal abundance of 3% is consistent with the chemistry of the kimberlite.

Diamond, Coesite Unobserved

The most distinctive feature of kimberlite is the presence of diamond as a characteristic member of the heavy mineral suite. The presence of diamond is significant from an economic point of view, of course, but petrologically their significance is that diamonds virtually assure that the rock containing them originated in the mantle, if the diamond crystallized is within its stability field.

A search was made for the high-pressure polymorphs, diamond and coesite, in the heavy mineral concentrate from a 200-pound sample of Moses Rock kimberlite (MR-1416A) sampled at the type locality (shown in Plate 10). None were found. The dense, non-magnetic fraction contained a suite of heterogeneous zircons, subordinate barite and and isotropic, transparent yellow mineral with very high relief and an apparent octohedral crystal form. X-ray diffraction (Photograph by W. B. Kamb) and electron microprobe analysis revealed this mineral to be a nearly iron-free sphalerite, not diamond. No coesite was observed.

Even in the Kimberley Mines, the concentration of diamond is in the part-per-million to part-per-billion range (Williams, 1932). Thus, it is quite possible that a small sample would not encounter diamond, particularly large coarse-grained ones. It seems unlikely that large diamonds would have gone unnoticed on the Navajo Reservation because the Navajos are remarkably astute observers of their natural surroundings. Garnets are abundant and well known locally. Diamond was not observed during detailed mapping.

Several explanations are possible. First, the Moses Rock kimberlite formed outside the pressure-temperature stability field of diamond; a conclusion at odds with data presented later in this report; second, diamond is present but unobserved (believed to be unlikely); third, kimberlite formed within the pressure-temperature stability field of diamond but the other local conditions were not consistent with its formation; for example, low carbon concentration or high oxygen pressure.

Serpentine

About 80 to 90% of the kimberlite by volume is serpentine or similar hydrated ferromagnesian sheet structure minerals. Serpentine, talc and possibly chlorite were identified by x-ray diffraction of a whole rock sample. The fine-grained groundmass comprises about 50% of the rock. The rest is psuedomorphic alteration products of olivine and orthopyroxene.

There are some crucial questions regarding the origin of these occurrences of serpentine which bear heavily on the problem of the genesis of the kimberlite. Either, 1) serpentine was present in the reservoir prior to eruption, 2) serpentinization of the material occurred during the eruption, 3) serpentinization occurred after it was emplaced at its present site, or 4) part or all of the serpentinized material was derived from the vent walls and mixed with unserpentinized fragments. It is clear that the serpentine which is psuedomorphic after olivine and orthopyroxene was derived by hydration of those minerals (Plate 21C). The question is, where and at what stage of emplacement? First, was the olivine present in the reservoir? If so, was serpentine present as a stable phase in the reservoir also and were these fragments transported to the surface with little change? Or were the olivine grains transported from depth emplaced and altered in their present site? Or did they originate as unaltered olivine, to be altered (or partially altered) during transport, with little subsequent alteration.

Probably even more important is the origin of the groundmass serpentine. The same questions apply as above, but, in addition, could this fine-grained groundmass-serpentine be completely derived from the vent walls?

A reconnaissance microprobe investigation of the composition of the serpentine in each textural mode produced puzzling results. In a polished thin section of kimberlite, partial chemical analyses were obtained from an olivine grain, psuedomorphic serpentine derived from this grain, a nearby orthopyroxene grain, psuedomorphic serpentine after this pyroxene and several points in nearby fine-grained groundmass serpentine (Table 19). Several differences between the orthopyroxene and olivine are useful in considering the serpentine compositions. First, the orthopyroxene contains more silica but also has a significant Al_2O_3 content, about 4.4 wt %. If serpentinization had occurred without significant chemical exchange then there should be a significant difference in the composition of the serpentine produced from olivine as opposed to that formed from the orthopyroxene.

The analyses, however, indicate that the serpentine produced from the same olivine grain is by no means homogeneous, rather varies widely in its alumina and silica content. It appears that silica and alumina were highly mobile in the system because the serpentines differ so drastically from the parent minerals from which they were produced (in Al_2O_3 content and Mg/Fe ratio, for example, Figure 40). Because the serpentine compositions are so variable there is no suggestion of equilibrium. The groundmass composition is consistent with serpentine produced from a rock with pyroxene-olivine ratio, ranging from 3:1 to about 5:1.

The kimberlite whole-rock chemical analyses and the serpentine-rich schist also are intermediate between olivine and orthopyroxene in bulk composition.

Table 19. Partial Chemical Analyses of Minerals from Polished Thin Section of Moses Rock Kimberlite (MR-1416A), Including Analyses of Psuedomorphic Serpentine and Unserpentinized Parent Minerals and Groundmass Serpentine

	Olivine	Olivine	Psuedomorphic Serpentine from Olivine		Opx	Serp After Opx	Groundmass Serpentine	
	4	3	17	18	21	21	19	20
SiO_2	41.6	42.4	38.4	41.0	55.8	44.3	39.2	41.2
Al_2O_3	0.00	0.00	0.01	1.67	4.37	1.71	.56	.76
CaO	0.00	0.00	.05	0.03	0.69	0.03	.08	.02
FeO	7.65	7.54	8.17	4.62	6.27	5.27	6.44	6.49
MgO	49.9	49.8	35.9	38.0	32.7	36.8	36.8	36.4
Na_2O	0.00	0.00	0.02	0.02	0.13	.01	.02	.03
	99.1	99.7	82.5	85.4	99.9	88.1	83.1	84.9

Analyses of Serpentine
Recalculated to 100%
on Anhydrous Basis

SiO_2			46.6	48.1		50.3	47.2	48.5
Al_2O_3			.01	1.96		1.94	.67	.90
CaO			.06	.04		.03	.10	.02
FeO			9.90	5.41		5.97	7.75	7.65
MgO			43.5	44.5		41.7	44.3	43.0
Na_2O			.02	.02		.01	.02	.04

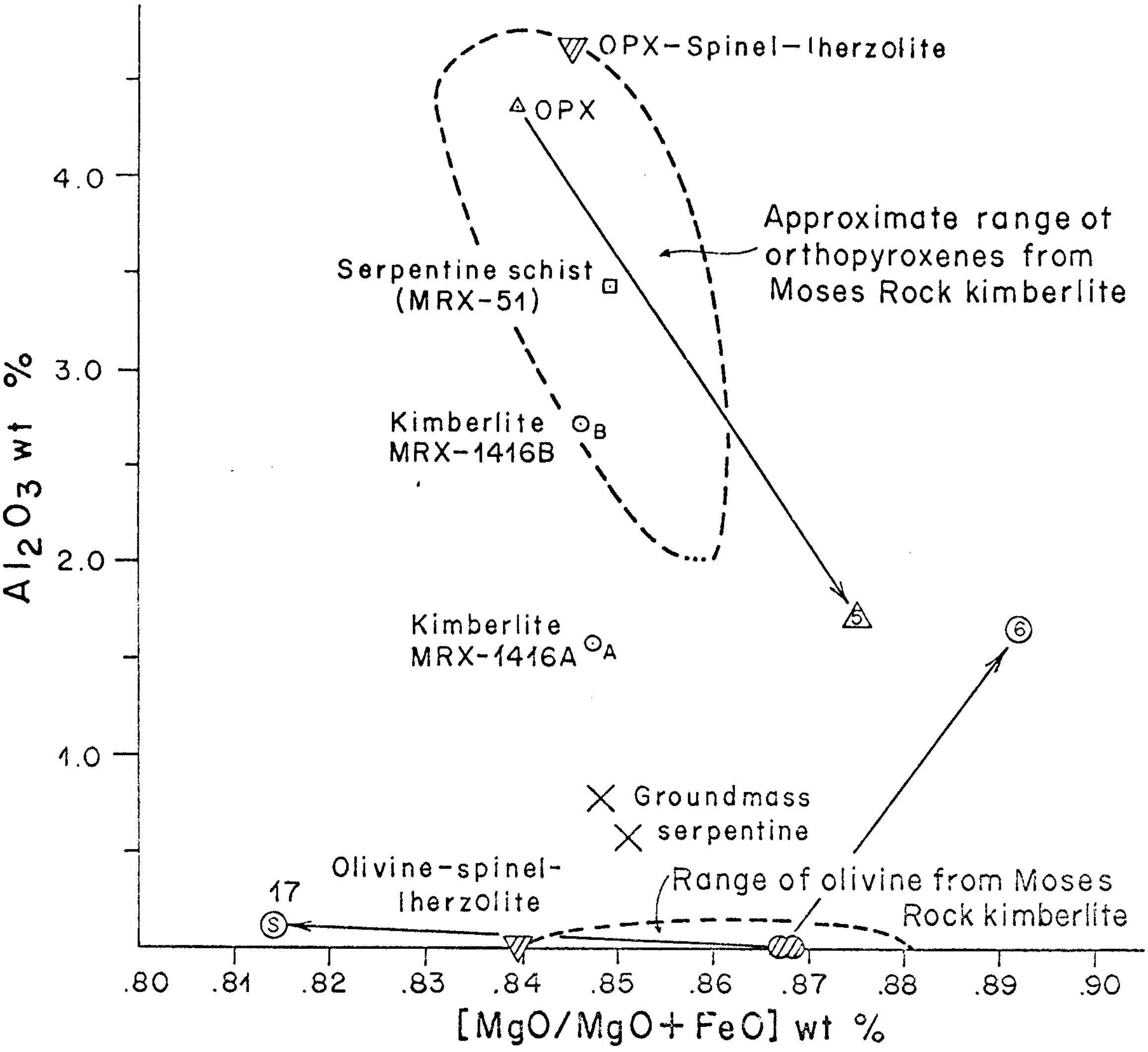

Figure 31. Al_2O_3 content and MgO/MgO+FeO ratio in olivine, orthopyroxene, psuedomorphic serpentine and groundmass serpentine in kimberlite (MR-1416A). Also shown are data from whole-rock analyses of kimberlite (MR-1416A, MR-1416B) and serpentine-schist (MRX-51)

To sum up the observations: 1) serpentine in the kimberlite occurs in two distinct textural modes, a) groundmass, b) pseudomorphs after olivine and orthopyroxene, 2) alteration of olivine grains is pervasive; alteration of orthopyroxene is slight, 3) alteration products of both olivine and pyroxene approach nearly stoichiometric serpentine, which means SiO_2 and MgO were mobile (as was Al_2O_3), 4) no severe volumne changes or dilational effects are observed; optical continuity is preserved, 5) in crushing it was noted that serpentine grains with olivine commonly survived intact, suggesting that the grains may not be mechanically delicate, which suggests that partially altered olivine might survive transport, 6) very little alteration occurred at wall-rock contacts, so apparently no gross chemical mobility occurred across the contacts, at the level now exposed, 7) the groundmass serpentine appears to be intermediate in composition between kimberlite olivine and orthopyroxene, and is quite unlike the serpentine-schist (MRX-51), especially in terms of its aluminum content.

What, then, can be said about the origin of the various serpentines in the kimberlite? The groundmass serpentine is probably <u>not</u> comminuted serpentine-schist derived from the vent walls. The most likely source for the groundmass serpentine appears to be the kimberlite olivine and orthopyroxene, in a ratio of 3:1 to 5:1.

The inferred conditions of formation for the kimberlite clinopyroxenes preclude the existence of serpentine as a stable phase in the reservoir.

Either the serpentinization occurred during the eruption or after the kimberlite was emplaced, either immediately after or long after, perhaps by groundwater action.

The apparent lack of deformation or local volume increase suggests that the serpentinization was either iso-volumetric if it took place at the present site, or it took place before emplacement at the surface. The lack of alteration of the contact rocks precludes gross mobility of constituents across the dike contact at the present site. This does not rule out local movement of these materials within small volumes.

If water as a phase was present in the system at the time immediately after the kimberlite was emplaced, interstitially between unserpentinized mineral fragments, then serpentinization could occur without significant bulk expansion. If water was introduced into the system from outside, then a significant expansion would be required, approximately equal to the specific volume of the water introduced (Hess, 1954). This latter possibility appears to be precluded by the lack of strain exhibited in the texture.

It does not seem to be possible to decide between the remaining alternatives. It seems equally likely that 1) some alteration of olivine and orthopyroxene took place during transport and prior to emplacement at the present site, or 2) that serpentine was produced _in situ_ but from water which was introduced simultaneously with the particulate fragments which were altered to serpentine shortly after their emplacement.

It is suggested that the groundmass serpentine in the kimberlite is produced in part by reaction of comminuted olivine and orthopyroxene from the reservoir with water, which was also present in the reservoir, probably during transport toward the surface as the medium expanded and cooled and immediately after emplacement at its present site. Subsequent alteration has undoubtedly occurred.

Microprobe Investigations of Kimberlite Minerals

Introduction

Chemical analyses of mineral grains in kimberlite and other rocks permit some discussion of their origin and relationship to each other. About 400 analyses for 9 major elements were obtained for olivine, orthopyroxene, clinopyroxene, garnet, spinel, clinohumite and some other mineral phases. Of particular interest are comparisons between minerals in kimberlite when compared to minerals in the dense rock fragments and to inclusions in pyropic garnets.

These investigations show that the minerals in kimberlite appear to be closely related to minerals in two distinct, but possibly overlapping, assemblages; spinel-lherzolite and garnet-lherzolite. A single fragment of spinel-lherzolite (MRX-2) was observed in the Moses Rock dike; the garnet-lherzolite assemblage has been reconstructed on the basis of mineral inclusions observed within chrome-rich pyropic garnets.

Of particular interest are the calcium-rich pyroxenes because their composition is sensitive to the conditions of their formation. Applying experimentally determined phase relations to the natural minerals from the Moses Rock dike provides a means of estimating the conditions of formation of these phases. Estimates of the conditions of crystallization of the Moses Rock minerals range from just below the base of the crust to about 150 kilometers. Temperatures indicated are near 900° C, below the liquidous temperatures in ultramafic systems with very low K_2O contents.

The occurrence of titanoclinohumite in the garnet-peridotite assemblage is possibly of great importance as a plausible site for water at high pressure and modest temperature in the lower parts of the upper mantle.

More data were gathered than can be reasonably presented here, so summaries of some of the interesting compositional relations will be made.

In the following pages the mineral investigations will be reviewed. First, garnets observed in the kimberlite will be described. Although garnets similar to those in crystalline rock fragments are observed in the kimberlite, a deep wine-colored, gem-quality, chrome-rich pyrope is the most abundant type. These pyropes were not observed in any fragment. An investigation of these pyropic garnets revealed that mineral grains were included within them. Before proceeding on to describe the compositions of the other minerals in kimberlite, the results of the microprobe investigation of these inclusions will be presented. The population of inclusions suggests that a garnet-lherzolite assemblage existed somewhere, even though no fragments were observed.

Following the discussion of the garnets and inclusions in the garnets, the observations of each mineral group will be reviewed. The compositions of these minerals can be compared with minerals from the dense fragments and the mineral inclusions in pyrope. It will be seen that the kimberlite minerals generally fall either into two distinct groups, one similar to spinel-lherzolite minerals, the other like inclusions in pyrope (garnet-lherzolite?), or their compositions form a continuum between these two extremes.

Garnet

The garnet population in the kimberlite is heterogeneous. Refractive index data (Figure 32) extends previously published data on garnets from Garnet Ridge and Green Knobs to the Moses Rock dike. O'Hara and Mercy (1966) found a heterogeneous suite of garnets in ant hills, including gem-quality pyrope-rich specimens, which varied in color from pink to orange to deep purplish-burgundy wine-colored. They report chemical analyses of these garnets to be Cr_2O_3-rich, typical of kimberlite garnets elsewhere in the world.

Partial chemical analyses of thirty-five hand-picked garnets from heavy mineral concentrates from Moses Rock kimberlite (MR-1416A), confirms the conclusions drawn from optical data. The garnet population in the kimberlite is heterogeneous. Some garnets show clear affinity to the garnets from the eclogite; others to the garnets from the various metamorphic rocks. Yet another group of pyrope-rich grains is similar to the large, gem-quality, wine-colored specimens collected from the ant hill. This latter group is the most abundant.

A summary of the composition of the garnet population from kimberlite (Figure 33), when compared to garnets from crystalline rock fragments in the Moses Rock dike shows that many specimens were apparently derived from metamorphic rocks or eclogite. The chrome-rich

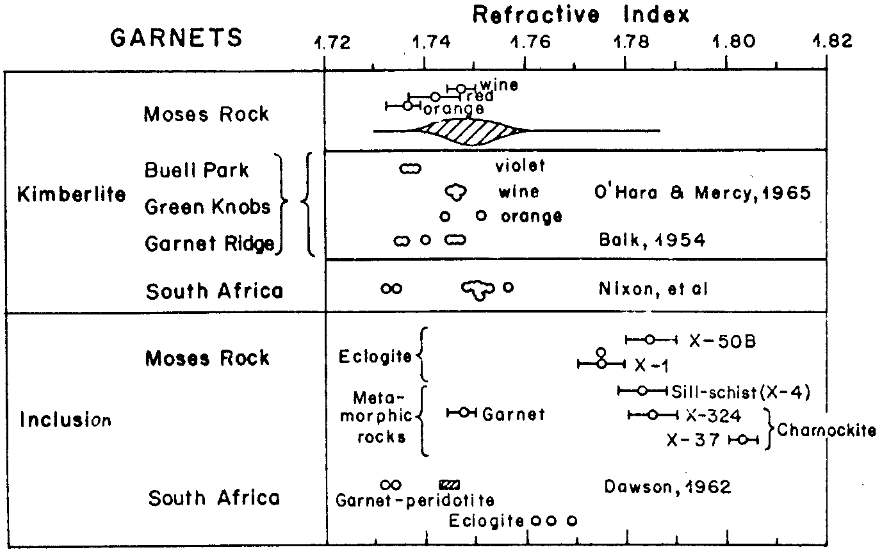

Figure 32. Summary of refractive index data for garnets from kimberlite and crystalline rock inclusions in the Moses Rock dike

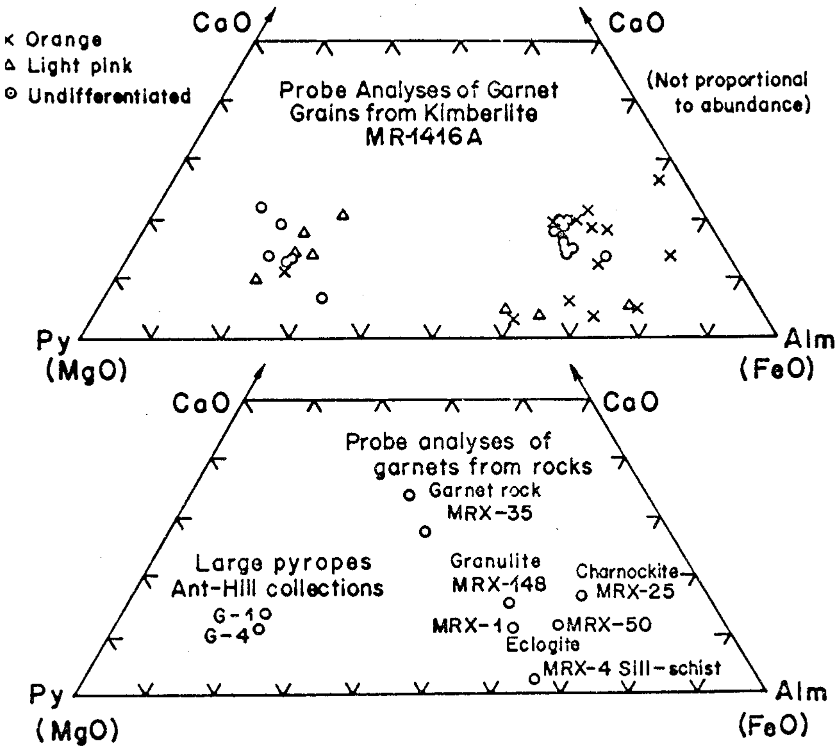

Figure 33. Comparison of garnet composition from Moses Rock kimberlite (MR 1416A) and from various crystalline inclusions in the Moses Rock dike

pyropic-garnet, however, appear to be unique to the kimberlite.

Inclusions in Pyrope

Perhaps the most interesting specimens collected at the Moses Rock dike were large pyrope garnets from ant hills, where they are highly concentrated at the surface in the apron of coarse mineral grains ejected from below by the ants. In a thin section of one large garnet specimen, a small grain of orthopyroxene was observed which lead to a search for more inclusions in a large population of pyropes. The result was the discovery of inclusions of olivine, pyroxene, clinohumite, rutile, geikielite and an unidentified sheet structure believed to be mica or chlorite.

Photomicrographs on the following page of a representative suite of inclusions shows the typical form and setting of these inclusions. The grains generally have ellipsoidal shapes, and commonly are surrounded by a radiating curved array of fractures or a birefringent halo. Both effects apparently result from stresses produced by differential volume change of inclusion and host in response to transport to near-surface pressure and temperature conditions from a different set of conditions at depth in which they were in mechanical equilibrium. Stresses arise from the differences in thermal expansion coefficients and compressibilities of the two phases. This problem has been discussed by Rosenfeld and Chase (1961).

The garnets are commonly quite homogeneous and the inclusions, while not always homogeneous, are not severely unzoned (Figure 34).

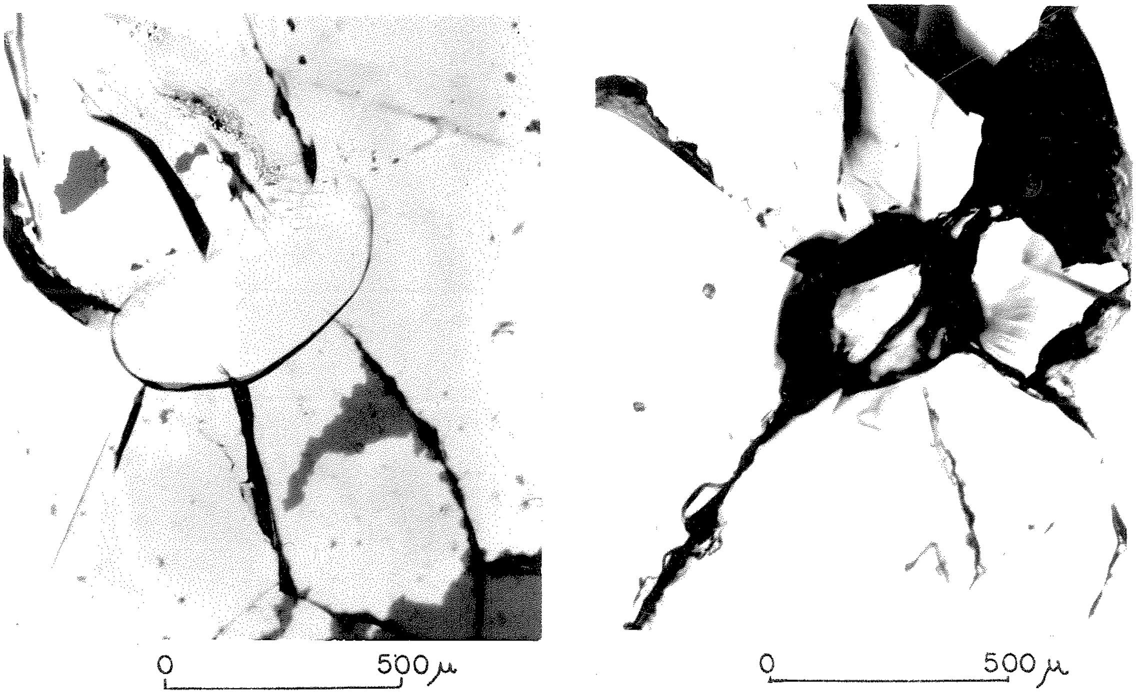

PG1B67 Orthopyroxene
Ordinary light

PG-9 Chrome diopside
Ordinary light

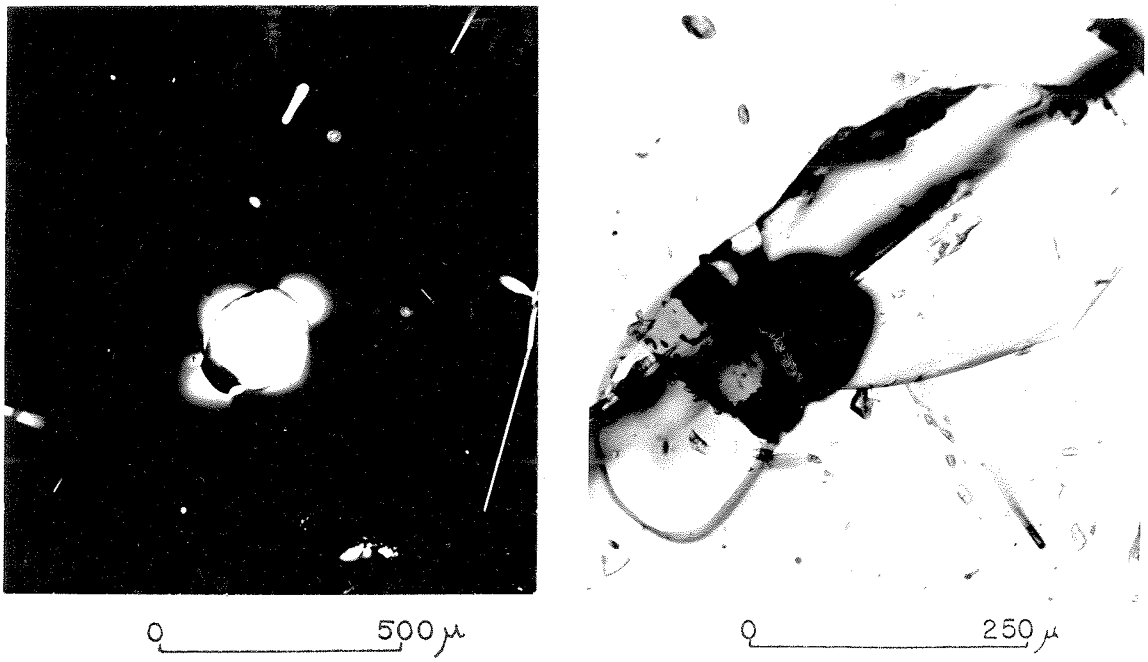

PG-24 Olivine
Polarized light

PG-2 Olivine with clinohumite,
geikielite and mica (?)
below surface
Ordinary light

Plate 22. Photomicrographs of inclusions in pyropic-garnets
(Compositional data summarized in Table 20)

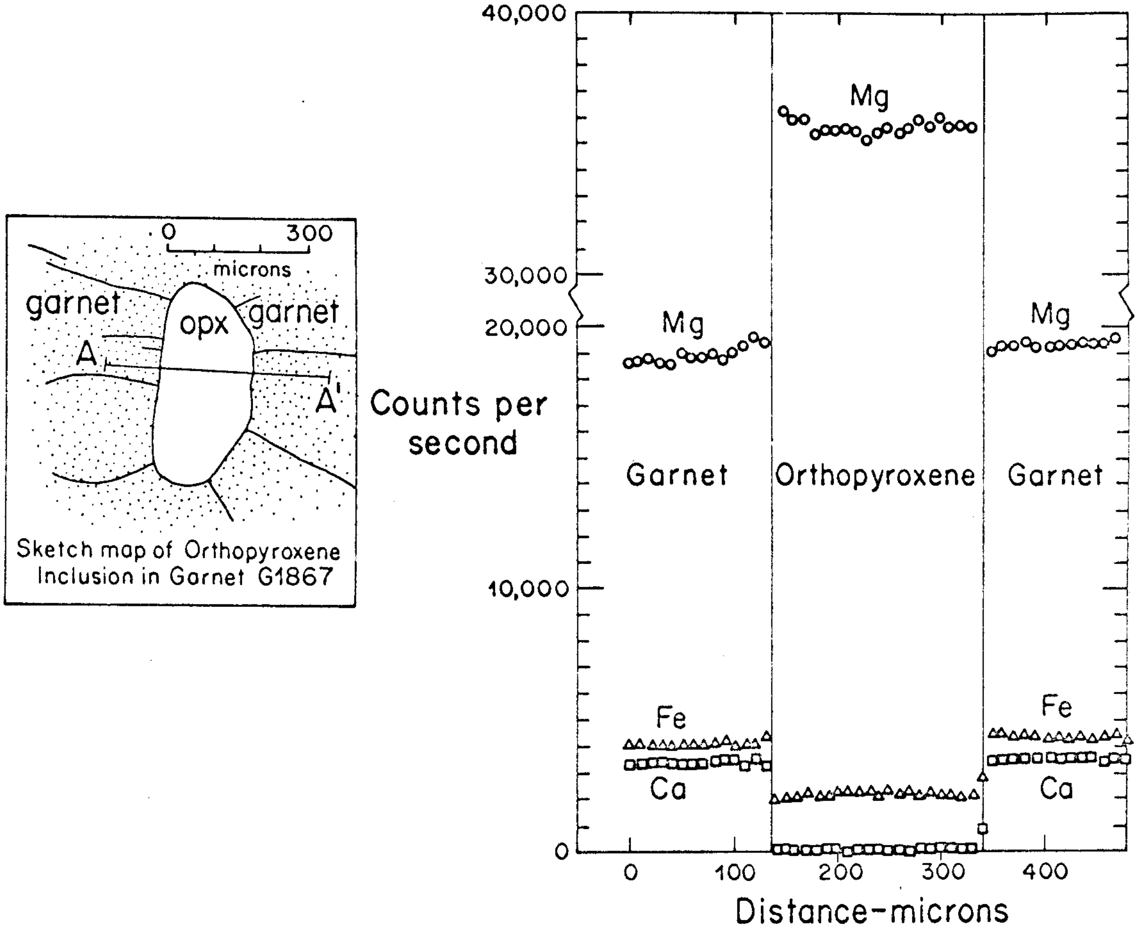

Figure 34. Microprobe traverse of orthopyroxene inclusion in garnet (G1B67) showing absence of significant zoning

The compositions of the host garnets and the inclusions are rather uniform from grain to grain. Compositional data are summarized on the following page. The garnets are typically near the composition Mg:Fe:Ca=69:19:12 and have Cr_2O_3 contents between 1 and 3%. Olivine, orthopyroxene, clinopyroxene and clinohumite have Mg/Mg+Fe ratios near 94. The alumina content of the orthopyroxene is low, between 0.5 and 1.1; in the clinopyroxenes, the alumina (or combined R_2O_3) in excess of jadeite-type ($NaRSi_2O_6$) molecules is modest. The clinopyroxenes are chrome diopsides, Cr_2O_3 between 1.5 and 2% with some jadeite and R_2O_3 (Tschermak) solid solution. The iron content of the clinopyroxenes is modest. Rutile is a common inclusion but it does not occur as the abundant needle-like exsolution rods so well developed in more iron-rich garnets and in the eclogite garnets. Also, analyses of the rutile commonly contain several percent Cr, Fe and Mg. An opaque phase, Ti-rich ilmenite (geikielite) is present which contains a considerable amount of Mg. Finally, titanoclinohumite is present within pyropes, a textural setting which virtually precludes its origin as a near surface alteration mineral.

Inclusions of clinopyroxene were observed in two orange garnets (OG-11, OG-16). These garnets are more iron-rich and contained very little chromium. The clinopyroxenes were also chrome-poor. These garnets may be gradational to eclogitic types and are not considered to be part of the pyrope population.

The suite of inclusions described above constitutes the mineral assemblage of a garnet-lherzolite. Thus, although not represented at the surface as a discrete rock, it suggests the possibility that

Table 20. Summary of Compositional Data on Inclusions Observed in Pyropic Garnets from the Moses Rock Dike

	Host Garnet		Inclusions	
	Mg:Fe:Ca	Cr_2O_3		
PG-2	70:18:12	1.7	olivine	Mg/Mg+Fe=94
			clinohumite	Mg/Mg+Fe=93; TiO_2=6.8
			ilmenite	
			mica or chlorite	(not exposed at surface)
PG-24	68:19:13	1.5	olivine	Mg/Mg+Fe=93
PG1B67	68:18:13	2.0	orthopyroxene	Mg/Mg+Fe=94; Al_2O_3=1.1; Cr_2O_3=0.3
PG-23	69:19:12	2.3	orthopyroxene	Mg/Mg+Fe=94; Al_2O_3=0.5; Cr_2O_3=0.1
			ilmenite(geikielite)	TiO_2=56; FeO=27; MgO=15; Cr_2O_3=1
			rutile	TiO_2=95.0; Cr_2O_3=2.7; FeO=1.5; MgO=0.9
PG-6	65:24:11	1.4	ilmenite	TiO_2=57; FeO=33; MgO=12; Cr_2O_3=1
PG-3	69:19:12	3.0	rutile	TiO_2=93.3; Cr_2O_3=5.3; FeO=1.1

			Ca-Rich Pyroxene Inclusions					
			Ca/Ca+Mg	Al_2O_3	Cr_2O_3	Na_2O	FeO	Fe/Fe+Mg
PG-4	68:18:14	2.4	.498	2.3	1.3	1.2	1.3	.959
PG-5	68:20:12	1.6	.495	3.0	1.2	2.4	2.6	.917
PG-9	69:19:12	2.7	.481	2.6	1.7	2.3	1.8	.941
OG-11	46:32:22	.04	.507	1.7	0.1	1.5	2.7	.916
			.505	1.7	0.1	1.7	2.6	.917
OG-16	56:35:09	.35	.484	6.7	0.5	4.7	3.2	.883

garnet peridotites exist at depth.

Olivine

Partial chemical analyses of 40 olivine grains in kimberlite were obtained. The (Mg/Fe+Mg) atom ratios range from 89 to 95, with modal values being about 92 (Figure 35). Traverses of grains revealed Ca, Mg, Fe variations of about 2 relative % across millimeter-sized grains, so the olivine is essentially unzoned.

Olivine grains in the Moses Rock kimberlite range from fo_{89} to fo_{95}. Olivine in the spinel-lherzolite is fo_{90}; olivine inclusions in the pyrope-rich garnets is fo_{93-94}. The olivine population in kimberlite spans the compositional range between the olivines observed to coexist with spinel and garnet.

Olivines from South African kimberlites have similar compositions to those in the Moses Rock kimberlite. Dawson (1962) reports fo_{89-92} from Basutoland pipes; Nixon, von Knorring and Rooke (1963) report kimberlite olivines of composition fo_{90} or more, in the ultrabasic inclusions in the South African pipes, but olivines of higher Fe/Mg ratio are commonly found in the kimberlite.

Orthopyroxene

Partial chemical analyses of 39 orthopyroxene grains separated from kimberlite (MR-1416A) show that the range of (Mg/Mg+Fe) atom ratios is 90 to 93 (Figure 36). The Al_2O_3 content ranges up to about 5% by weight. There appears to be no apparent correlation between (Mg/Fe+Mg) ratio and Al_2O_3 content (Figure 37).

Orthopyroxenes similar in composition to those in spinel-lherzolite

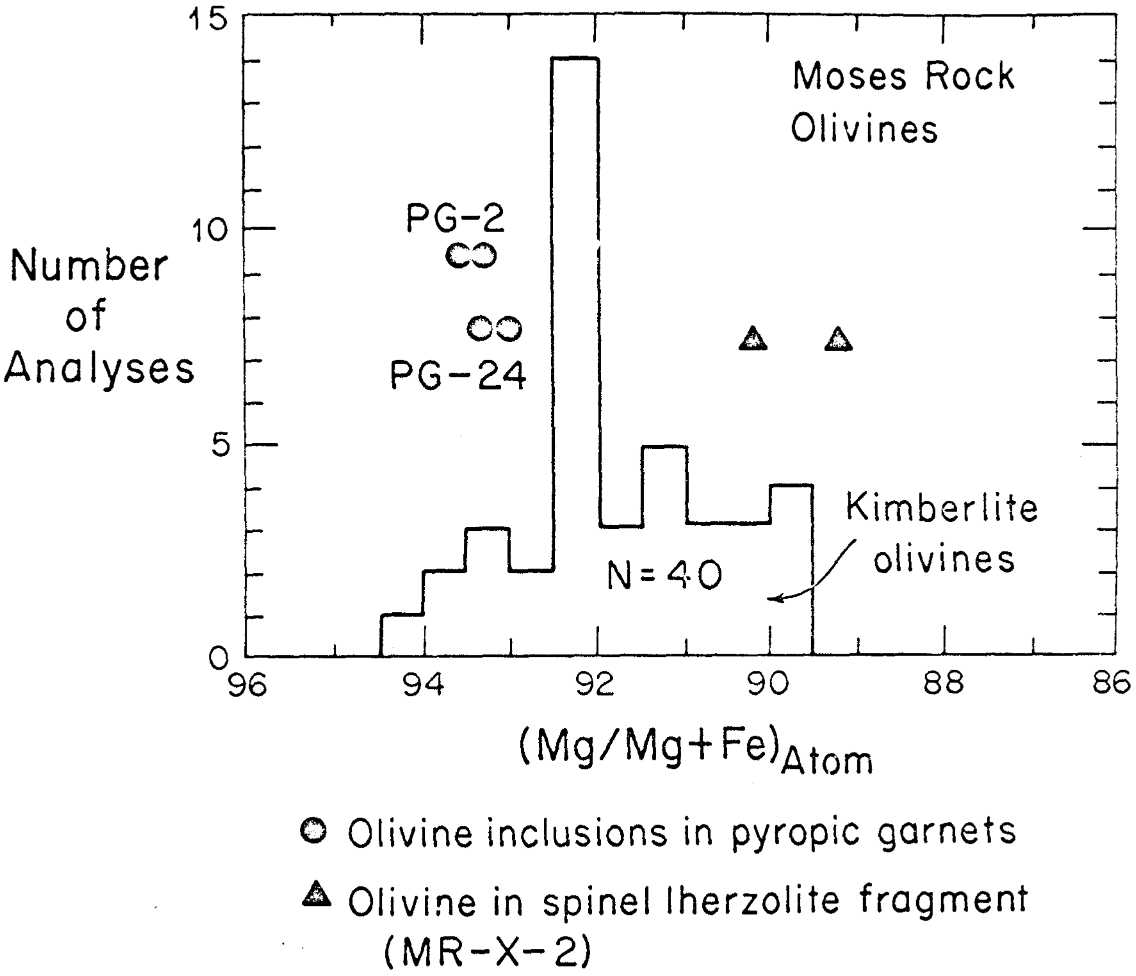

Figure 35. Mg/Mg+Fe ratios of kimberlite olivine grains and olivines from associated rocks and minerals

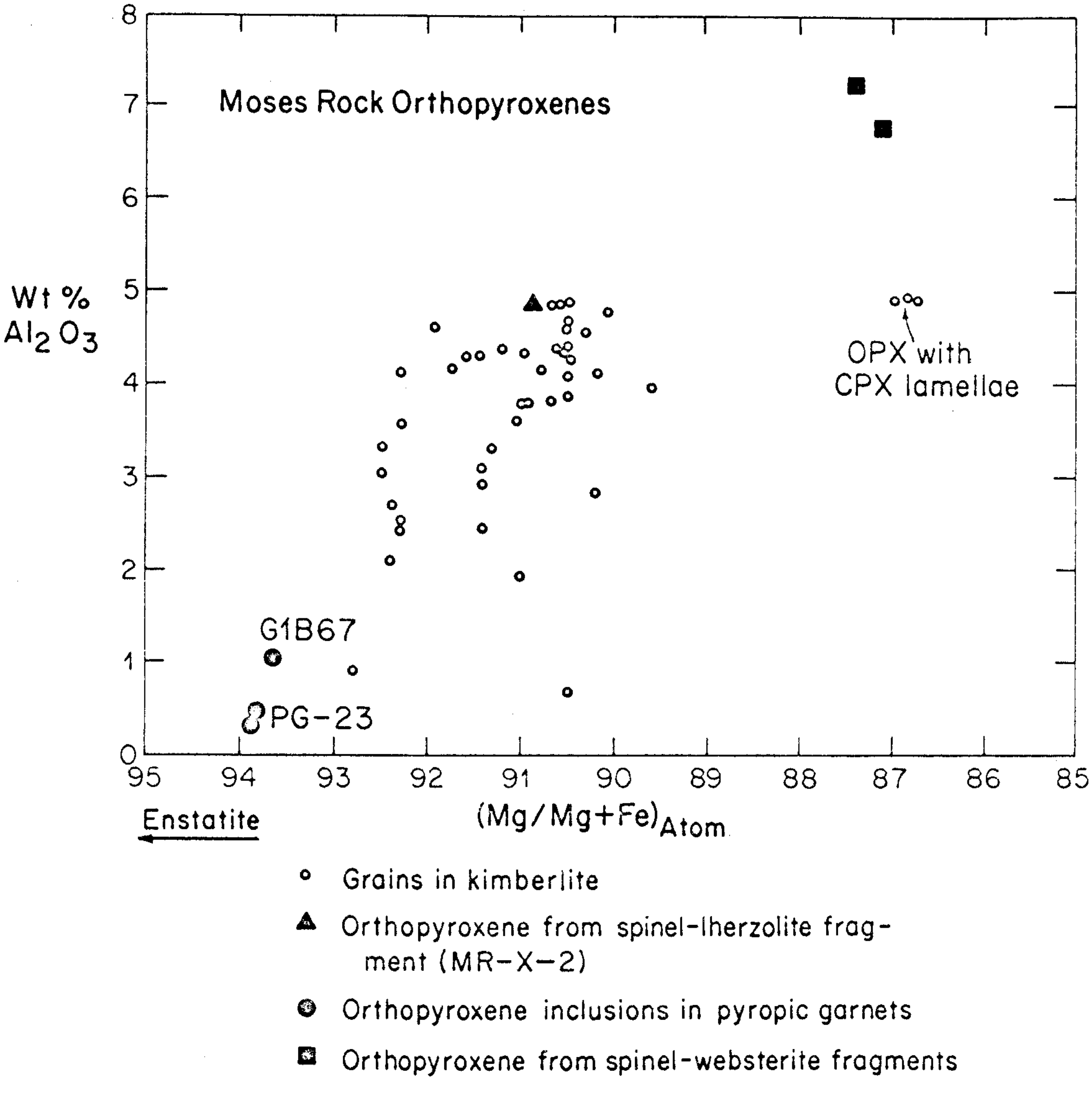

Figure 36. Plot of Mg/Mg+Fe ratio against Al_2O_3 content for kimberlite orthopyroxenes and orthopyroxenes from associated rocks and minerals

(MRX-2) are common; kimberlite orthopyroxenes similar to the orthopyroxene inclusions in the pyropic garnets are not common. Thus, nearly all the orthopyroxenes have a compositional affinity to spinel-lherzolite, high alumina contents and low Mg/Mg+Fe ratios. This suggests that if a garnet peridotite does exist at depth, that it may be depleted in orthopyroxene.

Minerals analysed were selected from 4 different separations to cover the spread of high and low density and magnetic susceptibility, so it is believed that no masking of certain compositions was introduced artificially. In order to confirm this, 10 additional grains were picked from the most magnesian fraction (which in this case was the most magnetic because of the compensating effect of chromium). No low-aluminum specimens were observed. Furthermore, exsolved calcium-rich pyroxene lamellae of the order of 10 microns wide were observed in several grains. Their compositions were similar to the spinel-lherzolite type clinopyroxenes, and virtually no zoning was observed in traverses, taking 3 micron steps. More iron-rich grains were observed, however, extending the (Mg/Fe+Mg) range to .87.

Clinopyroxene

Partial chemical analyses of 37 calcium-rich pyroxenes from kimberlite (MR-1416A) were obtained. If the data are plotted on a diagram with Al_2O_3 against Ca/Ca+Mg ratio, it is immediately apparent that these minerals fall into two groups (see Figure 37). One group, characterized by high alumina contents and Ca/Ca+Mg ratios commonly greater than .50, is similar in composition to clinopyroxenes in the spinel-lherzolite fragment (MRX-2), and also to a clinopyroxene grain observed intergrown with a spinel. The other group, with low alumina contents and Ca/Ca+Mg ratios below .50, is similar to those clinopyroxene inclusions in pyropic garnets. The ratio of clinopyroxenes similar to those associated with spinel relative to those with garnet is about 2 to 1.

Compared to clinopyroxenes in the websterite, eclogite and clinopyroxenite, those in the kimberlite have much lower solid solution of jadeite molecule.

Compared to the South African kimberlite clinopyroxenes, those from the Moses Rock kimberlite are not as iron-rich (Figure 38), although the comparison is complicated by the uncertainty in Fe^{+3}/Fe^{+2} ratio. Some of the Moses Rock kimberlite clinopyroxenes are much more aluminous than the South African ones (Figure 39).

There is a rough inverse correlation between chromium and aluminum (Figure 40). Alumina content is apparently independent of Na_2O, however there may be some correlation between Na_2O and chrome content. The chromium-soda correlation seems best developed in the group clinopyroxenes with low alumina content, and is apparently uncorrelated in the group with high alumina content.

The (Ca/Ca+Mg) ratio of the kimberlite clinopyroxenes is of particular interest because of the sensitive thermometer in the enstatite-diopside system, provided by the diopside solvus (Boyd and Davis, 1964; Davis and Boyd, 1966). In order to use these diagrams, it is necessary to assume that clinopyroxene coexisted in equilibrium with orthopyroxene. Boyd has noted that in the South African occurrences of ultrabasic fragments in kimberlite, that orthopyroxene is commonly

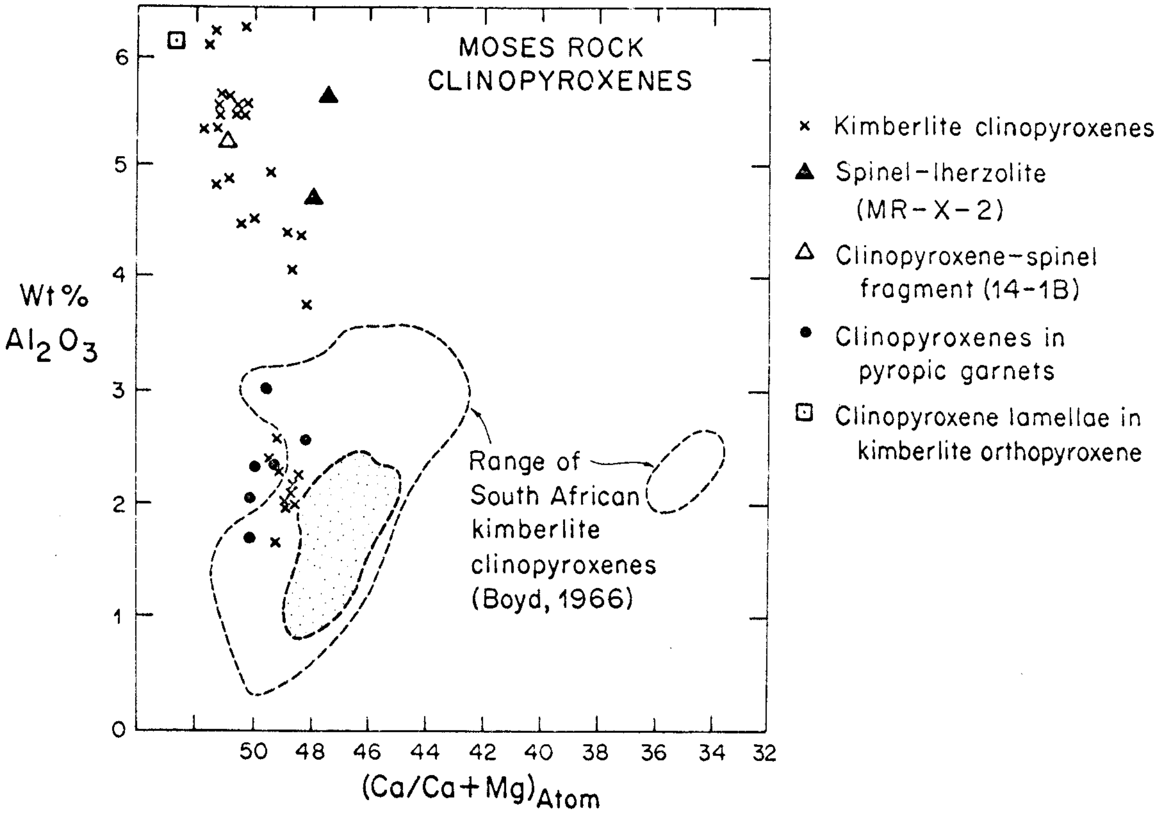

Figure 37. Plot of Ca/Ca+Mg ratio against Al_2O_3 content for kimberlite clinopyroxenes and clinopyroxenes from associated rocks and minerals

found without clinopyroxene, but clinopyroxene is essentially always accompanied by orthopyroxene. In the suite of heavy minerals from the kimberlite at Moses Rock, orthopyroxene is more abundant than the clinopyroxene by about a factor of 5.

A comparison of Ca/Ca+Mg ratios of the South African and Moses Rock clinopyroxenes (Figure 41) suggests that most of the Moses Rock kimberlite clinopyroxenes formed at somewhat lower temperatures than most of those from South Africa. The maximum formation temperature suggested for the Moses Rock pyroxene is approximately 950° C. However, since their alumina content is fairly high, this temperature estimate may be too low because O'Hara has shown that Al_2O_3 extends the miscibility gap in the enstatite-diopside system (Boyd, 1966). Thus, the crystallization of these clinopyroxenes perhaps occurred over a range of temperatures, with a maximum at perhaps 1000° C.

The conditions of crystallization of these clinopyroxenes can be inferred by applying the diopside-enstatite thermometer just described and the solid solution relations in the system diopside-enstatite (O'Hara and Yoder, 1967). These results will be developed later.

To sum up, at Moses Rock the kimberlite clinopyroxenes fall neatly into two groups, one like spinel-lherzolite clinopyroxenes, the other like inclusions in pyrope garnet. They are compositionally distinct from clinopyroxenes in eclogite, websterite and clinopyroxenite fragments.

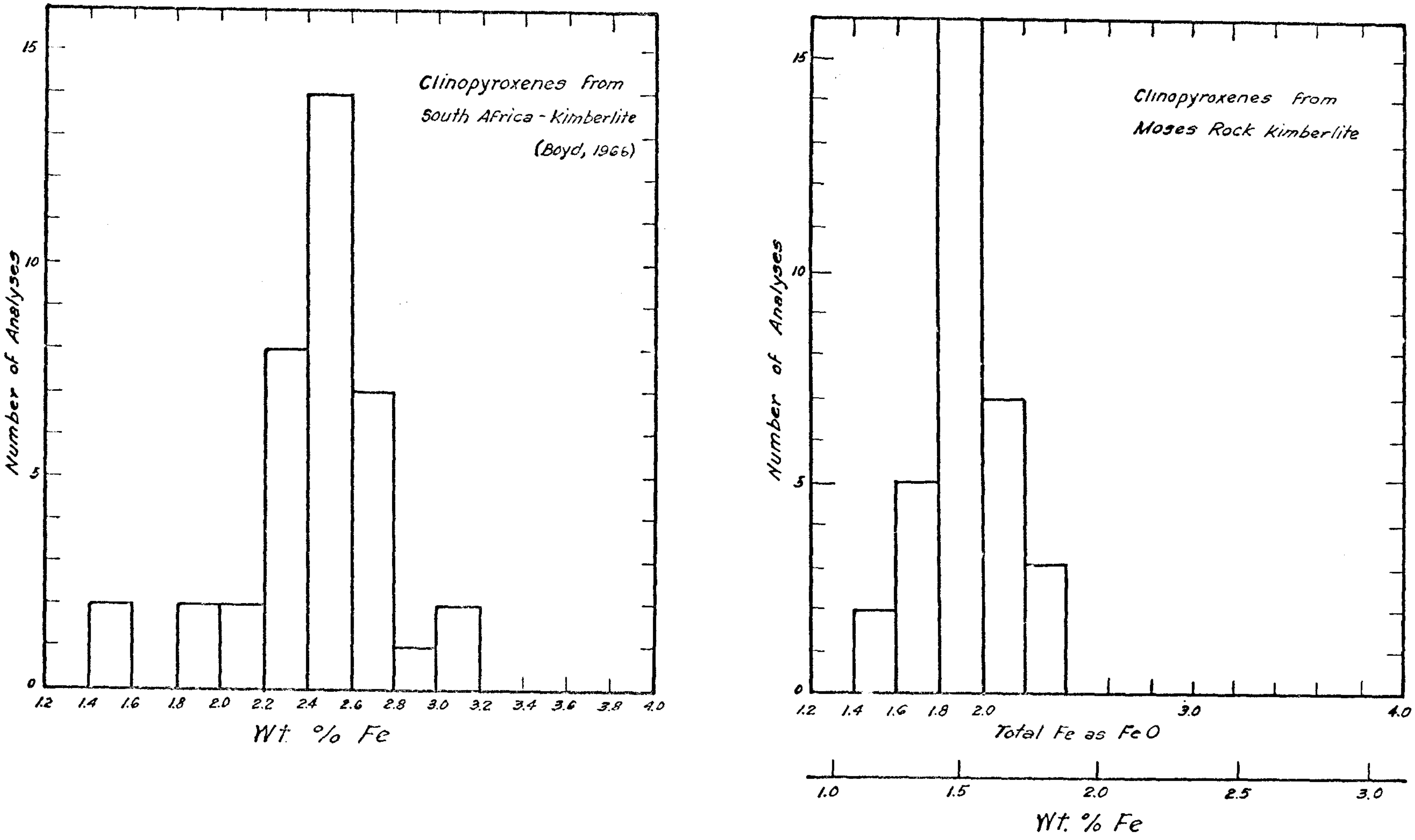

Figure 38. Comparison of iron content of clinopyroxenes from South African and Moses Rock kimberlite

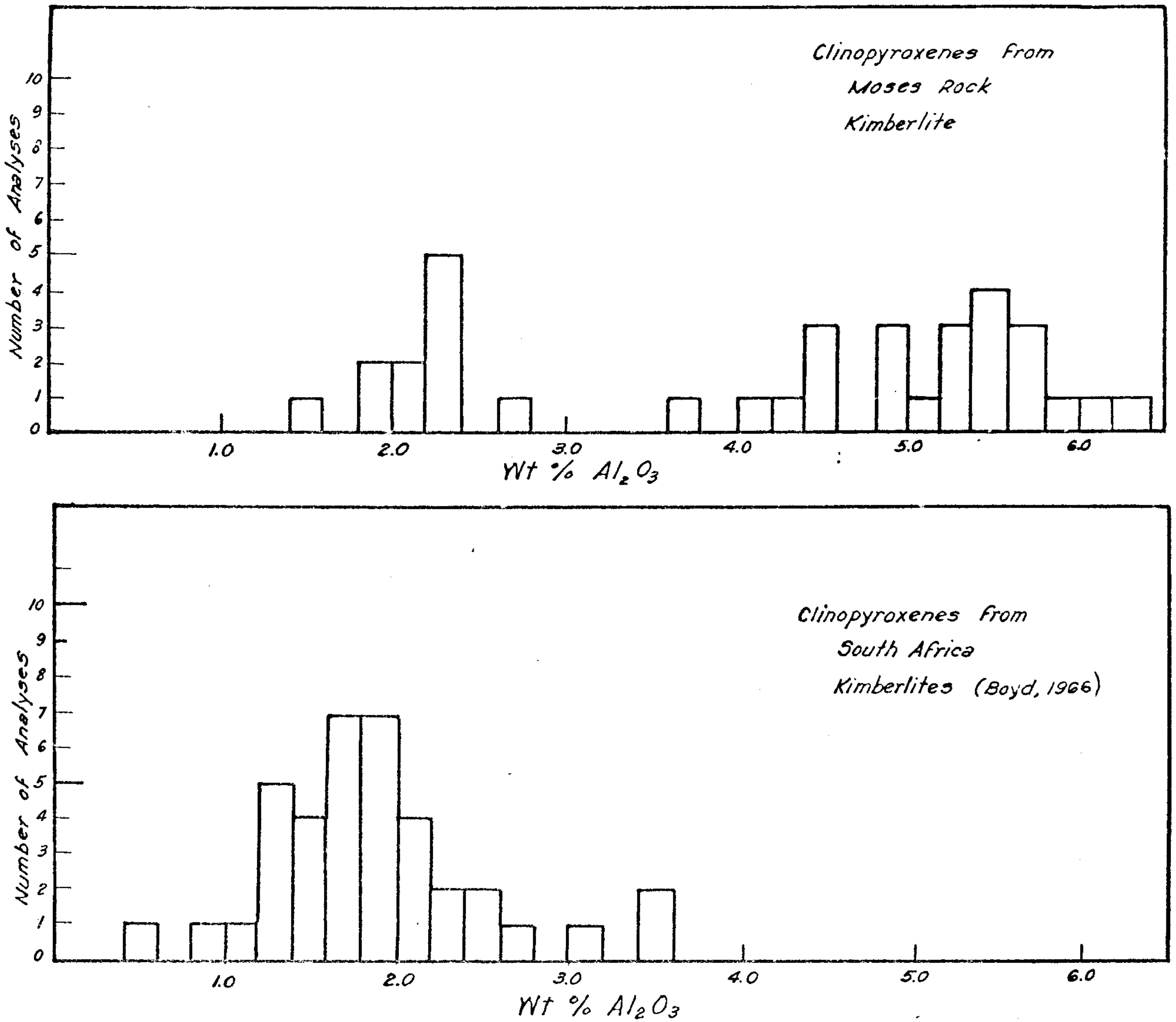

Figure 39. Comparison of alumina content of clinopyroxenes from South African and Moses Rock clinopyroxenes

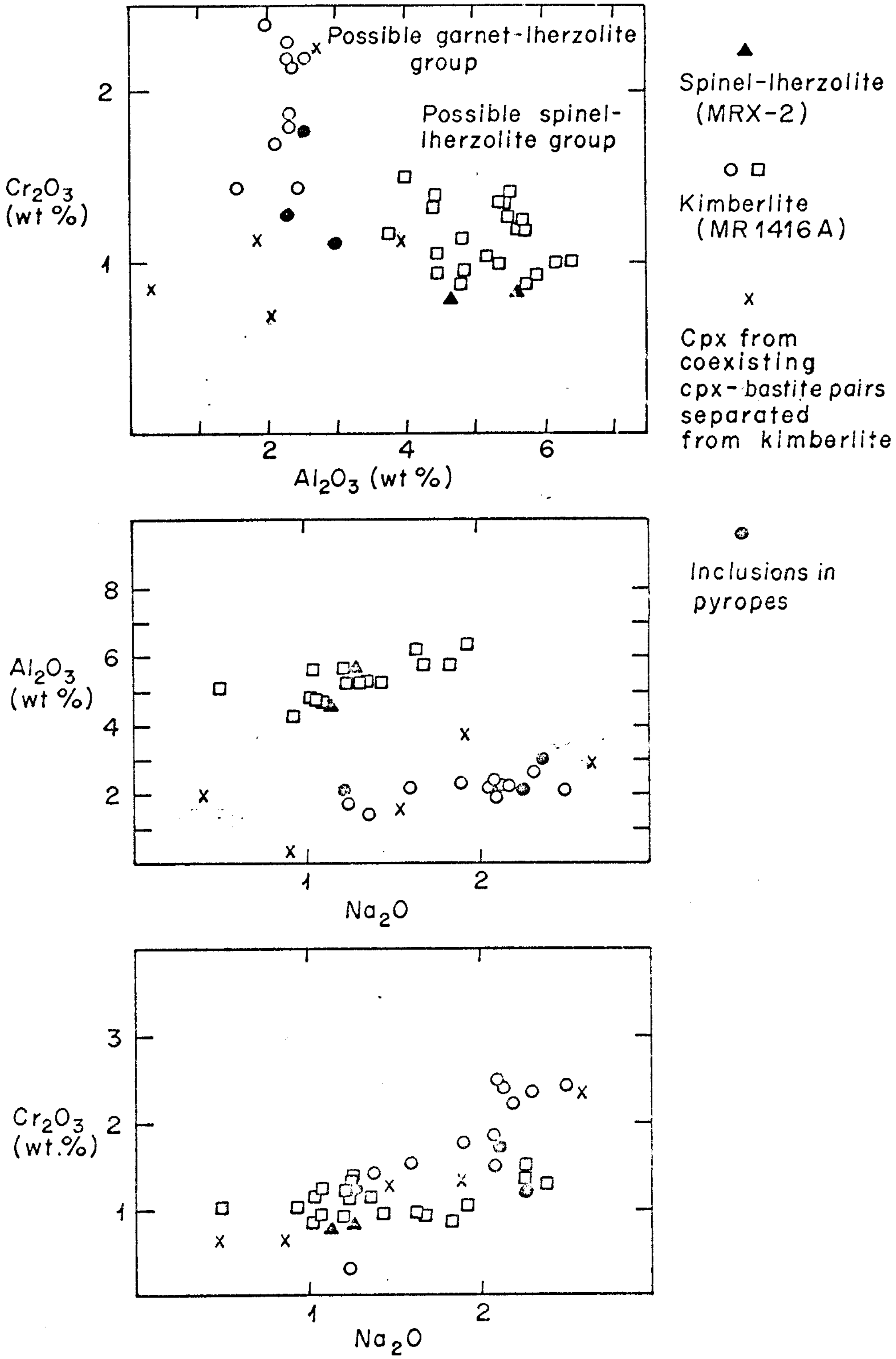

Figure 40. Relationships between chrome-alumina-soda in clinopyroxenes from Moses Rock kimberlite (MR-1416A)

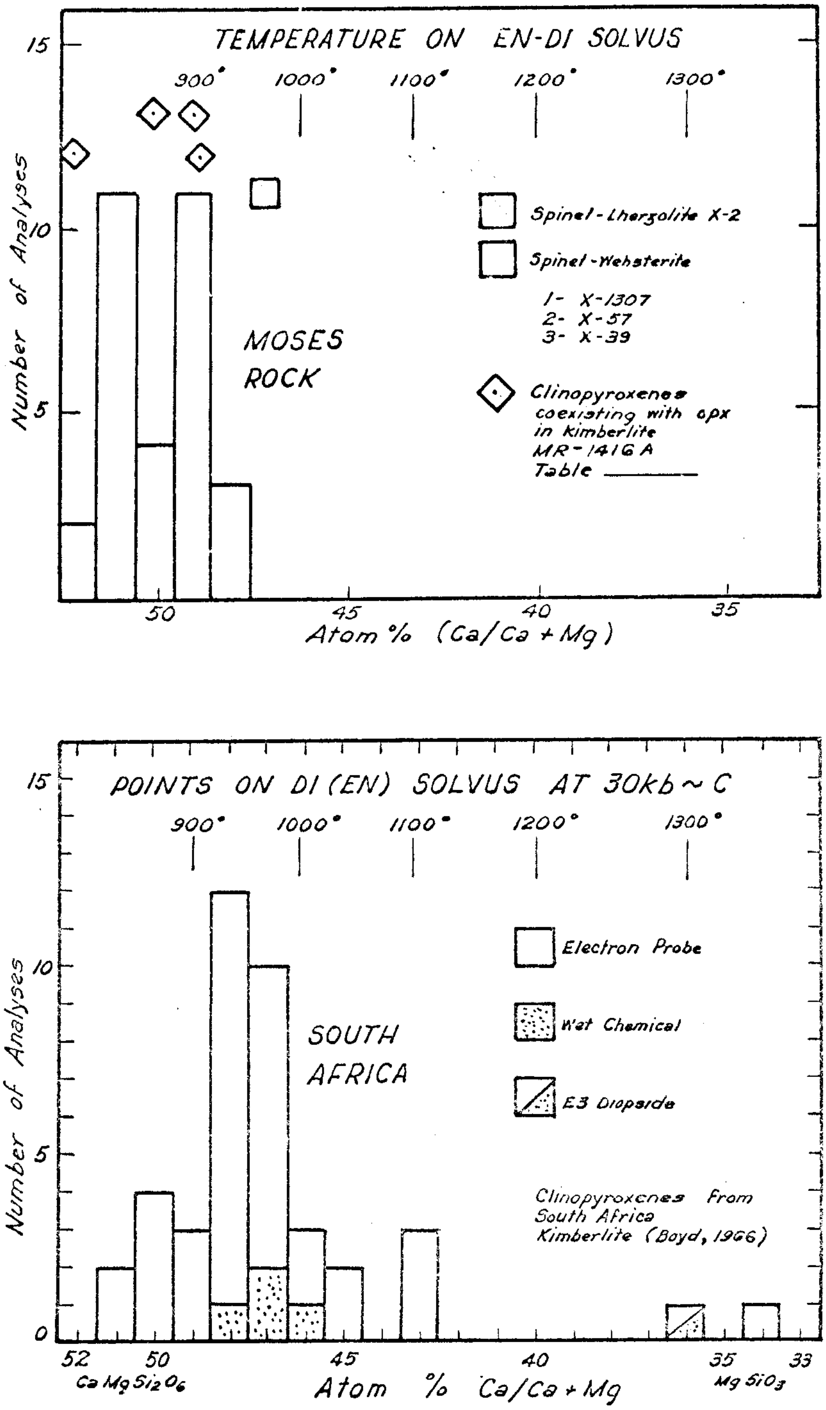

Figure 41. Comparison of Ca/Ca+Mg ratios in clinopyroxenes from South African and Moses Rock kimberlite, including data from dense inclusions in the Moses Rock dike

Spinel

Brown spinel is present in accessory abundance in the kimberlite, and in one instance was observed coexisting with a clinopyroxene fragment. Microprobe analyses of 6 grains showed compositions ranging between $(Mg_{1.1}Fe_{0.9})(Al_{2.5}Cr_{1.5})O_8$ and $(Mg_{1.4}Fe_{0.6})(Al_{3.5}Cr_{0.5})O_8$. The variation in composition is systematic (Figure 42), and fall along a line connecting these compositions. The Al and Mg rich specimens are similar to those in the spinel-lherzolite fragment (MRX-2).

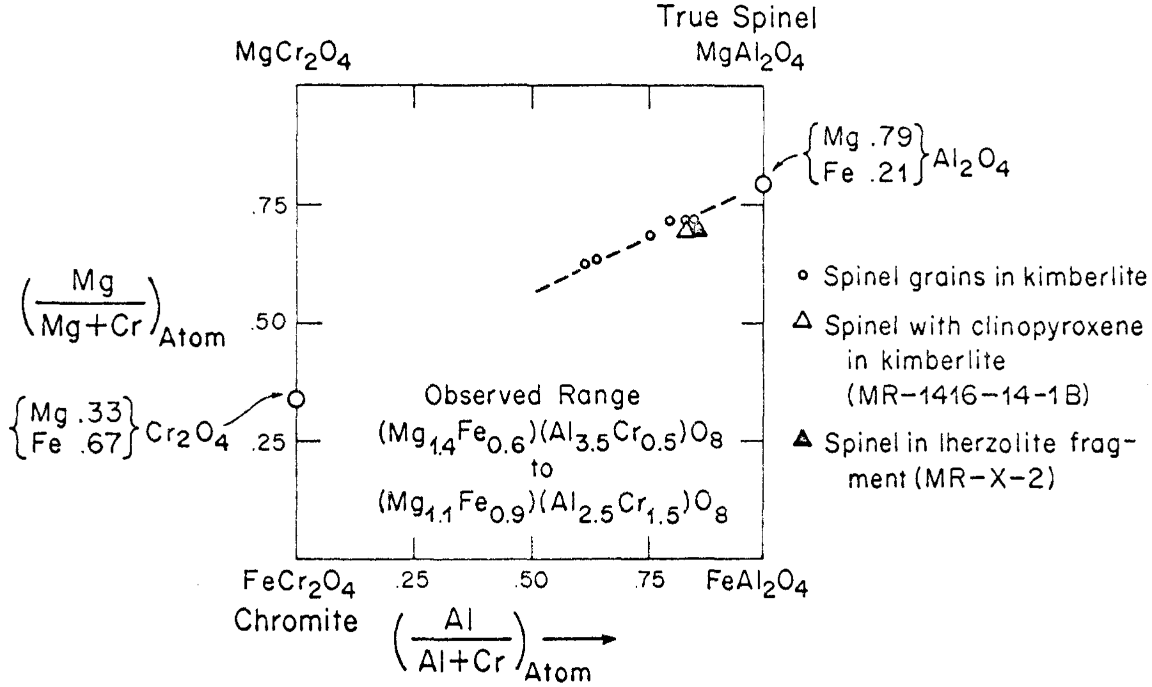

Figure 42. Compositions of spinel grains in kimberlite and rock fragments

Titanoclinohumite

Clinohumite has been observed in polished sections as discrete grains and in grains coexisting with olivine in kimberlite and also as an inclusion in pyropic garnet (PG-2). It has a bright yellow color in ordinary light which permits easy distinction from olivine. Its textural relationships with olivine in the kimberlite and as an inclusion within the pyrope virtually precludes its origin as a near-surface alteration product, therefore it must have been an integral part of an olivine-pyrope bearing assemblage at depth, perhaps garnet-peridotite.

Analyses of four grains from the mineral separates are available at this writing, on which nine major elements were determined with the microprobe. Grains from these same separates were powdered and positively identified as clinohumite by x-ray diffraction. TiO_2 contents are 4.7, 5.0, 5.0, and 5.6; Mg/Mg+Fe ratios .93, .92, .90 and .89. All grains contained trace amounts of Cr and Mn.

Preliminary reduction of more data on coexisting olivine and clinohumite indicate that Mg/Fe ratio of coexisting phases are virtually equal. A preliminary experiment on a concentrate of clinohumite grains suggests that their α-activity may be rather high, perhaps in the range of tens of ppm uranium equivalents.

Density of the clinohumite grains in approximately 3.25 gm/cc.

Humite group minerals are not commonly reported members of kimberlite assemblages, although Balk has reported clinohumite at Buell Park (Allen and Balk, 1954).

Clinohumite is not quantitatively important in the kimberlite at Moses Rock (about 1%) but the possible significance of this phase is great. Structurally the humite group is believed to consist of inter-layered olivine and brucite; clinohumite has 3 olivine to 1 brucite and presumably the TiO_2 is accepted in the brucite layer. It is a dense hydrous phase in the system $MgO-SiO_2-H_2O$, and could be one site where water could reside in the lower parts of the upper mantle. Kitahara, Takenouchi and Kennedy (1966) studied the system $MgO-SiO_2-H_2O$ to 30 kilobars and observed no humite group minerals. The high pressure stability field of clinohumite, particularly in Ti-rich systems is not known. The presence of a hydrous, titanium-rich, possibly radioactive phase in the upper mantle may be important from the point of view of petrogenesis of kimberlite and basaltic melt, as well, because dehydration of this mineral could release water, titanium and possibly the large radii, radioactive elements as well. The stability relations of titanoclinohumite at mantle conditions would be of interest to investigate.

Other Coexisting Minerals

In polished thin sections of kimberlite, more than one mineral was occasionally observed to coexist within a single grain or fragment. These assemblages are summarized in the table on the following page. Of particular interest are the spinel-clinopyroxene, orthopyroxene-clinopyroxene, orthopyroxene-olivine pairs. All three mineral pairs are similar in composition to minerals in the spinel-lherzolite.

Four examples of bastite (pseudomorphs after orthopyroxene) clinopyroxene intergrowths were observed. There appears to be little correlation in the compositions of the coexisting mineral pairs suggesting that the alteration of the orthopyroxene has disrupted any systematic relationships which might have existed prior to the hydration of the orthopyroxene.

Microprobe analyses on all the assemblages listed has been obtained but is not completely reduced at this writing.

Table 21. Summary of Minerals Observed to Coexist in Single Fragments in Kimberlite (Other than Inclusions in Pyropes)

K-1-5	Orthopyroxene	Mg/Mg+Fe=.912; Al_2O_3=2.8; 3.7
	Olivine	Mg/Mg+Fe=.915
1416A 14-1B	Spinel	$Mg_{1.4}Fe_{0.6}Al_{3.4}Cr_{0.6}O_8$ (brown)
	Clinopyroxene	Ca/Ca+Mg=.512; Al_2O_3=5.2; Cr_2O_3=1.1; Na_2O=1.6; FeO=2.1; Mg/Mg+Fe=.929
1416A 16-3	Orthopyroxene	Mg/Mg+Fe=.910; Al_2O_3=4.0; Cr_2O_3=0.6
	Clinopyroxene	Mg/Mg+Fe=.936; Ca/Ca+Mg=.502; Al_2O_3=5.5; Cr_2O_3=1.2; Na_2O=1.8; FeO=1.9
Many	Olivine Clinohumite	
MR 1416A 16	Clinohumite Serpentine Opaque Chlorite or Mica	
Many	Olivine Clinohumite Serpentine	
MR 1416A 14	Serpentine Carbonate Chlorite or Mica	 Mg/Mg+Ca 0
	Bastite Clinopyroxene	

		63-5-2	63-5-1	63-4-4	63-3-5
Bastite	Mg/Mg+Fe	.948	.905	.959	.870
	Al_2O_3	12.9	0.7	2.6	0.9
Ca-px	Ca/Ca+Mg	.501	.495	.492	.504
	Al_2O_3	.3	2.7	1.8	3.8
	Cr_2O_3	.75	2.7	1.4	1.5
	Na_2O	.95	2.7	1.5	2.0
	FeO	2.1	1.6	1.4	2.0
	Mg/Mg+Fe	.936	.947	.956	.933

Opaques

No systematic investigation of the opaque mineral phases has been attempted, although geikielite (titanium-rich ilmenite) is reported as inclusions in the pyropic garnets. Two additional opaque grains were analysed in the polished sections and these contained TiO_2, 13.7, 21.2 and FeO, 80.0 and 73.1 respectively. Titanium-rich opaque phases appear to be typical.

Other Minerals: Carbonate, Mica (?)

Carbonate and micaeous minerals are also present in the kimberlite assemblage. The carbonate phases observed in polished thin sections and in grains are nearly free of Mg.

Commonly, small veins of carbonate are observed running through the kimberlite, which cut across grains in some instances. Microprobe analyses of these carbonate veins revealed that they are nearly pure $CaCO_3$, almost free of Mg. Analysis of a 1/2" thick fibrous carbonate plate, fragments of which are a common constituent in the breccia, was also found to be nearly free of Mg. Lithic fragments of limey siltstone (Cutler or Rico Formation) in the kimberlite contained carbonate with appreciable Mg. It appears that this magnesium-free carbonate is typical of the kimberlite at the Moses Rock dike.

A diverse suite of sheet structure minerals, apparently including micas (phlogopite, biotite), serpentine and chlorite is observed. Brown, black and light-purplish mica are common constituents of the kimberlite at Moses Rock, and form approximately 1% of the rock. A systematic selection of these micas has been made and analysed with the microprobe but results are not available at this time. A mica (?) from kimberlite was analysed during reconnaissance investigations and a mica from a nearby minette dike was examined for comparison. The kimberlite mica is quite iron-rich,(FeO 14%; MgO 14%),(properly called biotite) and is highly zoned. The minette phlogopite is Mg-rich (FeO 5%; MgO 22%) and unzoned. Mica in the kimberlite locally was observed juxtaposed against calcite. No dolomite or orthoclase was observed. Reaction involving these phases has been studied at moderate pressure by Bailey (1964). He found that phlogopite and calcite in the presence of CO_2 and H_2O break down to orthoclase and dolomite at low temperatures. The thermal boundary of the stability field of phlogopite and calcite is determined in part by the H_2O/CO_2 ratio. This suggests a minimum temperature of emplacement of 300^{o} C, if the fluid phase was H_2O, with no CO_2. Since the kimberlite mica is Fe-rich, it is not clear that the phase diagram applies.

Wones and Eugster (1965) have shown that the stability relationships of biotite-bearing assemblages are a function of many variables which include the composition of the biotite, H_2O, O_2, H, temperature. From the data of Wones and Eugster it appears that temperatures for the formation of phlogopite could not have exceeded about 1000^{o} C under any pressure conditions, and if it coexisted with olivine (fo_{90}), not more than 800^{o} C. The general effect of total pressure on this diagram is to shift the biotite stability to higher temperatures while P_{H_2O} and P_H have little effect on the relationship shown (Wones and Eugster, 1965, p. 1263). Bailey's diagram suggests that the biotite had to form at temperatures exceeding 300^{o} C, provided the present textural juxtaposition of calcite and mica implies equilibrium.

It is of considerable interest to know whether or not the mica was present in the reservoir or grew on the way to the surface. If it was present at depth, and indeed did coexist with magnesian-olivine, then this places a temperature limit which appears to be something above 800^{o} C, depending on how much the Wones-Eugster diagram is shifted by pressures of 20-50 kilobars.

In the kimberlite the mica (?) occurs as large discrete grains but was observed intergrown with carbonate and serpentine in single grains in thin section. This textural setting supports existence at depth, rather than growth during or after transport. Davidson (1964) pointed out that dated micas commonly yield ages significantly older than the maximum geological age of kimberlite intrusions, suggesting that they were not formed at the time of the event, but were transported from below. This suggests that mica in kimberlite may have been part of a mineral assemblage in the reservoir. However, another plausible explanation is that the mica could have grown during transport in an environment rich in radiogenic argon. This is consistent with the K-rich nature of kimberlite relative to other ultramafic rocks.

Questions related to the micas must await reduction of the probe data.

Summary of Investigations of Kimberlite Mineral Compositions

Garnets in kimberlite are compositionally heterogeneous. Some were derived from garnet-bearing crystalline fragments. However, chrome-rich pyropes are the most abundant garnet in kimberlite and this type was observed only in kimberlite, not in the rock fragments.

Inclusions in pyropic garnets are consistent with a garnet-lherzolite assemblage bearing Al-poor pyroxenes with accessory rutile, ilmenite (geikielite) and titanoclinohumite.

Olivines from kimberlite range from fo_{89} to fo_{95} and form a continuum of compositions betweeen olivines in the spinel-lherzolite (fo_{90}) and olivine inclusions in pyropes (fo_{94}).

Orthopyroxenes in kimberlite have Fe/Mg ratios similar to those in spinel-lherzolite and are more iron-rich than the inclusions in pyrope. Furthermore, nearly all are aluminous ($Al_2O_3 > 2\%$), unlike the aluminum-poor pyroxenes associated with garnet.

Clinopyroxenes fall neatly into two compositional groups, one similar to inclusions in pyropes, the other like the pyroxenes in spinel-lherzolite. All have Cr_2O_3 contents between 1 and 2.5%; those in the garnet-like group have higher Cr contents. The kimberlite clinopyroxenes have markedly lower Al_2O_3 contents than the calcium-rich pyroxenes in eclogite (X-1, X-50B), jadeite-rich clinopyroxenite (X-44) and websterite fragment.

Spinels are Mg- and Al-rich, similar to those in the spinel-lherzolite but contain significant amounts of Fe and Cr.

Opaque minerals are typically TiO_2-rich.

Carbonates observed are Mg-free and mineralogically calcite.

Clasts of Paleozoic limestones from below are typically dolomitic.

A diverse suite of sheet structure minerals exists which appears to include phlogopite, serpentine, possibly chlorite. This group of minerals is under investigation at present and results are not yet available.

Several suites of minerals observed to coexist within single fragments in polished sections of kimberlite include pyroxenes with olivine, spinel with pyroxene, two pyroxene pairs and carbonate with micaceous and serpentine-like minerals. The olivine-pyroxene, two-pyroxene pairs, and spinel-pyroxene intergrowths are similar to spinel-lherzolite minerals. The other assemblages are still under investigation.

Finally, titanoclinohumite was observed in kimberlite polished sections as discrete grains and intergrown with olivine and also as inclusions within pyropic garnets. The textural relations preclude its origin as an alteration mineral. It appears that clinohumite existed at depth within a peridotite assemblage. This observation may be important because it suggests a possible site for water in the upper mantle in a dense, hydrous olivine-like mineral phase.

Inferences Drawn from Petrologic Investigations

Introduction

From the observations already presented it is possible to draw some inferences about the nature of the earth's interior under the Moses Rock dike and perhaps the processes which lead to the eruption. In this section several problems are discussed and some conclusions are reached.

1) The relationship between the dense crystalline rock fragments and the kimberlite is examined and it is concluded that all except the spinel-lherzolite fragment are virtually unrelated to the minerals in kimberlite but are merely accidental inclusions of material sampled from the vent wall during the eruption.

2) The location of the reservoir from which the kimberlite was erupted is inferred from compositional relations in kimberlite pyroxenes and pyroxene inclusions in pyrope. The composition of calcium-rich pyroxene is a sensitive indicator of the P-T conditions of formation because of solid solution relationships with other minerals. By applying results of laboratory investigations on natural and synthetic mineral systems to the observed compositions, it is concluded that the clinopyroxenes in the Moses Rock dike were derived from over a range of depths extending from the base of the crust to about 150 kilometers. Indicated temperatures are modest, generally below 1000° C.

3) The source rocks from which the kimberlite was derived are inferred from the compositions of the minerals in kimberlite. Com-

parison of these minerals with those in spinel-lherzolite fragments and inclusions in pyrope suggests that the kimberlite consists of minerals derived rather directly from spinel-lherzolite and garnet-lherzolite assemblages. Since the conditions suggested by the pyroxene data are well below normal liquidus temperatures in low-K_2O ultramafic systems, it is suggested that the kimberlite may have been emplaced from the upper mantle as a volatile-solid particle system. The relatively great abundance of hydrous minerals in kimberlite suggests that the volatile phase was mostly water, supercritical at depth but gaseous near the surface.

4) The reconstruction of a column through the crust and upper mantle is attacked using data gathered on the diverse and abundant suite of crystalline rock fragments in the Moses Rock dike. This suite of rocks suggests that a long vertical column of rocks has been sampled, perhaps spanning the entire crust and part of the upper mantle. Field observations of size and relative abundance of crystalline rock fragments combined with lab studies of their petrography resulted in the construction of such a crustal-upper mantle model, which has the following characteristics. The upper crust consists of granitic and meta-basalt in rocks in the upper portions, mafic amphibolite and granulite gneiss at depth, and possibly hydrated ultramafic rocks similar to the antigorite schist fragments. In this model, the upper mantle consists of eclogite, partially hydrated ultramafic rock, predominantly spinel-lherzolite, and abundant pyroxenite. At greater depth the mantle consists of garnet-lherzolite. The thermal and physical properties of this model are investigated.

5) The nature of the Mohorovicic discontinuity is discussed. The Moho occurs at 42 kilometers locally and is defined by transition between regions with p-wave velocities of 6.8 and 7.8 km/sec. The observations suggest that the Moho may occur in a petrologically complex region and that the transition between crust and mantle may involve a) hydration-dehydration, b) basalt (mafic granulite gneiss)-eclogite, and c) mafic-ultramafic transitions. Hydration, phase and compositional changes are probably involved in the seismic discontinuity.

Relationship of Kimberlite and Dense Inclusions

The abundant partial chemical analyses of mineral grains from kimberlite and of minerals from the various inclusions permit some comparisons to be made and conclusions to be drawn about the genesis of these rocks.

There are striking chemical differences between minerals observed in the crystalline rock fragments compared to the kimberlite. The Al_2O_3 content of clinopyroxene in eclogite, websterite and jadeite-clinopyroxenite is out of the range of the kimberlite clinopyroxenes. The kimberlite clinopyroxenes form two distinct compositional groups; one like the spinel-lherzolite clinopyroxenes, the other like clinopyroxene inclusions in pyrope. The websterite orthopyroxenes are much more aluminous than kimberlite ones; the spinel-lherzolite orthopyroxenes are within the kimberlite range. Spinel-lherzolite is the only olivine-bearing inclusion collected and the composition of its olivine is just within the kimberlite range, on the iron-rich end. Garnets, like those from eclogite and metamorphic rock fragments are observed in the kimberlite garnet suite, but the abundant chrome-rich pyrope garnets in the kimberlite were not observed in any crystalline fragment type.

The minerals in websterite, jadeite-clinopyroxenite and eclogite (clinopyroxenes) are chemically distinct from the kimberlite minerals, so we conclude that kimberlite was not formed from physical disaggregation and/or alteration of these rocks in any significant degree volumetrically. The spinel-lherzolite, however, could represent a direct parent for some, but not all, of the kimberlite phases.

The bulk rock chemical composition of the serpentine-rich schist differs from the kimberlite (in Al_2O_3, CaO and alkali content), and thus is not believed to be a direct source of a significant amount of material in the kimberlite.

The textures of some dense fragments contain important clues to their origin. The spinel-lherzolite and websterite have granoblastic (recrystallized) textures which preclude their origin as simple crystal-accumulates or partial melting residues related to a magma. The jadeite-clinopyroxenite, however, has a disequilibrium foliated texture (zoned subhedral crystals of unequal size), thus possibly could be related to a magmatic process. The presence of pyrite in this rock, however, precludes liquidus temperatures. Thus the jadeite-pyroxenite could have formed under a wide variety of conditions, but it is definitely not a source of mineral fragments in the kimberlite.

It appears most likely that websterite, jadeite-clinopyroxenite-eclogite, and serpentine-rich schist were not present in abundance in the kimberlite reservoir but rather represent "accidental" inclusions of material derived from the vent walls as the kimberlite erupted. It is felt that they may be mantle rocks, sampled from below the crust and somewhere above 150 kilometers. The spinel-lherzolite could be derived from depths just below the crust or it could have been present at greater depth if it coexisted metastably with garnet-lherzolite.

The websterite, jadeite-clinopyroxenite, and eclogite are all highly aluminous rocks which may be important in regards to their genesis. The melting experiments on garnet-lherzolite by Ito and Kennedy (1967), and Yoder and Tilley (1962) suggest that these rocks could have originated by a process of partial melting of garnet-peridotite, then crystallized and later recrystallized all within the mantle. According to Ito and Kennedy (1967), first melting of garnet-lherzolites is reported to occur on the garnet-clinopyroxene grain boundaries producing aluminous liquids.

It is believed that eclogite, clinopyroxenite, websterite and serpentine schist fragments were derived from the vent walls during the eruption of the kimberlite and transported to the surface as "accidental" xenolithic fragments, unrelated to the kimberlite in any direct way.

Location of the Reservoir Inferred from Clinopyroxene Compositions

Minerals in natural four-phase peridotites (rocks containing plagioclase, spinel or garnet in addition to olivine and two pyroxenes) consist of complex solid solutions whose compositions are variable depending on the conditions of their genesis. The mineral whose composition is most sensitive to conditions is calcium-rich pyroxene, because of solid solution relationships with both garnet or spinel and with calcium-poor pyroxene. Experiments have shown that in the system MgO-CaO-Al_2O_3-SiO_2, at a given temperature and pressure, the composition of a clinopyroxene coexisting with orthopyroxene, olivine and spinel or garnet is uniquely determined.

Specific P-T assignments can be made to individual clinopyroxenes in four-phase peridotite assemblages on the basis of their Ca/Ca+Mg ratio and Al_2O_3 content (in excess of jadeitic ($NaRSi_2O_6$) component). The Ca/Ca+Mg ratio is a measure of the amount of enstatite solid solution in the clinopyroxene; the alumina content (or rather $R_2O_3 = Al_2O_3 + Cr_2O_3 + Fe_2O_3$) is a measure of the garnet solid solution. Both solid solution relations are P-T dependent each with different functional relations to P and T. As a result, the composition of clinopyroxenes within the stability field of a given four-phase peridotite assemblage is unique, at least in theory.

Experimentally determined phase diagrams are the basis of these interpretations. O'Hara (1967) has recently summarized the experimental and observational work of many authors on mineral relationships in the system CaO-MgO-Al_2O_3-SiO_2 and natural systems which approach this compositional tetrahedron.

An excellent review of experiment and observation on ultramafic systems and rocks can be found in Wyllie (1967), so no attempt is made to summarize previous investigations here. It is important to point out that the effects of additional components on the behavior of these systems has not been fully evaluated. The most important substitutions quantitatively are Cr and Fe^{+3} for Al, Fe^{+2} for Mg and the addition of TiO_2, Na_2O and K_2O. Trace amounts of other constituents such as MnO, NiO are probably unimportant.

Figure 43 is O'Hara's provisional grid of compositional parameters for clinopyroxenes projected into P-T space. The compositional parameter alpha (α) is based on the diopside enstatite solid solution relation; beta (β) on the solid solution of garnet molecule (R_2O_3) in clinopyroxene, where:

$$\alpha = \frac{wo}{wo + en} \times 100 \qquad \text{and} \qquad \beta = \frac{al}{(al + wo + en)} \times 100$$

and:

$wo = CaSiO_3$ wt %

$en = MgSiO_3$ wt %

$al = Al_2O_3$ wt %

The conversion of natural pyroxenes into this sytem was accomplished by the convention used by O'Hara as follows: wo = weight $CaSiO_3$ equivalent to CaO in the analysis; en = weight $MgSiO_3$ equivalent to MgO, FeO, MnO and NiO present; al = weight Al_2O_3 equivalent to all Al_2O_3, Cr_2O_3 and Fe_2O_3, less and amount equivalent to any Na_2O and K_2O present as $NaRSi_2O_6$ or $KRSi_2O_6$ molecule.

O'Hara's tabulation of observed natural pyroxenes is shown in Figure 44. Especially noteworthy are the results for nodules in kimberlites and the single lherzolite nodule from the Navajo (Green Knobs) diatreme. The nodules in South African kimberlites range from 30 to 45 kilobars and from 1000 to 1200° C, quite near the calculated steady-state Precambrian shield geotherm of Clark and

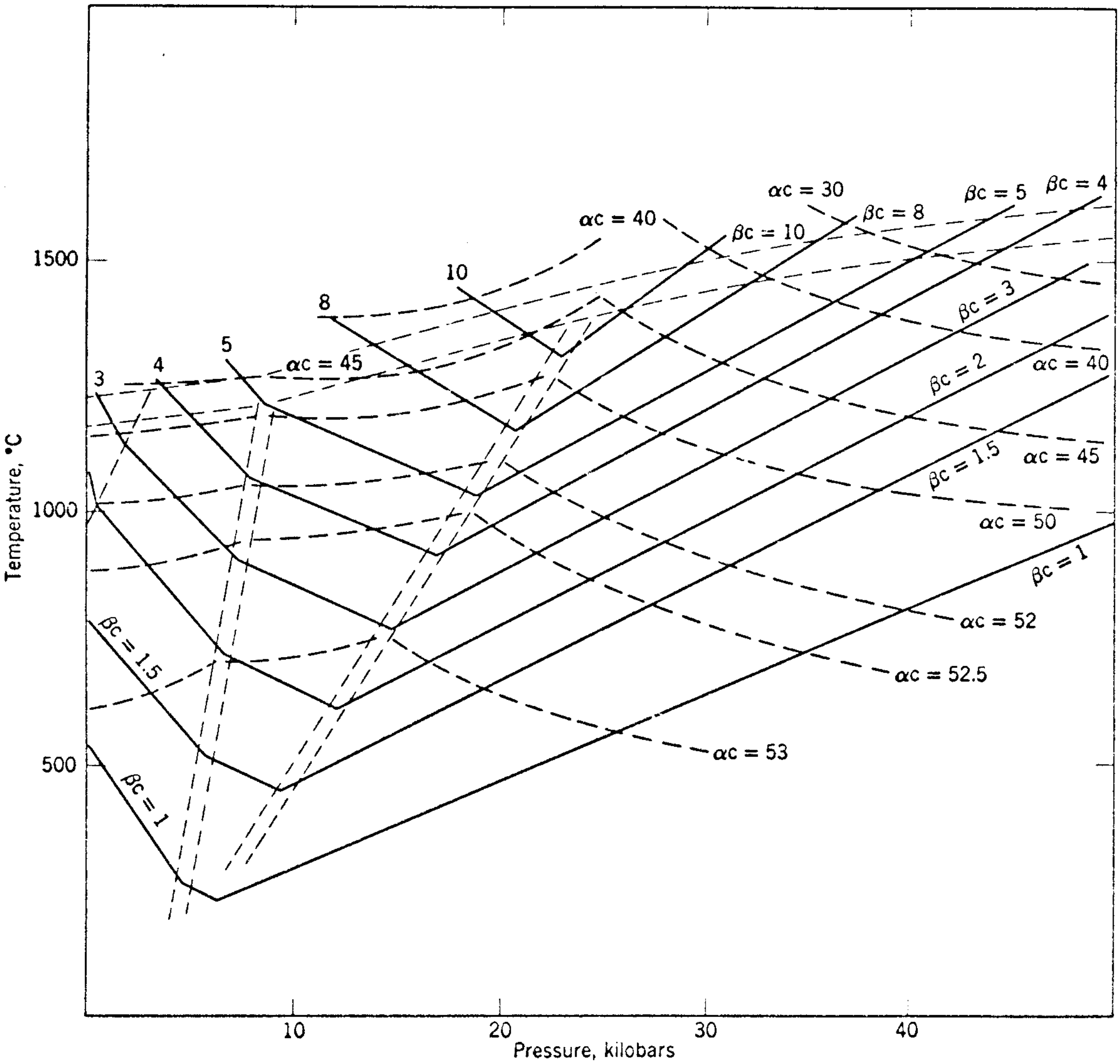

Provisional P-T projection of mineral facies and their bounding equilibria including the melting interval, for natural aluminous four-phase peridotites (see Fig. 1.3). Superimposed is a provisional grid of values of the functions α_c and β_c (defined in text) referring to chemical properties of the clinopyroxenes in equilibrium with olivine, orthopyroxene, and an Al_2O_3-rich phase.

Figure 43. Provisional P-T projection of compositional parameters for clinopyroxenes in four-phase peridotite assemblages (after O'Hara, 1967)

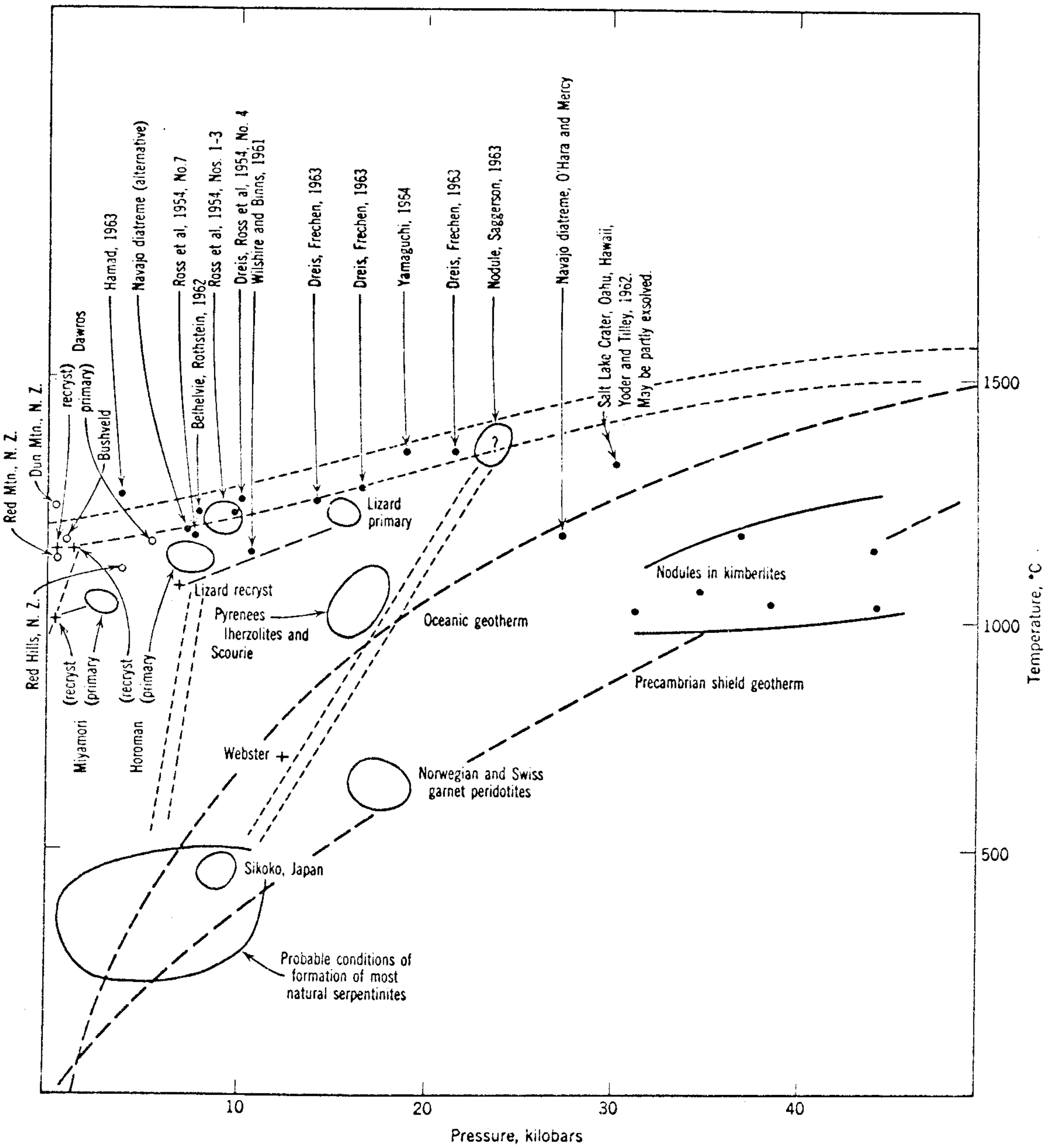

Provisional assignment of conditions of equilibration to some natural ultrabasic assemblages on the basis of the hypothesis embodied in Fig. 12.4. Data sources may be traced through the caption to Fig. 12.5. The geothermal gradients, anhydrous facies boundaries and melting interval are transferred from Figs. 1.1, 1.4, and 12.4.

Figure 44. Provisional assignment of P-T conditions of equilibrium for some natural ultrabasic assemblages (after O'Hara, 1967)

Ringwood (1964). The Navajo (Green Knobs) peridotite (lherzolite with neither spinel or garnet observed) originated at about 27 kilobars and 1200° C.

Before P-T assignments were made from the microprobe analyses of clinopyroxene analyses from the Moses Rock dike it was necessary to make some estimate of the Fe^{+3}/Fe^{+2} ratio because the microprobe does not distinguish between oxidation states. This was done by assuming ratio ferric iron to total iron has a linear relationship with soda similar to that in chemically analysed clinopyroxenes in peridotites (Ross, Foster and Myers, 1954). (A suite of clinopyroxenes is in preparation for Fe^{+3}/Fe^{+2} analyses). The curve used is shown in Figure 45.

After calculating the ferric-ferrous ratio, the compositional parameters α and β were determined from the clinopyroxene analyses, and plotted on O'Hara's provisional diagram P-T as functions of α and β (Figure 46).

Results for clinopyroxene grains from Moses Rock kimberlite, dense rock fragments and inclusions in pyropic garnets suggest: 1) if the clinopyroxenes from the Moses Rock kimberlite were in equilibrium with a four-phase peridotite assemblage, that they formed over a range of depths extending from the base of the crust to about 150 kilometers, 2) that temperatures indicated are modest, probably below liquidous temperatures in ultramafic systems of low K_2O content, 3) pyroxenes in the lherzolite fragment (MRX-2) appear to have originated at about 18 kilobars (55 kilometers) and 1200° C, 4) pyroxene inclusions in garnet, and several kimberlite clinopyroxenes,

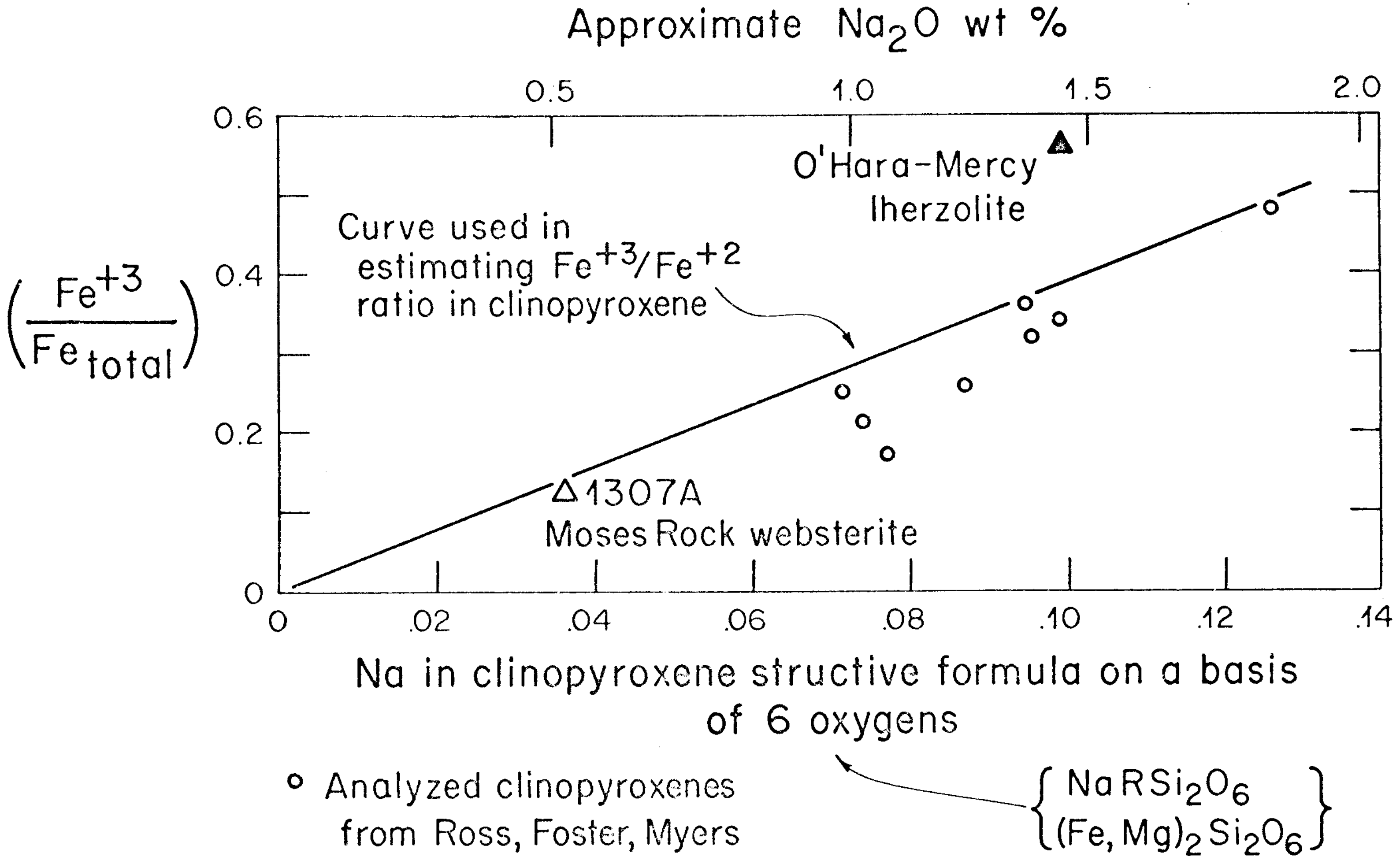

Figure 45. Fe^{+3}/Fe (total iron) ratio vs. Na content in analysed clinopyroxenes from ultrabasic rocks taken from the literature

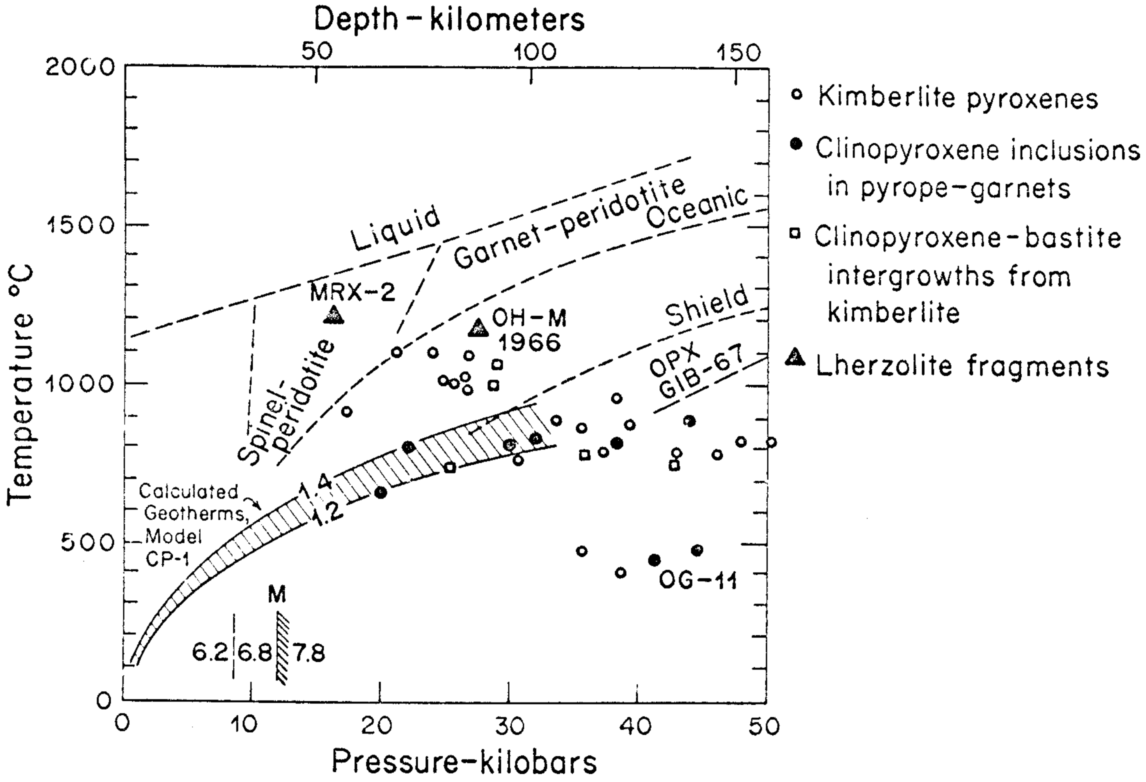

Figure 46. Provisional assignment of equilibrium conditions of formation of clinopyroxenes from kimberlite, and rock and mineral fragments in the Moses Rock dike

plot along a calculated geotherm for specific crustal-upper mantle model (CP-1), developed from the crystalline rock fragments in the Moses Rock dike (model discussed in the next section), 5) a cluster of points falls near 40 kilobars and 500° C, unlikely conditions at such depths. Included in this group of points is a pyroxene inclusion in an almandine-rich garnet (OG-11), which may be part of an eclogite rather than a peridotite assemblage. That pyroxene may not be eligible for this treatment and interpretation.

Uncertainty introduced by analytical errors are believed to be small. Random analytic errors are of the order of 1% of the value or less, except for quantities present in amounts below a few weight percent. The errors in P-T determinations due to analytical error therefore are small, although the sensitivity to error is not constant throughout P-T space. For example, it is clear from the spacing of the isopleths in Figure 43 that the effect is much greater at low temperatures and pressure (such as at 500° C and 20 kilobars) than at high temperatures and pressure (1200° C and 40 kilobars).

However, a great deal of uncertainty still exists in assignment of specific P-T conditions of formation for the minerals, primarily because of the presence of components other than SiO_2-Al_2O_3-MgO-CaO. Plotted in Figure 47 are envelopes of possible P-T conditions, which although extreme, would still be consistent with the analytical data on clinopyroxenes from pyropic garnets and from the spinel-lherzolite fragment. Since the Fe^{+3}/Fe^{+2} ratio is unknown, possible extremes in the β value are 1) a maximum if all iron is Fe^{+3}, and 2) a minimum if all iron is Fe^{+2}. Similar extremes in α

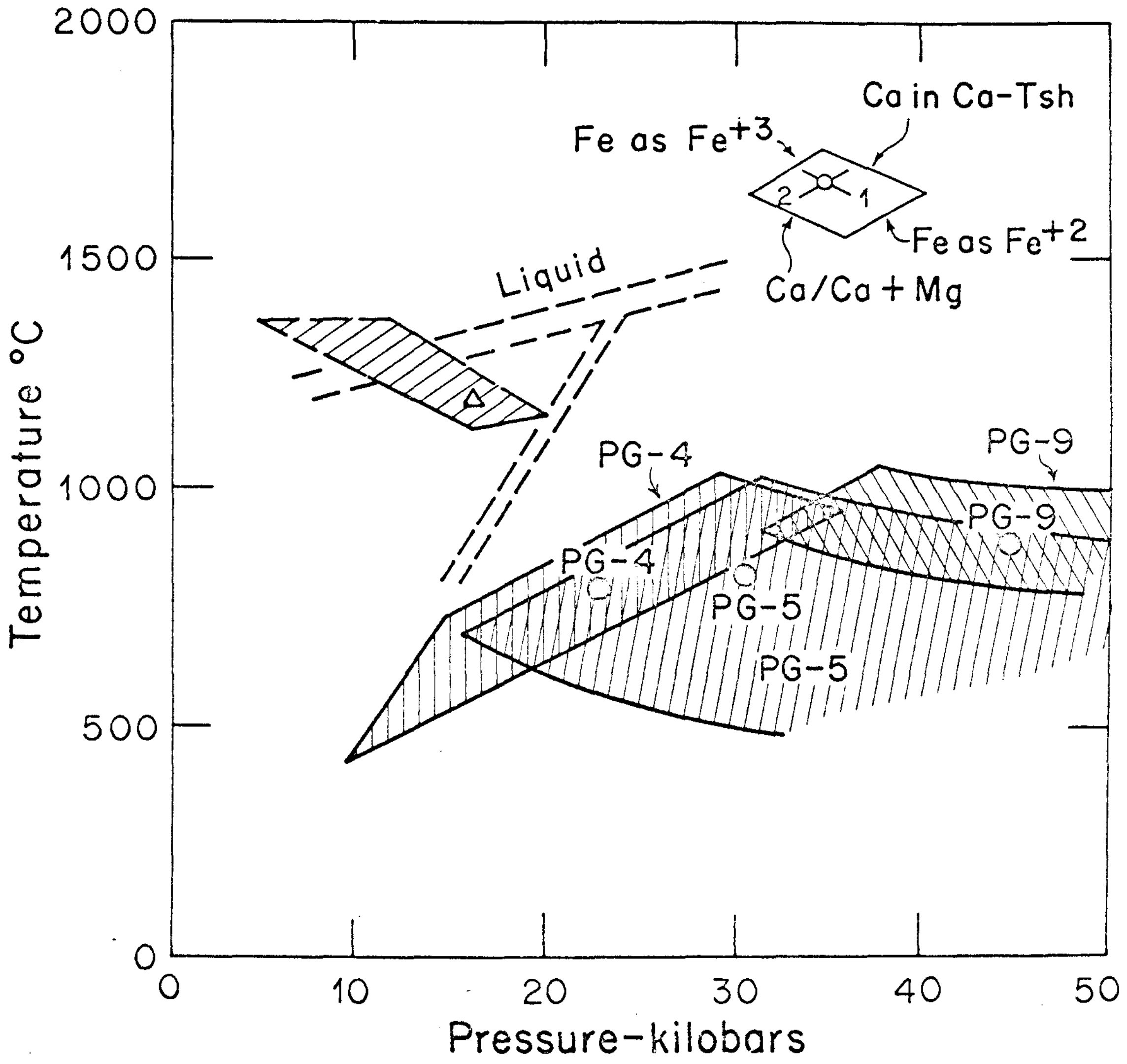

Figure 47. Diagram showing envelopes of uncertainty in P-T assignments using clinopyroxene compositional parameters due to ambiguities in treatment of data (does not include analytical error)

can be obtained 1) if one assumed that all R_2O_3 solid solution occurred as lime-Tschermak's molecule (CaR_2SiO_6) which would reduce the calcium in enstatite-diopside system to produce a minimum α value. A maximum α value is obtained by ignoring Fe, Mn, Ni and using only the Ca/Ca+Mg ratio to calculate α. These limiting values for α and β define limiting envelopes within which the clinopyroxenes must lie. The envelopes are probably extreme; furthermore shifts due to these effects would be systematic in the sense that all points would be displaced along nearly similar paths, both in direction and length.

Other problems exist in interpretation of observed analyses in terms of P-T conditions of their formations. Aside from the analytical and interpretive uncertainties, are the necessary assumptions that the mineral phases coexisted in equilibrium. This cannot be demonstrated for individual clinopyroxene grains, separated from kimberlite. Individual grains are generally unzoned. For inclusions in the pyropic garnets, orthopyroxene and olivine inclusions are observed in compositionally identical pyropes so all may have existed in a related four-phase assemblage. For the spinel-lherzolite fragment, no such assumptions are required, since spinel, olivine and two pyroxenes are observed to coexist in a granoblastic texture of essentially unzoned minerals.

It has been demonstrated experimentally that the solid solution relations between two minerals observed in binary systems do not behave identically in four-phase assemblages. An important example is the contraction of diopside-enstatite solvus region in four-phase assemblages (O'Hara and Yoder, 1967). An erroneously high temperature would be estimated by using the two-component diagram.

With all the uncertainties in mind, it appears that kimberlite clinopyroxenes originated from a range of depths extending from the base of the crust to about 150 kilometers. Indicated temperatures are somewhat less than 1000° C.

Source Rocks and Genesis of the Moses Rock Kimberlite

The observations of the occurrence of kimberlite in the Moses Rock dike suggest that kimberlite was not a silicate melt when emplaced but rather was a fluidized system consisting of gas (or very low density fluid phase, mainly water) and particulate solids.

The possibility that the kimberlite was emplaced at the present level of erosion as a magma, that is, as a true silicate melt, is dismissed for the following reasons. The kimberlite is composed of discrete angular particles in a fine-grained matrix itself composed of small particles. A silicate melt in this ultramafic system, regardless of its water content, implies temperatures greater than 1000° C and probably more. The K_2O content of the kimberlite is less than 1%, so the presence of a low-temperature silicate melt at the present surface is precluded. The thermal effects on limestone chips and small red-bed fragments in undiluted kimberlite are trivial and restricted to minor bleaching. Thermal effects on contact rocks is restricted to minor bleaching of red-beds. There is no suggestion of flow structure in the kimberlite. In fact, its petrography implies the rock is a physical agglomeration of fundamentally angular particulate chunks of minerals and rocks. The rock fragments in kimberlite have size frequency distributions like material ground in mechanical comminution processes, such as ball-mills. In the complex breccias mapped, the dilution of kimberlite with fragmental debris commonly reached 10 to 1, or more in the rubble unit. The kimberlite was intricately mixed with this debris on a fine scale such that the rock was nothing more than a friable conglomeration of homogenized particles from divergent sources.

It is concluded that the kimberlite was not a magma at this level but rather consisted of particulate and fluid phases. No trace of the fluid phase is left; presumably it was H_2O and CO_2 in some proportion.

The intricately mixed nature of the breccia suggests that the intruding material at the level of the present surface was highly fluid and probably highly gaseous. The lack of thermal effects on inclusions and contacts suggests the system was relatively cool. There is nothing in the texture of the kimberlite or its field occurrence which suggests that it was even partly silicate melt at the level now exposed. This does not preclude the possibility that the kimberlite or some part of it, was a true silicate melt at depth or within the reservoir.

The experimental results of Kitahara, Takenouchi and Kennedy (1966) suggest that no melt exists in the system $MgO-SiO_2-H_2O$ at 30 kb near 900° C. The addition of K_2O to this system does not produce a K-rich, Mg-poor silicate melt coexisting with fluid and solid phases, but the K_2O content of the Moses Rock kimberlite is low. The amount of melt which might be produced because of the presence of K_2O would be very small.

The preponderance in abundance of hydrous minerals over carbonate phases suggests that H_2O was the dominant fluid phase, rather than CO_2.

The genesis of kimberlite and kindred rocks has been the subject of much interest and controversy. It appears that a continuum may exist between carbonatites and kimberlites, perhaps depending on the ratio of CO_2 to H_2O.

If the kimberlite was not produced from a silicate magma, then the mineral fragments must have been derived from preexisting rocks in the vicinity of the reservoir.

If one assumed that 1) only two assemblages were present, garnet-peridotite and spinel-lherzolite, 2) the kimberlite was derived from these rocks and 3) the observed modes of the kimberlite and spinel-lherzolite were representative of large volumes of material, then the relative proportions of mineral phases in these rocks places a limit on the modal composition and relative abundance of garnet-lherzolites.

The following table shows the range of garnet-lherzolite modes which are consistent with a hypothesis that the kimberlite formed as a simple mixture of spinel-lherzolite (MRX-2) and garnet-lherzolite, assuming the kimberlite and spinel-lherzolite modes shown. The garnet-lherzolite mode is controlled by the relative volume fractions of spinel-lherzolite (X_s) and garnet-lherzolite (X_g), because $X_g + X_s = 1.00$. For an assumed X_g, there is only one modal composition for the garnet-lherzolite which is consistent with the kimberlite and spinel-lherzolite modes assumed.

Table 22. Range of Possible Garnet-Peridotite Modes Consistent with the Origin of Kimberlite as a Simple Mixture of Spinel and Garnet-Peridotites

	Kimberlite Mode (MR-1416A)	Spinel-Lherzolite Mode (MRX-2)	Fraction of Garnet-Lherzolite in Mixture					
			.676	.7	.75	.8	.9	.95
OL	80	54	92.5	91.1	88.7	86.5	82.9	81.4
OPX	12	37	-	.8	3.7	5.8	9.2	10.7
CPX	3	7	1.1	1.3	1.7	2.0	2.6	2.8
Garnet	3	-	4.4	4.3	4.0	3.7	3.3	3.2
Spinel	1	2	-	-	-	-	-	-
Other	1	-	2.0	2.5	1.9	2.0	2.0	1.9

The estimated relative abundance of mineral phases in spinel-lherzolite (MRX-2) and kimberlite (MR-1416A) determined by several methods, is shown below.

	(1)	(2)	(3)	(4)
Olivine	54	55	79	85
Opx	37	31	8	12
Cpx	7	-	2	1
Garnet	-	4.5	6	1
Others	2	1.5	5	1
	100	100	100	100

(Others = Spinel, Mica + Opaques)

(1) Mode of spinel-lherzolite (MRX-2)

(2) CIPW norm of kimberlite (MR-1416A) converted to garnet-bearing assemblage with reactions
   a) corundum + enstatite → pyrope
   b) magnetite as FeO and FeO + hypersthene → olivine

(3) Minerals in heavy mineral concentrates from kimberlite (MR-1416A)

(4) Recalculated mode of kimberlite (MR-1416A), assuming groundmass serpentine represents ol:opx = 4:1

It is possible to make some estimates of the relative proportions of garnet-peridotite (X_g) by using the relative abundance of various mineral phases in the spinel-lherzolite and kimberlite, and the observed affinities of minerals in kimberlite to either spinel or garnet assemblages. First, X_g cannot be less than .676 to avoid negative orthopyroxene abundances in the garnet-lherzolite.

Next, kimberlite clinopyroxenes with affinities to spinel assemblages outnumbered those like clinopyroxenes in garnet by about 2 to 1, thus we may write:

$$\frac{X_g \; CPX_g}{X_s \; CPX_s} \simeq \frac{1}{2}$$

where X_g, X_s are the volume fractions of garnet and spinel-lherzolite and CPX_g, CPX_s are the abundance of clinopyroxene in each rock. From the modal analysis of the spinel-lherzolite CPX_s is .07. Taking $X_s = 1 - X_g$, we find that the ratio above is about 0.5, when the volume fraction of garnet-peridotite (X_g) is about 0.72.

Another estimate of the volume fraction of garnet-peridotite can be made from the observed very low abundance of kimberlite orthopyroxenes similar to those in the garnets. Only one in forty was similar to the garnet orthopyroxene in Al_2O_3 content, although even this specimen had a markedly lower Mg/Mg+Fe ratio. Hence, the ratio of spinel to garnet-lherzolite orthopyroxenes is high. Suppose we take the ratio to be only 20:1. The abundance of orthopyroxene in spinel-lherzolite is known from the mode (.37) and again taking $X_s = 1 - X_g$, we find only a value of X_g = .68 to .70 would produce such a low ratio of orthopyroxenes in kimberlite.

Finally, two orthopyroxene inclusions were observed in pyropic garnets; five clinopyroxene inclusions were observed, although only 3 of these were in chrome-rich pyropes in the typical narrow compositional range. The two pyroxenes may be present in roughly equal abundance in the garnet-bearing assemblage. In order to satisfy this condition, the garnet-peridotite volume fraction must be very near .70.

Referring to the table of possible garnet-peridotite modes, it is seen that at a garnet-peridotite volume fraction of .70 (spinel-lherzolite .30) that the required mode is olivine 91, orthopyroxene 1, clinopyroxene 1, garnet 4, others 3. This rock is a garnet-lherzolite approaching a garnet-dunite in composition.

This petrographic model is based on modal analyses of only two rocks, spinel-lherzolite (MRX-2) and kimberlite (MR-1416A) and has obvious limitations.

The observations at the Moses Rock dike are consistent with the hypothesis that the kimberlite was emplaced from the mantle, at depths extending to 150 kilometers, from a reservoir of unknown extent and geometry which contained H_2O as a free phase, and that the erupting kimberlite consists of this volatile phase plus the products of physical disaggregation of spinel-lherzolite and garnet-lherzolite assemblages, with high-aluminum and low aluminum pyroxenes respectively. Volume proportions of spinel and garnet-lherzolite, of 30 to 70, respectively, are consistent with observed mineral compositions and abundances. Temperatures indicated by clinopyroxenes are below liquidus temperatures for silicate magmas in the compositional system represented by kimberlite. The generally unzoned character of inclusions in pyropes and the observable strain effects in the garnet surrounding these inclusions argues that these fragments existed as discrete crystalline entities before their incorporation in the erupting kimberlite and transport to the surface and that they were mechanical equilibrium in a P-T environment radically displaced from the surface.

It is believed that spinel and garnet-lherzolite are the rocks which formed the reservoir from which the eruption occurred, and that most, if not all, of the crystalline phases in the kimberlite (olivine, pyroxene, garnet, spinel, clinohumite, ilmenite, mica) were derived from disaggregation of rocks at depth.

The table on the following page summarizes the inferred relative abundances, modal and mineralogical compositions of the two assemblages from which the Moses Rock kimberlite was derived.

It was concluded in an earlier discussion that the serpentine-type minerals in kimberlite were formed by hydration of preexisting olivine and orthopyroxene, most of which occurred either during transport or immediately after emplacement by water derived from the volatile phase.

Table 23. Inferred Assemblages from which the Moses Rock Kimberlite was Derived

Spinel-Lherzolite

54	Olivine	Mg/Mg+Fe=90
37	Orthopyroxene	Mg/Mg+Fe=91; Al_2O_3=2.5 to 5%
7	Clinopyroxene	Ca/Ca+Mg=48 to 52; Al_2O_3=4 to 6.5%; Cr_2O_3=.8; Mg/Mg+Fe=94; Na_2O=1.2; FeO=1.8
2	Spinel	Mg/Mg+Fe=60 to 70; Al/Al+Cr=60 to 80
	Serpentine	

Garnet-Lherzolite

91	Olivine	Mg/Mg+Fe=94
1	Orthopyroxene	Mg/Mg+Fe=94; Al_2O_3=0.5 to 1%
1	Clinopyroxene	Ca/Ca+Mg=48 to 50; Al_2O_3=1.5 to 3.0; Cr_2O_3=1.5; Mg/Mg+Fe=92 to 96; Na_2O=1.2 to 2.5; FeO=1.3 to 2.5
4	Garnet	Mg:Fe:Ca=69:19:12; Cr_2O_3=1.4 to 2.5
3	Ilmenite (Geikielite)	TiO_2=58; FeO=33; MgO=12
	Rutile	Some Cr, Fe, Mg in solid solution
	Clinohumite	Mg/Fe+Mg=88 to 93; TiO_2=4 to 6%
	Mica or Chlorite	

$$\text{Kimberlite}\left\{\begin{array}{l}\text{7 Part Garnet-Lherzolite}\\ \text{3 Part Spinel-Lherzolite}\end{array}\right. + \text{Volatiles}$$

Reconstruction of a Column Through the Crust and Upper Mantle

By combining the field and petrologic results with the relatively abundant geophysical data available locally and regionally, some interesting conjectures on the vertical structure of the crust and upper mantle can be developed.

Since it has been shown that some minerals in the kimberlite were probably in equilibrium at pressures equivalent to a depth of 150 kilometers, then the crystalline fragments represent the equivalent of badly scrambled cuttings of a 150 kilometer long drill hole.

Field studies of the block size distribution of the sedimentary rock fragments in the Moses Rock dike have shown that an inverse size-depth relationship exists. If a similar law holds for the crystalline fragments, then their relative depths of origin can be inferred from their relative size, subject to possible differences in grinding coefficients, initial size and other factors.

A great deal is known about the local subsurface structure. A reversed seismic refraction profile was recorded between Hanksville, Utah, and Chinle, Arizona, which passes through Monument Valley, very near the Moses Rock dike. The variation of P-wave velocity with depth in the vicinity of the dike was interpreted by Roller (1965) to be:

Depth	P-wave Velocity
Surface-3 km	3 km/sec
3-28 km	6.2 km/sec
28-43 km	6.8 km/sec
Below 43 km	7.8 km/sec

The upper mantle in the western United States is characterized by a low P-wave velocity and low density (Pakiser and Zietz, 1965). Upper mantle P-wave velocities of 7.8 km/sec are typical in the west; 8.0 km/sec or greater in the east.

Heat flow data are sparse. Roy (1963) has measured two relatively high values in Utah, both in mining districts which probably are not typical of the region. More recent data suggest a regional heat flow slightly above normal, in the range 1.2 to 1.5 (Roy, personal communication).

Regional northeast-southwest trends have been reported in aeromagnetic and gravity surveys which are believed to be regional trends in the buried crystalline rocks (Case and Joesting, 1961).

Crystalline basement rocks do not crop out in the vicinity of the Moses Rock dike. Such rocks are exposed in the region, however, in the San Juan Mountains and on the Uncompaghre Uplift in southwest Colorado, on the Defiance Uplift in New Mexico, and in the inner gorge of the Grand Canyon, Arizona. Foliated rocks generally trend north-eastward, parallel to the regional gravity trends. Rocks from drill holes in south-western Colorado, about 60 miles east of Moses Rock, have been described by Edwards (1966) as orthogneiss, granitized paragneiss, granitic igneous rocks and calcareous and quartzo-feldspathic, pelitic and basic paragneiss, with northeast trending foliation where exposed. Drill holes near Bluff, Utah, about 20 miles east of Moses Rock, produced granite and quartzite (Fitzsimmons, 1963, p. 14). He reports that chlorite schist or phyllite, consisting of chlorite and quartz was encountered at

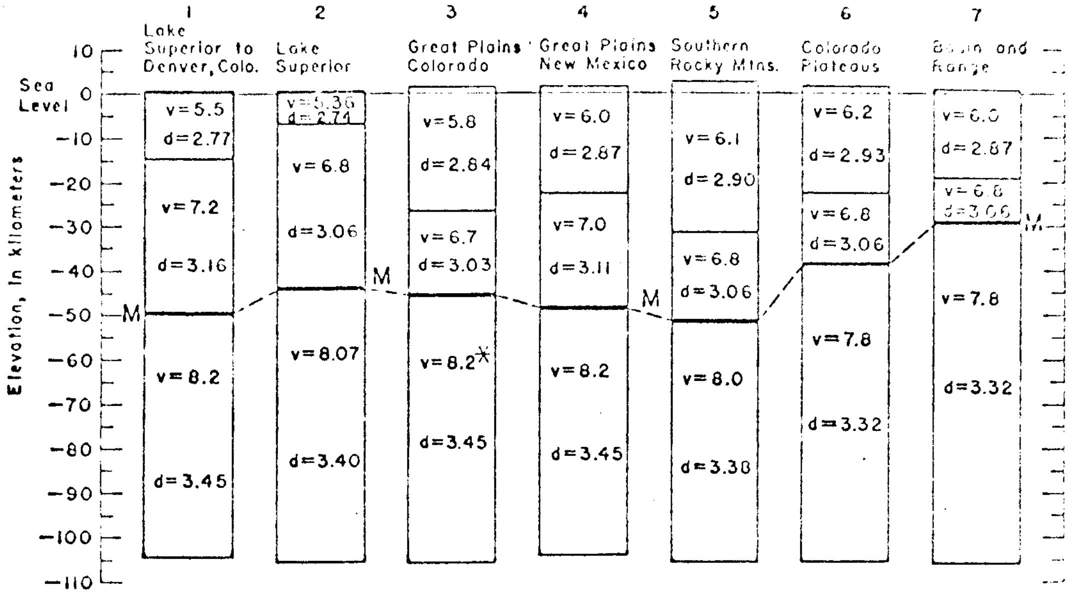

Figure 48. Crustal and upper mantle seismic structure in western United States (Roller and Jackson, 1966)

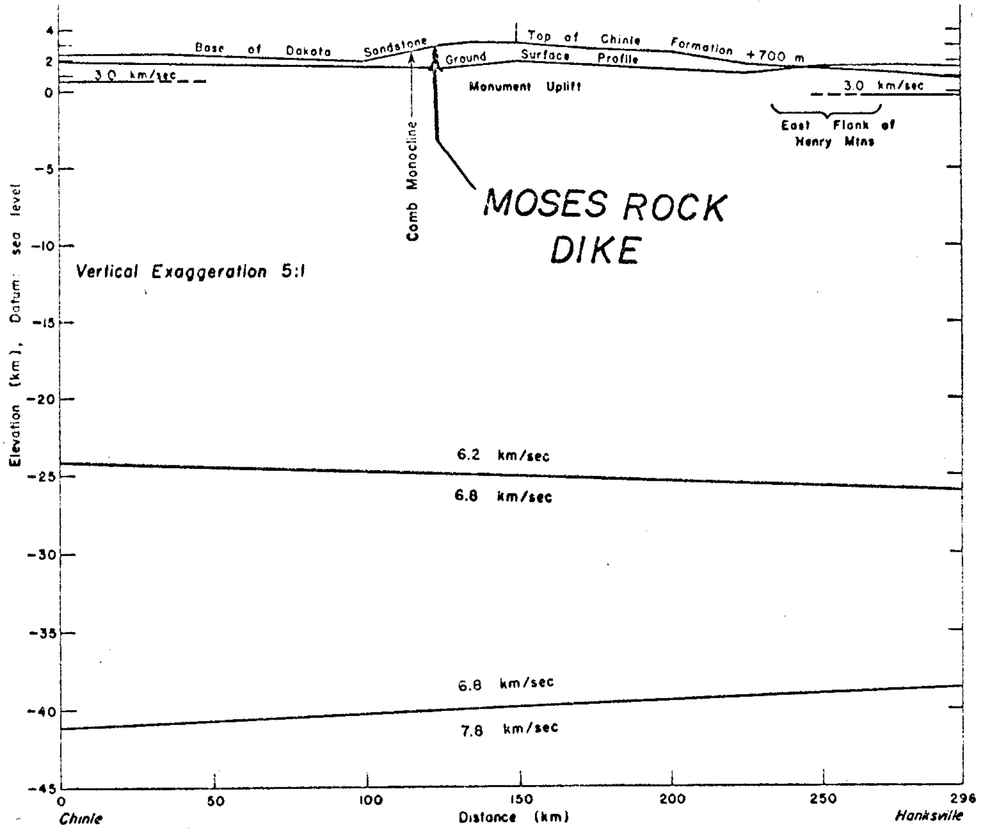

Figure 49. Crustal structure from seismic refraction profile in vicinity of Moses Rock dike (Roller, 1965)

Bluff. Thus, the literature suggests the exposed basement consists of granitic rocks mixed with basic meta-volcanics and meta-sediments (?) of amphibolite and greenschist metamorphic grade.

The crystalline rock fragments in the Moses Rock dike represent a wider range of types, undoubtedly reflecting variation through a wide vertical span.

The detailed mapping of blocks within the dike revealed that a general inverse block size-depth relationship exists among the sedimentary rock blocks transported upward. This relationship provides an empirical rationale for reconstruction of the original vertical sequence of crystalline rocks. This implies to first order, that the smaller the blocks of a given type, the greater the distance up the vent they had travelled, the deeper their original location. Such a relationship could result from either (or both) fluid mechanical sorting of fragments by differential settling of blocks according to density, size and shape in the moving fluid medium, or comminution during transport. Large basement fragments nearly always have very well-rounded shapes implying abrasion and polishing. Repeated impacts would probably produce angular debris. The size-frequency distribution for basement inclusions in not as simple. The observations may suggest that during the eruption, the system is only "fluidized" near the surface, at depth the material would be ground and abraded rather than comminuted by repeated violent impacts. In either case, the size of a given fragment should be reduced with increasing distance transported up the vent, whether by violent comminution due to impact or by abrasion.

Many factors make a simple block size depth correlation uncertain, including the effects of differences in relative abundance in the vent walls, rate of introduction, size of blocks initially introduced, volume of material introduced, grinding coefficients, strength, jointing, susceptibility to weathering and survival at the surface.

If it is assumed that the relative size of the basement fragments is a simple inverse function of their depth of origin, then the mean size index (as defined in the text and displayed in Figure 19 and 20 is a measure of the depth of origin of a given rock type; the relative magnitude of size indices of two types is a measure of the relative depths to their original positions. The mean size indices would indicate that granite (75) and granite gneiss (73) originated higher in the sequence than basic granulite gneiss (50), which in turn originated higher in the section than eclogite (25) or websterite (4).

We can further assume that the relative abundance of rock types observed at the surface is proportional to their relative abundance in the column. If this assumption is correct, then the table on the accompanying page, which lists the crystalline rock fragment types observed in the Moses Rock dike in order of decreasing mean size index and showing their relative abundances, is an approximate reconstructed crustal column, reading from the top down.

Table 24. Summary of Field Data on Crystalline Rock Fragments Observed in the Moses Rock Dike Listed in Order of Decreasing Mean Size Index

Crystalline Fragment Type	Sample Number[1]	Mean Size Index	Estimated Relative Abundance in Wt.%
Meta-basalt	MRX-13	85	34
Granite	MRX-105,260	75	1
Granite gneiss	MRX-66	73	1
Gabbro	MRX-100	55	19
Basalt	MRX-27,97	55	10
Chlorite schists	MRX-128	55	2-3
Serpentine schist	MRX-51	55	2-3
Diorite	MRX-95	52	11
Granulite gneiss	MRX-148	50	17
Jadeite-Clinopyroxenite	MRX-35	35	< 1
Rhyolite	MRX-6,60	28	1
Amphibolite	MRX-220	27	2
Eclogite[2]	MRX-1,50B	25	< 1
Websterite[2]	MRX-1307A	4	<< 1
Spinel-lherzolite[2]	MRX-2		<<< 1

1. Whole rock chemical analysis, petrographic description and measured density available on most specimens listed (Appendix C)

2. Microprobe data available on mineral phases

Minor rearrangements are possible,but generally granites and meta-basalt occupy the top of the column. Granites were observed at the top of the basement in drill holes at Bluff, Utah. Rhyolite, although it has a small size index, could not have originated deep in the column since it is unfoliated and not seriously metamorphosed. Rhyolites are commonly jointed on a fine scale. Thus it is concluded that the rhyolites were from high in the column but were easily comminuted. Basic granulites and gabbro occupy the bulk of the lower crustal section.

The petrographic character of the rock types is also a clue. Unfoliated rocks must be younger or shallower (or both) relative to foliated rocks. Low-grade rocks probably are shallower in origin than high-grade rocks.

The principal observations relevant to all attempts to reconstruct the column are: (1) Meta-basalts and granite are the largest fragment types observed in the dike, therefore are inferred to be abundant in the upper crust. (2) Gabbro and diorite fragments are moderately large and generally have not suffered a retrograde metamorphism. They are either young or shallow or both. The size data suggest they are shallow, therefore they may be both shallow and young (relative to the metamorphic rocks). (3) Rhyolite fragments are relatively small in size which would suggest that they are deep in origin, but they are unaltered. Also, they would reasonably constitute a member of a relatively younger or shallower terrain. (Preliminary lead-isotopic dates suggest these rocks are Precambrian, about 1670 m.y.). It is felt that the rhyolites are shallow in origin and their anomalously small size is due to a pervasively fractured habit, thus their small size could be accounted for by differential comminution during transport. (4) Metamorphic rocks of amphibolite and granulite grade probably constitute the lower parts of the crust. Basic types are more abundant than acid types although charnockites and aluminous schists are observed. Sillimanite was observed commonly but not kyanite or andalusite. The metamorphic rocks show the effects of a retrograde metamorphism. (5) Pyroxene granulite rocks may give way with depth (or may coexist with) plagioclase-bearing eclogites, in the lower crust. (6) Serpentine schist may constitute a part of the lower crust but these rocks are fundamentally hydrated ultramafics. (7) The upper mantle is believed to consist of spinel-lherzolite and garnet-lherzolite, perhaps in the relative abundance of about 30:70. However, the dense fragment types (eclogite, websterite, jadeite-clinopyroxenite, and antigorite schist), apparently introduced as accidental inclusions from the vent walls may be abundant in the uppermost mantle. Especially noteworthy are the antigorite schists, which may indicate that the upper mantle is <u>heavily</u> hydrated.

An inferred crustal-upper mantle model, hereafter called CP-1, is presented in Figure 50, with measured or estimated K_2O contents of rocks believed to be representative of each element of volume in the diagram. This model is based fundamentally on the size and relative abundance of the crystalline fragments as <u>observed</u> but has been modified to be consistent with petrographic observations as well as plausible (and hopefully reasonable) petrologic inference.

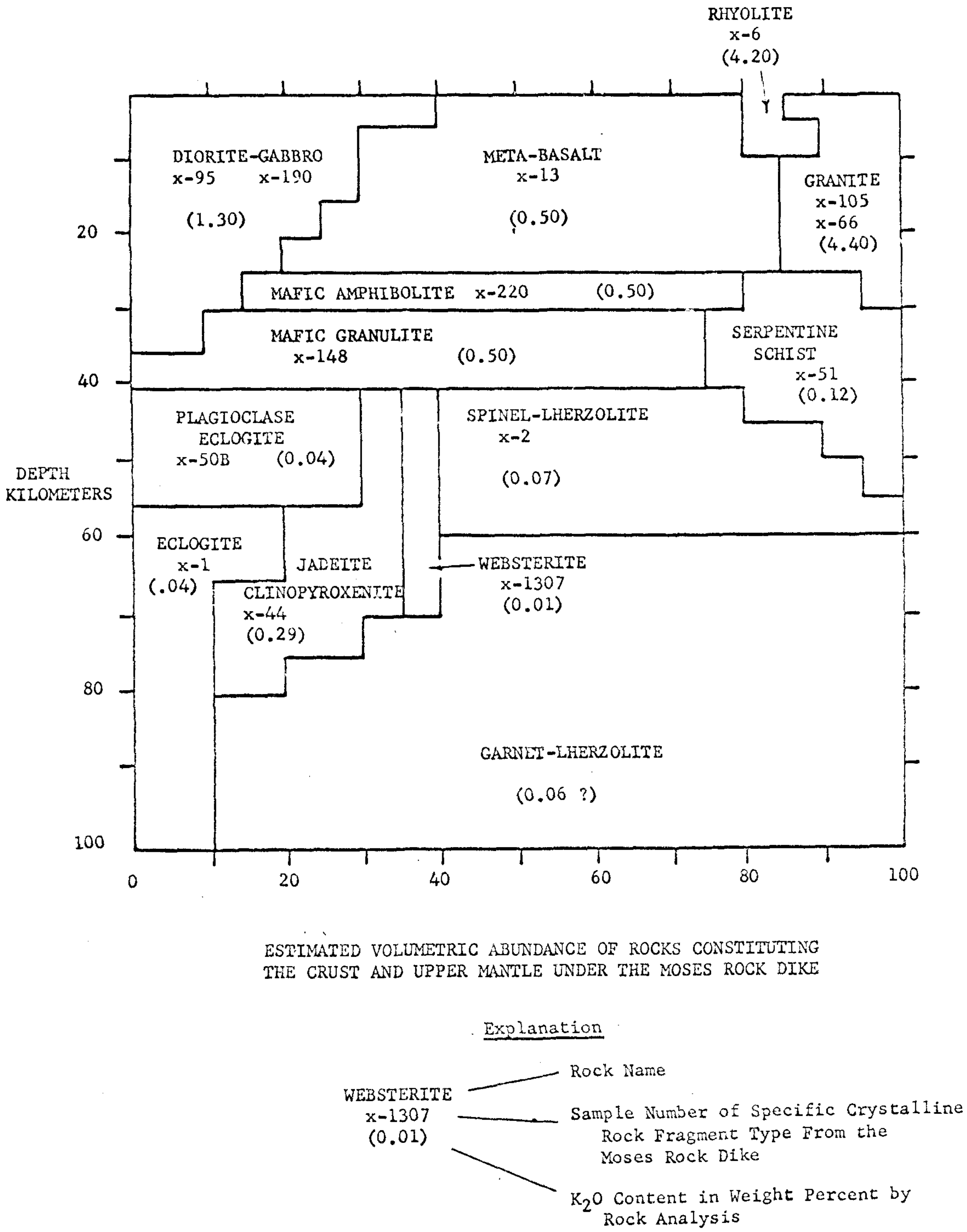

Figure 50. Schematic summary diagram showing inferred volumetric relationships for various rock types with depth in the crust and upper mantle under the Moses Rock dike

The distribution of crustal rocks, in model CP-1, suggests that the upper part of the crust is granite, gneissic granite, meta-basalt, diorite and gabbro. These rocks are either unaltered or have been subjected to greenschist-grade metamorphism. In this model, the lower crust consists of amphibolite and granulite grade metamorphic rocks, mostly high-rank mafic gneisses, all of which bear the imprint of retrograde metamorphism to amphibolite grade. A minor amount of eclogite and possibly some pyroxenite may occur in this high rank terrain in the lower crust.

It is inferred that the Mohorovicic occurs in a petrographically complex region near 43 kilometers depth and represents a composition transition between basic granulites and gabbroic to partially hydrated spinel-lherzolite, with some layers of pervasively-altered peridotite, now serpentinized-schist. Eclogite lenses and pods of jadeite-clinopyroxene are fairly common; present but more rare are domains of websterite. At greater depth garnet-lherzolite replaces spinel-lherzolite as the dominant rock type.

It is possible that some of the eclogite, websterite and jadeite-clinopyroxenite originated as partial melting products of the garnet-peridotite mantle which crystallized before reaching the crust. The diorite and gabbroic bodies of the crust are chemically quite similar to eclogite (MRX-50B). Therefore, they could be similar material which crystallized at sufficiently low pressure to stabilize plagioclase. Granite diorite and gabbroic plutons may extend from the amphibolite and granulite terrain.

The geophysical properties of crustal-upper mantle model CP-1 are worth exploring. The properties of each layer can be calculated by the appropriate type of averaging of the known (or assumed) rock properties. The results of these calculations for model CP-1 are discussed in the following pages and shown in Figure 51.

The density of a mixture of the fragment types shown in CP-1 is proportional to their relative volumes. Neglecting compressibility and thermal expansion, the resulting density profile for the upper 100 kilometers varies between 2.80 gm/cc near the surface to 2.94 just above the Moho; increases to 3.24 just below the Moho and reaches 3.4 at 80 kilometers.

No seismic wave propagation velocities or elastic properties have been measured on the specimens, however estimates of P-wave velocities for the rocks in CP-1 were made by selecting similar (?) rocks from Press' tabulation (in Clark, 1966). Since little detailed petrographic data are included in the tabulations, these estimates are tenuous. A very rough temperature correction was applied graphically, which amounted to about .1 km/sec at 1000° C (near kb). The wave propagation velocites of heterogeneous mixtures depends on the geometry of the mixture. A simple harmonic average was applied, where:

$$V_p = 1/\sum_i \left(\frac{x}{v_p}\right)_i$$

where x = volume fraction and v = velocity of each component rock. The result for model CP-1 can be compared with the seismic velocity with depth inferred by Roller (1965) from a 400 mile long reserved refraction profile from Hanksville, Utah to Chinle, Arizona which passed quite near the Moses Rock dike. The coincidence of the location of the seismic discontinuities is insignificant because the seismic data were used in establishing the boundaries of the petrologic model, CP-1. It is of interest to compare the velocities. The upper crustal velocities suggested by CP-1 are higher than those observed by Roller by about 0.3 to 0.4 km/sec; the lower crustal velocities by about 0.3, suggesting that the abundance of low density, therefore generally acid rocks, may be underestimated. The mantle velocities are in reasonably good agreement near the Moho.

The bulk of radioactive heat generation in rocks is due to the nuclides K^{40}, U^{235}, U^{238} and Th^{232}. Whole rock chemical analyses are available on most of the rocks in model CP-1, so the K_2O content is known for most of the rocks in the model. Analyses are not available on the spinel peridotite (MRX-2) and no specimen of garnet peridotite was found, inferred to be abundant in the mantle. Potassium contents of the mineral grains separated from the kimberlite were not determined. However, analyses of two kimberlite samples (MR-1416A, MR-1416B) are available and the observed K_2O content of these rocks can be used as an upper bound on the K_2O content of the mantle. Using these kimberlite values as typical of the upper mantle, the K_2O content with depth was determined.

Since U and Th concentrations were not determined in any specimens, some estimate of their abundance is required in order to calculate the total heat production rate. Wasserburg, MacDonald, Hoyle and Fowler (1964) concluded that the best estimates of the ratios of potassium, uranium and thorium for the outer portions of

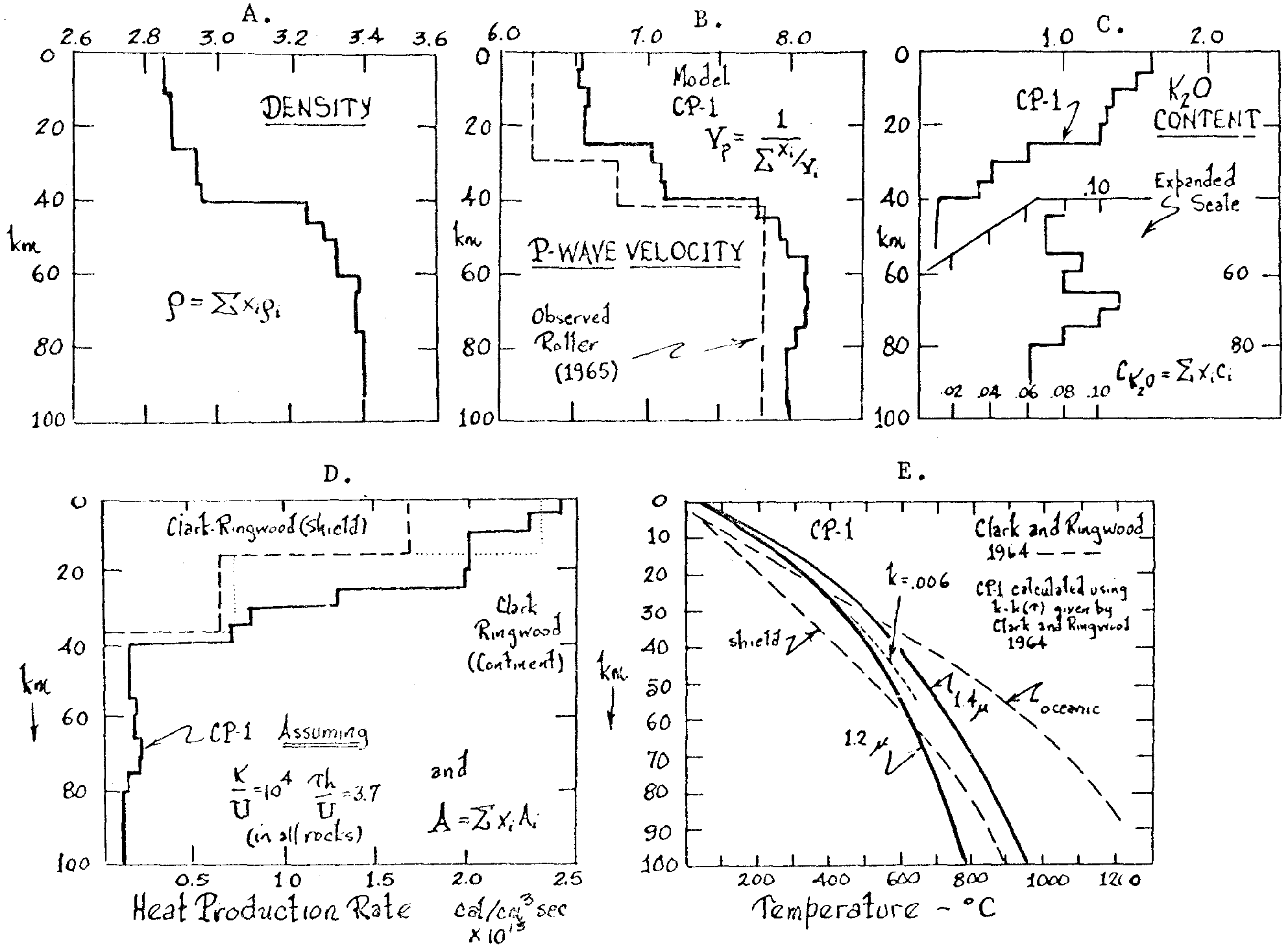

Figure 51. Some calculated geophysical properties of crustal-upper mantle model CP-1

the earth are: $K/U = 10^4$ and $Th/U = 3.7$. Using these ratios and the energies given by Wetherill (in Clark, 1966), for the decay of K, U, Th, the total radioactive heat production rates of rocks in CP-1 were estimated. The resulting heat production rate with depth is similar to, but somewhat "hotter" than that assumed by Clark and Ringwood (1964) for continental areas, and considerably hotter than their shield model.

Temperature estimates are of particular interest because of the inferred P-T conditions from clinopyroxenes in the kimberlite. Calculations of the steady-state temperature within the earth are common in the literature. Perhaps the most well known recent treatment of the problem is that of Clark and Ringwood (1964). Solutions to the heat flow equation for simple geometries are well known (Carslaw and Jaeger, 1959). The one-dimensional, steady-state solution for temperature as a function of position requires knowledge only of the surface flux, the conductivity and heat production as functions of position. Surface heat flow measurements in the region are not abundant but it is believed that the surface flux in the Colorado Plateau Province is near normal, about 1.2 to 1.4 cal/cm^2 (Roy, 1967, oral communication). The estimated radioactive heat production rate for model CP-1 has already been estimated. In general, the thermal conductivities of silicate rocks are not precisely known, especially at elevated temperatures. No determinations of thermal conductivity have been made on the specimens from CP-1. Clark and Ringwood (1964) attempted to estimate the change in conductivity with temperature for typical silicate rocks, taking into account radiative transfer at high temperature. (They note that hydrous phases greatly reduce the infra-red transparency of silicates due to the presence of O-H bonds. Since serpentines are inferred to be abundant rocks in the lower crust and, possibly, upper mantle, the thermal conductivity there might be anomolously low). Using Clark and Ringwood's (1964) estimate of thermal conductivity and the radioactive heat production rates developed above, steady-state geotherms for assumed surface flux of 1.2, and 1.4 cal/cm^2 sec were numerically calculated for CP-1. The results (Figure 51) show: 1) more curvature than Clark and Ringwood's (1964) results, which is due to the relatively higher radioactivity of model CP-1; 2) a surface flux in the range 1.2 to 1.4 cal/cm^2 sec which is consistent with the conditions of crystallization of the kimberlite clinopyroxenes, although there are examples which deviate from this steady-state curve (see Figure 46); 3) the possible effect of hydrous phases in the lower crust and upper mantle could alter the results somewhat. The dotted line in Figure 51E shows the deviation of the geotherm calculated for 1.2 surface flux for an assumed upper mantle conductivity of .006 cgs. The geotherm is deflected to higher temperatures. The effect of abundant serpentine near the Moho, however, probably would not displace the geotherm at greater depth by more than about 100° C.

This calculated geotherm can be compared with the experimentally determined boundaries of stability fields for mineral assemblages of interest. The geotherms for CP-1 (between 1.2 and 1.4 assumed surface flux) cross from the garnet-peridotite field into the spinel-peridotite field between about 14 and 16 kilobars (about 42 to 48 kilometers), using the experimental results of Boyd and MacGregor (1964). The recent results of Ito and Kennedy (1967) suggest that spinel-peridotite might not be stable along this envelope of geotherms at all.

The stability field of serpentine is intersected between 12 to 15 kilobars using the experimental results of Takenouchi, Kitahara and Kennedy (1966). This suggests that if water was present in an olivine-rich mantle at depths less than 45 kilometers, serpentine would be present.

Assuming equilibrium assemblages in the mantle, spinel-peridotite would be stable above about 50 kilometers and garnet-peridotite below. Both could be mixed with eclogite and pyroxenite. The peridotites, however, may be partially hydrated above 50 kilometers. Such a structure and composition is consistent with the observed anomolously low upper mantle P-wave velocity (7.8 km/sec) characteristic of the western United States. The observed P-wave velocity in the depth range 30 to 43 kilometers observed in the vicinity is 7.2 km/sec. If the mantle is anhydrous, crustal rocks must reach depths of 43 kilometers. However, if the mantle is wet, then serpentine may be stable above 50 kilometers which would suggest that the layer between 30 and 42 kilometers might be serpentinized or partially serpentinized peridotites. The abundance of antigorite-tremolite schist fragments (MRX-51) is consistent with this view. Also, the spinel-lherzolite specimen (MRX-2) collected was partially serpentinized. Modal analysis of this rock indicated that it was 18%

serpentine. Christensen (1966) studied seismic velocities of partially serpentinized peridotites. Using Christensen's results, the P-wave velocity of the spinel-lherzolite, approximately ($ol_{40}px_{40}serp_{20}$), would be about 7.5 km/sec, uncorrected for temperature. Thus, a slightly more sepentinized spinel-lherzolite (serpentine content 30%) would have a P-wave velocity (7.2 km/sec) quite like that of the 30 to 43 km layer under the Moses Rock dike.

Maxwell (Hess, 1955) originally suggested that the uplift of the Plateau could be due to serpentinization. 30% hydration of a 13 kilometer thick layer would account for about 1 kilometer of tectonic uplift. About 5 kilometers of Tertiary uplift is observed in the region. Thus, this layer is not sufficiently thick to account for the Tertiary uplift of the province. Hess pointed out that the volume increase due to serpentinization of olivine is approximately equal to the specific volume of water introduced. A similar volume increase would result if water were added to olivine and they coexisted as separate phases with no reaction. Thus one could speculate that the other 4 kilometers of uplift might be due to introduction of water or volatiles in the mantle at a level deeper than the level of the serpentine isotherm which, therefore, existed in equilibrium as free H_2O or fluid phase. So, for example, if a 100 km thick layer of upper mantle contained 1.2% by weight water (as a free phase), the mantle above 100 km would occupy 4% more volume than prior to the introduction of the water. This could account for the additional 4 kilometers uplift, although one is then left with the problem of accounting for the source of water.

The dehydration of titanoclinohumite to olivine and water would result in about 3% volume increase, assuming densities of 3.25, 3.3 and 1.0 respectively, and 2% H_2O content for clinohumite. If the deep upper mantle were entirely clinohumite, a 130 kilometer thick column must be dehydrated to account for 4 kilometers of uplift by this dehydration process. The TiO_2 content of the kimberlite is so low, however, that an upper limit on the clinohumite content in the reservoir is 2%. Unless low titanium humite group minerals exist in the mantle in abundance, this appears to be an insufficient source of vast amounts of water. Dehydration of other hydrous mineral phases, such as phologopite and amphibole (Oxburgh, 1963) might account for some water but neither seem as potentially attractive as the humite group.

Finally, it is clear that the history of these crystalline rock fragments is complex and involves plutonism, volcanism, a granulite-grade metamorphism, retrograde metamorphism, all prior to inclusion and transport to the surface in the erupting kimberlite. The episodes recorded in the textures of these fragments carry the imprint of the processes which were active deep in the crust and which ultimately were responsible for shaping the surface of the Colorado Plateau. The historical, tectonic, and geophysical significance of the data which might be extracted from these rocks is great, indeed.

The Moho

The location and petrographic and seismic definition of the Mohorovicic discontinuity in the western United States is somewhat ambiguous. Seismic P-wave velocities of 7.8 km/sec are reached at 42 kilometers in the vicinity of the Moses Rock dike, a value characteristic of the west. 7.8 km/sec is anomalously low for "mantle" rocks and the cause of the anomaly is not understood. This study suggests that the chemical transition from "crustal" rocks (rocks of mafic chemical composition, either gabbro or mafic, high-rank metamorphic gneisses) to true ultrabasic rocks (serpentine-schist, perhaps, pyroxenites, or altered spinel-lherzolite) could occur almost anywhere in the range 30 to 42 kilometers. Conceivably, the transition between basic to ultrabasic rocks could occur at any location between 30 and 43 because hydration is observed to be pervasive in the crystalline fragments and is apparently not a weathering feature imposed at the surface. If the degree of serpentinization was fortuitously that which would produce rocks of nearly equal seismic velocity across the interface, an important chemical change with depth need not be profound seismically. Hydrated ultramafic rocks are important members of the suite of dense or ultramafic rocks and the significance of the serpentine cannot be ignored.

The Mohorovicic discontinuity under the Moses Rock dike may occur in a petrologically complex region and possibly involved, not one, but three types of transitions: 1) phase transition involving mafic gneisses and eclogites, 2) possibly hydration of ultramafic rocks, and 3) chemical transition with depth from mafic crustal to true ultramafic rocks, peridotites and pyroxenites.

The upper mantle may be petrographically as complex as the crust.

Summary of Principal Conclusions of Petrologic Investigations

The microprobe investigations of mineral grains in kimberlite have shown that kimberlite minerals are compositionally unlike those in associated xenoliths, except for some overlap with a spinel-lherzolite fragment and with small mineral inclusions in pyropic garnets. The dense and ultramafic xenolithic fragments (except for the spinel-lherzolite) are apparently unrelated to the kimberlite and are considered to be accidental inclusions derived from the vent walls during the eruption.

Tentative P-T assignments to kimberlite clinopyroxene grains suggest their derivation over a significant depth range in the upper mantle extending to about 150 kilometers.

A plausible source for the kimberlite is physical disaggregation of both Al-poor and Al-rich assemblages in the mantle, believed to be spinel-lherzolite and garnet-lherzolite, plausibly in the ratio 30 to 70.

Titanoclinohumite may be an important member of the kimberlite assemblage and should be considered as an important site for water in the upper mantle.

The kimberlite was emplaced in a fluidized state apparently from a very large reservoir in the mantle as a volatile-solid system in which the volatile phase was mostly H_2O, supercritical at depth, and the solid phase, physically disaggregated mantle, primarily the rocks in the reservoir, spinel-lherzolite and garnet-lherzolite. No significant amount of silicate melt was present at the present level of exposure. No severe themal perturbation at depth is implied by the pyroxene data.

A model for the crust and upper mantle traversed during the eruption was constructed based on observations of the crystalline rock fragments and kimberlite. Apparently, there are systematics in the size-depth relationships of the crystalline rock fragments, similar to that in the sedimentary rock fragments derived from strata near the surface. The largest and most abundant crystalline fragments are meta-basalt, granite and granite gneiss. These rocks are believed to be abundant in the upper parts of the crust. Basic unfoliated meta-volcanics, retrograded basic pyroxene granulite, unfoliated and unaltered diorite and gabbro, and amphibolite grade rocks of basic to aluminous compositons are also abundant and probably form the middle and lower parts of the crust. The assemblage of crustal rocks is apparently meta-volcanic in origin rather than meta-sedimentary. The geophysical properties of this model have been explored and calculated geotherms are consistent with P-T inferences based on investigations of the clinopyroxenes.

The dense or ultramafic rock fragments which may be of mantle origin are serpentine schist, eclogite, jadeite-rich clinopyroxenite, spinel websterite and spinel-lherzolite. Although no garnet peridotite was observed as discrete rock fragments, its presence and importance are inferred from the composition of mineral grains in kimberlite and from the suite of mineral inclusions in pyropic garnets. All fragments except the spinel and garnet-lherzolite are believed to be accidental inclusions, not related directly to the kimberlite.

The Mohorovicic discontinuity under the Moses Rock dike apparently occurs in a petrographically complex region and may involve downward transitions between 1) basic pyroxene granulite to eclogite, 2) severely hydrated ultramafic rocks (serpentine schist) to slightly hydrated ultramafic rocks (spinel-lherzolite), and 3) predominantly basic rocks to predominantly ultrabasic rocks. The rock fragments observed in the dike suggests that all three petrologic transitions may be present suggesting that the Mohorovicic discontinuity may involve phase, hydration, and compositional changes. The variety of dense and ultramafic fragment types and the complex histories evident in their textures suggests that the mantle may be as complicated as the crust in terms of its composition and history.

The transition between spinel to garnet-lherzolite with increasing depth in the mantle as suggested by Boyd, Ringwood, and others, and recently by Ito and Kennedy (1967) appears to be consistent with the observations here.

The abundant serpentine schist fragments and abundant serpentine, titanoclinohumite, and possibly H_2O phase in kimberlite suggests that Maxwell (Hess, 1954) may have been correct in his speculation that the Colorado Plateau was uplifted, at least in part, by serpentinization of the upper mantle. This mechanism is insufficient to explain the entire uplift but perhaps the presence of supercritical water phase itself, deeper than the hydration isotherm accounts for the rest of the uplift. This underscores the possible great significance of the role of water to tectonics. It is in this context that the titanoclinohumite is interesting, because it is a possible site for water in the lower parts of the upper mantle. Virtually nothing is known about the high pressure stability relations in this system. Local concentration of volatiles apparently was important (and possibly was responsible) for the kimberlite eruption. It is probably also important in the genesis of the alkali basalts observed locally.

PART IV

MODE OF EMPLACEMENT

Introduction

The emplacement mechanism of volcanic necks, pipes and dikes, the origin of diatremes and kimberlite pipes and dikes are topics of long-standing interest (Daubree, 1891; Einarsson, 1950; Cloos, 1941; Geike, 1902, 1920; Williams, 1932; Goguel, 1953, 1956; Shoemaker, 1962; McBirney, 1959, 1963; Dawson, 1962; and many others).

Several mechanisms have been proposed to explain diatreme structure: 1) violent gas release, called explosive boring or gas coring, 2) churning caused by successive surges or pulses of magma, and 3) large-scale convection of magma in the vent.

The observations and conclusions of the previous two parts of this report permit some inferences to be drawn about the mechanism by which the Moses Rock dike was emplaced. It has been concluded that certain minerals in the kimberlite in the Moses Rock dike originated in the mantle. Here it will be suggested that the dike was emplaced as a violent fissure eruption of a fluidized particulate medium which, near the surface, was highly gaseous. Field relations suggest that the flow in the dike with time became channeled into a few vents, which probably formed maar-type volcanoes at the surface at the time of eruption. The mechanism of the eruption is believed to be a complex process involving gas-coring like that described by Shoemaker and others (1962) for the emplacement of the diatremes in the Hopi Buttes but different in some details.

The hypothesis for the mode of emplacement of the dike is developed in three stages. First the geological observations and inferences are reviewed. Next, calculations of fluid velocities for idealized hydrodynamic models of kimberlite eruptions are made which predict velocity and dike cross-sectional area with depth as functions of volatile content and initial dike width for steady eruptions. Finally, the sequence of events which produced the dike are reconstructed from the observations and theory.

The idealized hydrodynamic models of the eruption are calculated from hydrodynamic theory for flow and expansion in a vertical dike shaped duct where viscous effects are considered. These models are developed by constructing the P-V-T relationships of an idealized "kimberlite" which is assumed to be mixtures of water and solids initially at 1000° C, this permits the pressure-density behavior of such a mixture to be predicted as it erupts from depth to the surface. These estimates of velocity are then compared with fluid velocities required to transport the largest upward displaced rock fragment in the dike.

Finally, a step-by-step description of the inferred mode of emplacement of the Moses Rock dike is presented in which the events responsible for the observed structure are traced in some detail.

So, we will begin the discussion of the mode of emplacement by reviewing the important conclusions drawn from the geology.

Constraints on the Mode of Emplacement Based on Geological Field Observations

Much can be inferred directly from field observations about the emplacement of the Moses Rock dike.

The dike was propagated to the surface along a plane which approximately parallels the fold axes of the Comb Ridge monocline. It may have been a fault at depth, or alternatively, the dike could have propagated its own crack in a direction normal to the least principal compressive stress at the time. The dike cut across preexisting regional joints rather than being controlled by them. The relationships of the minor structures (folds, fractures, dikes and sills) in the dike wall rocks suggest that early in the sequence of events the fluid pressure exerted on the walls was sufficient to locally deform the rocks in the vent walls in a compressive sense and to forcefully intrude sills and dikes along planes of weakness. Subsequently, the fluid pressure exerted normal to the walls decreased and tensile fractures developed. Eventually the walls failed by spalling and slumping of large blocks into the dike. This process of failure of the dike walls was the fundamental process by which the dike widened. These large blocks from the dike walls, once included within the dike, became fragmented into smaller particles and this rock debris forms the bulk of the breccia in the dike. It was mixed with lesser amounts of minerals from kimberlite and rock debris from below. The systematic changes in the composition of the breccias suggest that the erupting material changed with time. The rock fragments from below, both crystalline and sedimentary types increased in size, and the amount of fragmental debris from the walls locally increased so that the kimberlite and crystalline fragments became more and more diluted. The particulate and mixed nature of the breccias indicates that they were emplaced in a fluidized state. As the eruption progressed the flow became restricted to progressively fewer and fewer channels along the dike and eventually flow was concentrated to several very well developed ones. It is believed that craters of the maar type developed at the surface, surrounded by an ejecta apron of kimberlite-bearing tuff.

This description of the sequence of events based on the geological field observations forms the observational constraints within which the hydrodynamic problem must be formulated. Turning now to that problem the kimberlite will be treated as a two-phase "fluid" consisting of solids and volatiles. Some numerical results will be obtained for fluid properties using the semi-empirical (engineering) equations for viscous flow in pipes for idealized models of kimberlite eruptions.

Hydrodynamics

The hydrodynamics of the movement of the kimberlite from the mantle to the surface through a duct, probably a dike, can be treated as a somewhat complicated case of fluid flow in a long narrow duct. From the point of view of the hydrodynamics problem, the important inferences drawn from the geology and petrology are 1) the kimberlite was emplaced from the mantle at or about 100 km and 1000° C, 2) the erupting material was a system consisting of particulate solid fragments of small size (averaging about 1 mm) and a fluid (volatile) phase, probably water, and very little or no silicate melt. It is implied that although the kimberlite was not a silicate melt, it moved to the surface as a fluid.

A Comment on the Nature of Fluidized Beds

It is important to review some of the well known characteristics of "fluidized" systems. As a fluid is passed upward through a bed of solids the fluid tends to buoy up the solids. When the fluid velocity is increased a sequence of much studied changes occurs in the system. As the particles become buoyed, they separate from adjacent grains, become agitated, eventually move relative to each other and finally are carried in suspension in the fluid. The whole assemblage takes on properties of a fluid. These effects are discussed in detail in the monographs on fluidization by Leva (1959), Zabrodsky (1963), Zenz and Othmer (1958), and the discussion by Reynolds (1954).

As upward fluid velocities become significant with respect to the free-fall velocity of particles in such a fluid and progressively increase , the system can be described as a "quiescent fluidized bed", "turbulent fluidized bed", and "dispersed suspension". The following descriptions are from Murphy (1949). A quiescent fluidized bed is a dense fluidized bed which exhibits little or no mixing of the solid particles. In a turbulent fluidized bed mixing of masses of solids takes place. The degree of mixing increases from the lower limit of quiescent-bed conditions to violent mixing depending on the dynamics of the systems. Such a bed can operate at a gas velocity below the free-fall velocity of the bulk of the particles, and it can also be maintained at a velocity materially above the free-fall velocity if a continuous feed of solids is supplied to the system. The upper boundary of such systems is generally diffuse. A dispersed suspension is a mass of solid particles or aggregates suspended in a current of liquid or gas rising past the particles which differs from a fluidized bed in that an upper surface is not formed. Particulate material is entrained in the gas.

In beds fluidized by a gas, rather than a liquid, channelling commonly develops in which a disproportionate quantity of the flow is carried along in a small number of preferred paths. Such paths, once developed, are self-sustaining.

It appears that the material in the Moses Rock dike attained a state described as a turbulent fluidized bed, and probably also as dispersed suspension. It also seems apparent that channelling was well developed.

Statement of the Hydrodynamic Problem Considered

In this section numerical solutions for flow models are obtained for viscous, compressible fluid flow using a constructed equation of state for the erupting kimberlite which takes into account expansion of the fluid phase as the pressure decreases as the erupting medium moves upward toward the surface. The calculations use the engineering equations for pressure drop in ducts to calculate fluid velocity and duct dimensions required for steady flow as a function of position (depth) for assumed initial volatile content and duct dimensions at depth. The volatile phase is assumed to be water; the solids, crystals of density 3.3 gm/cc. The results of the calculations for velocity are compared with velocity estimates made from field observations of large rock fragments transported upward in the dike.

In order to approach the hydrodynamic problem quantitatively, the following simplifying assumptions were made: 1) the flow is steady, 2) the mass ratio of solids and volatiles is constant, hence effect of fragments from the walls is ignored, 3) the eruption originates at 100 km and 1000° C, 4) no slip occurs between solids and volatiles, 5) heat transfer to and from the walls is ignored, 6) the fluid pressure (the pressure exerted on the dike walls normal to the direction of flow) is equal to the local load or lithostatic pressure, 7) the volatile phase is water, supercritical at depth.

This idealized model at best is a poor approximation because of the obvious complex nature of the eruption apparent from the field observations. While it is clear that the calculations are approximations, they are of some interest because they place plausible theoretical bounds on conditions during the eruption and permit some comparisons to be made with estimates of velocity based on field observations such as velocities required to transport large blocks upward in the dike, or with direct observations of erupting volcanoes.

Some of the apparent weaknesses in the calculated model are the following. It treats steady flow of a two-phase medium consisting of solids and water through a clean and stable duct or channel from 100 km to the surface. It is known that the composition of the breccia changed with time, the walls failed and debris was introduced to an extent that the intruding material became progressively more and more diluted with fragmental debris from the walls as the eruption continued. These observations imply that the instability of the walls grew progressively worse. The mineral constituents of kimberlite itself, apparently were derived from over a wide range in the upper mantle. The nature of the material as it left its original site in the mantle probably was different from place to place. The fluid pressure exerted on the dike walls probably differed from the assumed exact balance with the lithostatic load although probably by amounts not exceeding the tensile strength of the rocks. Time dependent fluctuations in pressure, especially short term ones, might have contributed to the instability of the walls as well.

Basic Equations of Hydrodynamics

In the mathematical description of a moving medium in three dimensions, the conservation of mass, momentum and energy, along with the equation of state of the medium, lead to six fundamental equations of hydrodynamics; three equations of motion from the conservation of momentum, and one each from the conservation of mass, energy and the equation of state. These six equations determine the six unknown quantities which characterize the motion, the three components of velocity, the density, pressure, and temperature or entropy (Stanyakovich, 1960).

In the Eulerian viewpoint (a coordinate system fixed in space), variables are expressed as functions of position and time. If a flow is assumed to be one-dimensional, then the fluid properties vary only with one coordinate parallel with the flow, and are assumed to be uniform across the flow. This does not imply that cross-sectional areas are uniform. A solution requires knowledge of the fluid properties as functions of position and time, which for one dimension can be written:

$p = p(Z,t)$

$\rho = \rho(Z,t)$

$u = u(Z,t)$

$T = T(Z,t)$

or

$S = S(Z,t)$

where

p = pressure

ρ = density

u = velocity

T = temperature

S = entropy

Z = vertical distance

t = time

According to Stanyakovich (1960), the one-dimensional conservation of momentum in a gravity field is:

$$\frac{\partial u}{\partial t} + u\frac{\partial u}{\partial Z} + \frac{1}{\rho}\frac{\partial p}{\partial Z} + g = 0 \qquad (1)$$

the continuity equation (conservation of mass):

$$\frac{\partial \rho}{\partial t} + u\frac{\partial \rho}{\partial Z} + \rho\frac{\partial u}{\partial Z} = 0 \qquad (2)$$

the energy equation (conservation of energy):

$$\frac{\partial S}{\partial t} + u\frac{\partial S}{\partial Z} = 0 \qquad (3)$$

the equation of state:

$$S = S\ (p,\ \rho) \text{ or } p = p\ (\rho,\ S) \qquad (4)$$

For steady isentropic flow the combined momentum and energy equations yield Bernoulli's equation which for incompressible flow is:

$$\frac{p}{\rho} + \frac{1}{2}u^2 + gZ = \text{constant} \qquad (5)$$

and for compressible flow:

$$\int \frac{dp}{\rho} + \frac{1}{2} u^2 + gZ = \text{constant} \qquad (6)$$

For fluid flow through long narrow ducts the effect of shear stresses are not negligible. Analysis of flow with friction requires solutions of the Navier-Stokes equations. Such solutions exist for only certain very simple cases. In engineering practice semi-empirical correction factors are applied to Bernoulli's equation to express the correction for viscous effects. This correction factor, known as the Fanning friction factor, C_f, appears in Bernoulli's equation (for incompressible flow) as follows:

$$\frac{p}{\rho} + \frac{1}{2} u^2 + gZ + \frac{1}{2} C_f \frac{L}{D} U_m^2 = \text{constant} \qquad (7)$$

where L is the length of the duct, D is its diameter, U_m is the mean velocity, and Z the vertical distance above the reservoir.

By making use of the simplifying assumption that the fluid pressure exerted on the walls normal to the direction of flow always equals the local lithostatic load we may write:

$$p = \rho_r \, g \, d$$

where r is the rock density, d the depth and g gravity. Let H be the depth of the reservoir from which the eruption originated. If the reservoir is large then the fluid velocity in the reservoir is negligibly small and if we set $U \sim U_m$, then we write Bernoulli's equation as:

$$\frac{\rho r}{\rho f} g \, (H-Z) + \frac{1}{2} u^2 \, (1+C_f \frac{Z}{D}) + gZ = \frac{\rho r}{\rho f} gH \qquad (8)$$

which upon rearrangement yields the velocity as a function of the distance, Z, above the reservoir:

$$u\ (Z) = \left[\frac{2\left(\frac{\rho r}{\rho f} - 1\right) gZ}{1 + (C_f \frac{Z}{D})} \right]^{\frac{1}{2}} \tag{9}$$

The Effect of Friction

From the previous expression it is seen that for incompressible frictionless flow ($C_f \approx 0$), the fluid velocity increases with duct length due to the increase in hydrostatic head. However, for flow in long ducts of real (viscous) fluids where $C_f > 0$, then the quantity $C_f \frac{Z}{D} \gg 1$, and the flow velocity becomes essentially independent of the length of the duct, as viscous losses just balance gain in hydrostatic head.

The friction factor, C_f, is a number which is correlated to the characteristics of the flow by the dimensionless Reynolds number, Re, where:

$$Re = \frac{\rho\ u\ D}{\mu}$$

and μ is viscosity. In general, C_f is a function of the Reynolds number. Moody (1942) studied the flow of fluids in rough pipes and found that in the regime of fully developed turbulent flow (high Reynolds numbers) that the friction factor is nearly independent of the Reynolds number and rather depends on the roughness of the pipe. Pipe roughness is conventionally expressed as relative roughness, ϵ/D, where ϵ is the magnitude of irregularities and D, the characteristic dimension of the duct, the diameter for a pipe of circular crossection. Figure 52 shows the friction factor as a function of Reynolds number and relative roughness. In the completely turbulent regime the friction factor, indeed is nearly independent of the Reynolds number over a wide range of conditions and depends only on relative roughness of the duct. In Figure 52, the Fanning friction factor, C_f, is plotted against relative roughness, ϵ/D, for fully developed turbulent flow. The friction factor changes by about a factor of 2 for an order of magnitude change in relative roughness. Thus, an error in the estimate of relative roughness produces a relatively small error in the friction factor. Moody's experiments were performed on pipes of circular crossection. Most kimberlite pipes become dike-form at depth. Thus it is relevant to inquire about the effect of roughness on flow in a dike compared to flow in a circular pipe of equivalent characteristic dimensions. The characteristic dimension of a dike would be its width, W. One might speculate that for fully developed turbulent flow that the effect of small roughness at the boundary is to create a layer of low velocity, thus the effect is proportional to the relative proportion of <u>cross-sectional area</u> occupied by the irregularities at the surface.

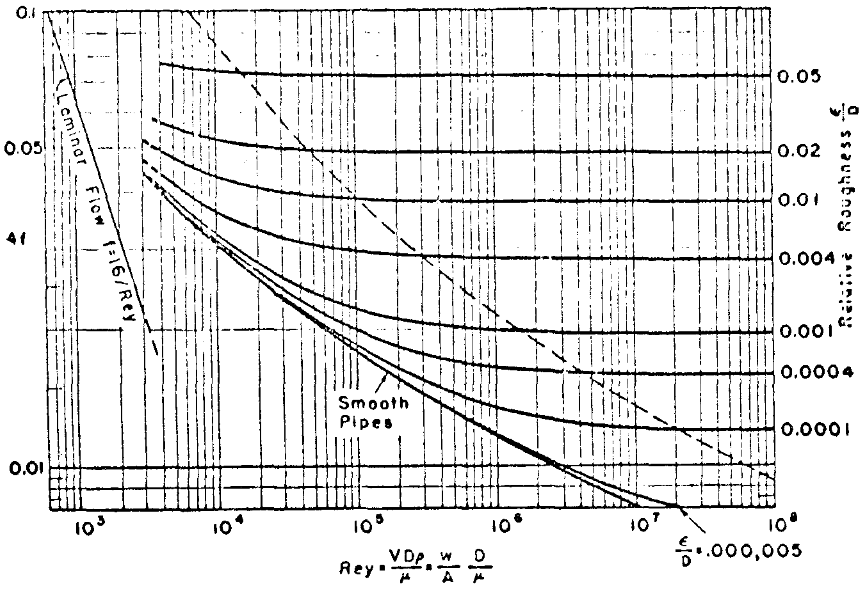

Friction coefficient versus pipe Reynolds number for incompressible, fully developed flow. Roughness of pipe is measured by ϵ,

Figure 52. Friction factor as a function of Reynolds number with relative roughness as a parameter

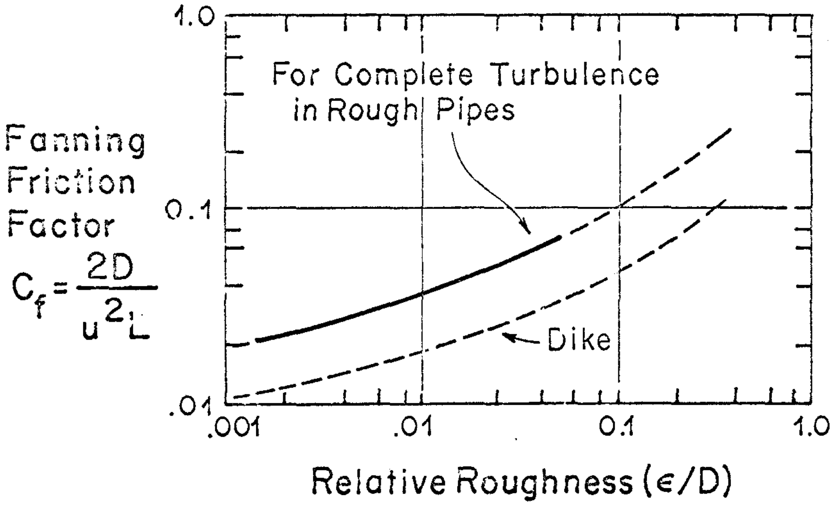

Figure 53. Friction factor as a function of relative roughness for completely turbulent flow, with correction for dike geometry

If so, it follows from geometry that:

$$\frac{\varepsilon}{W}_{\text{dike}} \simeq 2\,\frac{\varepsilon}{D}_{\text{circular pipe}}$$

where W = D and $\varepsilon \ll W$ or D. Thus, the frictional effect of a characteristic roughness would be twice as great on a circular pipe as on a dike of the same characteristic dimension.

One can only speculate on the precise three dimensional geometry and relative roughness of any volcanic vent, especially at depth. ε / D might range from 1/20 to 1/2, and perhaps 1/10 to 1/5 is a plausible estimate. Let us assume that $\varepsilon/D \sim 0.1$ to 0.2 and that a Fanning friction factor of about 0.1 is reasonable for fully turbulent flow in a typical volcanic dike or pipe.

Effect of Expansion of Volatile Phase (Equation of State):

The above expressions were developed for incompressible flow and the expansion of volatile-rich fluids near the surface cannot be ignored. If the equation of state of a fluid has a simple form, such as a perfect gas, then Bernoulli's equation can be integrated directly. If the equation of state is more complicated then the integration can be done numerically.

Relative to systems involving silicate melts and associated vapor phases, the erupting kimberlite may be significantly simpler, in that kimberlite apparently consists largely of a fluid phase and solid particles even at depth. In this case, no exsolution occurs and the pressure-density relation of the medium is relatively simple. The specific volume ($1/\rho$) of such a fluid-solid mixture is, simply:

$$v_m = x_f v_f + x_s v_s$$

where:

x_f = mass fraction of fluid

v_f = specific volume of fluid ($= 1/\rho_f$)

x_s = mass fraction of solid ($= 1-x_f$)

v_s = specific volume of solid ($= 1/\rho_s$)

ρ = density

If the fluid phase is H_2O or CO_2, a real gas, not a perfect gas, the P-V-T relations of such a two-phase medium still can be inferred using experimental data. The results have some relatively simple qualitative features. Let us assume the volatile phase is H_2O. At low pressures and moderate or high temperatures H_2O and CO_2 (or mixtures of the two) exhibit near perfect gas behavior (Kennedy and Holser, 1966; Greenwood and Barnes, 1966). (Figure 54). The presence of CO_2 has the effect of decreasing the specific volume of a water-rich fluid phase. At high pressures, between 10 and 100 kilometers, the specific volume of H_2O varies only slightly and is near unity.

The P-V-T relationships of H_2O (Figure 54) suggest that the hydrodynamics problem can be subdivided into several overlapping domains: at depth, a domain of incompressible, possibly essentially isothermal flow; at intermediate depths, a region of slightly compressible, but nearly isothermal flow; and near the surface a region of compressible adiabatic flow (Figure 55). At depth, the medium will be essentially incompressible, because water is essentially incompressible above 10 kilobars. As it flows from the reservoir some heat may be exchanged with the walls of the duct as it moves upward to regions of lower temperature, and some heat may be generated by

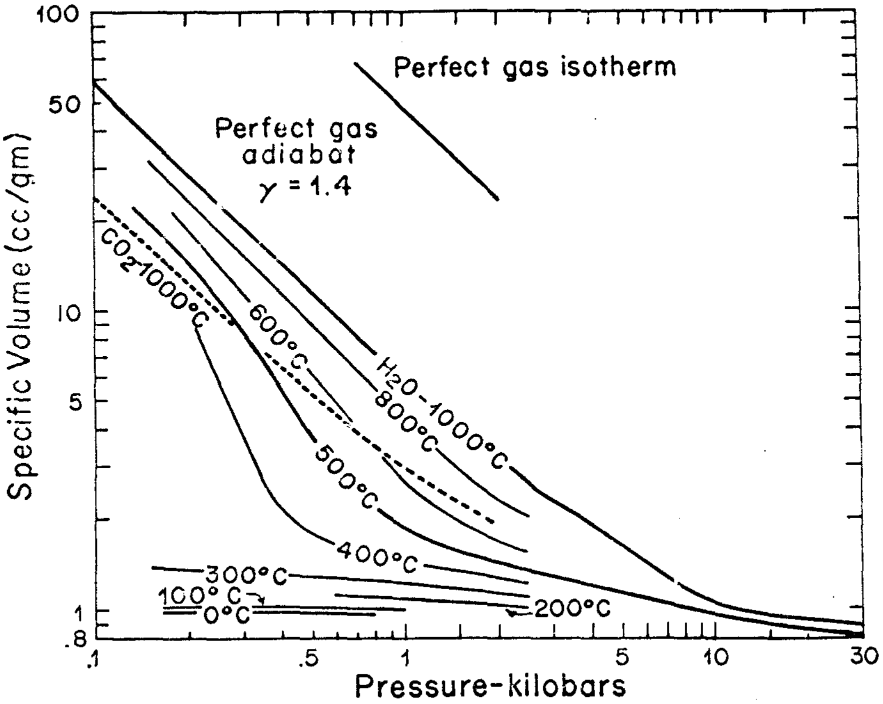

Figure 54. P-V-T relationships for water (Kennedy and Holser, in Clark, 1966)

internal friction or friction on the walls of the duct. The fluid phase, however, will have essentially a constant specific volume through a significant pressure range.

As the medium moves upward and the pressure decreases below 10 kilobars, the fluid phase will expand. Initially heat transfer between solids and the fluid phase is efficient since the volume occupied by the fluid is relatively small and the surface area of the solids is relatively large. Some cooling of the medium will occur because of the expansion of the gas, but this probably will be very minor because the mass fraction of the solid is large and the volume of the fluid still small.

As the medium rises toward the surface, the fluid pressure continues to decrease and expansion continues. The specific volume of the fluid phase increases until it equals and eventually greatly exceeds the volume occupied by the solid phase. The efficiency of heat transport between fluid and solid phase decreases until at some volume ratio, the fluid expands essentially adiabatically. Further expansion would proceed as if the fluid (gas) were expanding adiabatically, with no solids in the system. Flow in this regime is quite similar to the much-studied problem of two-phase flow in rocket engines where the gas-to-solid ratio is high (Rannie, 1962; Summerfield, 1959).

It is possible to graphically construct the P-V-T relations of mixtures of water and solids using the experimental results on P-V-T relations in water (Kennedy and Holser, 1966) and the equation $v_m = x_f v_f + x_s v_s$. In Figure 56, P-V-T curves are shown for mixtures

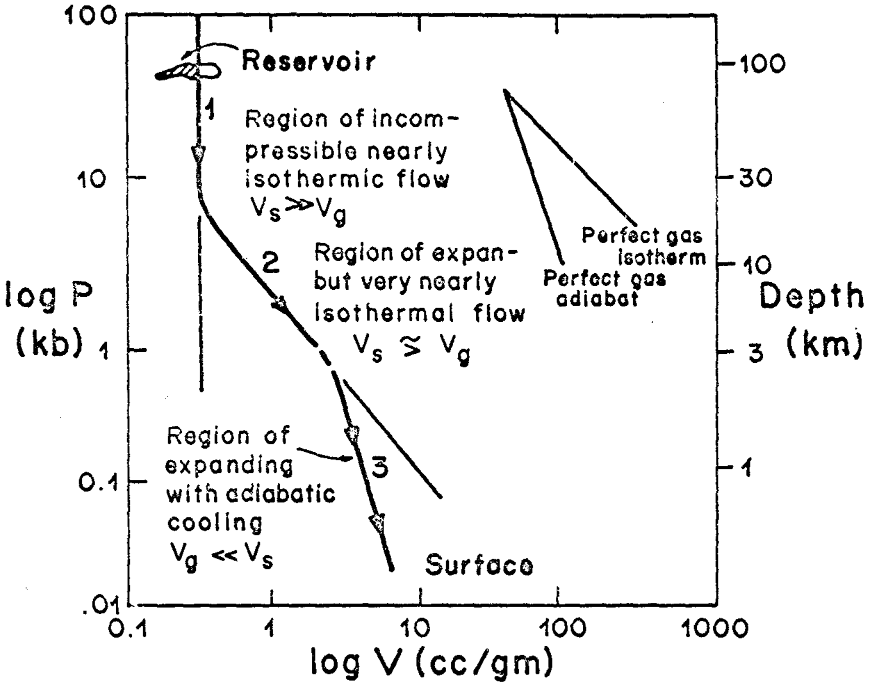

Figure 55. Schematic diagram of P-V-T relations in erupting two-phase system.

of water (at 1000° C) of various mass fractions (x_{fluid} = .01, .04, .10, .25 and .50), mixed with a solid of density 3.3 gm/cc.

The transition between isothermal to adiabatic expansion depends on the rate of gas expansion compared with the rate of heat transfer from solid particles to gas neglecting heat transfer to the dike walls as well as fragments derived from the walls. For the sake of illustration, if it is arbitrarily assumed that this transition occurs when the medium reaches 10 times its initial volume a second family of curves is generated which approximate the adiabatic expansion near the surface.

In the numerical calculations which follow, the pressure density curve used will be from Figure 56. Hence, it is (artificially) assumed that the fluid phase was water at 1000° C initially and that expansion was isothermal until the volume was 10 V_o after which expansion was adiabatic. Probably the fluid phase was cooler due to heat transfer to the duct walls and included fragments during eruption. The crossover from isothermal to adiabatic expansion would occur when heat transfer between the condensed and fluid (vapor) phases became relatively inefficient. Relative to other uncertainties, errors from this source are probably minor, since if one calculated models for both complete isothermal or complete adiabatic expansion the results would differ by more than a few percent only very near the surface.

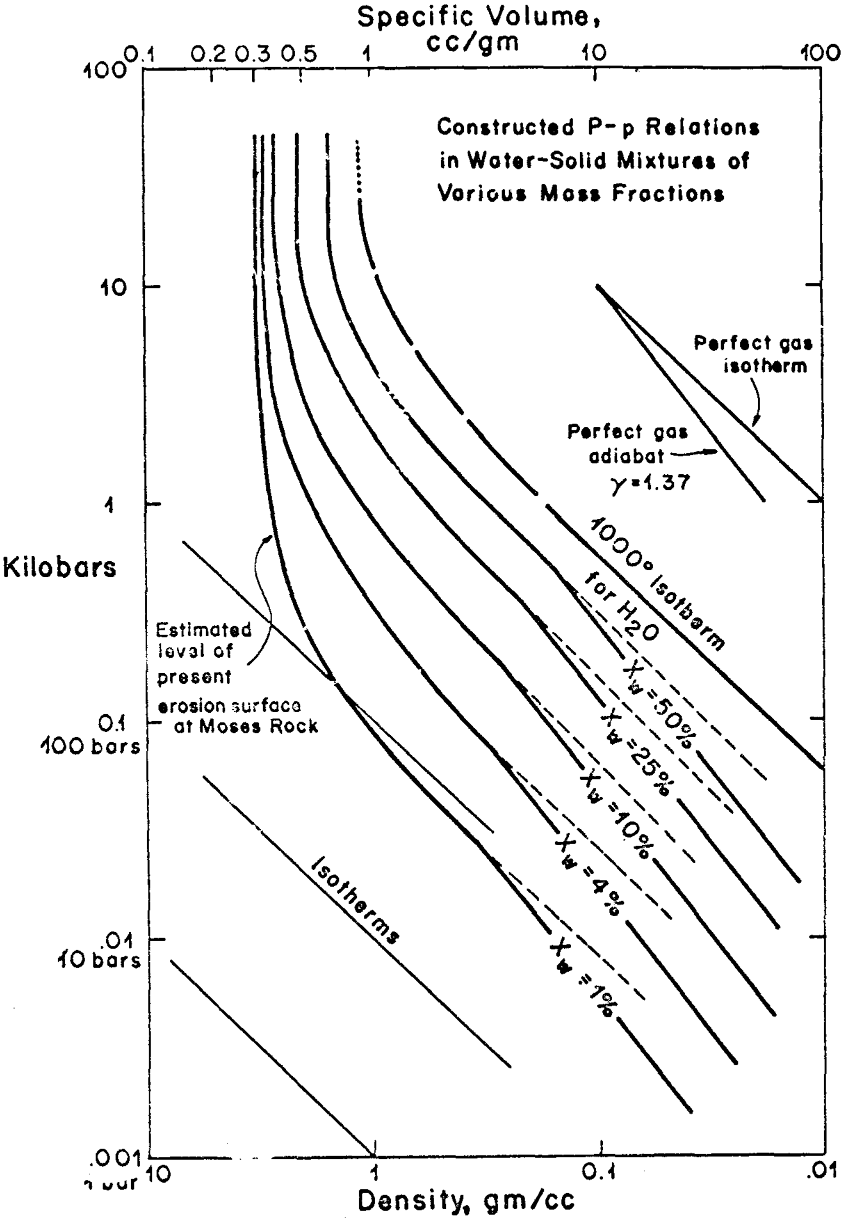

Figure 56. Constructed pressure-density relations in H_2O-solid mixtures of various mass ratios erupting from 100 km with an initial temperature of 1000° C

Numerical Solution for Fluid Velocity from the Hydrodynamic Models of Kimberlite Eruptions

The numerical solutions for the fluid velocity were obtained by subdividing the dike vertically into many small units, each of which could be treated as a short incompressible fluid flow problem. The approximate rock density is known as a function of depth. The fluid density used in the calculations is that described in the previous section (Figure 56). Flow velocity is calculated for each section of the duct using the modified Bernoulli equation (equation 9), and an assumed two-dimensional geometry (a dike). Equation 9 can be rewritten to express the velocity at one site along the dike, a short vertical distance, ΔZ , above another location in the dike where the velocity, u_0, is known.

$$u_1 = \left[\frac{2\left(\frac{\bar{\rho}_f (Z)}{\rho_r (Z)} - 1\right) g\Delta Z + u_0^2}{1 + C_f \frac{\Delta Z}{W_0}} \right]^{\frac{1}{2}} \tag{10}$$

In this equation the subscripts 0 and 1 refer to properties at the bottom and top of the short section of dike, and where ΔZ is the incremental distance measured vertically up the dike. $\bar{\rho}_f (Z)$ is the mean value of the fluid density in the depth range represented by ΔZ , W the dike width, and C_f the Fanning friction factor.

The conservation of mass requires:

$$W_1 = W_0 \left[\frac{(\rho_f)_0 \, u_0}{(\rho_f)_1 \, u_1} \right] \tag{11}$$

where W is dike width, ρ_f is fluid density, and u is fluid velocity. The above relations are written for a two-dimensional geometry (that is an infinitely long dike). For other geometries, such as a pipe of circular cross-section, the conservation of mass could be written in terms of cross-sectional area, A, and the Fanning friction factor, C_f, adjusted for that geometry.

The computations for velocity and dike width were made by solving equations (10) and (11) numerically in a step-wise fashion between 100 kilometers and the surface with a computer. The length of the segments near the surface were short commensurate with the relatively rapid change in fluid density.

Water content and dike width were varied as parameters. The cases considered included water contents (mass fraction water) of 4, 10, 25, 50% and dike widths at 100 kilometers depth of 3, 10, 30, 100, 300 meters. Numerical solutions were obtained for all the combinations of these parameters (see table below) and are included in Appendix E.

Initial Assumed Dike Width
Between 90 and 100 Kilometers

Mass Fraction Water	D_0, meters					
	3	10	30	100	300	3000
4%	A	B	C	D	E	-
10	Ⓕ	G	H	I	-	J
25	K	L	Ⓜ	N	O	
50	P	Q	R	S	Ⓣ	

Results of Numerical Calculations

Let us examine the results of the calculations for two contrasting models; cases F and T (cases F, M and T are shown in Table 25). Case F treats flow for a modest water content (x_w = 10%) in a thin dike (D_0 = 3 meters); case T, treats flow for a water-rich kimberlite (x_w = 50%) and a wide dike (D_0 = 300 meters).

In case F, the dike remains approximately 3 meters wide through most of the distance to the surface. The velocity is nearly constant through 90 kilometers varying between 10 and 15 m/sec. Near the surface the dike widens to 8 meters and the flow accelerates from 58 to 220 meters/sec between 1 kilometer and 50 meters depth. In this case, the kimberlite erupts at something over 200 meters per second; the velocity was nearly constant between 100 and 10 kilometers depth.

Taking the other extreme, a wide dike with a high water content (case T), the results are qualitatively similar but the larger initial width of the dike reduced the effects of frictional drag on the walls. The greater water content and lower fluid density greatly increased the acceleration near the surface. The flow velocity at depth is nearly 250 meters/second through most of the vertical distance and the dike width is nearly constant at 300 meters. Near the surface the velocity increases to 1500 meters/second and the dike flares to the enormous width of 7.7 kilometers.

The qualitative features shared by all the calculated models are: 1) fluid velocity and dike width are almost constant between 100 kilometers and 10 kilometers depth because gain in hydrostatic head is just offset by frictional losses on the dike walls, and 2) between

	Case F		Case M		Case T	
X_o W_o	10% 3 meters		25% 30 meters		50% 300 meters	
Depth	Velocity m/sec	Width m	Velocity m/sec	Width m	Velocity m/sec	Width m
50 m	222	8.7	750	282	1506	7750
100	174	7.8	672	185	1429	4600
200	122	5.8	573	126	1325	3050
400	91	4.8	464	91	1190	1920
1 km	59	4.0	318	63	1005	1137
2	39	3.6	227	53	795	881
6	22	2.9	121	36	498	440
10	16	3.0	76	33	392	377
20	10	3.9	65	35	288	332
40	10	3.6	54	33	236	297
60	12	2.9	58	30	247	275
90	11	3.0	57	30	226	300

X_o = mass fraction H_2O

W_o = dike width at 100 kilometers

Table 25. Results of numerical calculations for velocity and dike width for three eruption models

2 kilometers and the surface the dike width increases greatly and the velocity increases between a factor of 2 and 10 depending on the water content and geometry.

Since most of the acceleration takes place in the upper part of the duct, the surface velocity for an eruption originating at 10 kilometers will be quite similar to one which originates at 100 kilometers for equivalent water content and temperature. The reason is that most of the potential energy (hydrostatic head) is dissipated in viscous losses and not converted to kinetic energy. Most of the kinetic energy comes from expansion near the surface.

If changes in water content and dike geometry occur relatively slowly (ignoring the instability apparent from the field observations), then a sequence of steady-flow models would represent the <u>evolution</u> of the dike with time. There is no direct way of knowing how the volatile content would change during the course of an eruption, but one might speculate that early in the eruption the kimberlite was water-rich. It is plausible that as the eruption progressed the dike widened and as the reservoir was expended the water content of the erupting kimberlite decreased, hence the evolution of the eruption might be toward decreasing water content as well as increasing dike width with time. Such an evolution expressed in terms of a series of steady-flow models through a sequence might be consecutively cases P→L→H→D→E, or alternatively cases K→L→M→I→E. Call these, respectively, sequence I and sequence II. In sequence I, the water content decreases rapidly with respect to the rate of widening of the dike; in sequence II, the water content stays constant while the dike widens, then decreases late in the sequence. The velocity and dike width through these two sequences is shown in Figure 57.

In sequence I, the surface velocity decreases while the dike widens, reflecting the assumed progressive decrease in water content. Near surface velocities are of the order of 600 meters/second and decrease to about 400 late in the sequence. Meanwhile, the dike widens from about 8 meters to nearly a kilometer and a half. Deeper in the dike the velocity remains nearly constant while the dike widens through time.

The results for sequence II are rather different. For this sequence the water content is assumed to remain nearly constant while the dike widens initially. While the dike width at 100 kilometers increases from 3 to 30 meters, the near surface width increases from 16 to 280 meters and the surface velocity from 415 to 750 meters/second. Subsequently as the dike widens the water content is assumed to decrease from 25 to 4% and as a result the velocity decreases from 750 to 400 meters/second and surface width increases to over a kilometer.

The calculated geometry of these models can be compared to the observed geometric configurations of diatremes and kimberlite pipes. Maar type volcanoes as exposed in the Hopi Buttes commonly flare widely as they approach the surface. The kimberlite-bearing pipe at Buell Park apparently has a funnel shape. The pipes and dikes in the Monument Valley area are now exposed at about a mile below the surface at the time of their emplacement, thus their near surface geometric shape must be inferred. The diamond-bearing kimberlite

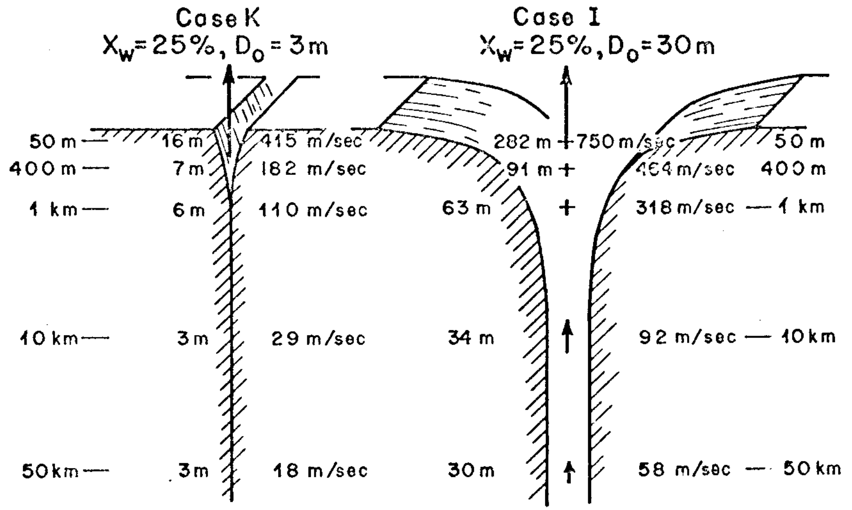

(A) Schematic drawings illustrating solutions for velocity and dike width for two cases of calculated kimberlite eruptions.

A) Schematic drawings illustrating solutions for velocity and dike width for two cases of calculated kimberlite eruptions

Figure 57. Selected Eruption Models

Figure 57 (Con't)

Eruption Sequence I P → L → H → D → E

	P		L		H		D		E	
X_w	50%		25%		10%		4%		4%	
D_o	3m		10m		30m		100m		300m	
	D(m)	U(m/sec)	D(m)	U(m/sec)	D(m)	U(m/sec)	D(m)	U(m/sec)	D(m)	U(m/sec)
50m	22	606	70	585	141	426	389	337	1581	397
400m	10	274	27	310	56	247	141	214	521	281
1km	7	179	19	195	42	173	98	153	330	219
10km	4	44	11	54	30	50	100	47	361	63
50km	3	26	10	33	29	39	96	42	271	70

Eruption Sequence II K → L → M → I → E

	K		L		M		I		E	
X_w	25%		25%		25%		10%		4%	
D_o	3m		10m		30m		100m		300m	
	D(m)	U(m/sec)	D(m)	U(m/sec)	D(m)	U(m/sec)	D(m)	U(m/sec)	D(m)	U(m/sec)
50m	16	415	70	585	282	750	661	535	1581	397
400m	7	182	27	310	91	464	222	364	512	281
1km	6	110	20	195	63	318	152	279	330	219
10km	3	29	11	54	34	92	99	90	361	63
50km	3	18	10	33	30	58	93	70	271	70

B) Flow velocity and dike width for two eruption sequences consisting of series of steady-flow models pipes of South Africa, however, have been mined to depths of about a kilometer and their shapes are well known. Williams (1932) shows sketches of the Kimberley Mine as well as maps of the pipe areas at various depths which show that the pipes commonly become dikes at depth, and their alignment suggests that they may join along a common fissure at depth. The geometry of the Kimberley mine has an upward-flaring shape, very similar to the calculated dike geometries. Also, the projections of wall rocks into the Kimberley pipe are about 20% of the pipe diameter. This would suggest a relative roughness, ϵ/D, of approximately .2, indicating that the Fanning friction factor of about 0.1 used in the calculations is reasonable.

One might inquire about which calculated model for flow velocity and water content is consistent with the geometry of the Kimberley Mine. The observed present surface diameter is 200 to 300 meters and at 1 kilometer depth, approximately 60 meters. The elevation of the original surface with respect to the present erosion surface is unknown, but the widely flaring shape suggests that it was not a great distance above the present surface. Assume the present surface to be the original surface. Of the models computed, the agreement in geometry is best for case M. The geometry of the Kimberley Mine and the calculated results for case M are shown on the next page.

	Kimberley Mine	Case M H_2O = 25% (mass) D_0 = 30 meters	
	Approximate Diameter (Meters)	Dike Width (Meters)	Flow Velocity (Meters/Second)
Near surface	~ 250	282	750
400 meters	~ 100	91	464
1000 meters	~ 60	62	318

Within the limitations of all the assumptions required to make computations, this result would suggest that the kimberlite erupted through the pipe at the Kimberley Mine at several hundred meters/second and reached the surface at velocities approaching a kilometer/second, and that the medium was very water-rich, closer to 25% than 10%.

A similar comparison will be made for the Moses Rock dike after the field evidence is reviewed.

Velocity Estimates Based on the Upward Transport of Large Blocks

The fluid velocity calculated from hydrodynamic theory can be compared with estimates based on field observations of large rock fragments in the Moses Rock dike derived from the vent walls and displaced upward from their original stratigraphic position. Whatever the physical properties of the medium were at the level now exposed at the dike, the erupting medium was capable of carrying a tabular block of Rico formation measuring 210 x 100 feet and at least 20 feet thick, 460 feet upward from its original stratigraphic position in the undisturbed dike walls. The fluid had to be moving upward at a greater velocity than the settling velocity of that block in the fluid. Thus the settling velocity of this block and other large blocks is a lower limit on the velocity of the medium. This block has the same surface to volume ratio of a sphere about 10 meters in diameter. The largest highly spherical blocks displaced upward are about 10 meters in diameter. It appears that the erupting medium at the Moses Rock dike was capable of transporting upward, spherical blocks 10 meters in diameter of density 2.4 to 2.7 gm/cc.

The settling velocity of a spherical object of known density in a fluid medium of known density is well known. It is generally expressed as a function of the drag coefficient, C_D, where drag coefficient is a function of the Reynolds number, $(Re=VD/\eta)$.

$$V^2 = \frac{4}{3}\,\frac{gD_p}{C_D}\left(\frac{\rho_s - \rho_f}{\rho_f}\right)$$

(Kay, 1963, p. 247)

where:

V = settling velocity of a particle

D_p= particle diameter

C_D= drag coefficient

g = gravity

ρ_s= density of the particle

ρ_f= fluid density

For relatively high settling velocity in a medium of low viscosity, the drag coefficient for spherically shaped particles approaches a constant value of approximately 0.4 (Schlichting, 1961, p. 9.9). In this flow regime (Newtonian) the settling velocity of particles of various size can be easily calculated if the densities of the particles and fluid are known.

The drag coefficient for non-spherical particles for high Reynolds numbers is greater than for spherical particles. Tek (in Streeter, 1961, p. 17-31) shows experimentally determined drag coefficients for different sphericities, ψ , defined as the ratio between the <u>surface area</u> of a sphere having the same volume as the particle and the actual surface area of the particle. These data show that for a high Reynolds number, a highly non-spherical particle could have a drag coefficient much greater than a spherical particle, hence non-spherical particles settle more slowly.

If the density of the erupting fluid were known one could estimate its velocity from Figure 58. Let us assume that the volatile phase in the erupting medium was water, its temperature was 400 to 500° C, the fluid pressure at the present level was equal to the lithostatic load, or about .25 to .40 kb, and the mass fraction of water was between 3 and 10%. For these assumptions the fluid density ranges from .7 to 1.9 gm/cc. The range of settling velocities corresponding to these densities are about 35 to 9 km/sec, respectively.

Another, perhaps less direct method of estimating the fluid density follows from the inferrence that the breccia in the dike was emplaced as a fluidized system. No satisfactory theory exists to explain the relationship between fluid parameters in fluidized systems. Published relations are empirical and are not valid outside the experimental range (Leva, 1961; Zabrodsky, 1963). Obviously, no experiments exist on the scale of the diatremes. Leva (1961) has observed that

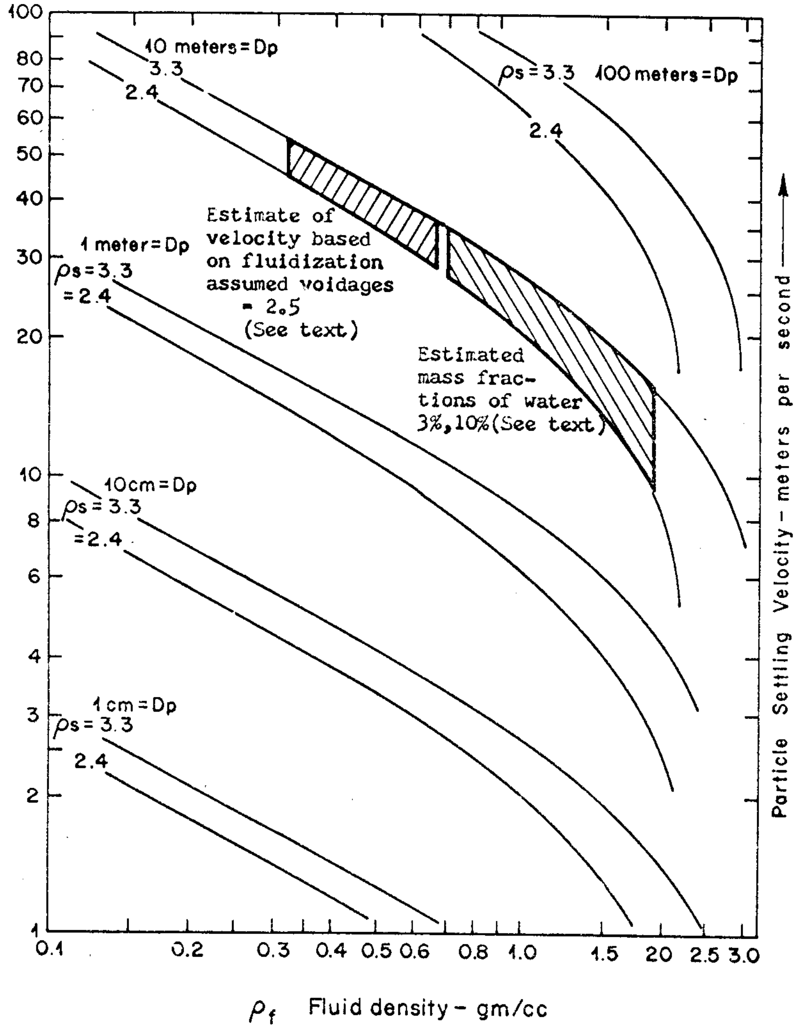

Solutions for velocity shown are for the equation:

$$V^2 = \frac{4}{3}\frac{1}{C_D}gD_p \quad \frac{\rho_s - \rho_f}{\rho_f}$$

where $C_D = .4$

Figure 58. Calculated terminal settling velocity of spherical particles at high Reynolds number

the minimum voidage necessary for the onset of fluidization is .4, where voidage is that part of the total volume occupied by voids filled with gas or fluid. So perhaps plausible values for the volume occupied by fluid phase might range from 20 to 50%. If the fluid medium was mostly water at about 400° C and .25 to .40 kb, its specific volume was between 2 and 6 cc/gm (Figure 59). The specific volume of such a mixture is:

$$v_{mixture} = \epsilon\, v_{fluid} + (1-\epsilon)v_{solid}$$

where:

v = specific volume, $1/\rho$

ϵ = voidage

Taking $v_{fluid} \cong 6$ cc/gm and $v_{solid} = .4$ cc/gm, we find that for $\epsilon = .5$, $v_{mix} = 3.1$ cc/gm or $\rho_{mix} = .32$ gm/cc and for $\epsilon = .2$, $v_{mix} = 1.5$ cc/gm or $\rho_{mix} = .67$ gm/cc.

These values of the fluid density are less than those of the previous estimates and suggest minimum fluid velocities of about 25 to 55 meters/sec (Figure 58).

Hence, minimum estimates of the upward velocity of the erupting medium at the Moses Rock dike, based on the upward displacement of blocks, range from about 10 to 60 meters/second. These velocity determinations are based on rather tenuous estimates of the density of the erupting material and the field observation that spherical blocks of about 10 meters in diameter were transported <u>upward</u>, relative to their stratigraphic position in the undisturbed walls.

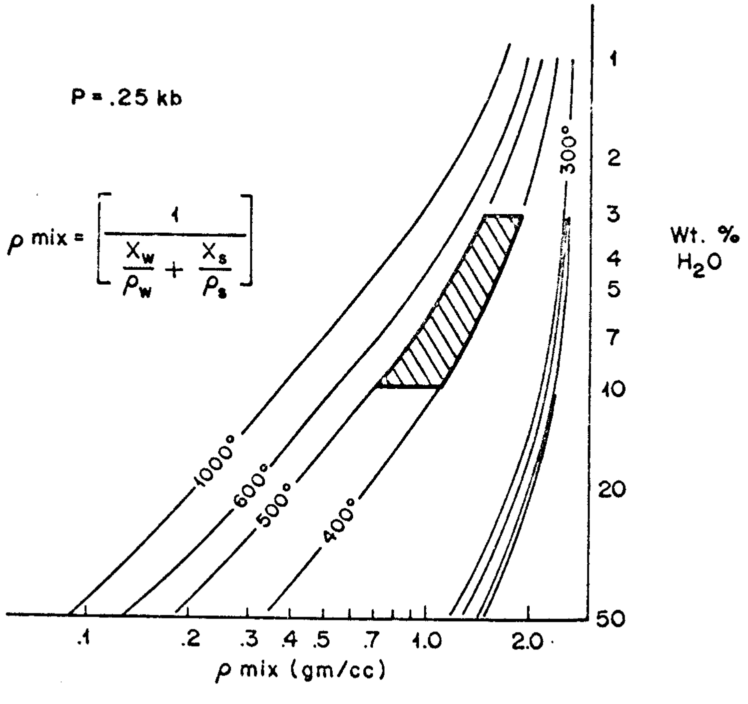

Figure 59. Calculated density of mixtures of water and solids (of density 3.0) at .25 at various temperatures

Comparison of the Models with the Moses Rock Dike

It is of interest to inquire which of the calculated hydrodynamic models is most consistent with both the configuration of the Moses Rock dike and the velocity estimates based on field observations. Taking a fluid velocity of about 50 meters per second, depth of about 2 kilometers and dike width of about 100 meters, several calculated models are fit reasonably well, especially cases D, I, and N (Appendix E). Case D is the best fit and its near surface properties are reproduced below:

Model D
Water Content, 4%
D_0= 100 meters

depth	width meters	velocity m/sec
50 meters	389	337
400 meters	140	214
1 km	98	153
2 km	88	106

The hydrodynamic model (Case D) would suggest that the craters over the channels in the Moses Rock dike were of the order of several hundred meters, perhaps half a kilometer in diameter, that the surface velocity may have been of the order of 300 to 400 meters/second, and that the water content was of the order of a few percent by weight (Figure 60).

Estimated near-surface conditions for the Moses Rock dike and Kimberley Mine are shown in Figure 60, based on the hydrodynamic model which seems most consistent with observation at each diatreme.

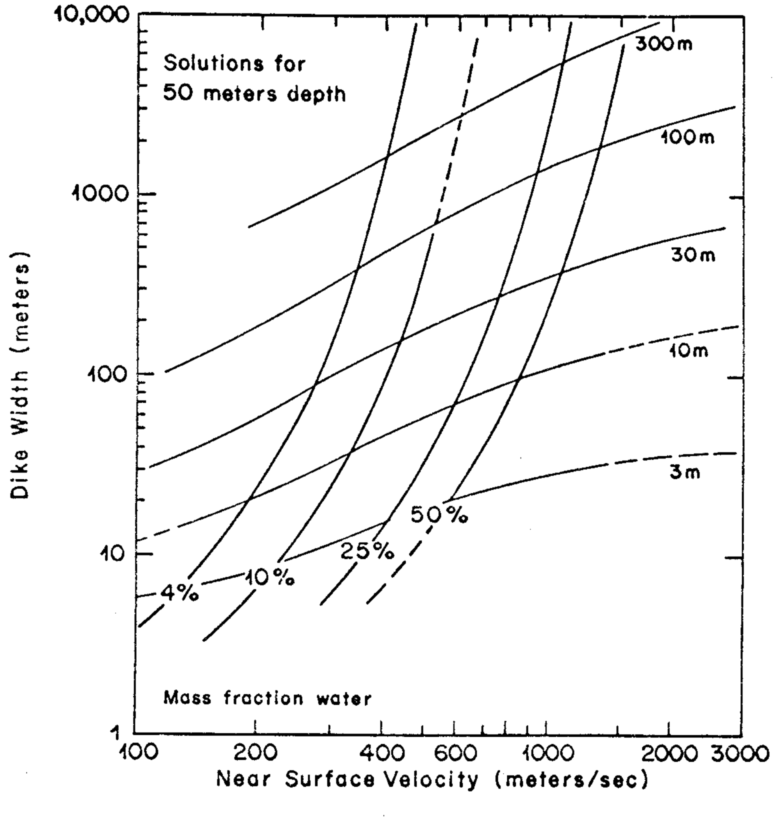

Figure 60. Solutions for near-surface velocity as a function of dike width near the surface with water content as a parameter

A Comment on the Reynolds Number

In all the calculations, a Reynolds number in the fully turbulent regime has been assumed. Both drag coefficient and friction factor are functions of the Reynolds number, hence it is important to confirm that the approximate value of the Reynolds number assumed is consistent.

The Reynolds number, Re, is:

$$Re \sim \frac{vd}{\eta}$$

v = velocity

d = characteristic diameter

η = viscosity of the fluid

The results just discussed suggest that:

$$V \sim 30 \times 10^{2} \text{ cm/sec}$$

$$d \sim 10 \times 10^{2} \text{ cm}$$

Kjelland-Fosterud (1959) and Bruges, Latto and Ray (1966) have investigated the viscosity of water at moderate temperatures and high pressures. The viscosity of steam at .3 kb and 400° C is approximately:

$$1 \times 10^{-3} \text{ poises.}$$

The viscosity of a mixture or slurry will be higher, perhaps 10^{-2} or 10^{-1}. Taking $\eta \sim 1 \times 10^{-3}$, we find $Re \sim 10^{9}$; or if $\eta \sim 1$, $Re \sim 10^{6}$. For $Re \sim 10^{6}$ to 10^{9} the flow is well within the turbulent regime.

Since the drag coefficient enters the settling velocity equation as a square root, the calculations could be in error by a factor of 2, in the extreme. This is probably unlikely. Errors in the friction factors are probably smaller, and due primarily to ignorance of the actual relative roughness.

Temperature of the Kimberlite Near the Surface

Boyd (1961) has shown that for a small ratio of gas to condensed phases and a reversible adiabatic process where thermal equilibrium exists between the phases, that the relationship between temperature and pressure is:

$$\frac{dT}{T} = \left(\frac{X_w R}{C}\right) \frac{dP}{\underline{P}}$$

where X_w is the fraction water, R is the gas constant, C the heat capacity. If $\underline{P} = \rho gx$, then we may write:

$$\frac{dT}{T} = -\left(\frac{X_w R}{C}\right) \frac{dx}{x}$$

Assuming X_w, R and C are constant, this becomes:

$$\frac{T}{T_0} = \left(\frac{x}{x_0}\right)^{-a}$$

where:

$$a = \frac{X_w R}{C}$$

and where x_0 is the depth at which adiabatic expansion begins, and T_0 is the temperature at that depth. This then is an expression for the temperature as a function of position. We can inquire what the temperature of the erupting kimberlite might have been at the present erosion surface (x = 2 km). The depth where the expansion starts (x_0) depends on the volatile content and temperature.

Taking values of x_0 shown below for various water contents $R \sim 2$ cal/°C mole and $C \sim 8$ cal/°C mole, and assuming $T_0 = 1000°$ C (1273° K), the resulting temperatures at the present erosion surface, T_s, are:

X_w	x_0 (km)	a	T/T_0	T_s (°C)
.50	30	.125	.71	631
.25	20	.063	.865	828
.10	8	.025	.966	957
.4	5	.010	.996	995

The approximation used is valid only for small amounts of gas but the results indicate that only a minor amount of cooling from the initial temperature could have occurred due to expansion. The lack of metamorphic alteration of included rock fragments and dike contacts precludes high temperatures. Hence, if initial temperatures at depth were as high as 1000° C, cooling must have occurred by other means, such as heat transfer to the duct walls at depth, or heat exchange with comminuted fragmental debris.

Results and Conclusions of the Hydrodynamic Models

The hydrodynamic models of kimberlite eruptions considered are highly idealized. The geological observations establish beyond doubt the complexity of the process by which the Moses Rock dike formed, hence the models treated must be limited cases, not necessarily similar in detail to any real event. However, the calculations suggest the following conclusions:

1) The flow velocity of kimberlite erupting from the mantle is probably controlled by a) viscous dissipation of potential energy by drag on the dike walls, and b) expansion of the volatile phase near

the surface. It is suggested that the flow can be subdivided into two or possibly three overlapping domaines. At depth, flow is nearly incompressible; near the surface it is nearly adiabatic and compressible, quite like a perfect gas. Numerical results for fluid velocity in the models show approximately constant flow rate between 100 and 10 kilometers; at 10 kilometers velocity begins to increase, and above 2 kilometers depth the flow velocity increased greatly due to the expansion of the volatile phase.

2) The stable channel shape for idealized steady flow has an upward divergent form, widely flaring near the surface.

3) Field observations of the largest blocks transported upward at the Moses Rock dike lead to estimates of the minimum upward flow velocity between 10 and 50 meters per second at the present erosion surface which is about one mile below the surface at the time of the eruption. The calculated eruption model most consistent with the field observations at the Moses Rock dike is Model D, assuming for Moses Rock that the present surface is 2 km below the original surface, channel width is 100 m and a fluid velocity of 55 m/sec. Model D has a water content of 4%, predicts a crater about 400 meters wide near the surface and a near-surface velocity of about 350 m/sec.

4) The calculated size and geometry of several models agrees well with the observed size and geometry of the pipe at the fabled Kimberley Mine, South Africa. The best fit was a model with 25% water by weight and suggests a fluid velocity of 318 m/sec at a depth of 1000 meters, 464 m/sec at 400 meters, and 750 m/sec near the surface.

Emplacement of the Moses Rock Dike

The hydrodynamic calculations have suggested some quantitative results for fluid velocity and dike shape for some very simplified models of the eruption of kimberlite. The geological field relationships provide much detailed information about the actual event. Let us attempt to integrate these ideas and observations and to reconstruct the specific event which produced the Moses Rock dike.

Petrologic observations indicate that mineral grains in the kimberlite at Moses Rock were derived from the upper mantle over a range extending to more than 100 kilometers. It is inferred that the kimberlite was emplaced from the upper mantle. In the upper mantle volatiles, H_2O and CO_2 primarily, coexisted with the solid mineral grains of garnet-lherzolite and spinel-lherzolite. Phases also present in the assemblage include at least one mica, titanium-rich clinohumite and possibly carbonate. The source of the volatiles is unknown but they are presumably derived from the earth's interior, perhaps from dehydration of deep seated hydrous phases such as clinohumite or amphibole. The geometry and size of the volume in the mantle from which the kimberlite was derived, that is, the "reservoir", are unknown but a plausible model is a large dendritic volume in which volatiles were accumulated in the intergranular intersticies of the rocks of the upper mantle to an extent that they occupied a significant fraction of the volume. The volatiles are believed to have existed as a free fluid phase, inferred to be H_2O and CO_2, with at most only a very minor amount of silicate melt.

The eruption is believed to have occurred as follows. The fundamental instability responsible for the eruption is the density contrast between the rocks outside the reservoir compared to the bulk density of the material within it. As the volatile phase accumulates in the reservoir, stresses develop at its boundary due to the formation of a hydrostatic head whose magnitude is $\Delta\delta$ gh, where $\Delta\delta$ is the density contrast and h the vertical extent of the reservoir. When this stress exceeds the tensile strength of the surrounding rocks a fracture is propagated into them, in a way similar to hydraulic fracturing of reservoir rocks in oil production practice. The direction of propagation of the fracture depends on the state of stress in the rocks, and generally parallels the least compressive stress. Unless the maximum principal compressive stress is oriented vertically, the fracture would propagate up the lithostatic gradient toward the surface and fluid flow would set up in the crack.

Initially the fluid flowing behind the tip of the propagating crack exerts pressure on the walls in excess of the local load, the dike dilates and apophyses are injected along planes of weakness in the surrounding rocks. In the early stages, the fluid probably consists mostly of volatiles with minor amounts of entrained particulate solids from the mantle.

As the erupting fluid approaches the surface it expands greatly and flow velocities increase in response to this expansion. When the surface is breached the fissure probably carries mostly gas, with some entrained fragmental debris derived from the walls. The mechanics of the process to this point are probably very similar to the blow-out of gas wells, well known to petroleum and drilling engineers. In those serious gas well blow-outs in which the flow becomes concentrated outside the well casing, the entire string can be extruded and the crater produced by the ensuing flow is similar in form to volcanic craters of the maar type.

At depth within the dike during its early stages of formation the flow velocity will adjust itself to a value such that the decrease in pressure on the fluid will roughly be balanced by frictional losses induced by shear on the vent walls and within the moving fluid. Flow is probably quite unsteady and the conditions unstable. The duct walls are subjected to abrasion by the fluid, highly charged with solid debris, and to fluctuating fluid pressure. The strength of the duct walls certainly varies from place to place and the relatively weak portions probably fail most readily. The means of failure of the walls is probably complicated and involves several processes, including abrasion, plucking, slumping or spalling, and injection of fluid into cracks or planes of weakness. The fluid pressure exerted on the walls never greatly exceeds the local load plus the effective tensile strength of the rocks because such pressure excess results in forced injection of fluid into the vent walls.

As the dike widens viscous drag on the walls decreases because the ratio of wetted to cross-sectional area is decreasing. The result is an increase in the fluid velocity, and consequently a decrease in the fluid pressure exerted on the duct walls by the fluid normal to the direction of flow due to the Venturi effect. Also, a pressure decrease may be propagated downward, as a wave, from the surface when the surface is breached by the eruption. When the pressure decrease becomes severe, tensile fractures form in the walls parallel to the contact and blocks begin to slump and spall into the flow. At depth slope failure may be violent as in rock bursting in deep mines. The medium flowing from the reservoir now becomes progressively more charged with solids and erosional capacity of the medium increases.

With time the instability of the walls becomes progressively more severe. As walls fail throughout the length of the dike the rock fragments introduced into the flow are comminuted by abrasion and impact and transported in the flow according to their size, shape and density. The fragmentary rock debris are thoroughly mixed with the mineral fragments from the mantle. With time these mineral fragments become progressively more and more diluted with rock debris from the walls.

Near the surface as the eruption progresses, larger fragments from deeply buried formations appear. The erupting material is now largely fragmental rock debris from many sources, mixed with minor amounts of mineral grains from the mantle, all carried upward in gas. The flow becomes concentrated into well defined channels along the dike, over which craters form, surrounded by ejecta of blocks, fragments and some kimberlite-tuff.

Eventually the volatiles in the reservoir are expended and flow in the dike ceases. The solid particles collapse into the vent, the cloud of debris in the air settles out, and locally the vent walls collapse by slope failure near the surface.

Post eruption alteration of the crater includes further slumping. Probably loose material would be washed down the slopes and into the bottom of the crater. Eventually erosion removed the blanket of ejecta thrown out of the crater, and after a long time erosion revealed the Moses Rock dike at its present level, about a mile below the surface at the time of eruption.

Sequence of Events Shown on Schematic Diagram of the Eruption

The inferred sequence of events during the emplacement of the dike, summarized schematically in time-depth coordinates in Figure illustrates some major points discussed above.

The reservoir can be visualized as a vessel which is maintained at a constant pressure, the local lithostatic load pressure, by a piston at ① . This is equivalent to saying that the mantle rocks have very little strength near the reservoir and could not support a void.

The duct leading from the top of this reservoir is closed by another piston ② which in the simplest model has a force applied to it which equals the local load plus the effective strength of the rock. This piston represents the tip of a fracture. Its location is meta-stable since for a small upward displacement ΔZ, an unbalanced hydrostatic head equal to the amount, $\Delta\rho g \Delta Z$ will be exerted on the piston from below and it will be accelerated upward. As the fracture propagates, the movement of the fracture toward the surface traces a line in time-distance space ③. Velocity in this diagram is the inverse of the slopes of lines. A vertical line would mean an infinite velocity; a horizontal line, zero velocity.

In the mantle below 10 kilobars, the medium is essentially incompressible and the crack will propagate at nearly constant velocity depending on the duct geometry. Fluid flowing through the duct behind the moving fracture traces lines in time-distance space as represented by the dotted lines ④. As the fracture approaches the surface the fluid begins expanding and accelerating, breaking through at high velocity ⑤. As material flows from the reservoir the volume of the reservoir decreases ⑥.

Fluid particle velocity increases as the duct is forced open and viscous drag decreases. Fluid pressure on the vent walls decrease eventually just equalling the local lithostatic load ⑦. As velocities continue increasing the walls begin to fail and particulate debris is introduced into the flow ⑧.

A fragment of mantle rock introduced into the flow at ⑨ will be carried upward or will sink depending on its size. Very fine debris will be carried along essentially at the fluid velocity. A moderate-sized fragment would be carried upward but would travel at some velocity less than the fluid particles since it is sinking relative to the fluid. It may undergo abrasion and comminution on the way to the surface. A huge block of the same material might sink. Large blocks could be smashed to fragments by impact with other particles ⑩ and the fragmental debris would be carried along according to its size, density and shape.

Fragments introduced into the flow, higher in the vent as at ⑪, for example, would rise or sink in the flow as determined by the local fluid properties and their size, shape and density. The path lines followed by fragments of various size are shown. We will return to discuss this point after describing the termination of the eruption.

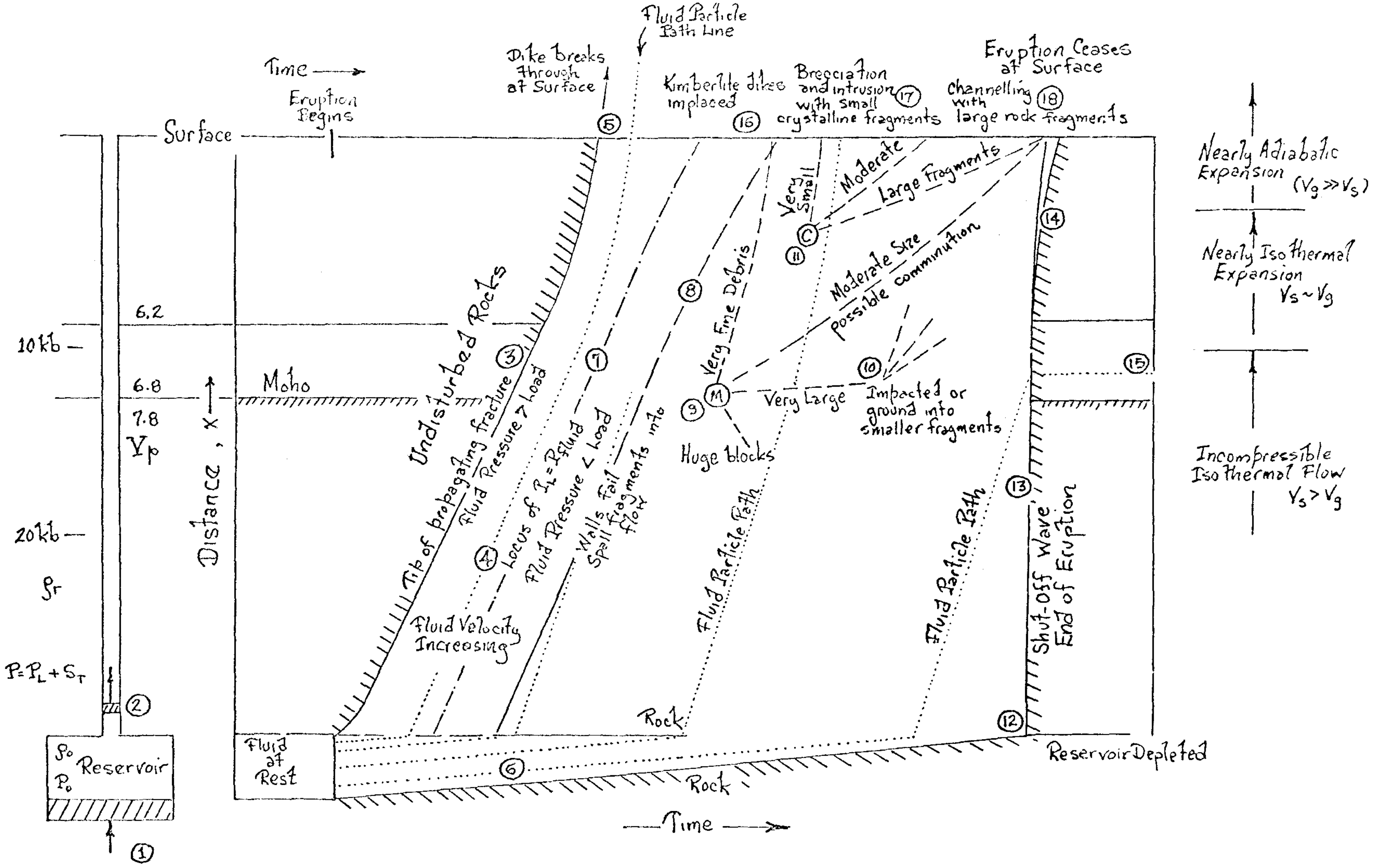

Figure 61. Schematic diagram showing time-depth relationships during eruption which produced the Moses Rock dike

When the fluid in the reservoir is expanded ⑫, an expansion wave propagates upward through the medium in the duct, which causes the flow to cease. In the lower part of the duct in the incompressible regime, the acoustic velocity of the medium is high and the "shut-off" wave propagates upward very rapidly ⑬, perhaps at several kilometers per second. In the expanded region near the surface where the velocity is greater and the pressure and density lower, (and the acoustic velocity perhaps somewhat lower) the shut-off wave may propagate slightly more slowly but still at a large velocity ⑭. A particle traced through this shut-off would follow a path as shown by ⑮. Having left the reservoir it had propagated toward the surface but was decelerated and stopped by the passage of the expansion wave which produced the shut-off. Through future time, then, this particle will reside at ⑮ unless displaced.

An observer at some time after the eruption who investigates the crystalline rock fragments near the surface will collect debris which was transported from below. It has been inferred from the geological observations at Moses Rock that various stages of the eruption are preserved at different localities. Thus, at localities inferred to represent relatively early stages in the eruption (Cross Section 41, for example) one would see material represented by point ⑯. Therefore, only small fragments of crystalline rock mixed with kimberlite are observed. At localities where the eruption became slightly more mature ⑰ and early channelling developed (Cross Section 25, for example), moderate-sized fragments of crystalline rock are observed. Where the eruption was most mature (as in the well-developed channel shown in Cross Section 37), the observer can sample fragments representative of point ⑱. At this locality he observes large blocks of crystalline rock fragments derived from ⑪, and moderate-sized mantle fragments derived from ⑨. The detailed history of fragments from various sources is undoubtedly complicated. The collection of fragments observed at one place represents an array derived from many localities introduced at different times. This accounts for the apparent observed inverse size-depth relations in the rock fragments in the Moses Rock dike.

PART V: SUMMARY

The Moses Rock dike is a superbly exposed, four mile long, kimberlite-bearing, breccia filled intrusion in the east central Colorado Plateau, one of eight known kimberlite-bearing diatremes in the province. Kimberlite pipes and dikes are of great interest because kimberlite and certain crystalline rock fragments contained in the breccias filling these structures are believed to originate in the mantle, therefore provide geologists with deep seated rocks at the surface.

Included in this report are descriptions and discussions of 1) field geology, 2) petrology of the kimberlite and crystalline rock fragments, and 3) hydrodynamics of the emplacement of the kimberlite. Field studies included detailed mapping of the dike at 1:2400 scale and extensive sample collection of the breccias and crystalline rock fragments. Mapping was concentrated on the interior structure of the dike and its contact with the wall rocks. Petrologic investigations included reconnaissance petrography, whole-rock chemical and trace element analysis of 15 representative specimens, and extensive microprobe analysis of minerals from the kimberlite and ultramafic or dense fragments. Of special interest are microprobe investigations of mineral inclusions in pyropic garnets. Theoretical analysis of the hydrodynamics of the eruption includes computer solutions for 20 idealized steady-state, two-phase kimberlite eruptions which yield fluid velocity and stable dike geometry as functions of depth.

Field investigation revealed much about the structure of the dike and has provided information about its mode of emplacement. The dike parallels the Comb Ridge monocline, an important regional structure. It has steeply dipping contacts with undeformed and unmetamorphosed Permian red beds which form the dike walls. A system of joints parallels the contact everywhere. The dike is filled with breccia; 12% consists of mineral grains derived from kimberlite, mostly dispersed throughout mixed debris in the various breccia units. Kimberlite as a discrete rock occupies only about 1% of the area within the dike. 72% of the fragments are derived from the Cutler Formation, the strata now at the walls; 12% are limestone fragments from the underlying Paleozoic strata; and 3% are crystalline rocks from farther below. About 1% of the crystalline fragments are dense or ultramafic rocks. Relationship of the breccia units suggests that channels developed through which flow was concentrated. In these channels upward displaced blocks are large, the degree of dilution of kimberlite with debris is great and the crystalline rock fragments are large. Craters probably developed at the surface over the channels. The surface was at least 1500 (and probably about 5000 feet) above the present erosion surface because blocks are observed displaced downward this distance. The age of the intrusion is not precisely known, but is probably older than 10 but younger than 60 million years old. No silicate melt was present at the level now exposed. Kimberlite and other intrusive breccias were probably emplaced in a fluidized state consisting of volatiles and solids. The breccias are particulate on all scales, have size frequency distributions like comminution curves, are intricately mixed, and the mineral components of kimberlite are commonly highly diluted in the breccias. Apparently the dike was emplaced as a fissure eruption along which channels developed as the eruption progressed. The largest spherical fragments displaced upward are limestone blocks about 10 meters in diameter.

A reconstruction of the column of crustal and upper mantle rocks was made on the basis of size and abundance of crystalline rock fragments. There is an observed inverse relationship between the size of fragments derived from the underlying Paleozoic strata and now observed at the present surface in the dike and the distance these blocks have been displaced upward from their original stratigraphic position in the undisturbed vent walls. If a similar relationship exists within the crystalline rock fragment population, then it provides an empirical rationale for reconstruction of the vertical stratigraphy of the long column of crystalline rocks between the reservoir and the surface. Using statistics gathered in the field on size and relative abundance of the crystalline rock fragments, a crustal-upper mantle model has been constructed. In this model, called CP-1, meta-basalt, granite and granite gneiss are abundant near the surface, diorite, gabbro and mafic amphibolite constitute intermediate zones in the crust and retrograded mafic pyroxene granulite (plagioclase-pyroxene±garnet gneiss) is abundant at depth in the crust. The population of crystalline fragments of apparent crustal origin is predominantly metavolcanic or metaplutonic, rather than metasedimentary in origin.

Dense and ultramafic fragments of possible mantle origin were studied in more detail. Included in the suite of possible mantle rocks, in decreasing order of relative abundance are: antigorite-tremolite schist, jadeite-rich clinopyroxenite, eclogite, spinel-websterite, and spinel-lherzolite. Pyroxenites are more abundant than peridotites. Although no garnet peridotite was observed as discrete rock fragments its presence is inferred from the suite of mineral inclusions observed within pyropic garnets.

It was concluded from the microprobe investigations of mineral grains in kimberlite, that the kimberlite minerals are compositionally unlike those in the associated xenoliths except for the spinel-lherzolite fragment and the mineral inclusions in the pyropes. All but the spinel and garnet peridotite are believed to be accidental inclusions derived from the vent walls during the eruption and are apparently unrelated to the kimberlite in any direct way. A plausible source for the kimberlite is physical disaggregation of mantle assemblages with Al-rich and Al-poor pyroxenes believed to be spinel-lherzolite and garnet-lherzolite approximately in the ratio 30:70.

Tentative P-T assignments to kimberlite clinopyroxenes suggest their derivation over a significant depth range in the upper mantle extending to about 150 kilometers. Indicated temperatures at 150 kilometers are modest, about 900° C.

Titanoclinohymite is present in kimberlite and as an inclusion in a pyropic garnet. Minerals of this dense hydrous group should be considered as a possible important site for water in the upper mantle.

The observed rocks and microprobe data suggest that the Mohorovicic discontinuity under the Moses Rock dike may occur in a petrologically complex region and may involve three types of downward transitions: 1) mafic pyroxene granulite gneisses to eclogite; 2) serpentine schist to slightly hydrated spinel-lherzolite, and 3) predominantly basic to predominantly ultrabasic rocks. The data are consistent with a lower crust composed of hydrated ultramafic rock (serpentine) and mafic garnet and plagioclase-bearing gneiss and an upper mantle of partially hydrated ultramafic rock, mixed with eclogite and pyroxenite. A downward transition from spinel-bearing to garnet-bearing peridotite assemblages in the upper mantle suggested by experimental phase petrology is consistent with the observations at the Moses Rock dike and supports the view that the minerals and rocks in the dike were derived over a great vertical distance. The variety of types and the complex textures observed in the ultramafic rocks suggests that the upper mantle may be as complicated as the crust in terms of its history and composition.

The numerical hydrodynamic models for the eruption of kimberlite show that the flow is controlled by viscous drag on the dike walls and the expansion of the volatile phase near the surface. In the models, velocity and dike width are nearly constant at depth but the dike flares near the surface into the shape of an upward-divergent nozzle and the computed fluid velocities increase greatly near the surface. Field observations of large blocks displaced upward in the dike suggest flow velocities of 10 to 50 m/sec at the present surface (for assumed fluid densities believed to be plausible). Using the theoretical models to extrapolate this upward suggests a near-surface velocity of about 350 m/sec and a dike width of 400 meters for the

Moses Rock dike over the channels.

Finally, geological and petrological observations and the hydrodynamic models of the eruption are consistent with the following view of the origin and emplacement of the Moses Rock dike. The eruption originated from a large reservoir in the mantle, driven by a volatile phase, mostly H_2O, supercritical at depth. The mineral constituents of kimberlite consists of physically disaggregated mantle, primarily the rocks in the reservoir, spinel-lherzolite and garnet-lherzolite. Since no large thermal perturbation is implied by the pyroxene data, it is believed that the eruption was caused by a localization of volatiles in the mantle, perhaps derived from the dehydration of dense hydrous phases in the lower parts of the upper mantle. The erupting kimberlite could have propagated its own fracture or it could have flowed along a preexisting zone of weakness toward the surface. The kimberlite and other breccias filling the Moses Rock dike were emplaced in a fluidized state, consisting of volatiles and solids. Apparently the dike walls were highly unstable during the eruption and probably failed in a progressively more severe way as the eruption progressed, producing breccias composed of more and more debris from the walls. The hydrodynamic models suggest that the flow velocities were modest at depth due to viscous losses but that expansion of the volatile phase near the surface resulted in large flow velocities at the surface. The inferred surface expression of the dike is a chain of several well developed maar type craters.

APPENDIX A

Analytical Techniques

Whole Rock Chemical Analyses:

The Analytical Branch, U. S. Geological Survey, Denver, Colorado, provided the major and trace element analyses by gravimetric and spectrographic methods. Specimens selected for chemical analysis were taken from a suite of crystalline rock fragments collected at the Moses Rock dike on the basis of hand specimen and thin section petrography. Rocks were selected to represent the range of chemical and petrographic types on the basis of reconnaissance and some detailed petrography. Selected specimens were carefully powdered to -200 mesh with a diatomite mortar and pestle.

Measured Densities

Whole-rock densities were measured on small 3 to 5 gram chips using a Jolly balance, distilled water, and Archimedes principle. Measurements were repeated 5 times on each sample, and the stated error is the standard deviation of those measurements.

Electron Microprobe

Partial chemical analyses were made on an Allied Research Laboratory three-channel electron microprobe (EMX) equipped with pulse height analysers on each channel. Data print out was on an I.B.M. typewriter. All channels had sealed proportional gas-counter detectors. Analyses were made at an operating voltage of 15 KV and a sample current of 0.05 μ amps; rarely a sample current of 0.10 μ amp was used. The size of the spot produced by the electron beam ranged from 2 to about 10 microns. Volatization of specimens was not an experimental problem. Sample current readings were made on brass mounts or currents measured on specimen surfaces were calibrated to brass. No correction was necessary for dead time because counting rates in excess of 10,000 counts per second were not encountered. Background counts were taken routinely on all analyses, both standard and unknown minerals. Counts on unknowns generally ranged between 10^4 and 10^5 counts obtained in 10 second runs on each spot.

Analyses of unknowns were obtained in two ways from counts: 1) by reference to standard curves (courtesy of Mr. D. Smith) which were constructed from counts made on previously analysed, homogeneous minerals in the reference collection of the microprobe laboratory, Division of Geological Sciences, California Institute of Technology, and 2) direct reduction of counts to oxide weight percent using the technique of Bence and Albee (1967) and a CITRAN computer program constructed by Drs. A. Bence and R. Naylor. The analyses quoted in this report were obtained by the second method. Discrepancies between the two methods were usually negligible or attributable to doubtful results of wet chemical analyses of the standards.

Sample Preparation for Electron Microprobe Analysis

Two types of samples were prepared for electron microprobe analysis: 1) polished thinsections of rocks, and 2) grains mounted in apoxy. Polished thin sections were prepared by Mr. Rudulf von Huene, California Institute of Technology. Individual grains were separated from the kimberlite.

Grains were obtained from kimberlite in the following way. Large samples of kimberlite were pulverised, and the dense minerals concentrated using a Wilfely table, heavy liquids (and STBE), split into +100, 100-200, and -200 mesh fractions and separated by magnetic susceptibility with a Franz-electromagnetic separator. From the resulting fractions, grains were hand picked with a binocular microscope. These grains were mounted in apoxy and polished to exposure by A. A. Chodos.

Polished thin sections and grain mounts were coated using a graphite arc in an evacuated glass bell jar in order to make the specimen surface electrically conducting.

When working with polished thin sections, the grains to be analysed were circled with india ink on top of the carbon coating. A sketch map of the thin section was then made showing the location of the circles. This permitted easy location of the desired grains when the section was mounted in the probe. Generally polaroid photomicrographs of grains were taken prior to actual probe runs so identification and reproduction of spots was relatively simple.

During analysis of grains in the grain mounts, maps showing the distribution and outline of each individual grain were constructed which permitted spots to be reproduced. This was necessary, of course, because only three elements at a time could be analysed. It is felt that no serious problem of reproducibility of location was encountered. Also, a characteristic feature of mineral grains separated from the kimberlite is their lack of zoning, so errors in spot location would introduce only minor errors in analyses.

APPENDIX B

Electron Microprobe Partial Chemical Analyses of Olivine Orthopyroxene, Clinopyroxene and Garnet Grains Separated from Moses Rock Kimberlite (MR 1416A)

Approximately 150 partial chemical analyses are presented in the following tables. Electron microprobe analyses were obtained on individual mineral grains separated from a kimberlite sample (MR 1416A) from the type locality in the Moses Rock dike.

Microprobe data, in counts per second, corrected for background, were reduced to oxide weight percent using the empirical correction factors of Bence and Albee (1967). Actual reduction of these data and computation of structure formulae were performed using CITRAN computer programs written by Drs. A. Bence and R. Naylor.

In the chemical analyses Fe is expressed as FeO. It is possible that iron exists in significant amounts in the ferric oxidation state in both garnet and clinopyroxene.

Mineral structure formulae were calculated to an appropriate number of oxygen atoms assuming Fe was present as FeO and Al as Al_2O_3.

Results are shown to hundreds of 1 oxide weight percent, although probably only three figures are significant.

Olivine

Mount	62-2	62-2		
Grain	6	7	8	9
SiO_2	41.05	40.32	40.44	40.34
TiO_2	-	.00	.00	-
Al_2O_3	-	-	-	-
Cr_2O_3	.02	.01	.02	.02
MgO	52.05	50.70	49.92	50.75
FeO	7.85	9.57	9.86	9.08
CaO	-	-	.01	-
MnO	.13	.15	.17	.16
Na_2O	.02	.02	.01	.01
	101.12	100.77	100.44	100.36

Structure Formulae

	6	7	8	9
Si	.987	.981	.988	.983
Ti	-	.000	.000	-
Al	-	-	-	-
Cr	.001	.000	.000	.000
Mg	1.865	1.839	1.818	1.844
Fe	.158	.195	.201	.185
Ca	-	-	.000	-
Mn	.003	.003	.004	.003
Na	.001	.001	.001	.001
	3.013	3.019	3.012	3.017
O	4.000	4.000	4.000	4.000
Mg/Mg+Fe	.922	.904	.900	.909

Olivine

Mount	62-4					
Grain	3	4	5	6	7	9
SiO_2	40.16	40.04	40.17	40.25	40.35	40.27
TiO_2	.01	.00	.00	-	-	-
Al_2O_3	-	-	-	-	-	-
Cr_2O_3	.01	.01	.01	.01	.01	.01
MgO	50.65	50.84	49.90	50.77	50.97	49.86
FeO	8.75	7.92	10.31	8.14	7.80	8.26
CaO	-	-	-	-	-	-
MnO	.15	.14	.15	.14	.14	.15
Na_2O	.01	.02	.02	.02	.02	.02
	99.74	98.97	100.58	99.33	99.30	98.58

Structure Formulae

Si	.984	.985	.982	.987	.988	.995
Ti	.000	.000	.000	-	-	-
Al	-	-	-	-	-	-
Cr	.000	.000	.000	.000	.000	.000
Mg	1.849	1.864	1.819	1.856	1.860	1.836
Fe	.179	.163	.211	.167	.160	.171
Ca	-	-	-	-	-	-
Mn	.003	.003	.003	.003	.003	.003
Na	.001	.001	.001	.001	.001	.001
	3.016	3.015	3.018	3.013	3.012	3.005
O	4.000	4.000	4.000	4.000	4.000	4.000
Mg/Fe+Mg	.912	.920	.896	.917	.921	.915

Olivine

Mount	62-4			62-6		
Grain	10	11	12	3	4	5
SiO_2	40.81	41.10	40.59	40.74	41.30	41.13
TiO_2	.00	-	.01	.00	.00	.00
Al_2O_3	-	-	-	-	-	-
Cr_2O_3	.02	.01	.02	.01	.01	.00
MgO	49.08	50.33	48.16	50.47	50.61	49.51
FeO	10.11	7.70	8.33	7.64	7.57	8.30
CaO	-	-	-	-	-	-
MnO	.00	.00	.00	.00	.00	.00
Na_2O	.02	.02	.01	.01	.01	.00
	100.20	99.30	97.25	99.00	99.63	99.11

Structure Formulae

Si	.996	1.000	1.011	.999	1.000	1.004
Ti	.000	.000	.000	.000	.000	.000
Al	-	-	-	-	-	-
Cr	.000	.000	.000	.000	.000	.000
Mg	1.797	1.839	1.800	1.843	1.842	1.816
Fe	.207	.158	.174	.156	.154	.171
Ca	-	-	-	-	-	-
Mn	.003	.003	.003	.003	.003	.003
Na	.001	.001	.000	.001	.001	.000
	3.004	3.000	2.989	3.001	3.000	2.995
O	4.000	4.000	4.000	4.000	4.000	4.000
Mg/Fe+Mg	.897	.921	.912	.922	.923	.914

Olivine

Mount	62-5	62-6	63-9	62-2		
Grain	2	1	1	4	5	10
SiO_2	40.08	40.31	40.47	40.35	40.30	40.31
TiO_2	.00	.01	-	.01	.00	.00
Al_2O_3	-	-	-	-	-	-
Cr_2O_3	.02	.00	.01	.01	.01	.01
MgO	49.14	49.43	49.30	50.80	50.59	50.72
FeO	8.45	7.21	7.50	8.64	9.41	10.28
CaO	-	-	-	-	-	-
MnO	.17	.13	.15	.14	.15	.14
Na_2O	.01	.01	.01	.01	.01	.01
	97.89	97.12	97.44	99.95	100.48	101.47

Structure Formulae

Si	.998	1.005	1.006	.985	.983	.977
Ti	.000	.000	-	.000	.000	.000
Al	-	-	.000	-	-	-
Cr	.000	.000	.000	.000	.000	.000
Mg	1.823	1.836	1.827	1.849	1.839	1.833
Fe	.176	.150	.156	.177	.192	.208
Ca	-	-	-	-	-	-
Mn	.004	.003	.003	.003	.003	.003
Na	.001	.001	.001	.001	.001	.001
	3.002	2.995	2.993	3.014	3.017	3.023
O	4.000	4.000	4.000	4.000	4.000	4.000
Mg/Fe+Mg	.912	.924	.921	.912	.905	.898

Olivine

Mount	62-6	62-4		62-2	62-4	62-5
Grain	2	1	2	3	9	1
SiO_2	40.49	40.26	40.45	40.92	40.28	40.10
TiO_2	-	.01	-	.01	.00	.00
Al_2O_3	-	-	-	-	-	-
Cr_2O_3	.01	.01	.01	.01	.01	.07
MgO	50.32	50.65	52.31	51.80	50.29	48.05
FeO	6.64	9.57	6.81	7.97	9.05	7.56
CaO	-	-	-	-	-	-
MnO	.12	.15	.11	.13	.15	.15
Na_2O	.01	-	.01	.02	.01	.01
	97.74	100.67	99.72	100.86	99.80	95.97

Structure Formulae

Si	1.000	.981	.982	.987	.987
Ti	-	.000	-	.000	.000
Al	-	-	-	-	-
Cr	.000	.001	.000	.000	.000
Mg	1.858	1.839	1.894	1.862	1.836
Fe	.137	.195	.138	.161	.186
Ca	-	-	-	-	-
Mn	.002	.003	.002	.003	.003
Na	.001	.001	.001	.001	.000
	3.000	3.019	3.018	3.013	3.013
O	4.000	4.000	4.000	4.000	4.000
Mg/Fe+Mg	.931	.904	.932	.920	.908

Olivine

Mount	62-6					
Grain	6	7	8	9	10	11
SiO_2	41.06	41.42	41.30	40.86	41.20	40.79
TiO_2	.00	.00	.00	.01	.01	.01
Al_2O_3	-	-	-	-	-	-
Cr_2O_3	.00	.01	.00	.02	.01	.02
MgO	49.84	50.85	51.83	50.00	51.18	49.84
FeO	7.28	6.75	6.09	7.66	6.30	7.47
CaO	-	-	-	-	-	-
MnO	.00	.00	.00	.00	.00	.00
Na_2O	.01	.02	.01	.01	.02	.01
	98.33	99.17	99.34	98.68	98.80	98.27

Structure Formulae

Si	1.006	1.004	.997	1.000	1.000	1.002
Ti	.000	.000	.000	.000	.000	.000
Al	-	-	-	-	-	-
Cr	.000	.000	.000	.000	.000	.000
Mg	1.834	1.851	1.880	1.838	1.868	1.838
Fe	.150	.138	.124	.158	.129	.154
Ca	-	-	-	-	-	-
Mn	.003	.003	.002	.003	.002	.003
Na	.000	.001	.000	.000	.001	.001
	2.994	2.997	3.003	3.000	3.000	2.998
O	4.000	4.000	4.000	4.000	4.000	4.000
Mg/Fe+Mg	.924	.931	.938	.921	.935	.923

Olivine

Mount	62-6	63-9	62-2	
Grain	12	2	1	2
SiO_2	41.41	41.08	40.68	40.70
TiO_2	.00	.00	-	.00
Al_2O_3	-	-	--	-
Cr_2O_3	.00	.00	.01	.01
MgO	50.95	50.69	51.52	51.70
FeO	5.53	7.93	7.93	7.30
CaO	-	-	-	-
MnO	.00	.00	.13	.13
Na_2O	.02	.01	-	.02
	98.03	99.86	100.29	99.85

Structure Formulae

Si	1.009	.995	.987	.988
Ti	.000	.000	-	.000
Al	-	-	-	-
Cr	.000	.000	.000	.000
Mg	1.866	1.844	1.862	1.871
Fe	.113	.162	.161	.148
Ca	-	-	-	-
Mn	.002	.003	.003	.003
Na	.001	.001	.001	.001
	2.992	3.005	3.013	3.012
O	4.000	4.000	4.000	4.000
Mg/Fe+Mg	.943	.919	.920	.927

Titanoclinohumite

Mount	61-4	61-6	61-4	61-6
Grain	7	4	8	11
SiO_2	35.79	35.44	36.28	36.50
TiO_2	4.81	5.11	5.77	5.30
Al_2O_3	-	-	-	-
Cr_2O_3	.13	.07	.01	.05
MgO	49.95	47.01	48.73	45.56
FeO	7.07	9.07	7.29	10.13
CaO	-	-	-	-
MnO	.13	.17	.00	.00
Na_2O	.01	.01	.00	.01
	97.89	96.87	98.27	97.75

Structure Formulae

Si	.898		.903	.924
Ti	.091		.109	.101
Al	-		-	-
Cr	.003		.001	.001
Mg	1.867		1.819	1.728
Fe	.148		.152	.215
Ca	-		-	-
Mn	.003		.003	.004
Na	.001		.000	.001
	3.010		2.988	2.974
O	4.000		4.000	4.000
Mg/Mg+Fe	.927		.923	.889

Clinopyroxene

Mount	63-1					
Grain	2-1	3-1	4-1	5-2	6-1	7-1
SiO_2	54.56	54.07	52.60	52.46	52.35	54.01
TiO_2	.14	.12	.05	.26	.13	.13
Al_2O_3	2.32	2.08	4.43	5.83	5.45	2.28
Cr_2O_3	2.29	1.68	1.04	.91	1.42	1.89
MgO	15.83	16.42	15.96	14.79	15.22	15.31
FeO	1.83	1.44	2.00	1.91	2.02	1.77
CaO	21.01	21.85	22.43	21.48	21.41	20.62
Na_2O	2.11	1.61	.94	1.68	1.35	2.05
	100.09	99.27	99.46	99.32	99.35	98.08

Structure Formulae

Si	1.974	1.971	1.916	1.908	1.905	1.989
Ti	.004	.003	.001	.007	.004	.004
Al	.099	.089	.190	.250	.234	.099
Cr	.066	.049	.030	.026	.041	.055
Mg	.854	.892	.866	.802	.826	.841
Fe	.055	.044	.061	.058	.061	.055
Ca	.814	.853	.875	.837	.835	.814
Na	.148	.114	.067	.118	.096	.150
	4.014	4.014	4.006	4.006	4.001	4.003
O	6.000	6.000	6.000	6.000	6.000	6.000
Mg/Fe+Mg	.4882	.4890	.5026	.5108	.5028	.4919

Clinopyroxene

Mount	63-1			63-2		
Grain	10	11	12	1-1	2-1	3-1
SiO_2	52.00	52.44	52.23	52.71	52.08	54.67
TiO_2	.07	.05	.19	.06	.24	.04
Al_2O_3	5.58	5.57	5.27	4.86	6.39	1.54
Cr_2O_3	1.24	1.20	1.36	1.15	1.01	1.44
MgO	15.54	15.29	15.36	15.74	14.51	16.77
FeO	2.04	2.01	2.28	1.98	1.97	1.45
CaO	22.54	22.14	21.96	22.99	21.39	22.46
Na_2O	1.06	1.21	1.23	1.04	1.92	1.36
	100.08	99.92	99.88	100.53	99.53	99.74

Structure Formulae

Si	1.885	1.900	1.897	1.903	1.893	1.983
Ti	.002	.001	.005	.002	.007	.001
Al	.239	.238	.226	.206	.786	.066
Cr	.036	.034	.039	.033	.029	.041
Mg	.840	.825	.831	.847	.274	.906
Fe	.061	.061	.069	.060	.060	.044
Ca	.875	.860	.854	.889	.833	.873
Na	.075	.085	.087	.073	.136	.096
	4.013	4.005	4.009	4.012	4.017	4.010
O	6.000	6.000	6.000	6.000	6.000	6.000
Mg/Fe+Mg	.5105	.5101		.5123	.5145	.4906

Clinopyroxene

Mount	63-2		63-6	63-4		63-1
Grain	4-1	5-1	12	6	8	1-1
SiO_2	54.45	52.00	52.87	53.03	52.21	52.09
TiO_2	.22	.14	.03	.08	.22	.15
Al_2O_3	2.47	5.47	5.79	4.84	6.16	5.37
Cr_2O_3	1.44	1.29	.86	.94	.99	1.37
MgO	15.94	15.07	24.37	15.66	14.85	15.21
FeO	2.23	1.79	4.16	1.97	1.93	1.85
CaO	20.84	22.43	12.16	22.55	21.93	21.77
Na_2O	2.09	1.30	.03	1.08	1.65	1.23
	99.69	99.50	100.25	100.14	99.95	99.03

Structure Formulae

Si	1.976	1.895	1.867	1.916	1.891	1.903
Ti	.006	.004	.001	.002	.006	.004
Al	.106	.235	.241	.206	.263	.231
Cr	.006	.037	.024	.027	.028	.039
Mg	.862	.818	1.283	.843	.802	.828
Fe	.068	.054	.123	.059	.058	.056
Ca	.810	.876	.460	.873	.851	.852
Na	.147	.092	.002	.075	.116	.087
	4.017	4.012	4.000	4.003	4.015	4.002
O	6.000	6.000	6.000	6.000	6.000	6.000
Mg/Fe+Mg	.4845	.5169	.2640	.5086	.5150	.5071

Clinopyroxene

Mount	63-3					
Grain	2-1	3-1	4-1	6	8	9
SiO_2	51.99	53.71	54.78	54.67	52.19	52.53
TiO_2	.13	.34	.09	.16	.09	.21
Al_2O_3	4.80	4.40	2.02	1.93	5.72	5.74
Cr_2O_3	.88	1.37	2.30	.36	1.20	.87
MgO	16.19	14.81	14.93	16.50	14.58	14.03
FeO	2.08	1.97	2.20	1.95	2.02	2.01
CaO	21.95	20.58	19.85	21.75	20.81	20.29
Na_2O	1.01	2.36	2.48	1.26	1.38	1.83
	99.03	99.54	98.65	98.59	97.99	97.53

Structure Formulae

Si	1.901	1.949	2.007	1.998	1.921	1.937
Ti	.003	.039	.003	.004	.003	.577
Al	.207	.188	.087	.083	.249	.250
Cr	.026	.039	.067	.010	.035	.026
Mg	.882	.801	.815	.899	.799	.772
Fe	.064	.060	.067	.060	.062	.062
Ca	.860	.800	.779	.852	.818	.802
Na	.072	.166	.176	.089	.098	.131
	4.015	4.012	4.001	3.995	3.984	3.984
O	6.000	6.000	6.000	6.000	6.000	6.000
Ca/Ca+Mg	.4937	.4998	.4887	.4865	.5059	.5096

Clinopyroxene

Mount	63-3					
Grain	10	11	12	13	14	15
SiO_2	54.35	53.56	53.42	53.78	53.25	54.50
TiO_2	.21	.16	.31	.27	.14	.05
Al_2O_3	2.59	2.34	4.41	4.00	5.32	1.99
Cr_2O_3	2.20	2.16	1.41	1.50	.99	2.41
MgO	14.56	15.56	15.38	15.74	15.12	15.82
FeO	1.89	1.80	1.88	1.99	1.93	1.93
CaO	19.52	21.24	20.46	20.88	21.95	20.76
Na_2O	2.31	2.17	2.14	2.14	1.44	2.10
	97.63	99.00	99.41	100.29	100.16	99.57

Structure Formulae

Si	2.004	1.964	1.939	1.940	1.920	1.982
Ti	.006	.004	.008	.007	.004	.001
Al	.112	.101	.189	.170	.226	.085
Cr	.064	.063	.040	.043	.028	.069
Mg	.801	.851	.832	.846	.813	.858
Fe	.058	.055	.057	.060	.058	.058
Ca	.772	.834	.796	.807	.848	.809
Na	.166	.154	.150	.150	.101	.148
	3.983	4.027	4.012	4.021	3.999	4.013
O	6.000	6.000	6.000	6.000	6.000	6.000
Mg/Fe+Mg	.4907	.4952	.4890	.4881	.5107	.4854

Clinopyroxene

Mount	63-4			
Grain	1-1	2-1	3-1	5-1
SiO_2	53.17	54.71	52.24	52.37
TiO_2	.06	.14	.17	.24
Al_2O_3	5.16	2.31	4.46	3.72
Cr_2O_3	1.02	1.82	.93	1.18
MgO	15.73	16.40	17.14	17.77
FeO	1.74	1.73	1.87	1.61
CaO	22.82	21.09	22.44	22.88
Na_2O	.49	1.90	1.20	1.22
	100.19	100.11	100.44	101.00

Structure Formulae

Si	1.915	1.975	1.888	1.886
Ti	.002	.004	.005	.006
Al	.219	.098	.190	.158
Cr	.029	.052	.027	.034
Mg	.844	.882	.923	.954
Fe	.052	.052	.056	.049
Ca	.881	.816	.869	.883
Na	.035	.133	.084	.085
	3.977	4.013	4.041	4.055
O	6.000	6.000	6.000	6.000
Mg/Fe+Mg		.4804	.4850	.4807

Orthopyroxene

Mount	63-6				63-7	
Grain	10	11	13	14	2-1	3-3
SiO_2	55.43	56.21	55.61	54.57	56.69	55.47
TiO_2	.04	.02	.03	.16	.03	.03
Al_2O_3	4.11	2.93	4.08	4.31	.70	4.35
Cr_2O_3	.48	.45	.57	.51	.28	.50
MgO	32.47	35.10	34.39	34.08	35.51	34.36
FeO	4.81	5.91	6.44	5.70	6.67	6.20
CaO	1.73	.12	1.09	.22	.11	5.46
Na_2O	.03	.02	.05	.32	.02	.02
	99.11	100.76	102.27	99.88	100.02	101.48

Structure Formulae

Si	1.921	1.919	1.884	1.885	1.959	1.888
Ti	.001	.001	.001	.004	.001	.001
Al	.167	.118	.163	.176	.029	.175
Cr	.013	.012	.015	.014	.008	.013
Mg	1.681	1.791	1.740	1.754	1.829	1.743
Fe	.140	.169	.183	.165	.193	.177
Ca	.065	.004	.040	.008	.004	.020
Na	.002	.001	.003	.021	.001	.001
	3.989	4.016	4.028	4.027	4.023	4.017
O	6.000	6.000	6.000	6.000	6.000	6.000
Mg/Fe+Mg	.923	.914	.905	.914	.905	.908

Orthopyroxene

Mount	63-7					
Grain	4-1	5-1	6-1	7	8-1	9
SiO_2	56.25	55.05	55.19	55.85	56.58	55.04
TiO_2	.01	.03	.03	.02	.02	.04
Al_2O_3	2.54	4.38	3.56	3.05	2.45	4.78
Cr_2O_3	.62	.62	.43	.61	.54	.45
MgO	35.67	34.26	34.46	35.09	35.71	33.87
FeO	5.30	5.84	6.04	5.10	5.99	6.65
CaO	.26	.81	.50	.51	.35	.52
Na_2O	.02	.05	.02	.02	.01	.03
	100.68	101.05	100.23	100.25	101.65	101.37

Structure Formulae

Si	1.922	1.882	1.901	1.915	1.921	1.879
Ti	.000	.001	.001	.001	.000	.001
Al	.102	.177	.144	.123	.098	.192
Cr	.017	.017	.012	.016	.014	.012
Mg	1.816	1.746	1.769	1.793	1.806	1.723
Fe	.151	.167	.174	.146	.170	.190
Ca	.009	.030	.018	.019	.013	.019
Na	.002	.003	.001	.001	.001	.002
	4.019	4.022	4.021	4.015	4.023	4.019
O	6.000	6.000	6.000	6.000	6.000	6.000
Mg/Fe+Mg	.923	.913	.911	.925	.914	.901

Orthopyroxene

Mount	63-8					
Grain	1-1	2	3	4	5	6
SiO_2	56.31	55.20	54.83	55.43	55.91	55.56
TiO_2	.01	.14	.05	.03	.02	.05
Al_2O_3	3.59	3.78	4.71	1.97	3.32	3.08
Cr_2O_3	.77	.61	.54	.58	.72	.63
MgO	35.55	34.26	33.90	34.88	34.76	34.83
FeO	5.29	6.10	6.33	6.14	5.01	5.86
CaO	.36	.58	.67	.16	.70	.56
Na_2O	.02	.07	.07	.03	.03	.02
	101.91	100.74	101.11	99.24	100.47	100.60

Structure Formulae

Si	1.901	1.894	1.877	1.929	1.913	1.907
Ti	.000	.004	.001	.001	.000	.001
Al	.143	.153	.190	.081	.134	.124
Cr	.020	.016	.015	.016	.019	.017
Mg	1.789	1.752	1.729	1.809	1.773	1.782
Fe	.150	.175	.181	.179	.143	.168
Ca	.013	.021	.025	.006	.026	.021
Na	.001	.005	.005	.002	.002	.002
	4.017	4.020	4.022	4.023	4.011	4.022
O	6.000	6.000	6.000	6.000	6.000	6.000
Mg/Fe+Mg	.923	.909	.905	.910	.925	.914

Orthopyroxene

Mount	63-8					63-9
Grain	7	8-1	9-1	10-1	11-1	4
SiO_2	54.80	56.19	56.04	57.35	54.69	54.55
TiO_2	.06	.03	.04	.05	.03	.08
Al_2O_3	4.27	2.02	3.33	3.84	4.92	1.67
Cr_2O_3	.62	.52	.54	.52	.55	.50
MgO	33.66	35.85	35.06	34.54	33.77	33.81
FeO	5.51	5.29	5.93	6.09	6.22	5.96
CaO	1.00	.31	.19	.28	.36	.65
Na_2O	.05	.03	.02	.07	.02	.13
	99.98	100.26	101.16	102.74	100.58	97.53

Structure Formulae

Si	1.891	1.928	1.909	1.921	1.878	
Ti	.001	.001	.001	.001	.001	
Al	.174	.081	.134	.152	.200	
Cr	.017	.014	.015	.014	.015	
Mg	1.731	1.834	1.780	1.724	1.728	
Fe	.159	.151	.169	.171	.179	
Ca	.037	.012	.007	.010	.013	
Na	.004	.002	.001	.005	.002	
	4.014	4.024	4.016	3.997	4.015	
O	6.000	6.000	6.000	6.000	6.000	
Mg/Fe+Mg	.916	.924	.913	.910	.906	

Orthopyroxene

Mount	63-9					
Grain	3	4	5	6	7	8
SiO_2	54.42	55.78	56.82	55.78	56.42	55.38
TiO_2	.05	.03	.02	.07	.03	.03
Al_2O_3	1.49	4.63	2.47	3.84	2.68	4.17
Cr_2O_3	.47	.61	.60	.55	.42	.71
MgO	33.24	34.85	35.96	34.92	35.12	32.05
FeO	6.15	5.46	5.29	6.44	5.14	5.18
CaO	.71	.38	.69	.52	.13	3.09
Na_2O	.10	.05	.03	.09	.02	.11
	96.80	101.79	101.87	102.20	99.95	100.72
Structure Formulae						
Si		1.884	1.919	1.888	1.933	1.903
Ti		.001	.000	.002	.001	.001
Al		.184	.098	.153	.108	.169
Cr		.016	.016	.015	.012	.019
Mg		1.760	1.816	1.766	1.800	1.645
Fe		.155	.150	.182	.148	.149
Ca		.014	.025	.019	.005	.114
Na		.004	.002	.006	.001	.007
		4.017	4.025	4.030	4.007	4.006
O		6.000	6.000	6.000	6.000	6.000
Mg/Fe+Mg		.919	.923	.907	.924	.917

Orthopyroxene

Mount	63-9	63-3	62-5	63-6		63-7
Grain	5	7	3	1-1	1-3	1-1
SiO_2	54.39	54.98	46.52	57.44	54.73	54.02
TiO_2	.05	.03	.11	.02	.02	.21
Al_2O_3	1.45	3.87	.52	.95	4.34	2.87
Cr_2O_3	.53	.58	.06	.30	.62	.48
MgO	33.79	32.72	5.04	36.57	33.94	34.30
FeO	6.42	6.13	46.26	5.07	6.29	6.57
CaO	.51	.72	.56	.84	.95	.15
Na_2O	.04	.04	.01	.03	.04	.02
	97.34	99.07	99.58	101.22	100.93	98.63

Structure Formulae

Si		1.915	1.973	1.951	1.878	1.898
Ti		.001	.003	.001	.000	.005
Al		.159	.026	.038	.176	.119
Cr		.016	.002	.008	.017	.013
Mg		1.699	.318	1.851	1.736	1.796
Fe		.179	1.642	.144	.181	.193
Ca		.027	.025	.030	.035	.006
Na		.003	.001	.003	.003	.001
		3.998	4.010	4.026	4.026	4.031
O		6.000	6.000	6.000	6.000	6.000
Mg/Fe+Mg		.905	.162	.928	.906	.903

Garnet

Mount	61-1		61-2	61-1		
Grain	3	10	1	4	5	6
SiO_2	37.51	36.62	39.94	38.67	37.48	36.51
TiO_2	.10	.04	.01	.04	.03	.10
Al_2O_3	20.54	19.49	18.19	21.75	21.22	20.48
Cr_2O_3	.03	.01	6.95	.00	.01	.05
MgO	5.56	1.06	16.09	10.90	7.00	5.56
FeO	29.23	30.49	11.25	25.69	28.78	29.83
CaO	6.57	9.40	7.83	1.07	1.21	6.81
MnO	1.10	3.28	.76	2.76	5.53	.79
Na_2O	.01	.02	.03	.02	.02	.05
	100.67	100.43	101.05	100.90	101.30	100.20

Structure Formulae

Si	2.956	2.974	2.945	2.954	2.938	2.907
Ti	.006	.002	.001	.002	.002	.006
Al	1.909	1.866	1.580	1.959	1.962	1.922
Cr	.002	.001	.405	.000	.001	.003
Mg	.653	.129	1.768	1.241	.818	.660
Fe	1.927	2.072	.694	1.641	1.888	1.987
Ca	.555	.819	.618	.087	.101	.581
Mn	.073	.226	.047	.179	.367	.053
Na	.003	.003	.004	.003	.003	.008
	8.084	8.091	8.063	8.066	8.080	8.128
O	12.000	12.000	12.000	12.000	12.000	12.000

Garnet

Mount	61-1	61-2	61-3			
Grain	9	2	1	2	3	4
SiO_2	38.12	41.09	40.66	37.52	40.95	37.80
TiO_2	.14	.01	.08	.28	.08	.17
Al_2O_3	20.67	21.57	20.97	20.84	21.45	21.09
Cr_2O_3	.02	3.50	3.46	.01	2.99	.00
MgO	5.57	21.98	19.17	6.63	20.46	7.00
FeO	33.23	8.32	9.52	26.44	8.36	25.82
CaO	1.83	3.64	4.85	7.01	5.22	6.35
MnO	.61	.40	.67	.70	.41	.79
Na_2O	.03	.03	.05	.03	.02	.03
	100.23	100.55	99.43	99.47	99.97	99.06

Structure Formulae

Si	3.016	2.926	2.958	2.953	2.943	2.970
Ti	.008	.001	.004	.016	.004	.010
Al	.657	1.812	1.798	1.934	1.818	1.954
Cr	.001	.198	.199	.001	.170	.000
Mg	.657	2.333	2.078	.778	2.192	.820
Fe	2.200	.496	.580	1.741	.503	1.697
Ca	.155	.278	.378	.592	.402	.535
Mn	.041	.024	.041	.046	.025	.053
Na	.005	.004	.007	.004	.003	.005
	8.012	8.071	8.043	8.065	8.061	8.044
O	12.000	12.000	12.000	12.000	12.000	12.000

Garnet

Mount	61-1		61-2		61-1	
Grain	14	15	3	4	1	2
SiO_2	37.35	38.05	38.69	39.36	38.06	37.91
TiO_2	.03	.12	.08	.04	.05	.14
Al_2O_3	20.52	20.56	21.75	21.93	21.11	20.58
Cr_2O_3	.01	.01	.04	.06	.04	.01
MgO	2.63	4.71	9.55	11.32	8.80	7.01
FeO	34.37	31.44	28.17	25.76	28.94	25.86
CaO	4.91	6.69	1.59	1.68	2.24	7.28
MnO	2.58	1.21	1.36	.62	.07	.77
Na_2O	.03	.03	.01	.03	.03	.03
	102.43	102.82	101.26	100.78	99.99	99.61

Structure Formulae

Si	2.964	2.961	2.963	2.982	(3.000)	2.973
Ti	.002	.007	.005	.002	.002	.009
Al	1.920	1.886	1.965	1.959	1.962	1.903
Cr	.001	.001	.002	.003	.003	.001
Mg	.311	.546	1.091	1.278	1.033	.820
Fe	2.282	2.047	1.805	1.633	1.908	1.696
Ca	.417	.558	.130	.136	.190	.612
Mn	.174	.080	.088	.040	.048	.051
Na	.004	.004	.002	.004	.004	.006
	8.076	8.091	8.050	8.037	8.152	8.070
O	12.000	12.000	12.000	12.000	12.000	12.000

Garnet

Mount	61-2				61-6	
Grain	5	6	7	8	2	5
SiO_2	37.6	41.0	41.05	40.79	40.82	37.98
TiO_2	.03	.03	.03	.03	.07	.12
Al_2O_3	20.9	21.8	20.93	20.00	20.73	20.88
Cr_2O_3	.00	2.71	4.15	5.36	4.40	.03
MgO	5.49	18.9	19.36	18.26	18.86	6.25
FeO	32.5	10.9	9.33	9.71	9.00	25.65
CaO	1.49	4.95	5.34	6.31	5.47	6.58
MnO	.03	.01	.01	.01	.01	1.45
Na_2O	.02	.03	.03	.04	.04	.02
	101.06	101.06	100.83	101.09	99.91	98.98

Structure Formulae

Si	2.975	2.948	2.951	2.951	2.960	2.995
Ti	.002	.002	.001	.001	.004	.008
Al	1.950	1.839	1.769	1.701	1.767	1.941
Cr	.002	.154	.236	.307	.253	.002
Mg	.646	2.021	2.074	1.967	2.037	.735
Fe	2.147	.655	.561	.588	.546	1.692
Ca	.126	.382	.411	.489	.425	.557
Mn	.199	.051	.037	.037	.032	.097
Na	.003	.005	.004	.005	.005	.003
	8.049	8.056	8.047	8.047	8.029	8.028
O	12.000	12.000	12.000	12.000	12.000	12.000

Garnet

Mount	61-6					
Grain	6	7	8	9	10	12
SiO_2	41.46	38.79	38.66	38.78	38.59	41.85
TiO_2	.20	.05	.04	.15	.13	.16
Al_2O_3	22.30	21.45	21.43	20.37	20.25	22.00
Cr_2O_3	1.64	.03	.08	.03	.02	1.90
MgO	19.36	9.63	9.64	5.95	4.37	19.19
FeO	9.52	26.24	26.06	26.77	28.55	9.38
CaO	4.77	2.21	2.16	6.63	6.70	5.26
MnO	.44	1.01	1.01	1.00	1.35	.47
Na_2O	.05	.03	.02	.02	.02	.05
	99.74	99.44	99.09	99.70	99.98	100.26

Structure Formulae

Si	2.980	2.999	2.999	3.040	3.047	2.996
Ti	.011	.003	.002	.009	.008	.009
Al	1.890	1.956	1.960	1.883	1.885	1.857
Cr	.094	.002	.004	.002	.002	.107
Mg	2.074	1.110	1.114	.695	.515	2.047
Fe	.572	1.697	1.691	1.755	1.886	.562
Ca	.367	.183	.179	.557	.567	.403
Mn	.027	.066	.066	.066	.090	.028
Na	.007	.005	.003	.003	.004	.008
	8.021	8.021	8.019	8.010	8.003	8.017
O	12.000	12.000	12.000	12.000	12.000	12.000

Garnet

Mount	61-6			61-1		
Grain	13	14	15	11	12	13
SiO_2	41.61	42.34	42.10	37.80	38.38	38.38
TiO_2	.04	.02	.18	.07	.13	.14
Al_2O_3	22.00	21.99	22.13	20.74	20.96	21.09
Cr_2O_3	2.13	2.51	1.68	.00	.02	.03
MgO	18.63	20.43	18.86	4.82	7.04	6.90
FeO	9.51	7.42	9.31	30.31	27.85	27.79
CaO	5.35	5.00	4.78	5.73	6.70	6.93
MnO	.54	.39	.46	2.69	2.26	.61
Na_2O	.03	.03	.06	.02	.02	.02
	99.84	100.12	99.57	102.19	103.34	101.91

Structure Formulae

Si	2.996	3.007	3.023	2.958	2.935	2.956
Ti	.002	.001	.010	.004	.007	.008
Al	1.868	1.842	1.874	1.912	1.890	1.914
Cr	.121	.141	.095	.000	.001	.002
Mg	1.999	2.163	2.019	.562	.802	.792
Fe	.573	.441	.560	1.984	1.781	1.790
Ca	.413	.380	.368	.481	.549	.572
Mn	.033	.233	.028	.178	.146	.040
Na	.004	.003	.008	.003	.003	.004
	8.009	8.001	7.986	8.083	8.114	8.079
O	12.000	12.000	12.000	12.000	12.000	12.000

Garnet

Mount	61-4	61-6
Grain	11	1
SiO_2	41.38	40.19
TiO_2	.17	.04
Al_2O_3	22.61	19.06
Cr_2O_3	1.23	11.25
MgO	20.61	18.63
FeO	9.32	7.66
CaO	4.24	6.50
MnO	.43	.51
Na_2O	.05	.04
	100.03	103.87

Structure Formulae

Si	1.905	2.852
Ti	.009	.002
Al	1.905	1.594
Cr	.069	.632
Mg	2.195	1.971
Fe	.557	.454
Ca	.325	.494
Mn	.026	.030
Na	.008	.005
	8.050	8.035
O	12.000	12.000

APPENDIX C

Petrographic Descriptions of a Representative Suite of Crystalline Rock Fragments from the Moses Rock Dike

This appendix contains brief petrographic descriptions of a selected suite of crystalline rock fragments from the Moses Rock dike. From this suite 15 samples were selected from whole-rock chemical analysis (see Appendix D). The sample numbers referenced in this appendix are used in the text. This suite is representative but does not include all the observed crystalline rock types in the Moses Rock dike. The diagram below summarizes the rocks described.

		Acid	Intermediate	Basic	Ultrabasic or Dense	
Igneous	Plutonic	MRX-66 MRX-103 MRX-105,260	MRX-95 MRX-11	MRX-190	MRX-1 MRX-50B	(1)
					MRX-44	(2)
	Volcanic	MRX-6 MRX-60 MRX-7;MRX-8	MRX-153 MRX-97 MRX-26 MRX-19	MRX-13 MRX-10,19, 12,17	MRX-39 MRX-57 MRX-1307	(3)
Metamorphic	High Rank	MRX-137 MRX-37	MRX-20(R) MRX-25(R)	MRX-148b, 148	MRX-2	(4)
					MRX-51	(5)
	Intermediate Rank	MRX-43		MRX-220 MRX-134		
	Low Rank			MRX-128		

(1) eclogite
(2) jadeitic-clinopyroxene
(3) websterite
(4) spinel-lherzolite
(5) serpentine schist

Acid Plutonic Rocks

MRX-103: Gneissic porphyritic biotite-leuco-granite: Foliated porphytic rock, with poorly defined crystal outlines (xenomorphic) and various sized crystals (sericite); banded fabric is defined by parallelism of biotite (5% .5 mm average size), prismatic feldspar (microcline 20%, microperthite 20% subhedra, up to 5 mm, with interstitial albite), quartz (30% elongate subhedra up to 1.5 mm).

MRX-260: Sphene-biotite-granite: Phaneritic igneous rock, 10% quartz, 75% light, subhedral, alkali-feldspar, .5 to 1.5 mm (microcline and microperthite, with minor albite, slightly altered); 15% irregularly shaped clusters of biotite and sphene, 1 to 5 mm across. (Minor remnant px-acgerine-augite? with amphibole). 2% magnetite with feldspar and accessory apatite.

MRX-105: Medium-grained, porphyritic biotite-microcline-leucogranite: 40% slightly pink feldspar euhedra, 3 to 10 mm (microcline-perthite intergrowths and poikilitic microcline); remainder of rock is fairly fine grained; quartz (30% 1-2 mm), feldspar (20%; 1 mm, microcline and perthite subhedral partly altered), biotite (5%, irregular unoriented clusters 2-4 mm) and opaque (1% generally associated with biotite).

MRX-66: Medium-grained gneissic, biotite-granite:

Acid Volcanic Rocks

MRX-6: Rhyolite porphyry: Groundmass, 40% dull-purplish-pink aphanitic; porphyry, with K-spar, 20% euhedra, 2 mm average (up to 6 mm) quartz (20%, sub or euhedra, 1 to 2 mm) and 10% dark domains, 1-4 mm across. In thin section are composed of opaque core, surrounded by dark green microcrystalline minerals. Common ubiquitous rock. (Rhyolite C).

MRX-7: Rhyolite porphyry: About 50% light grey-aphanitic groundmass of microcrystalline, quartz, feldspar light and dark mica; containing 15% alkali feldspar euhedra 3 to 7 mm; 20% quartz subhedra, 1.5 to 6 mm, and dark lathlike clusters, 1 to 3 mm in length of very small biotite grains. (Rhyolite B)

MRX-8: Rhyolite porphyry: About 50% light olive-green aphanetic ground mass composed of microcrystalline quartz, feldspar and minor sencite; phenocrysts are: quartz, 10%, subhedral, average 1 mm; alkali-feldspar, 15% euhedra, .5 to 5 mm; plagioclase, 30%, subhedral, .5 to 1 mm, with minor opaques, surrounded by 1 mm rim of green glass. Qtz weathers to read jasper colored clusters. Groundmass weathers to light tan. (Rhyolite A)

MRX-60: Microporphyritic brick-red rhyolite: Fine-grained, brick red rhyolite (80% groundmass or microcrystalline quartz and feldspar) containing small phenocrysts of quartz (5-10%, euhedral, .5 to 1 mm), albite (about 5%,.1 to 15 mm, sub-euhedral), K-feldspar (about 7%, .5 mm, euhedral) and opaques (.3 mm including dispersed hematite rim).

Intermediate and Basic Plutonic Rocks

MRX-11: Altered (sericitized) gneissic, biotite-bearing andesine-quartz-diorite: Green rock with distinctive nodular weathered surface composed of green feldspar and quartz nodules which stand out from weathered dark biotite layers. Rock weakly foliated bands 5-8 mm wide, quite irregular. Contains sericite, opaque and accessory zircon, apatite.

MRX-95: Hornblende-biotite-andesine diorite: Glomeroporpheritic irregularly-shaped hornblende-biotite-magnetite cluster up to 8 mm across, composing 40% of rock, are interstitial to mosaic interlocking matrix of plagioclase (andesine, AN 40) sub-to anhedral,average size 1.5 mm; Accessory magnetite and zircon.

MRX-190: Slightly-altered, sub-ophitic labradorite gabbro: Medium-grained, dark-colored rock with diabasic texture. Plagioclase, laths about 3 mm long about 30%; px-hornblende as poorly formed dark black prisms, up to 3-4 mm, and dark green matrix is calcic-plagioclase. In thin section the px is pigeonite, altered to hornblende and chlorite; microcrystalline biotite clots occur with opaques. Plagioclase zoned.

Intermediate and Basic Volcanic and Meta-volcanic Rocks

MRX-10: Altered porphyritic basalt (or andesite): Rock is 60% greenish black aphanitic (microcrystalline and glassy) groundmass containing, feldspar (pseudomorphs 10-15% irregular shaped white to very pale green, 1 to 6 mm across, sericitized and epidotized (?), altered plagioclase (about 5%, average 3 mm, anhedral, with irregular resorbed (?) borders) and altered px (not visible in hand specimen or groundmass), similar to MRX-13. Weathers to very irregular vescicular appearing surface.

MRX-19: Altered pyroxene-andesite porphyry with large irregular feldspar pseudomorphic phenocrysts: About 50% dark-bluish-grey (5B 4/1) groundmass (microcrystalline stilpnomelene (?) and magnetite with glass); 50% feldspar pseudomorphs (large 1 to 7 mm, irregularly shaped, light bluish-grey on fresh, greenish-tan when weathered; completely altered to sericite, clay minerals and epidite?) and pyroxene (1% average 1 mm, pigeonite, altered to chlorite).

MRX-13: Very slightly altered andesite porphyry with large white angular phenocrysts: 50% dark, greyish-green to white angular subhedral plagioclase partly altered. 3-4 mm average; 10% subhedral hornblende, .1 to .5 mm, appears spherical blobs; groundmass composed of plagioclase and hornblende? microlites, .1 mm average.

MRX-12: Altered pyroxene-andesite (?) porphyry: About 30% greenish-black aphanitic groundmass (light-green glass with small microlites .01 mm), containing dark and light phenocrysts. Dark phenocrysts, subhedral prismatic hornblende (with px cores .1 to 3 mm), about 30%; light phenocrysts (moderately to severely altered, 12 to 3 mm, sub and anhedral, 25%; Irregularly-shaped domains or dark green glass (up to 1 cm but 1 mm average). Minor opaques.

MRX-17: Altered fine-grained porphyritic basalt or andesite: Dense, micro-crystalline, dark greenish-black, speckled rock; groundmass, 25% dark greenish-black, irregular interstitial to dark phenocrysts (30%, .2 to .5 mm, irregularly-shaped domains of glass or microcrystalline alteration products), plagioclase (25%, severely altered, subhedral, .2 mm average), hornblende (5%, altered .5 mm average size). Rock has a dark yellowish-green appearance on weathered surfaces; with light and dark, 1-2 mm flecks giving speckled appearance to hand specimens.

MRX-97: Altered feldspar pyroxene basalt (?) porphyry: In hand specimen, dark-green groundmass about 50-60%, contains feldspar pseudomorphs, about 25%, eu-, sub-, and anhedral, .5 to f mm, pink-flesh color on weathered or white on fresh surfaces; dark phenocrysts, 1%, 1-2 mm black px-amphibole and a few irregular light-green patches up to 2 or 3 cm across. In thin section, rock is highly altered.

MRX-26: Fine-grained hornblende-sodic plagioclase andesite (?): An even, fine-grained aphanitic, greenish-black, rock containing minor small (1 mm average) black phenocrysts of anhedral hornblende (uralized px- undetermined), and minor plagioclase euhedra about .2 mm. Groundmass is microcrystalline, composed of small plagioclase laths in hornblende and glass matrix, with minor hematite. Essentially black, aphanitic, low density rock.

Metamorphic Rocks

MRX-220: Plagioclase rich-hornblende amphibolite: Fine (.5 mm), even grained, slightly lineated. 55% hornblende, .4 mm average, 45% plagioclase (andesine) is whitish-grey, about .1 mm average size, equant grains, gives rock even black-white flecked appearance; trace opaques, pyrite probably. Minerals unaltered in thin section (Amphibolite facies).

MRX-4: Orthoclase ($OR_{70}AbAn_{30}$)-plagioclase (An_{30})-sillimanite-biotite-garnet gneiss: Strongly foliated, dense, medium-grained (grains 1 mm average, bands 1-2 mm), rock; fine foliated bands of biotite 1-2 mm; light minerals with sillimanite, 1-2 mm wide, and garnets red-orange average 1.0 mm, spotted throughout. (Almandine-amphibolite or granulite facies).

MRX-128: Fine-grained, low-grade quartz-carbonate-talc (?)-antigorite (?) schist: Greyish-green (5G 5/2), rather dense, finely foliated (0.1 mm) calc-silicate rock, specimens commonly intruded by carbonate lenses crosscutting foliation. Composed of microcrystalline antigorite (?) (clear green) and talc (?) about 70%; anhedral equant small (.01mm) quartz, 15%; small opaques (.005 mm), 15%.

MRX-43: Medium-grained (1 mm) biotite-microcline-quartz gneiss: Well-foliated, leuco-granite gneiss; bands up to 8 mm wide, grain-size averages 1 mm; biotite, about 4%, in individual and clusters of plates parallels foliation; quartz and microcline, sugary texture, elongate crystals, parallel foliation. Accessory opaques. (Amphibolite facies).

MRX-134: Plagioclase-hornblende, well-foliated, medium-grained gneiss: (Amphibolite gneiss) Foliated-gneissic bands (about 1 mm) composed of irregular splotchy bands of slightly altered plagioclase which widen into augen-like lenses, in dark greenish-black hornblende. Plagioclase hornblende. On weathered surfaces jasper-colored irregular patches produced from weathered opaques. In thin section, quartz, epidote (?), sphene, present.

MRX-20: *Lineated, slightly-altered andesine-garnet-hornblende gneiss:* Garnet and hornblende occur together generally, as rod-like cylinders of very irregular, wavy curved, not angular, outline in a mass of light-colored material which is moderately altered plagioclase (An_{47}). Approximately plagioclase 50%, hornblende 30%, G 20%, trace opaque. Rock has spotted, streaked appearance; G-hornblende wavy inclusions in plagioclase.

MRX-25: *Epidote-chlorite bearing, blue quartz-garnet, coarse-grained plagioclase rock:* Chiefly coarse-grained light-colored, slightly altered plagioclase 70%, containing garnet averaging 1-2 mm in diameter in clusters up to 1 mm across, slightly altered to green chlorite; individual quartz grains 1-2 mm with bluish tinge; epidote in thin section. Distinctive white plagioclase-spotted garnet-quartz rock.

MRX-137: *Quartz-albite garnet gneiss (charnockite):* Garnets ($\sim$ 10%, 1-2 mm) reddish-orange; quartz (60%, 1 mm average) equant grains, feldspar (25%, .5 mm average) is pervasively sericitized and epidotized (?). Distinctive appearing light-yellow-green rough-surfaced, medium-grained rock with garnets spotting surface. (Granulite facies).

MRX-148: *Hyperthene-plagioclase-garnet gneiss:* Slightly-altered, medium-grained (1-2 mm) Garnet (1-2 mm) commonly enclosed in dark green px which composes about 50% of rock; plagioclase is interstitial in worm-like bands, commonly 2 mm thick. (Granulate facies).

Ultrabasic Rocks

(See text for descriptions)

MRX-51: Serpentine-tremolite schist

MRX-1: Eclogite

MRX-50B: Eclogite

MRX-44: Jadeite-clinopyroxene

MRX-2: Spinel-lherzolite

APPENDIX D

Petrochemical Data and Petrographic Summary of a Representative Suite of Crystalline Rock Fragments from the Moses Rock Dike

APPENDIX D. Petrographic Data and Petrographic Summary of a Representative Suite of Crystalline Rock Fragments from the Moses Rock Dike

Table D1. Whole Rock Chemical Analyses for Major Elements (Analyses, U.S. Geological Survey, Branch of Analytical Laboratories, Denver, Colorado, William W. Niles)

1. Blackish-green kimberlite, Moses Rock dike	Sampled from small dike shown in Plate 10A
2. Green kimberlite, Moses Rock dike	
3. Jadeite-rich clinopyroxenite	Inclusions in Moses Rock dike
4. Eclogite	
5. Spinel-bearing websterite	
6. Garnet-sillimanite-bearing schist	
7. Rhyolite	
8. Rhyolite	
9. Meta-basalt porphyory	
10. Andesine-hornblende dunite	
11. Serpentine-rich schist	
12. Dense aphanetic meta-andesite	
13. Sub-ophitic gabbro	
14. Hornblende-plagioclase amphibolite	
15. Minette from dike 2 miles northeast of Moses Rock dike	

Table D2. Estimated Modes of Other Important Rocks Not Included in Analysed Suite

a) Basic Granulites:

MRX-148b	
g	5
hb (px)	25
plag	70

MRX-24	
plag	60
hb (px)	40
op	tr

b) Acid Granulites

MRX-137	
q	40
g	10
plag	50
opaque	tr

MRX-37	
q	20
alk-felds	30
hb	30
g	10
biot+chl	5
plag	5
op	1

c) Porphyritic Leuco-granites

MRX-103	
microcline	40
microperth	20
qtz	30
plag	5
biot	3
mt	1

MRX-260 (-105)	
microcline perthite	90
qtz	5-10
biot	5
plag	1
opaques	1
sphene	4
ap+zirc	tr

d) Fine-grained Gneissic Biotite Granite

MRX-66	
perthite	35
microcline	25
qtz	25
biot	10
musc	5
op	tr

e) Spinel-bearing Lherzolite

MRX-2		
ol	40	54
serp ol	14	
opx	33	37
serp opx	4	
cpx	7	
spinel	2	

Petro-chemical Data and Petrographic Summary of a Representative Suite of Crystalline Basement Rock Fragments from the Moses Rock Dike

Table D3. Whole Rock Chemical Analyses for Major Elements (Analyses, U.S. Geological Survey, Branch of Analytical Laboratories, Denver, Colorado, William W. Niles)

Field Number	(1) MR-1416A	(2) MR-1416B	(3) MRX-44	(4) MRX-50B	(5) MR-1307	(6) MRX-4
SiO_2	39.16	40.07	55.68	48.35	50.97	56.15
Al_2O_3	1.58*	2.73*	17.94	14.26	8.65*	21.49**
Fe_2O_3	3.34	3.18	4.56	3.77	.60	6.01
FeO	3.65	3.33	1.17	7.97	4.50	4.90
MgO	36.97	34.05	3.16	7.51	21.33	3.55
CaO	1.14	2.10	3.66	10.21	12.58	1.33
Na_2O	.05	.08	11.45	4.76	.54	1.28
K_2O	.06	.08	.29	.04	.01	2.61
H_2O^+	11.20	11.50	.27	.82	.18	.60
H_2O^-	.85	1.02	.11	.18	.05	.12
TiO_2	.09	.11	.93	1.61	.12	1.16
P_2O_3	.03	.04	.00	.02	.00	.30
MnO	.09	.10	.08	.20	.13	.20
CO_2	1.20	1.27	.03	.05	.03	.00
Cl	.05	.02	.00	.00	.03	.01
F	.01	.02	.00	.00	.00	.12
Subtotal	99.47	99.70	99.31	99.75	99.72	99.83
Less O	.01	.01	.00	.00	.01	.05
Total	99.46	99.69	99.31	99.75	99.71	99.78

**Contained considerable amount of a refractory mineral, presumably zircon. Both zircon and zirconium are reported as aluminum.

*Includes Cr_2O_3.

Petro-chemical Data and Petrographic Summary of a Representative Suite of Crystalline Basement Rock Fragments from the Moses Rock Dike

Table D3. Whole Rock Chemical Analyses for Major Elements (Analyses, U.S. Geological Survey, Branch of Analytical Laboratories, Denver, Colorado, William W. Niles)

Field Number	(7) MRX-6	(8) MRX-7	(9) MRX-13	(10) MRX-95	(11) MRX-51	(12) MRX-153
SiO_2	72.84	72.66	50.76	50.63	45.54	65.89
Al_2O_3	13.53	13.78	17.41	16.59	3.44*	13.22
Fe_2O_3	.64	.49	1.10	4.74	3.32	2.49
FeO	.59	1.67	5.65	6.34	2.52	5.45
MgO	.78	.50	8.00	4.39	31.09	1.84
CaO	.91	1.25	8.44	7.09	2.68	3.10
Na_2O	4.05	3.81	4.30	4.19	.59	5.68
K_2O	4.41	4.09	.46	1.23	.12	.52
H_2O^+	.60	.51	2.32	1.54	8.83	.68
H_2O^-	.18	.08	.07	.26	1.08	.03
TiO_2	.13	.19	.29	1.71	.04	.55
P_2O_3	.25	.14	.15	.75	.03	.25
MnO	.03	.05	.14	.22	.06	.10
CO_2	.62	.34	.66	.02	.31	.02
Cl	.01	.01	.01	.03	.01	.02
F	.17	.05	.03	.09	.01	.04
Subtotal	99.74	99.62	99.79	99.82	99.67	99.88
Less O	.07	.02	.01	.05	.00	.02
Total	99.67	99.60	99.78	99.77	99.67	99.86

*Includes Cr_2O_3.

Petro-chemical Data and Petrographic Summary of a Representative Suite of Crystalline Basement Rock Fragments from the Moses Rock Dike

Table D3. Whole Rock Chemical Analyses for Major Elements (Analyses, U.S. Geological Survey, Branch of Analytical Laboratories, Denver, Colorado, William W. Niles)

Field Number	(13) MRX-190	(14) MRX-220	(15) MEM-1
SiO_2	49.70	48.53	48.95
Al_2O_3	19.00	18.13	9.47
Fe_2O_3	1.46	2.43	4.25
FeO	6.55	8.37	3.53
MgO	5.77	6.12	9.41
CaO	10.96	12.11	9.95
Na_2O	2.27	1.81	1.66
K_2O	1.29	.47	4.98
H_2O^+	1.98	1.19	1.43
H_2O^-	.16	.07	1.55
TiO_2	.29	.54	2.57
P_2O_3	.13	.11	.83
MnO	.14	.20	.10
CO_2	.07	.01	.84
Cl	.02	.02	.01
F	.04	.03	.18
Subtotal	99.83	100.14	99.69
Less O	.02	.01	.08
Total	99.81	100.15	99.61

Table D4. C.I.P.W. Norms-Molecular Mineral Norms

	(1)	(2)	(3)	(4)	(5)	(6)
Rock	MR-1416A	MR-1416B	MRX-44	MRX-50B	MR-1307	MRX-4
Q	-	-	-	-	-	30.686
C	1.513	1.827	-	-	-	15.150
Or	0.356	0.479	1.726	0.237	.059	15.449
Ab	0.054	0.536	50.198	28.707	4.360	10.775
An	-	2.033	-	17.469	21.326	3.962
Wo	-	-	7.554	13.721	17.148	-
En	34.717	40.558	6.529	8.620	36.884	8.856
Fs	1.507	1.670	-	4.256	5.423	2.493
Fo	39.984	31.751	0.978	7.099	11.484	-
Fa	1.912	1.441	-	3.863	1.861	-
Mt	4.868	4.669	1.346	5.480	.872	8.729
Hm	-	-	1.807	-	-	-
Il	0.172	.212	1.779	3.065	.229	2.207
Ap	.071	.096	-	.047	-	.712
Fr	.015	.034	-	-	-	.192
Cc	1.955	2.925	.069	.114	.068	-
Mg	.664	-	-	-	-	-
Lc	-	-	-	-	-	-
Ne	-	-	22.262	6.323	-	-
Hl	-	-	-	-	.050	.017
	87.871	88.263	99.618	99.001	99.764	99.228

Table D4. C.I.P.W. Norms-Molecular Mineral Norms

Rock	(7) MRX-6	(8) MRX-7	(9) MRX-13	(10) MRX-95	(11) MRX-51	(12) MRX-153
Q	31.654	31.925	-	1.314	-	20.070
C	2.114	2.058	-	-	-	-
Or	26.128	24.261	2.724	7.282	.711	3.077
Ab	34.285	32.288	36.388	35.296	4.935	47.972
An	-	2.874	26.940	22.986	6.444	9.129
Wo	-	-	4.064	2.942	1.954	1.827
En	1.181	1.250	5.596	10.953	47.083	4.588
Fs	.397	2.450	2.597	5.321	1.174	7.237
Fo	-	-	10.070	-	21.446	-
Fa	-	-	5.151	-	.589	-
Mt	.930	.713	1.598	6.885	4.830	3.615
Hm	-	-	-	-	-	-
Il	.248	.362	.552	3.254	.076	1.046
AO	.594	.333	.356	1.780	.071	.593
Fr	.304	.077	.034	.048	.015	.036
Cc	.649	.776	1.504	.046	.707	.046
Mg	.644	-	-	-	-	-
Lc	-	-	-	-	-	-
Ne	-	-	-	-	-	-
Hl	.017	.017	.017	.050	.017	.033
	99.144	99.385	97.592	98.155	90.051	99.269

Table D4. C.I.P.W. Norms-Molecular Mineral Norms

	(13)	(14)	(15)
Rock	MRX-190	MRX-220	MEM-1
Q	-	-	-
C	-	-	-
Or	7.636	2.773	29.520
Ab	19.093	15.147	14.016
An	37.987	39.979	3.732
Wo	6.253	7.969	14.296
En	11.443	15.045	14.400
Fs	8.443	12.677	-
Fo	2.069	.123	6.383
Fa	1.682	.114	-
Mt	2.120	3.518	4.268
Hm	-	-	1.299
Il	.552	1.024	4.896
Ap	.308	.260	1.972
Fr	.058	.041	.218
Cc	.159	.023	1.916
Mg	-	-	-
Lc	-	-	-
Ne	-	-	-
Hl	.033	.033	.017
	97.837	98.727	96.934

Table D5. Estimated Modes

(1) MRX-1416A	(2) MRX-1416B	(3) MRX-44	(4) MRX-50B	(5) MRX-1307
gmass serp	46	cpx 97	g 30	cpx
ol 10	45	rut 2	cpx 67	opx
serp ol 35		py 1	ru 3	spinel 1
opx 1	1^+			
serp opx 0.6				
lithic frag	4^+			
garnet	<1			
cpx				
mica				
opaques				
other				

(6) MRX-4	(7) MRX-6	(8) MRX-7	(9) MRX-13	(10) MRX-95
g 8	gmass 40	gmass 60	gmass 50	plag 60
sill 15	kspar 20	qtz 20	plag 40	(An_{40})
biot 15	qtz 20	felds 15	(altered)	hb 30
Q 15	mafic 20	biot 5	Hb 10	biot 7
kspar 23			(alt)	hm 3
plag 20				mt
mt 4				

Table D5. Estimated Modes

(11) MRX-51		(12) MRX-153		(13) MRX-190		(14) MRX-220		(15) MEM-1	
serp		gmass	100	plag	68	hb	55	gmass	50
+	100			px	30	plag	45	biot	20
Chl(?)				(hb+chl)		opaq-tr		px	30
				biot	2				
				opaq					

Table D7. Measured Whole Rock Specific Gravities

(1)	(2)	(3)	(4)	(5)
MRX-1416A	MRX-1416B	MRX-44	MRX-50B	MRX-1307
2.61±.01		3.34±.01	3.44±.02	3.26±.02
(6)	(7)	(8)	(9)	(10)
MRX-4	MRX-6	MRX-7	MRX-13	MRX-95
2.99±.01	2.59±.01	2.64±.01	(2.88-2.94)	2.89±.01
(11)	(12)	(13)	(14)	(15)
2.53±.01	(2.9±.01)	(2.9±.01)	2.99±.02	2.83±.01

Note: Important rock types not in the analysed suite include the following: (sample numbers in parentheses)

	Measured Specific Gravity
a) Garnet-pyroxene-plagioclase granulite (MRX-148B)	(G = 2.90 - 3.08)
b) Pyroxene-plagioclase granulite (MRX-24)	(G ~ 2.96)
c) Porphyritic granite (X-103, -105, -260)	(G = 2.63, 2.65±.01)
d) Fine-grained gneissic biotite granite (MRX-66)	(G ~ 2.65)
e) Spinel-bearing lherzolite (MRX-2)	(G > 3.0)
f) Acid granulite (X-137, -37)	(G = 2.82±.01)

Table D7.

MEASURED DENSITY

Sample Number	Formation and Lithology	Measured Density
	Sedimentary Rocks	
Trw-TRM-65	Wingate Sandstone	2.43±.01
Trc-TRM-65	Chinle, Church Rock Member, sandstone	2.42±.01
Pcd-TRM-65	DeChelley Sandstone Member, Cutler Formation	2.41±.01
Pco-374-TRM-65	Organ Rock Member, Cutler Formation, siltstone	2.66±.01
Pcc-248-TRM-65	Cedar Mesa Sandstone Member, Cutler Formation	2.30±.01
Pcha-227-TRM-65	Halgaito Member, Cutler Formation, limey siltstone	2.65±.01
Pcha-237-TRM-65	Halgaito Member, Cutler Formation, limey siltstone	2.62±.02
Pvht-81-TRM-65	Honaker Trail Formation, limestone	2.57±.03
Pvht-75-TRM-65	Honaker Trail Formation, limestone	2.62±.02
	Crystalline Rocks	
MRK-6-TRM-64	Rhyolite	2.59±.01
MRK-9-TRM-64	Porphyritic Intermediate Meta-volcanics	2.94±.01
MRK-60-TRM-64	Rhyolite	2.64±.01
MRK-95-TRM-64	Diorite	2.89±.01
MRK-100-TRM-64	Gabbro	
MRK-103-TRM-64	Granite	2.63±.01
MRK-111-TRM-64	Porphyritic Granite	2.65±.01
MRK-260-TRM-64	Granite	2.65±.01
	Metamorphic Rocks	
MRK-4-TRM-64	Sill-garnet, granulite gneiss	2.99±.01
MRK-20-TRM-64	Plag-garnet-hornblende gneiss	3.08±.01
MRK-24-TRM-64	Granular Plag-hb rock	2.96±.01
MRK-47-TRM-64	Serpentine schists	3.00±.01
MRK-48-TRM-64	Serpentine schists	2.58±.01
MRK-51-TRM-64	Serpentine schists	2.53±.01

Table D7.

Sample Number	Formation and Lithology	Measured Density
MRX-86-TRM-64	Musc-G-Qtz-peletic schist	3.11±.02
MRX-120-TRM-64	Hg-musc-plag-- schist	3.04±.02
MRX-125-TRM-64	Peletic (musc-G-biot-chl) schist	2.94±.01
MRX-126-TRM-64	diorite paragneiss (biot-qtz-plag gneiss)	2.74±.01
MRX-137-TRM-64	Plag-Qtz-garnet granulite	2.82±.01
MRX-146-TRM-64	Peletic (G-sill-2 feldspar) schist	2.94±.02
MRX-188-TRM-64	Hb granulite (Plag-garnet-hb) gneiss	3.03±.01
MRX-209-TRM-64	Hb granulite (Hb-diopside-plag-G)	3.09±.02
MRX-220-TRM-64	Andesine-Hb amphibolite	2.99±.02
MRX-324-TRM-65	Diorite or Gabbro gneiss (Plag-garnet-hb)	2.90±.01

Dense Rocks

Eclogites

MRX-1-TRM-64	3.44±.02
MRX-3-TRM-64	3.39±.01
MRX-56-TRM-64	3.33±.02
MRX-57A-TRM-64	3.27±.02
MRX-80-TRM-64	3.34±.02
MRX-245-TRM-64	3.34±.02
MRX-247-TRM-64	3.22±.02
MRX-258-TRM-64	3.43±.02

Pyroxenites-Websterite (2 px)

MRX-39-TRM-64	3.26±.02
MRX-57-TRM-64	3.26±.02

Pyroxenite (Jadeite-rich pyroxene + sulfide)

MRX-44-TRM-64	3.34±.01
MRX-271-TRM-64	3.34±.01

Kimberlite

MR-1416A	Greenish-black kimberlite	2.61±.01

Minette

MEM-1	Fresh dike rock, minette	2.83±.01

Sample Number	Formation and Lithology	Measured Density
Garnets		
Orange Almandine	Orange, fractured garnets	3.83 ± .04
Pyropes (4)	Deep purplish red, pyropes	3.72 ± .04

Table D8. Spectrographic Analyses (U.S. Geological Survey, Branch of Analytical Laboratories, Denver, Colorado)

	(1)	(2)	(3)	(4)	(5)	(6)
	MR-1416A	MR-1416B	MRX-44	MRX-50B	MR-1307	MRX-4
	D101565	D101566	D101567	D101568	D101569	D101570
B	.01	.003	0	0	0	0
Ba	.01	.02	.007	.01	.0015	.03
Be	0	0	0	0	0	0
Co	.007	.007	.03	.01	.01	.01
Cr	.1	.15	.05	.02	1.	.015
Cu	.0003	.002	.005	.01	.007	.0001
Ga	0	0	.003	.002	.0005	.003
La	0	0	0	0	0	.003
Mo	0	0	.0007	<.0005	0	<.0005
Nb	0	0	0	0	0	0
Ni	.15	.15	.007	.01	.07	.007
Pb	0	0	0	0	0	0
Sc	.0005	.0005	.002	.007	.007	.003
Sr	.0015	.007	.01	.015	.003	.015
V	.002	.003	.03	.07	.02	.015
Y	0	0	0	.005	0	.003
Yb	0	0	<.0002	.0007	<.0002	.0005
Zr	0	0	.01	.007	0	.03

Looked for only when La or Cr found:

Nd	0	0	0	0	0	0

The following were looked for but not found in any of the samples:

Ag
As
Au
Bi
Cd
Ce
Ge
Hf
Hg
In
Li
Pd
Pt
Re
Sb
Sn
Ta
Te
Th
Tl
U
W
Zn

The following were looked for only when La or Ce found, but not found in any of the samples:

Pr
Sm
Eu

Table D8. Spectrographic Analyses (U.S. Geological Survey, Branch of Analytical Laboratories, Denver, Colorado)

	(7) MRX-6 D101571	(8) MRX-7 D101572	(9) MRX-13 D101573	(10) MRX-95 D101574	(11) MRX-51 D101575	(12) MRX-153 D101576
B	.005	0	0	0	0	0
Ba	.07	.1	.03	.05	.002	.02
Be	.0002	.00015	0	0	0	0
Co	.005	.015	.007	.005	.007	.02
Cr	.003	.007	.01	.007	.2	.01
Cu	.0002	.0002	.01	.003	.003	.0003
Ga	.003	.002	.001	.002	0	.0015
La	.003	.005	0	.003	0	.003
Mo	0	0	0	.0005	0	.0007
Nb	.002	.001	0	0	0	0
Ni	.0015	.001	.003	.003	.1	.0015
Pb	.001	.0015	0	0	0	0
Sc	.0005	.0005	.005	.003	.0015	.002
Sr	.01	.015	.02	.05	.005	.02
V	.001	.001	.02	.02	.007	.005
Y	.0015	.005	0	.005	0	.005
Yb	.0002	.0005	<.0002	.0005	0	.0005
Zr	.01	.015	0	.003	0	.01
Looked for only when La or Ce found:						
Nd	0	0	0	.007	0	0

The following were looked for but not found in any of the samples:

Ag, As, Au, Bi, Cd, Ce, Ge, Hf, Hg, In, Li, Pd, Pt, Re, Sb, Sn, Ta, Te, Th, Tl, U, W, Zn

The following were looked for only when La or Ce found, but not found in any of the samples:

Pr, Sm, Eu

Table D6. Spectrographic Analyses (U.S. Geological Survey, Branch of Analytical Laboratories, Denver, Colorado)

	(13) MRX-190 D101577	(14) MRX-220 D101578	(15) MEM-1 D101579
B	0	0	0
Ba	.03	.01	.2
Be	0	0	.0002
Ce	0	0	.03
Co	.01	.005	.005
Cr	.005	.005	.05
Cu	.015	.01	.007
Ga	.0015	.0015	.002
La	0	0	.02
Mo	0	0	0
Nb	0	0	.003
Ni	.003	.0015	.03
Pb	0	0	.003
Sc	.005	.005	.0015
Sr	.02	.02	.2
V	.02	.02	.02
Y	.0015	.0015	.002
Yb	.0002	.0002	.0002
Zr	.002	.0015	.02
Looked for only when La or Cr found:			
Nd	0	0	.02

The following were looked for but not found in any of the samples:

Ag
As
Au
Bi
Cd
Ge
Hf
Hg
In
Li
Pd
Pt
Re
Sb
Sn
Ta
Te
Th
Tl
U
W
Zn

The following were looked for only when La or Ce found, but not found in any of the samples:

Pr
Sm
Eu

APPENDIX E

This appendix contains a partial tabulation of the solutions to equations (10)(11) for velocity and dike width as functions of position for mass fraction water and assumed dike width at 100 km varied as parameters. The table below summarizes the cases computed. The solution for each case may be found in this appendix in alphabetical order.

Assumed Dike Width at 100 km in Meters
k (meters)

Assumed Mass Fraction Water X_w,%	3	10	30	100	300	50	3000
4	A	B	C	D	E	-	-
10	F	G	H	I	-	U	J
25	K	L	M	N	O	-	-
50	P	Q	R	S	T	-	-

The notation used in the print-out is:

2(N)	depth in kilometers below the surface
U(N)	fluid velocity in cm/sec
D(N)	dike width in cm
Q(N)	the product, $\rho \cdot U \cdot D$ at Z(N)

The constants assumed were:

Z(0)	100 kilometers
g	980 cm/sec^2

Other notation used in the program

R(N), rock density

$Z(N) > 40$ $R(N) = 3.3$

$40 > Z(N) > 25$ $R(N) = 3.0$

$25 > Z(N) > 3$ $R(N) = 2.7$

$3 > Z(N)$ $R(N) = 2.4$

F(N), fluid density (Values taken from Figure 67).

CITRAN program used in calculation of velocity U(N) and dike width, D(N).

```
1.1 P(N) = (R(N)/F(N))-1
1.15 D(0) = k
1.2 C(N) = x(N)/D(N-1)
1.3 A(N) = (A(N-1)+P(N)*g*x(N))/(1+0.1*C(N))
1.4 U(N) = sqrt(2*A(N))
1.5 J(N) = k*U(1)*F(1)
1.6 D(N) =J(N)/(U(N)*F(N))
1.7 Q(N) = F(N)*U(N)*D(N)

2.1  D(0) =k
2.2 do part 1 for N = 1(1)25

3.1 type N, Z(N), U(N), D(N), C(N) in form 1 for N = 1(1)25
```

H_2O= 4%

	Case A		Case B		Case C		Case D		Case E	
Depth	m/sec	m	m/sec	m	m/sec	m	m/sec	m	m/sec	m
50 m	126	6	193	22	262	85	337	389	397	1582
100	97	5	158	17	229	60	307	263	369	1042
200	71	4	122	13	186	44	264	183	330	699
600	41	3	73	10	118	31	185	116	252	408
1 km	32	3	57	9	94	27	153	98	219	330
2	20	3	36	9	61	26	106	88	161	276
4	15	2	26	8	45	24	77	83	116	261
6	11	3	21	9	35	26	59	91	91	281
10	3	3	17	9	(9)	(89)	47	100	63	361
20	(2)	(13)	4	41	(7)	(107)	17	267	35	607
30	6	4	11	12	17	41	25	163	37	525
50	7	3	13	10	23	29	41	96	70	272
90	7	3	13	10	23	30	40	100	63	300
Q	656996		398447		20501918		120735470		577087170	

H_2O= 10%

	Case F		Case G		Case H		Case I	
Depth	m/sec	m	m/sec	m	m/sec	m	m/sec	m
50 m	221	9	324	36	426	141	535	661
100	174	8	273	30	378	112	493	506
200	122	6	207	21	308	72	429	304
600	75	4	133	15	212	49	325	187
1 km	59	4	105	13	173	42	279	152
2	39	4	71	12	120	36	203	127
4	28	3	50	10	85	30	147	101
6	22	3	40	10	68	29	119	97
10	16	3	29	10	50	30	90	99
20	10	4	19	13	33	38	61	122
30	13	3	23	10	39	30	70	99
50	12	3	23	10	39	28	70	93
90	11	3	21	10	36	30	63	100
Q	924521		5606926		28850197		169898360	

H_2O= 25%

Depth	Case K		Case L		Case M		Case N		Case O	
	m/sec	m	m/sec	m	m/sec	m	m/sec	m	m/sec	m
50 m	415	16	585	70	750	282	920	1355	1060	5620
100	327	12	499	48	672	185	853	857	1001	3488
200	243	9	310	27	573	126	762	556	920	2201
600	154	7	264	24	402	81	588	327	761	1210
1 km	110	6	195	20	318	63	500	235	676	832
2	75	5	136	17	227	53	376	188	537	629
4	51	4	92	13	156	40	265	138	400	437
6	39	4	71	12	121	36	211	121	332	368
10	29	3	54	11	92	34	164	113	265	333
20	21	3	38	12	65	35	117	113	196	323
30	20	3	36	10	61	31	110	102	181	294
50	18	3	33	10	58	30	104	97	175	275
90	18	3	33	10	57	30	101	100	161	300
Q	1153081		6993066		35982520		211900490		--	

H_2O= 50%

Depth	Case P		Case Q		Case R		Case S		Case T	
	m/sec	m	m/sec	m	m/sec	m	m/sec	m	m/sec	m
50 m	606	22	846	95	1073	386	1312	1862	1506	7753
100	488	15	733	62	971	240	1225	1122	1429	4596
200	373	12	600	47	841	171	1108	763	1325	3049
600	228	8	391	30	603	100	874	406	1111	1525
1 km	179	7	316	25	506	80	765	312	1004	1137
2	118	7	211	23	348	72	564	260	671	559
4	79	5	144	16	242	48	407	169	604	544
6	59	4	108	14	184	42	321	143	498	440
10	44	4	80	13	137	38	244	127	392	377
20	30	4	55	12	96	35	172	116	288	332
30	28	3	51	11	88	31	157	104	250	299
50	26	3	48	10	82	30	147	97	249	276
90	26	3	47	10	80	30	142	100	226	300
Q	1196312		7255247		37331566		219844990		--	

H_2O= 10%

Depth	Case U m/sec	m	Case J m/sec	m
50 m	473	271	780	-
100	427	212	751	-
200	359	132	705	-
600	257	85	625	8370
1 km	215	72	583	6279
2	151	62	499	4441
4	108	50	419	3036
6	87	48	375	2653
10	65	50	326	2360
20	43	63	289	2202
30	50	50	228	2073
50	50	47	296	1903
90	46	50	181	3000

APPENDIX F

Detailed Geological Cross Sections of the Moses Rock Dike

On the following pages the geological cross sections based on detailed mapping at 1:2400 scale are presented in numerical sequence. The location of these cross sections is shown in Figure 14. The detailed photogeologic map upon which these cross sections are based is not included in this report.

Symbols used are the same as those shown on the generalized geologic map, (Figure 13). Numbered stratigraphic horizons refer to numbered marker horizons within the Cutler Formation shown in Figure 7 (or in Figure 6).

Control for topography is based on contour maps prepared by the U. S. Geological Survey at 1:2400 scale with a 10-foot contour interval and supplementary 5-foot contours where useful. The topographic map was prepared using the same high resolution stereo photographs used in the geologic mapping.

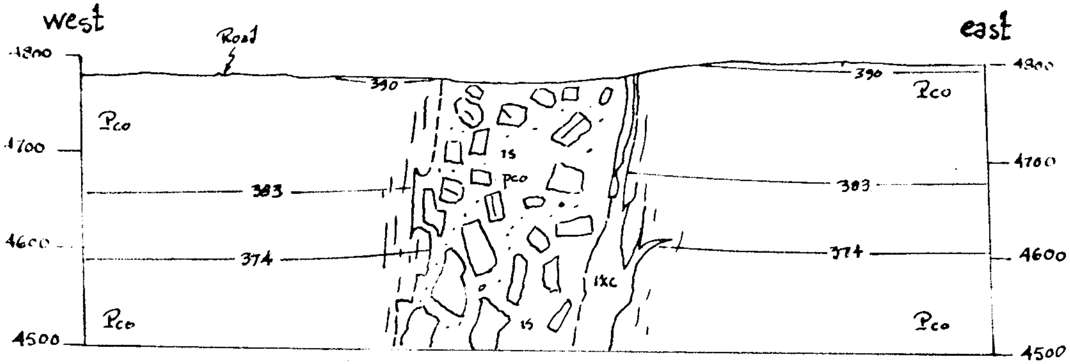

Crossection C1

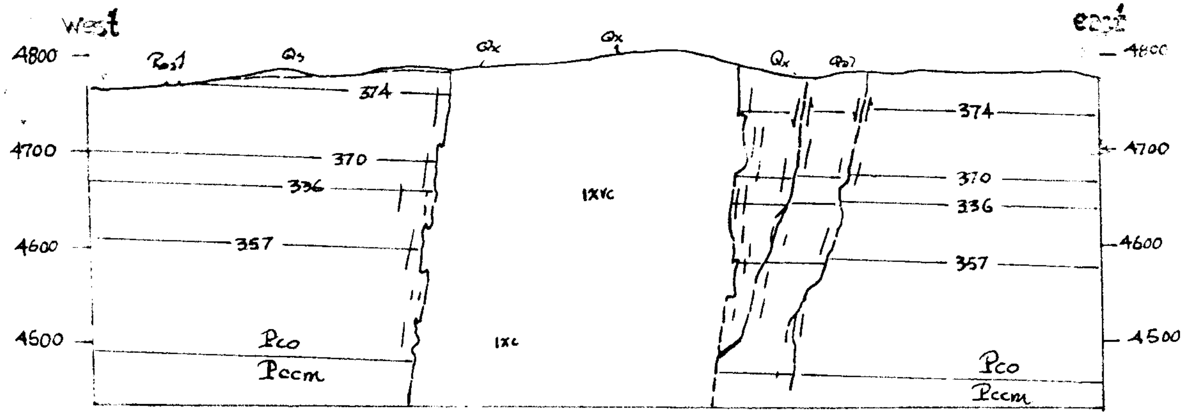

Crossection C2

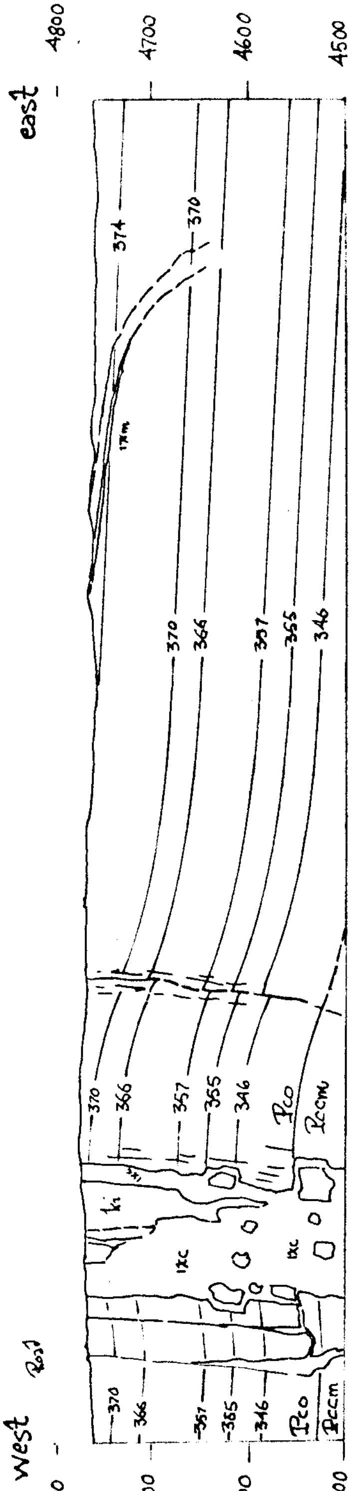

Crossection C6

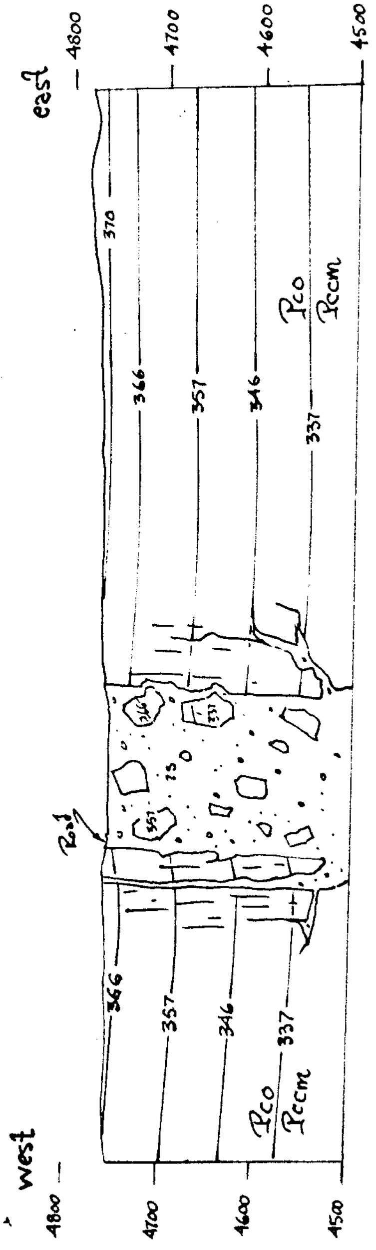

Crossection C7

Crossection C8

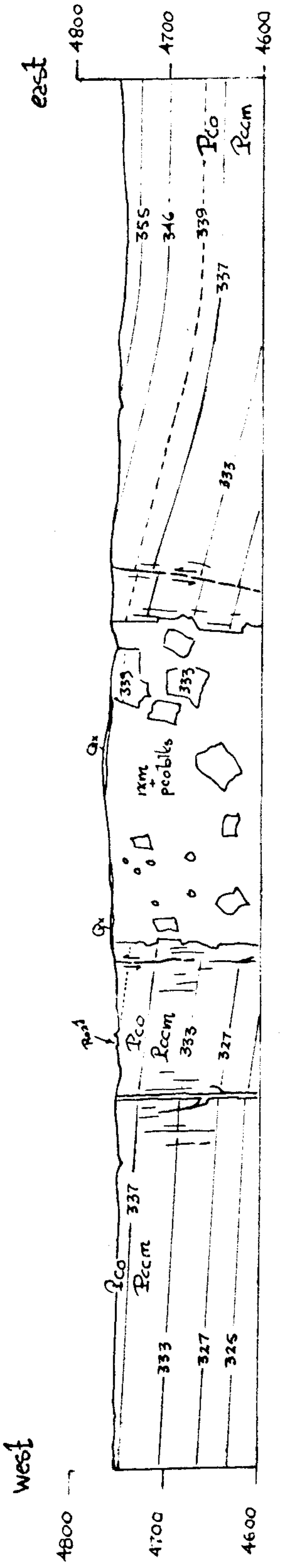

Crossection C9

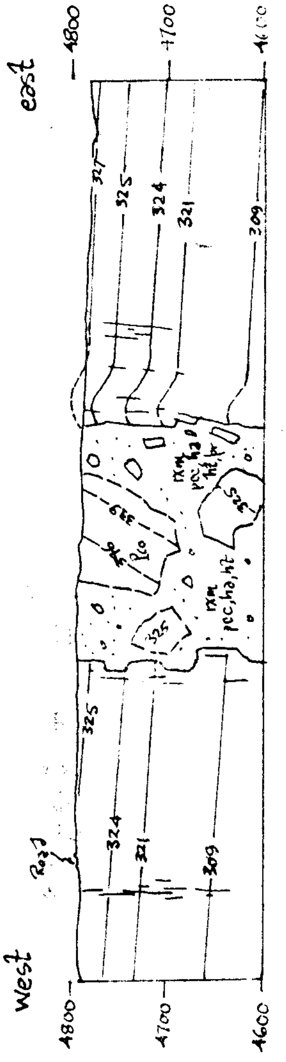

Crossection C10

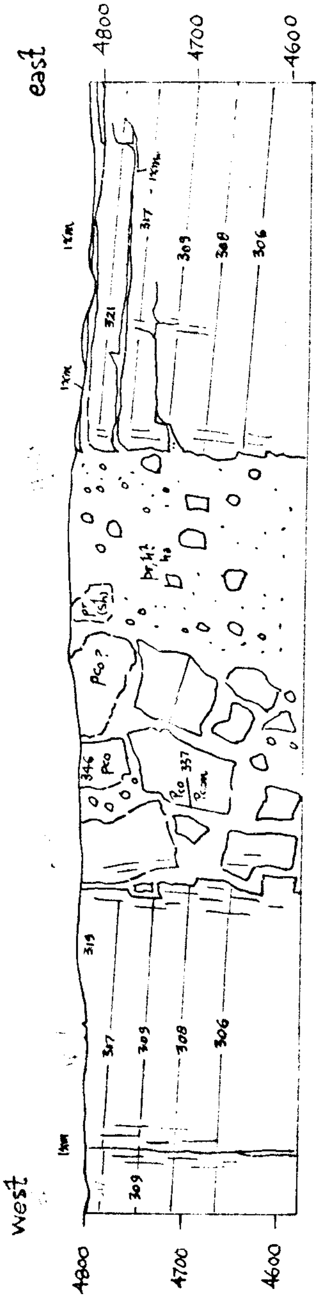

Crossection C11

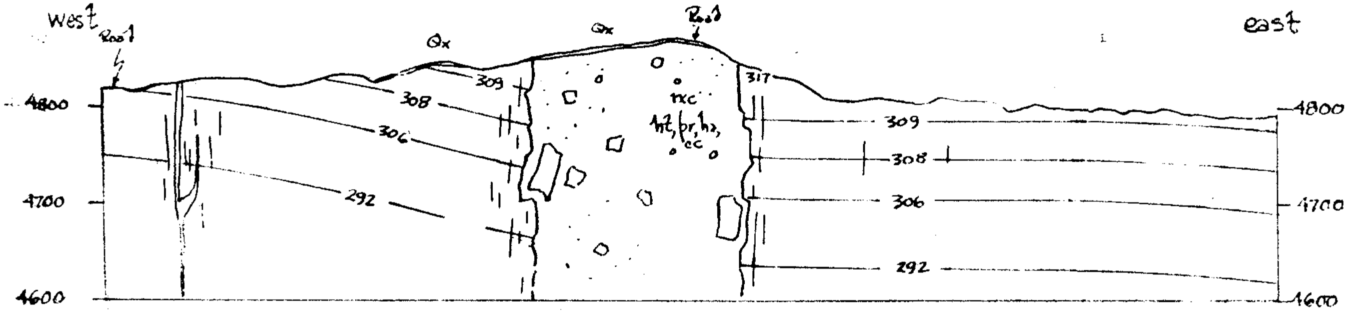

Crossection C_{12}

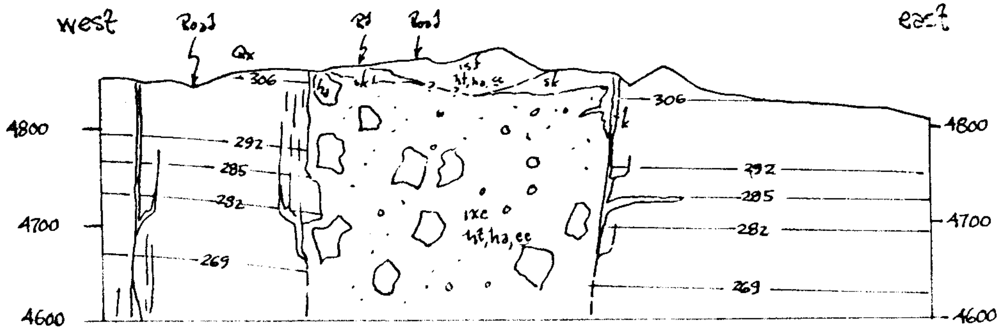

Crossection C_{13}

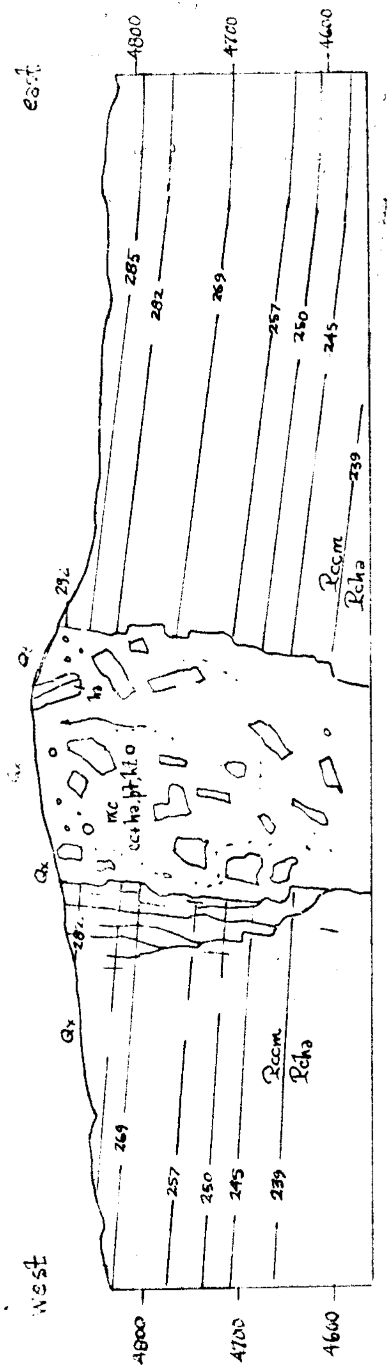

Crossection C14

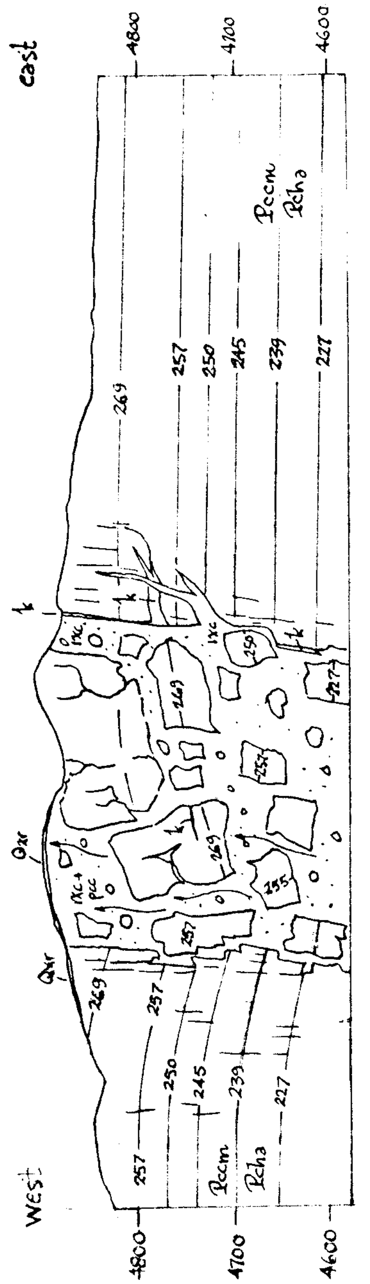

Crossection C16

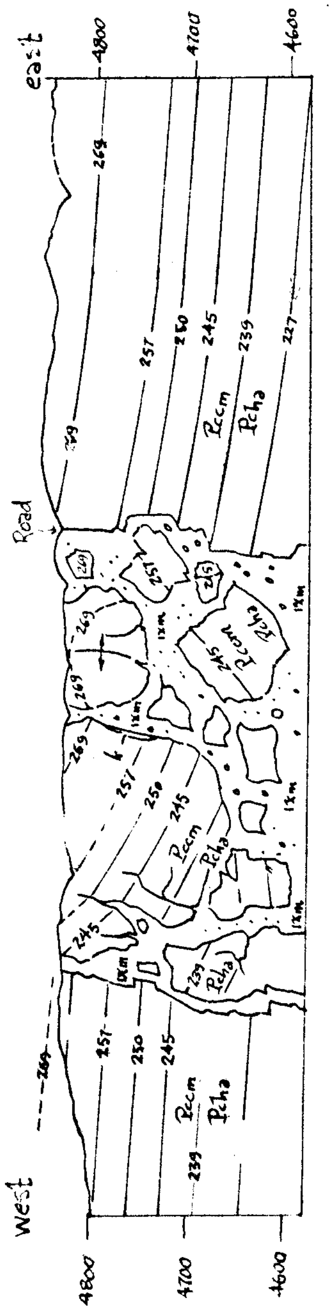

Crossection C_{18}

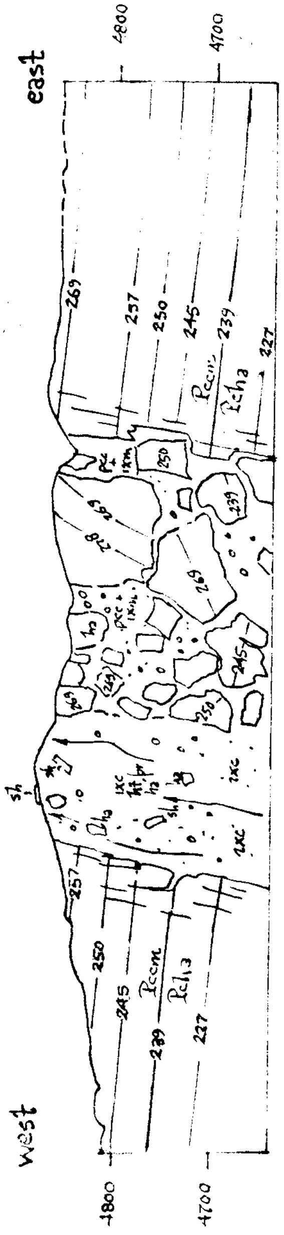

Crossection C_{21}

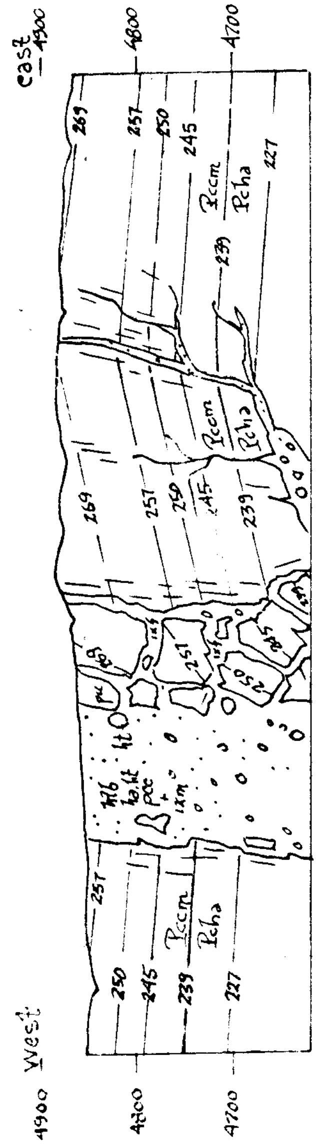

Crossection C_{22}

Crossection C_{23}

Crossection C25

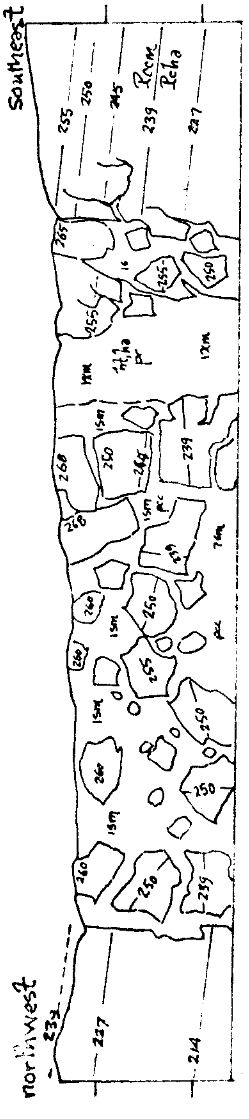

Crossection C27

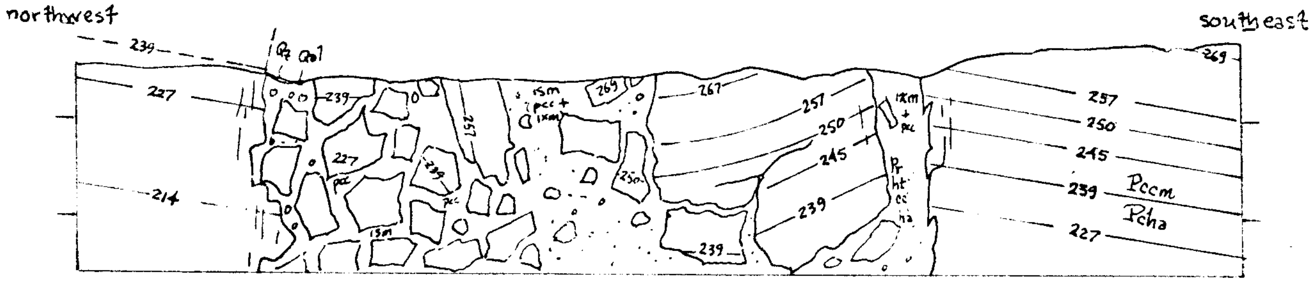

Crossection C29

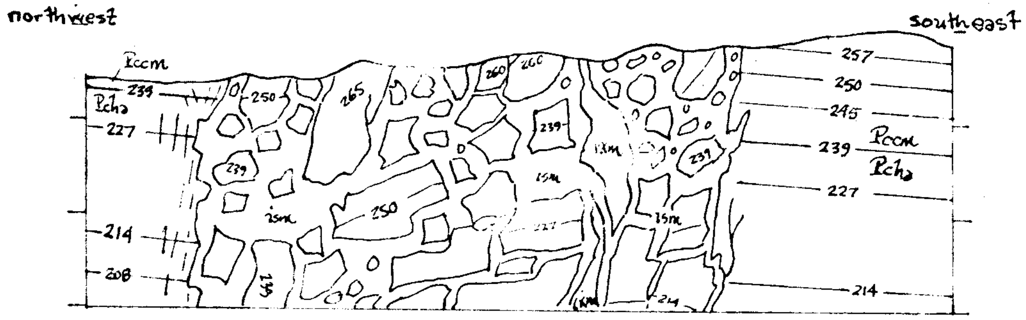

Crossection C30

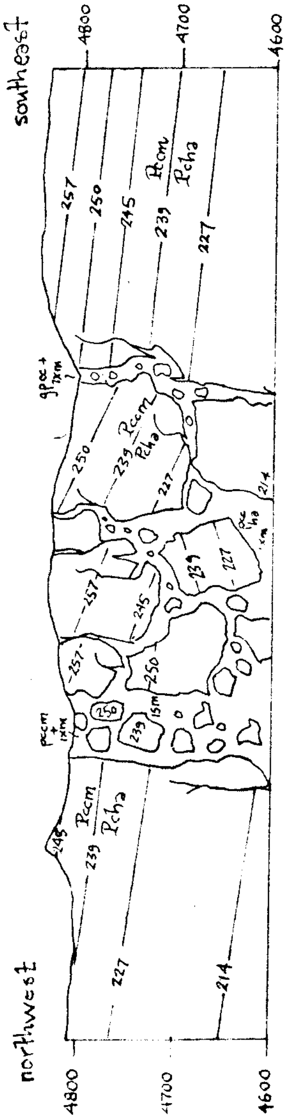

Crossection C32

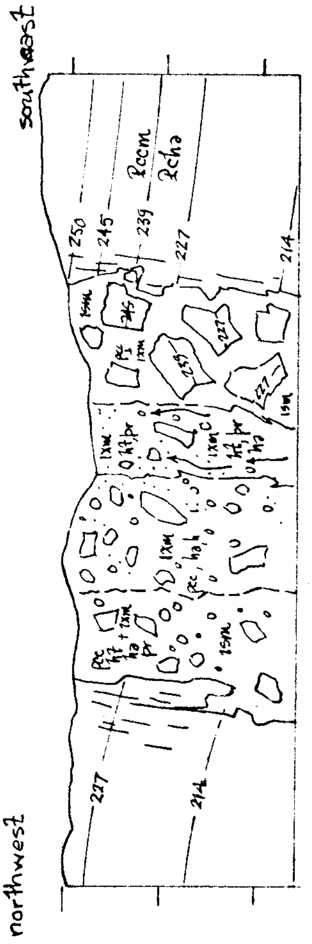

Crossection C33

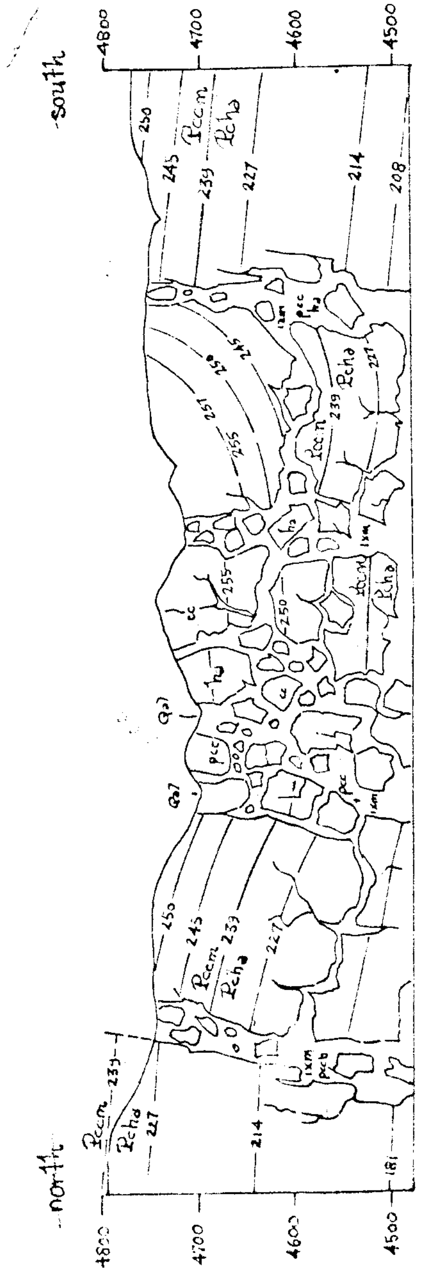

Crossection C34

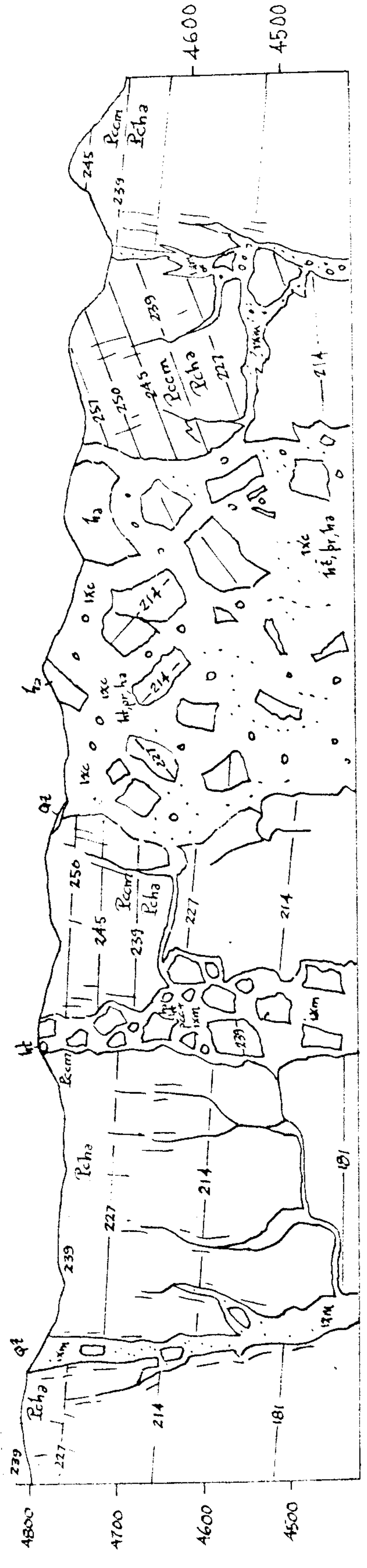

Crossection C35

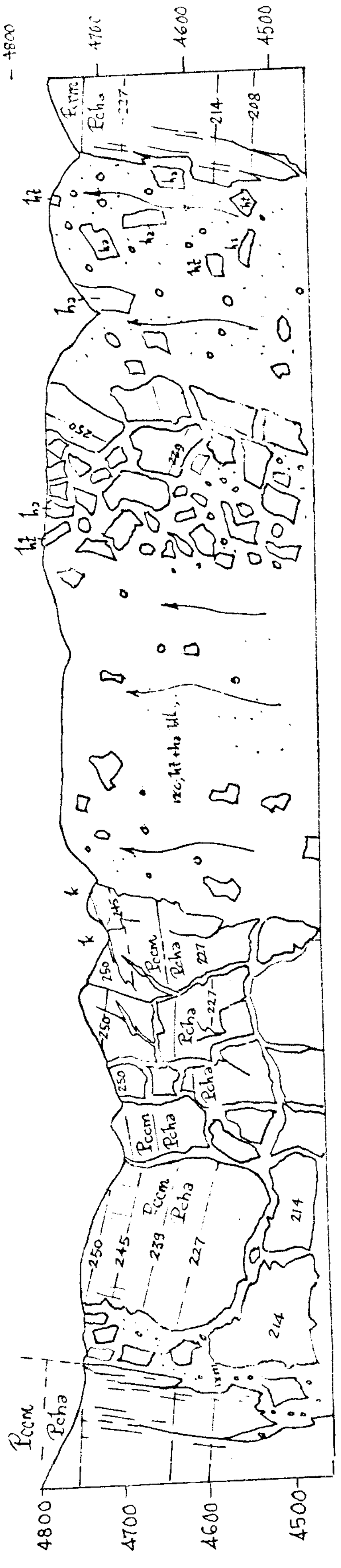

Crossection C36

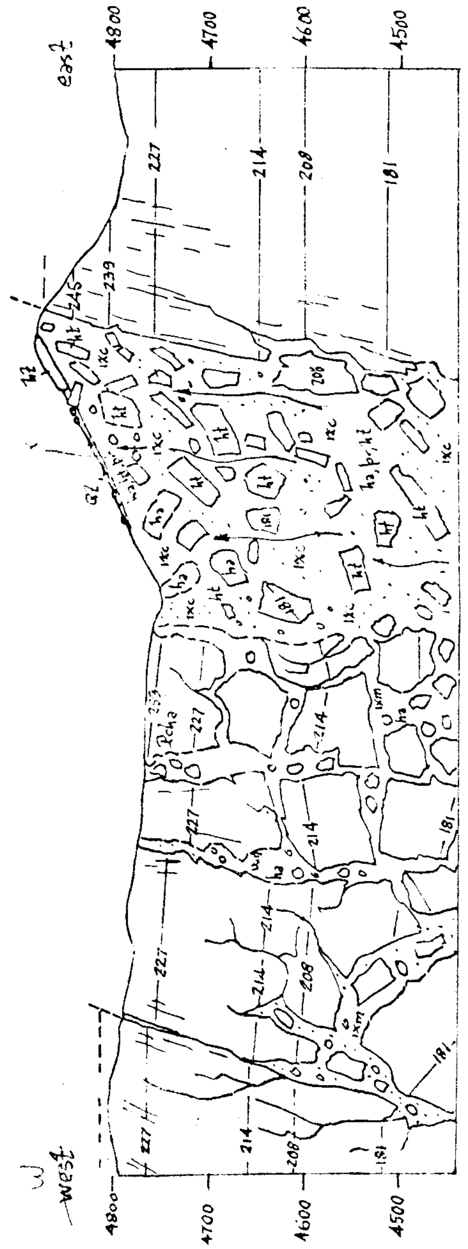

Crossection C37

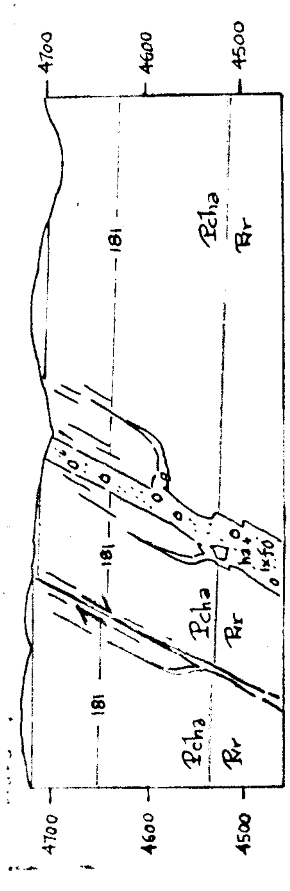

Crossection C_{41}

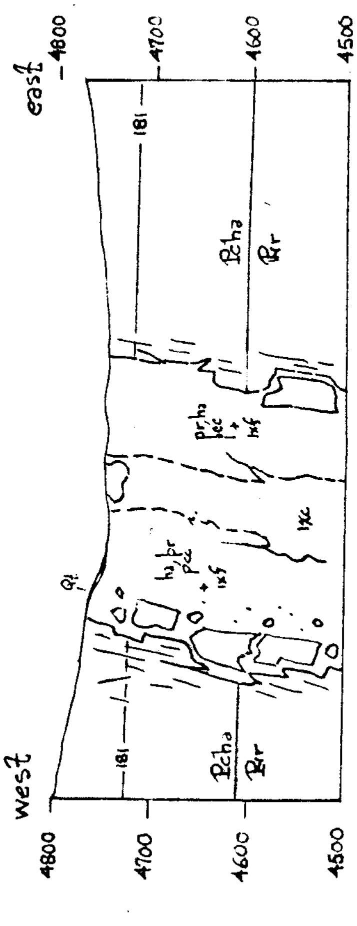

Crossection C_{44}

REFERENCES

Allen, J. E., and R. Balk, 1954, Mineral resources of Fort Defiance and Tohatchi quadrangles, Arizona and New Mexico: New Mexico Bur. Mines and Mineral Res. Bull. 36, p. 192.

Bailey, D. K., 1964, Temperature and vapor composition in carbonatite and kimberlite: Carnegie Inst. of Washington Yr. Book 63, p. 79-81.

Baker, A. A., 1936, Geology of the Monument Valley-Navajo Mountain region, San Juan County, Utah: U. S. Geological Survey Bull. 865.

__________, and J. B. Reeside, Jr., 1929, Correlation of the Permian of southern Utah, northern Arizona, northwestern New Mexico, and southwestern Colorado: Am. Assoc. Petroleum Geologists Bull., v. 13, no. 11, p. 1413-1448.

Balk, R., 1954, Petrology section in Allen and Balk, 1954, Mineral resources of Fort Defiance and Tohatchi quadrangles, Arizona and New Mexico: New Mexico Bureau Mines and Mineral Res. Bull. 36, p. 192.

Bass, R. O., 1963, (ed) Shelf Carbonates of the Paradox Basin, A Symposium: Four Corners Geological Society, Fourth Field Conference.

Bell, P. M., and B. T. C. Davis, 1965, Temperature composition section for jadeite-diopside: Carnegie Inst. Wash. Yearbook p. 120-123.

Boyd, F. R., 1961, Welded tufts and flows in the Rhyolite Plateau of Yellowstone Park, Wyoming.

__________, 1966, Electron microprobe study of diopsidic pyroxenes from kimberlites: Carnegie Inst. of Washington Yr. Book 65, p. 252-260.

__________, and B. T. C. Davis, 1964, Effects of pressure on the melting and polymorphism of enstatite, $MgSiO_3$: J. Geophys. Res., V. 69, p. 2101-2109.

__________, and I. D. MacGregor, 1964, Ultramafic rocks: Carnegie Institute of Washington Yr. Book 63, p. 152-156.

__________, and J. F. Schairer, 1964, The system $MgSiO_3$-$CaMgSi_2O_6$: J. Petrol., V. 5, p. 275-309.

Brock, M. R. and A. V. Heyl, Jr., 1961, Post-Cambrian Igneous Rocks of the Central Craton, western Appalachian Mountains and Gulf Coastal Plain of the United States: Geological Survey Research, Short Papers in the Geological and Hydrological Sciences, U. S. Geological Survey.

Carslaw, H. S., and J. C. Jaeger, 1959, Conduction of Heat in Solids: Oxford Univ. Press.

Case, J. W., and H. R. Joesting, 1961, Precambrian structures in the Blanding basin and Monument upwarp. southeast Utah; in Short papers in the geological and hydrologic sciences: U. S. Geol. Survey Prof. Paper 424-D, p. D287-D291.

Christensen, N. I., 1966, Elasticity of ultrabasic rocks: J. Geophys. Res., v. 71, p. 5921-5931.

Clark, S. P., 1966, Viscosity section R. in Handbook of Physical Constants, Geol. Soc. America, Mem. 97, 587 p., ed. S. P. Clark.

__________, and A. E. Ringwood, 1964, Density distribution and constitution of the mantle: Rev. Geophys., 2, p. 35-88.

Cloos, H., 1941, Bau and Tatigkeit von Tuffschloten-Untersuchungen an dem Schwabishen Vulkan: Geol. Rundschau v.32, H. 6-8, p. 709-800.

Coe, K., 1966, Intrusive tuffs of West Cork, Ireland: Q. Jour. Geol. Soc. Lond., v. 122, p. 1-28.

Coleman, R. G., D. E. Lee, L. B. Beatty, and W. W. Brannock, 1965, Eclogites and eclogites: Their differences and similarities: Geol. Soc. Am. Bull., v. 76, p. 483-508.

Daubree, A., 1891, Recherches experimentales sur le role possible des gaz a haute temperatures, doves de tres forte pressions et animes d'un mouvement fort rapide dans divers phenomenes geologiques: Bull. Soc. Geol. France, 3rd. Ser., 19, p. 313-354.

Davidson, D. F., 1964, On diamantiferous diatremes: Economic Geology, v. 59, p. 1368-1380.

Davis, B. T. C. and F. R. Boyd, 1966, The join Mg_2SiO_6-$CaMgSi_2O_6$ at 30 kb pressure and its application to pyroxenes from kimberlites: J. Geophys. Res., v. 71, p. 3567-3576.

Dawson, J. B., 1962, Basutoland kimberlites: Bull. Geol. Soc. Am., v. 73, p. 545-560.

Edwards, J. Jr., 1966, The petrology and structure of the buried Precambrian basement of Colorado: Quarterly of the Colorado School of Mines, v. 61, no. 4.

Edwards, C. B. and J. B. Howkins, 1966, Kimberlites in Tanganyika with special reference to the Mwadui occurrence: Economic Geology, v. 61, p. 537-554.

Einarsson, T., 1950, The eruption of Hekla, 1947-1948, IV, 5, The basic mechanism of volcanic eruptions and the ultimate causes of volcanism: Rit. Visind. Isl. (Soc. Sci. Islandica), Reykjavik, 30 pp.

Fitzsimmons, J. P., 1963, Precambrian of the four corners area: in Shelf Carbonates of the Paradox Basin, Four Corners Geological Society, Field Conference, R. O. Bass, editor.

Fenneman, N. M., 1931, Physiography of the Western United States, 534 pp.

Geike, A., 1902, The geology of eastern Fife: Geol. Survey Scotland, Mem., 421 pp.

__________, 1920, The geology of eastern Fife: Geol. Survey Scotland, Mem., p. 1-161.

Goguel, J., 1953, Le regime therique de l'eau souterraine: Annales de Mines, Ministere de l'Energy, v. 10, pp. 3-32.

__________, 1956, Le mechanism d'Explosions Phreatiques: Int. Union Geol. and Geophys., Trans., Ser. A., No. 19, pp. 165-175.

Greenwood, H. J. and H. L. Barnes, 1966, Binary Mixtures of Volatile Compounds: Section 17 in Handbook of Physical Constants, Geol. Soc. Amer., Mem. 97, ed. S. Clark.

Gregory, H. E., 1915, The igneous origin of the "glacial deposits" on the Navajo Reservation, Arizona and Utah: Am. Jour. Sci., 4th ser., v. 40, p. 97-115.

__________, 1938, The San Juan country, a geographic and geologic reconnaissance of southeastern Utah: U. S. Geol. Survey Prof. Paper 188, 123 pp.

Hess, H. H., 1954, Serpentine, orogeny and Epeirogeny: Geol. Soc. Amer., Special Paper 62, p. 391-408.

Holmes, A., 1936, Contributions to the petrology of kimberlites and its inclusions, Trans. Geol. Soc. S. Africa, 39, p. 379-428.

Hunt, C. B., 1956, Cenozoic geology of the Colorado Plateau: U. S. Geol. Survey Prof. Paper 279, 99 pp.

__________, P. Averitt, and R. L. Miller, 1953, Geology and geography of the Henry Mountains Region, Utah: U. S. Geological Survey Prof. Paper 228, 234 pp.

Ito, K. and G. C. Kennedy, 1967, Melting and Phase Relations in a natural peridotite to 40 kilobars: Am. Jour. Sci., v. 519, pp. 519-538.

Kay, J. M., 1963, Fluid Mechanics and Heat Transfer, Cambridge Univ. Press, 247 pp.

Kelley, V. C., 1955, Regional tectonics of the Colorado Plateau and relationship to the origin and distribution of uranium: Univ. New Mexico Publications in Geology, no. 5, Albuquerque, New Mexico, 120 pp.

Kennedy, G. C. and W. T. Holser, 1966, Pressure-Volume-Temperature and phase relations of water and carbon dioxide: Section 16, Handbook of Physical Constants, Geol. Soc. Am., Mem. 97, F. Birch, ed.

Kitahara, S., S. Takenouchi, and G. C. Kennedy, 1966, Phase relations in the system MgO-SiO_2-H_2O at high temperatures and pressures: Am. Jour. Sci., 264, p. 223-233.

Kullerud, G., 1964, Review and evaluation of recent research on geologically significant sulfide-type systems: Fortschritte der Mineralogie, Band 41, Heft 2, 221-270.

Krutojarsky, M. A., 1958, Kimberlites of the River Omonoos, Olenek district (Yakutia): All-Union Mineralog. Soc. Mem., v. 87, p. 166-180.

Leva, M., 1959, Fluidization, 327 pp., McGraw-Hill Publ. Comp., New York.

Malde, H. E., 1954, Serpentine pipes at Garnet Ridge: Science, v. 119, p. 618.j

__________, and R. E. Thaden, 1963, Serpentine at Garnet Ridge in geology, and uranium-vanadium deposits of the Monument Valley area, Apache and Navajo Counties, Arizona, by I. J. Witkind and R. E. Thaden: U. S. Geol. Survey Bull. 1103.

McBirney, A. R., 1959, Factors governing emplacement of volcanic necks: Am. J. Sci., v. 257, no. 6, p. 431-448.

__________, 1963, Breccia pipe near Cameron, Ariz.: Discussion: G. S. A. Bull., V. 74, pp. 227-232.

Meloy, T. P., 1963, Cumulative and weight retained tables for the Gaudin-Meloy size distribution: Trans. Soc. of Mining Eng. of Am. Inst. Mech. Eng., v. 226, p. 357-361.

Mercy, E. L. P., and M. J. O'Hara, 1965a, Websterite from Glenelg, Inverness-shire, Scottish Journal of Geology, v. 1, part 3.

__________, and __________, 1965b, Olivines and orthopyroxenes from gernetiferous peridotites and related rocks: Saertrykk av Norsk Geologish Tiasskrift, nr. 4.

Miser, H. D., 1922, Diamond-bearing peridotite in Pike County, Arkansas: Econ. Geol., v. 17, pp. 662-674.

__________, 1923, Diamond-bearing peridotite in Pike County, Arkansas: U. S. G. S. Bull. 735, p. 271-336.

__________, and C. S. Ross, 1925, Volcanic Rocks in the Upper Cretaceous of S. W. Arkansas and S. E. Oklahoma: Am. J. Sci., v. 9, pp. 113-126.

Moody, L. I., 1944, Friction Factors for Pipe Flow: Trans. Am. Soc. Mech. Eng., v. 66, p. 671.

Murphy, W. J., 1949, Fluidization Nomenclature and Symbols, Industrial and Engineering Chem., v. 41, no. 6, pp. 1249-1250.

Nixon, P. H., O. von Knorring and J. M. Rooke, 1963, Kimberlites and associated inclusions of Basutoland: A mineralogical and geochemical study: Am. Mineral. 48, 1090-1132.

O'Hara, M. J., 1967, Mineral paragenesis in ultrabasic rocks, chapter in Ultramafic and Related Rocks, ed. P. J. Wyllie, 1967, John Wiley and Sons, N. Y.

__________, and E. L. P. Mercy, 1966, Eclogite, peridotite, and pyrope from the Navajo Country, Arizona and New Mexico: American Mineralogist 51, p. 336-352.

__________, and H. S. Yoder, 1967, Formation and fractionation of basic magmas at high pressures: Scottish J. Geol., v. 3, pp. 67-117.

O'Sullivan, R. B., 1965, Geology of the Cedar Mesa-Boundary Butte area, San Juan County, Utah: U. S. Geol. Survey Bull. 1186.

Oxburgh, E. R., 1964, Petrological evidence for the presence of amphibole in the upper-mantle and its petrogenetic and geophysical implications: Geol. Mag 101, pp. 1-19.

Pakiser, L. C., and I. Zietz, 1965, Transcontinental crustal and upper-mantle structure: Reviews of Geophysics, v. 3, no. 4.

Press, F., 1966, Seismic velocities, Section 9 in Handbook of Physical Constants: Geol. Soc. of Amer. Memoir 97.

Rannie, W. D., 1962, Perturbation analysis of one-dimensional heterogeneous flow in rocket nozzles: pp. 117-144 in V. 6, Progress in Astronautics and Rocketry, ed. S. S. Penner and A. F. Williams, Academic Press, New York.

Reynolds, D. L., 1954, Fluidization as a geological process and its bearing on the problem of intrusive granites: Am. Jour. Sci., v. 252, no. 11, p. 577-613.

Ringwood, A. F., I. D. MacGregor, and F. R. Boyd, Jr., 1964, Petrological constitution of the upper mantle: Carnegie Institute of Washington Yr. Book 63, p. 147-152.

Robertson, E. C., F. Birch, and G. J. F. MacDonald, 1957, Experimental determination of jadeite stability relations to 25,000 bars: Amer. Journ. Sci., v. 255, p. 115.

Roller, J. C., 1965, Crustal structure in the eastern Colorado Plateaus (sic) Province from seismic-refraction measurements: S. S. A. Bull. 55, p. 107-119.

__________, and W. H. Jackson, 1966, Seismic wave propagation in the upper-mantle: Lake Superior, Wisconsin, to central Arizona: Jour. of Geophys. Res., v. 71, no. 24.

Rosenfeld, J. L., and A. B. Chase, 1961, Pressure and temperature of crystallization from elastic effects around solid inclusions in minerals: Amer. Jour. Sci., v. 259, p. 519-541.

Ross, C. S., M. D. Foster, and A. T. Myers, 1954, Origin of dunites and of olivine-rich inclusions in basaltic rocks: Am. Min. v. 39, p. 693-737.

Roy, R., 1963, Heat flow measurements in the United States: Ph.D. Thesis, Harvard Univ.

Schlichting, H., 1961, Boundary layer theory, Section 9 in V. L. Streeter, Handbook of Fluid Dynamics, McGraw Hill Book Comp., New York.

Shoemaker, E. M., 1954, Structural features of southeastern Utah and adjacent parts of Colorado, New Mexico and Arizona: in Uranium deposits and General Geology of Southeastern Utah, Guidebook to the Geology of Utah, No. 9, Utah Geological Survey, p. 48-69.

__________, 1956, Occurrence of uranium in diatremes on the Navajo and Hopi Reservations, Arizona and New Mexico, and Utah, in L. R. Page, H. E. Stocking, and H. B. Smith, compilers, Contributions to the Geology of Uranium and Thorium by the United States Geological Survey and Atomic Energy Commission for the United Nations International Conference on peaceful uses of atomic energy, Geneva, Switzerland, 1955: U. S. Geol. Survey Prof. Paper 300, p. 179-185.

__________, 1962, Interpretations of Lunar Craters, Ch. 8: Physics and Astronomy of the Moon, ed. Z. Kopal.

__________, C. H. Roach and F. M. Byers, Jr., 1962, Diatremes and uranium deposits in the Hopi Buttes, Arizona: Petrologic Studies: A Volume to Honor A. F. Buddington, p. 327-355.

__________, and H. J. Moore, 1957, Unpublished map, Mule Ear diatreme.

Skinner, B. J., and F. R. Boyd, 1964, Aluminous enstatites: Carnegie Inst. of Washington Yr. Book 63, p. 163-165.

Smirnos, G. I., 1959, Mineralogy of the Siberian kimberlites: Intern. Geol. Rev. 1, p. 21-39.

Stanyakovich, K. P., 1960, Unsteady Motion of Continuous Media: 745 pp., translation from the Russian by J. G. Adashko, ed. by M. Holt.

Sterret, D. B., 1909, Precious stones in mineral resources of the United States, Part 2: U. S. Geol. Survey, p. 823-827.

Stewart, J. H., 1957, Proposed nomenclature of part of upper Triassic strata in southeastern Utah: Am. Assoc. Petroleum Geol. Bull., v. 41, p. 441-465.

Streeter, 1961, Handbook of Fluid Dynamics: McGraw-Hill Publ. Co., New York.

Summerfield, M., 1959, The liquid propellant rocket engine, Section G, pp. 439-520 in Jet Propulsion Engines, v. xii, High Speed Aerodynamics and Jet Propulsion, ed. O. E. Lancaster, Princeton Univ. Press, Princeton, New Jersey.

Wagner, P. A., 1914, The diamond fields of Southern Africa: The Transvaal Leader, Johannesburg, Union of South Africa, 347 pp.

__________, 1928, The evidence of the kimberlite pipes of the constitution of the outer part of the earth: South African Jour. of Sci., v. XXV, p. 127-148.

Wasserburg, G. J., G. J. F. MacDonald, F. Hoyle and W. A. Fowler, 1964, Relative contributions of uranium, thorium and potassium to heat production in the Earth: Science, v. 143, p. 465-467.

Watson, K. D., 1960, Eclogite inclusions in serpentine pipes at Garnet Ridge, northeastern Arizona: Bull. Geol. Soc. Am. 71, p. 2082-2083.

Weeks, A. D., and R. M. Garrels, 1959, Geologic setting of the Colorado Plateau ores, in Geochemistry and Mineralogy of the Colorado Plateau Uranium Ores: U. S. Geol. Survey Prof. Paper 320, Part I, p. 3-11.

Wengerd, S. A., 1963, Stratigraphic section of Honaker Trail, San Juan Canyon, San Juan County, Utah: in Shelf Carbonates of the Paradox Basin, A Symposium, R. O. Bass, ed., Four Corners Geol. Soc., Fourth Field Conference, 273 pp.

White, R. W., 1966, Ultramafic inclusions in basaltic rocks from Hawaii: Contr. to Mineral. and Petrol. 12, p. 245-314.

Williams, A. F., 1932, The Genesis of the Diamond, 2 vol.

Williams, H., 1936, Pliocene volcanoes of the Navajo-Hopi Country: Geol. Soc. America Bull., v. 47, p. 111-172.

Witkind, I. J., and R. E. Thaden, 1963, Geology and uranium-vanadium deposits of the Monument Valley area, Apache and Navajo Counties, Arizona: U. S. Geol. Survey Bull. 1103, 171 pp.

Wones, D. R., and H. P. Eugster, 1965, Stability of biotite: Experiment, theory and application: Am. Mineralogist, 50, p. 1228-1272.

Woodruff, E. G., 1912, Geology of the San Juan oil field: U. S. Geol. Survey Bull. 471-A, p. 76-104.

Wyllie, P. J., 1967, Ultramafic and Related Rocks, 464 pp., John Wiley and Sons, New York.

Yoder, H. S., Jr., and C. E. Tilley, 1962, Origin of basalt magmas: An experimental study of natural and synthetic rock systems: Jour. Petrol. 3, p. 342-532.

Zabrodsky, S. S., 1963, Hydrodynamics and Heat Transfer in Fluidized Beds, 379 pp.

Zenz, F. A. and Othmer, D. F., 1960, Fluidized and Fluid Particle Systems: Reinhold Chem. Eng. Series: Reinhold Publ. Corp., New York, 513 pp.